LEABHARLANN CHOLÁISTE NA TRÍONÓIDE, BAILE ÁTHA CLIATH | TRINITY COLLEGE LIBRARY DUBLIN
Ollscoil Átha Cliath | The University of Dublin

**Terms and Conditions of Use of Digitised Theses from Trinity College Library Dublin**

**Copyright statement**

All material supplied by Trinity College Library is protected by copyright (under the Copyright and Related Rights Act, 2000 as amended) and other relevant Intellectual Property Rights. By accessing and using a Digitised Thesis from Trinity College Library you acknowledge that all Intellectual Property Rights in any Works supplied are the sole and exclusive property of the copyright and/or other IPR holder. Specific copyright holders may not be explicitly identified. Use of materials from other sources within a thesis should not be construed as a claim over them.

A non-exclusive, non-transferable licence is hereby granted to those using or reproducing, in whole or in part, the material for valid purposes, providing the copyright owners are acknowledged using the normal conventions. Where specific permission to use material is required, this is identified and such permission must be sought from the copyright holder or agency cited.

**Liability statement**

By using a Digitised Thesis, I accept that Trinity College Dublin bears no legal responsibility for the accuracy, legality or comprehensiveness of materials contained within the thesis, and that Trinity College Dublin accepts no liability for indirect, consequential, or incidental, damages or losses arising from use of the thesis for whatever reason. Information located in a thesis may be subject to specific use constraints, details of which may not be explicitly described. It is the responsibility of potential and actual users to be aware of such constraints and to abide by them. By making use of material from a digitised thesis, you accept these copyright and disclaimer provisions. Where it is brought to the attention of Trinity College Library that there may be a breach of copyright or other restraint, it is the policy to withdraw or take down access to a thesis while the issue is being resolved.

**Access Agreement**

By using a Digitised Thesis from Trinity College Library you are bound by the following Terms & Conditions. Please read them carefully.

I have read and I understand the following statement: All material supplied via a Digitised Thesis from Trinity College Library is protected by copyright and other intellectual property rights, and duplication or sale of all or part of any of a thesis is not permitted, except that material may be duplicated by you for your research use or for educational purposes in electronic or print form providing the copyright owners are acknowledged using the normal conventions. You must obtain permission for any other use. Electronic or print copies may not be offered, whether for sale or otherwise to anyone. This copy has been supplied on the understanding that it is copyright material and that no quotation from the thesis may be published without proper acknowledgement.

# Spectroscopic Investigations of SiGe Nano-Structures

By

John Matthew Anthony McCarthy

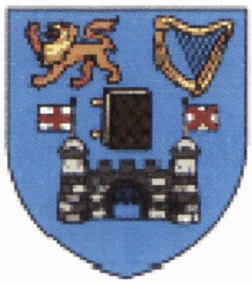

A thesis submitted for the degree of
Doctor of Philosophy
of the
University of Dublin

Department of Electronic and Electrical Engineering
University of Dublin, Trinity College Dublin

TRINITY COLLEGE
2 7 MAY 2008
LIBRARY DUBLIN
THESIS
8388

# Declaration

I, the undersigned, declare that this thesis is entirely my own work, except where otherwise accredited, and that it has not been submitted for a degree at any other university or institution. I furthermore agree that the library may lend or copy this thesis upon request.

Signed,

John McCarthy

22nd of May 2007

To you

# Abstract

This work investigates the growth of several novel structures using a variety of spectroscopic techniques.

Strained Si caps deposited on a relaxed SiGe layer are grown with resulting dislocations found to be perfectly confined to the underlying graded layer. Surface morphology is investigated and Moiré Fringes are used in conjunction with Raman spectroscopic techniques to provide an overall pic
ture of the stress present in the Si cap. The Si cap contains stress values greatly exceeding previously reported stress levels in the literature for similar structures. Ge p-n photodiode structures are grown using both novel and conventional techniques with the difference in resulting structure analysed in terms of dislocation density and stress variation of the top layers. The influence of foil thickness on elemental mapping is proven, while the confinement of dislocations in the graded layer sample is in excellent agreement with expected results. Strained Si quantum wells are grown using two distinct novel techniques, with the removal of the conventional SiGe graded layer shown to have negligible impact on the density of threading dislocations, with excellent layer growth reported. The use of a low temperature virtual substrate identified the importance of optimal temperature choice, with Raman techniques displaying a strong correlation between line width and relaxation levels. A generic interface is developed that allows for the integration of various data from a wide variety of disparate techniques. Statistical analysis is performed on Raman phonon positions within thin SiGe layers, with a new equation proposed that allows for more accurate Raman measurements in line with benchmarked X-Ray Diffraction (XRD) values. Subsequent validation of the proposed model revealed excellent agreement with XRD measurements. Finally Micro-Electro-Mechanical-Systems (MEMS) are characterised using both Raman and white light interferometry techniques. Suitable shape variation is identified in line with expected stress variations across the device. Detailed stress mapping, suitable to the development of stress templates at manufacturing level, is proposed using micro-Raman techniques.

## Acknowledgements

The research undertaken for this thesis was guided and encouraged throughout by Dr. A. Moore and Dr. T. Perova, to whom the author would like to express his gratitude and indebtedness.

The author also wishes to record his appreciation to Dr. S. Bhattarcharya, whose contribution of time and useful materials was much appreciated; to Dr. K. Lyutovich for her consultations and various samples and to Mr. T. Ó'Súilleabháin for his excellent contribution to the area of statistical analysis.

The author would like to take this opportunity to thank the various members of the MTL group for their sustained encouragement and interest; to Mr. M. Langan and G. O'Sullivan for providing stimulating exchange of ideas; to Mr. L. Barry for his technical assistance; to St. Judes G.A.A club who sustained his physical well being; and to my many friends who gave much needed companionship.

Finally, the author would like to express his thanks and appreciation to a number of family members and friends who made this thesis possible. To his parents, who provided valuable help, food and clean clothes on many occasions; to his four sisters, who with their patience and encouragement gave great succour during this long journey; to Éimhín, a woman blessed with vision and determination, who engaged this author at so many levels. Cuireann tú gliondar ar mo chroí agus rí-rá i mo shaol; and to the O'Muircheartaigh family whose contribution of time and useful suggestion in discussion was much appreciated.

# Table of Contents


| | |
|---|---|
| **Declaration** | ii |
| **Dedication** | iii |
| **Summary** | iv |
| **Acknowledgements** | v |
| **Table of Contents** | vi |
| **List of Figures** | xii |
| **List of Tables** | xix |
| **Acronyms and Abbreviations** | xx |
| **Author's Publications** | xxii |
| **Preface** | 1 |
| **1 Si/SiGe heterostructures** | 3 |
| 1.1 Introduction | 3 |
| 1.2 Moore's Law | 3 |
| 1.3 Tomorrow's Technology Today | 5 |
| 1.4 Silicon Germanium | 6 |
| 1.4.1 Strain and Lattice Constant | 10 |
| 1.4.2 Critical Thickness | 12 |
| 1.4.3 Strain Relaxed SiGe Buffer Layers | 15 |
| 1.4.4 Morphology | 18 |
| 1.4.5 Growth Techniques | 18 |
| 1.4.5 Bandgap Engineering | 19 |
| 1.5 Conclusions | 23 |

| | | |
|---|---|---|
| **2** | **Experimental Procedures Si/SiGe** | 27 |
| 2.1 | Introduction | 27 |
| 2.2 | Possible Methods of Analysis | 28 |
| | 2.2.1 X-Ray | 29 |
| | 2.2.1 Optical Metrology | 30 |
| 2.3 | Techniques Used | 30 |
| | 2.3.1 Transmission Electron Microscope (TEM) | 31 |
| | 2.3.1.1 Specimen Interaction | 33 |
| | 2.3.1.1.1 Unscattered Electrons | 34 |
| | 2.3.1.1.1 Elastically Scattered Electrons | 34 |
| | 2.3.1.1.1 Inelastically Scattered Electrons | 35 |
| | 2.3.1.2 Energy Dispersive X-Ray Spectroscopy (EDS) | 35 |
| | 2.3.1.3 Electron Energy Loss Spectroscopy (EELS) | 37 |
| | 2.3.1.4 TEM Specimen Preparation | 39 |
| | 2.3.2 Raman Spectroscopy | 40 |
| | 2.3.2.1 The Raman Effect | 41 |
| | 2.3.2.2 The Scattering Process | 42 |
| | 2.3.2.3 Raman Selection Rules and Intensities | 43 |
| | 2.3.2.4 Effect of Stress on the Raman modes of silicon | 47 |
| | 2.3.2.5 Raman Spectra Measurements | 49 |
| | 2.3.3 X-Ray Diffraction | 51 |
| | 2.3.3.1 Applications | 53 |
| 2.4 | Conclusions | 53 |

| | | |
|---|---|---|
| **3** | **Investigation of Strained Silicon Using a Variety of Techniques** | 57 |
| 3.1 | Introduction | 57 |
| 3.2 | Strained Silicon Process | 58 |
| 3.3 | Dislocations | 61 |
| | 3.3.1 Threading Dislocations | 62 |
| | 3.3.1.1 Concept of Critical Thickness and Dislocations | 62 |
| 3.4 | Raman Analysis for Si/SiGe | 65 |
| | 3.4.1 Depth of Penetration | 67 |
| | 3.4.2 Relaxation Factor | 68 |
| 3.5 | Growth and Analysis of Strained Silicon (S1,S2,S3) samples | 69 |
| | 3.5.1 Atomic Force Microscopy Analysis (AFM) | 72 |
| | 3.5.2 Raman Spectrum | 73 |
| | 3.5.3 TEM Analysis of Samples S1, S2, S3 | 73 |
| 3.6 | Virtual Substrates | 74 |
| 3.7 | Modified Growth and Analysis of Strained Silicon samples S6 and S11 | 75 |
| | 3.7.1 TEM Analysis of Strained Silicon samples S6 and S11 | 77 |
| | 3.7.2 AFM Analysis of samples S6 and S11 | 79 |
| | 3.7.3 Raman Analysis | 80 |
| | 3.7.3.1 Ge Composition and Stress Calculations in Heterostructure Materials | 81 |
| 3.8 | Moiré Fringes | 83 |
| | 3.8.1 Moiré Fringes: An explanation | 84 |
| 3.9 | Investigation of Moiré-Like Fringes | 84 |

| | | |
|---|---|---|
| | 3.9.1 Influence of Sample Thickness | 86 |
| | 3.9.2 Calculation of Strain | 88 |
| 3.9 | Conclusions | 90 |
| **4** | **Dislocation, Composition and Strain Analysis of SiGe Layers within Ge P-N photdiode structures** | 95 |
| 4.1 | Introduction | 95 |
| 4.2 | Thin Film Virtual Substrates versus SiGe Graded Layers | 96 |
| 4.3 | Sample Structure and Sample Preparation | 98 |
| 4.4 | TEM Measurements | 99 |
| 4.5 | Defect Dynamics and Structure in SiGe Graded Composition Layers | 99 |
| 4.6 | Dislocation Density | 102 |
| 4.7 | TEM Investigation of Graded SiGe Layers | 103 |
| 4.8 | Composition and Growth Gradient | 108 |
| 4.9 | EDS Analysis | 110 |
| 4.10 | EELS Analysis | 114 |
| | 4.10.1 Resolving the Effect of Foil Thickness | 117 |
| 4.11 | Strain Analysis | 119 |
| | 4.11.1 Raman Spectroscopy | 119 |
| | 4.11.2 XRD Strain Analysis | 124 |
| | 4.11.2.1 Calculation of Strain using XRD | 124 |
| 4.12 | XRD Structure Analysis | 127 |
| 4.13 | Conclusions | 129 |

| | | |
|---|---|---|
| **5** | **Interface Development and Dataset Analysis** | 133 |
| 5.1 | Introduction | 133 |
| 5.2 | Visual Basic for Applications (VBA) | 134 |
| 5.3 | Graphical User Interface (GUI) | 134 |
| 5.4 | Datasets | 138 |
| 5.5 | VBA Raman Analysis | 141 |
| 5.6 | Statistical Analysis | 149 |
| 5.6.1 | Data Mining and Cleaning | 149 |
| 5.6.2 | Single Factor Analysis | 150 |
| 5.6.3 | XGE Data Analysis | 154 |
| 5.6.4 | Multi Factor Analysis | 156 |
| 5.6.4.1 | ANOVA Table Explanation | 157 |
| 5.7 | Validation of Model | 159 |
| 5.8 | Conclusions | 159 |
| **6** | **Strained Si Quantum Wells** | 162 |
| 6.1 | Introduction | 162 |
| 6.2 | Strained Silicon Quantum Wells | 163 |
| 6.3 | Sample Growth | 166 |
| 6.4 | TEM Investigation | 169 |
| 6.5 | EELS Analysis | 171 |
| 6.6 | Micro-Raman Spectroscopy | 174 |
| 6.7 | Conclusions | 177 |

| | | |
|---|---|---|
| **7** | **Microvalve MEMS** | 181 |
| | 7.1 Introduction | 181 |
| | 7.2 Significance of MEMS | 182 |
| | 7.3 Reliability Assessment | 182 |
| | 7.4 Structure | 183 |
| | 7.5 Microvalve Formation | 184 |
| | 7.6 Results and Discussion | 184 |
| | 7.7 Stress and Strain Calculation of MEM | 185 |
| | 7.8 Raman Measurements | 187 |
| | 7.9 Conclusions | 190 |
| **8** | **Conclusions and Suggestions for Future Work** | 193 |
| | 8.1 Conclusions | 193 |
| | 8.2 Future Work | 196 |
| | **Appendix I** | 198 |
| | **Appendix II** | 205 |
| | **GUI Code:** **See Attached CD** | |

# List of Figures


| | | |
|---|---|---|
| **Fig.1.1** | Moore's Law graph | 4 |
| **Fig. 1.2** | Schematic of strained Si on SiGe buffer layer | 7 |
| **Fig. 1.3** | The economics of the semiconductor market as a function of year | 8 |
| **Fig. 1.4** | Cross section of the Texas Instruments SiGe bipolar CMOS integrated circuit showing where the SiGe is placed in the transistor | 9 |
| **Fig. 1.5** | Schematic of system-on-a-chip solution utilising several SiGe based technologies | 9 |
| **Fig. 1.6** | Schematic of lattice constant interaction of various deposited films | 11 |
| **Fig. 1.7** | A plot of critical thickness against composition for Si1−xGex on Si. The lowest curve gives the theoretical limit in thermal equilibrium [20], whereas the experimental curve is for a metastable layer grown at 550 $^0$C by MBE | 14 |
| **Fig. 1.8** | (a) TEM image of Ge P-N photodiodes<br>(b)Surface Micrograph | 15 |
| **Fig. 1.9** | TEM image of strained Si cap on relaxed SiGe buffer layer(B2), grown on SiGe graded layer(B1) | 17 |
| **Fig.1.10** | The partial filling of a conduction band due to the excitation of electrons in the valence band | 20 |
| **Fig. 1.11** | (a) The conduction band valleys of Ge along the [111] directions<br>(b) the conduction band valleys of silicon along the [100] directions | 21 |
| **Fig. 1.12** | The bandgap in meV for strained Si1−$x$Ge$x$ grown on bulk-silicon substrates and for unstrained $Si_{1-x}Ge_x$ | 22 |
| **Fig. 1.13** | Orbital orientation in strained silicon | 23 |
| **Fig. 2.1** | TEM internal diagram | 32 |
| **Fig. 2.2** | TEM Image of a Silicon Quantum Well | 33 |
| **Fig. 2.3** | Specimen Interaction | 34 |
| **Fig. 2.4** | EDS of upper SiGe layer | 36 |

| | |
|---|---|
| **Fig. 2.5** Si distribution across SiGe graded layer | 37 |
| **Fig. 2.6** Schematic of three-window elemental mapping technique | 39 |
| **Fig. 2.7** A TEM preparation desk | 40 |
| **Fig. 2.8** Energy level diagram for Raman scattering; (a) Stokes Raman scattering (b) anti-Stokes Raman scattering | 42 |
| **Fig. 2.9** Energy level diagram for Raman scattering; (a) Stokes Raman scattering (b) anti-Stokes Raman scattering | 46 |
| **Fig. 2.10** Schematic of Raman setup | 50 |
| **Fig. 2.11** Typical first order Raman spectrum for a strained Si cap on a $Si_{1-x}Ge_x$ layer | 51 |
| **Fig. 2.12** Schematic of setup used in XRD measurements | 52 |
| **Fig. 3.1** Effective Electron mobility v's Effective Field, for various levels of Ge concentration in SiGe layer | 59 |
| **Fig. 3.2** Effective Hole mobility v's Effective Field, for various levels of Ge concentration in SiGe layer | 60 |
| **Fig. 3.3** 3-D view of an edge dislocation | 61 |
| **Fig. 3.4** Graphic depicting the movement of a dislocation within the crystal structure | 62 |
| **Fig. 3.5** The concept of critical thickness for a SiGe system | 63 |
| **Fig. 3.6** (a) Enclosing the lattice dislocation (b) Burger Vector b, needed to close the path | 64 |
| **Fig. 3.7** Structure of S1, S2 and S3 | 69 |
| **Fig. 3.8** Structure of graded layers : (a) 9 steps in S1, (b) 18 steps in S2 and (c) 36 steps in S3. A pink rectangle represents a SiGe layer added in the graded region of buffer SiGe. The percentage of germanium in a SiGe step is constant | 71 |
| **Fig. 3.9** AFM images: of S1, S2 and S3 | 72 |
| **Fig. 3.10** Raman spectra of samples S1, S2 and S3 | 73 |
| **Fig. 3.11** TEM micrograph of upper SiGe layer of sample S2 | 74 |

| | |
|---|---|
| **Fig. 3.12** Structure of Strained Silicon grown by CVD process | 76 |
| **Fig. 3.13** HR TEM micrographs of sample S6: the step-graded layer. | 77 |
| **Fig. 3.14** HR TEM micrographs of sample S6 | 78 |
| **Fig 3.15** TEM images of sample S11 showing (a) defects in the linear graded SiGe region and (b) defect free upper layer of constant SiGe composition | 78 |
| **Fig 3.16** AFM images of (a) sample S6 and (b) sample S11 | 79 |
| **Fig. 3.16** Raman intensity versus wave-number for strained Si on SiGe layer (sample S6) | 80 |
| **Fig. 3.17** Raman spectrum of sample S6, focusing on the Si-Si phonon mode positions | 81 |
| **Fig. 3.18** Raman spectrum of sample S11 | 81 |
| **Fig. 3.19** Sample S6 viewed using a Philips Tecnai F20 200 kV with Field Emission Gun | 83 |
| **Fig. 3.20** S6 upper layer, with lines more evident, viewed again using a Philips Tecnai F20 200 kV with Field Emission Gun | 83 |
| **Fig. 3.21** Bright Field TEM image of sample S11 taken on a JEOL 200 with excitation voltage of 200kV and magnification of 50x. | 85 |
| **Fig. 3.22** Gain Normalised Image of the graded layer at 20x, indicating the presence of these Moiré -like Fringes | 86 |
| **Fig. 3.23** Si Elemental Map across S11 | 86 |
| **Fig. 3.24** Colour coded thickness map for Si foil, demonstrating variation of thickness across the sample | 87 |
| **Fig. 3.25** Elemental Silicon Map across the SiGe Buffer layer | 88 |
| **Fig. 3.26** Showing the presence of 'real' Moiré fringes, indicated by the small box in (a) and shown in more detail in (b) | 89 |
| **Fig. 4.1** A map of band gap versus lattice constant for the III±V alloys and Si and Ge | 97 |
| **Fig. 4.2** Schematic Structure of Sample 1653 | 99 |

| | |
|---|---|
| **Fig. 4.3** Schematic structure of Sample 1654 | 99 |
| **Fig. 4.4** TDs in SiGe buffer layer of sample 1654 | 100 |
| **Fig. 4.5** Schematic showing the concept of dislocation flow based on relaxed, graded SiGe data | 100 |
| **Fig. 4.6** TEM image of the SiGe buffer layer of sample 1654 | 101 |
| **Fig. 4.7** Sample 1653 Bright Field TEM, indicating structure of sample, taken at a magnification of 60K | 102 |
| **Fig. 4.8** SiGe buffer layer of 1654 detailing the Threading and misfit dislocations | 104 |
| **Fig. 4.9** Bright Field 1654 TEM image, at 12K | 105 |
| **Fig.4.10** Surface Micrograph with mag. X1000 on 65x45μm image size | 105 |
| **Fig. 4.11** Bright Field TEM Image, at 20K magnification. | 106 |
| **Fig. 4.12** (a) Bright field TEM micrograph of sample1653<br>(b) TEM image at 200x magnification focusing on a close up of the cap area | 108 |
| **Fig. 4.13** EDS spectrum from Si cap | 110 |
| **Fig. 4.14** EDS near Ge/SiGe interface | 110 |
| **Fig. 4.15** EDS of upper SiGe layer | 111 |
| **Fig. 4.16** Spectrum in lower layers of SiGe | 111 |
| **Fig. 4.17** EDS Spectrum of sample 1654 in bulk Si | 112 |
| **Fig. 4.18** TEM micrograph of sample1654 | 113 |
| **Fig. 4.19** Sample 1654 silicon L edge map | 114 |
| **Fig. 4.20** Sample 1654 silicon K edge map | 115 |
| **Fig. 4.21** Profile from K edge Si spectrum moving from the SiGe layer to cap | 116 |
| **Fig. 4.22** Ge EELS spectrum, showing Ge distribution from Si cap across Ge layers | 116 |

| | | |
|---|---|---|
| **Fig.4.23** | (a) EELS Colour Map, with Si in red and Ge in green, while (b) is a black and white copy of the same image with constituent elements identified. | 117 |
| **Fig. 4.24** | (a) Colour profile of thickness of the foil for sample 1654<br>(b) Colour/Thickness Scale Bar | 118 |
| **Fig. 4.25** | Thickness per wavelength spectrum for foil, showing influence of foil thickness across sample 1654 | 119 |
| **Fig. 4.26** | Raman spectrum of sample 1654 | 120 |
| **Fig. 4.27** | Ge-Ge phonon position and curve-fitting (indicated by the broken line) | 121 |
| **Fig. 4.28** | Si-Si phonon position, from cap, and curve fit | 121 |
| **Fig. 4.29** | Raman spectrum from Sample 1653 | 122 |
| **Fig. 4.30** | Ge-Ge phonon Raman spectrum | 123 |
| **Fig. 4.31** | Si-Si Raman spectrum of Si cap | 123 |
| **Fig. 4.32** | XRD spectra showing (a) $\omega$ scan along the $Ge_{004}$ plane for sample 1653 and (b) $\omega$ scan along the $Ge_{004}$ plane for sample 1654 | 125 |
| **Fig. 4.33** | XRD spectra showing (a) $2\Theta$ scan along the $Si_{004}$ plane of sample 1653, and (b) $2\Theta$ scan along the $Si_{004}$ plane of 1654 | 126 |
| **Fig. 4.34** | Coupled $2\Theta$ scan (a) for sample 1653 and (b) for sample 1654 | 128 |
| **Fig. 5.1** | Introductory UserForm | 134 |
| **Fig. 5.2** | Different methods of analysis possible are using the VBA GUI | 135 |
| **Fig. 5.3** | Form showing TEM images | 136 |
| **Fig. 5.4** | Userform showing EELS data displayed on request | 136 |
| **Fig. 5.5** | Userform depicting the relevant Raman spectrum | 137 |
| **Fig. 5.6** | Equations relating to the calculation of strain | 137 |
| **Fig. 5.7** | Explanation of terms presented in equations | 138 |

| | |
|---|---|
| **Fig. 5.8** Interactive user form allowing to user to choose which method of analysis to use | 141 |
| **Fig. 5.9** Userform15 showing the combination of different equations | 142 |
| **Fig. 5.10** List of all Strain related equation combinations – with user prompted info box | 143 |
| **Fig. 5.11** Userform illustrating the variation of Ge content using Eqn.5.10 | 144 |
| **Fig. 5.12** Userform illustrating the deviation of the Ge value away from the XRD calculated value | 145 |
| **Fig. 5.13** Userform showing information relating to particular (user selected) sample | 146 |
| **Fig. 5.14** (a) Ge variation per thickness<br>(b) Deviation across samples with common thickness | 147 |
| **Fig. 5.15** Userform illustrating the Eqns. used in the absence of strain | 148 |
| **Fig.5.16** X1 vs XRD with trendline and R squared values shown | 151 |
| **Fig.5.17** X2 vs XRD with trendline and R squared values shown | 151 |
| **Fig.5.18** X3 vs XRD with trendline and R squared values shown | 151 |
| **Fig.5.19** X4 vs XRD with trendline and R squared values shown | 152 |
| **Fig.5.20** X5 vs XRD with trendline and R squared values shown | 152 |
| **Fig.5.21** X6 vs XRD with trendline and R squared values shown | 152 |
| **Fig.5.22** X7 vs XRD with trendline and R squared values shown | 153 |
| **Fig.5.23** X8 vs XRD with trendline and R squared values shown | 153 |
| **Fig.5.24** XGE1 vs XRD with trendline and R squared values shown | 154 |
| **Fig.5.25** XGE5 vs XRD with trendline and R squared values shown | 154 |
| **Fig.5.26** XGE5 vs XRD with trendline and R squared values shown | 155 |
| | |

| | |
|---|---|
| **Fig. 6.1** Schematic cross-section of an nMODFET structure (xxxxx—Sb modulation doping) | 163 |
| **Fig. 6.2** Energy-band profile of a structure containing three quantum wells | 164 |
| **Fig. 6.3** Energy band profile of a structure containing two parabolic quantum wells | 165 |
| **Fig. 6.4** (a) Structure schematic for C2971<br>(b) Structure schematic for C2972 | 166 |
| **Fig. 6.5** Bright Field C2971 TEM image, with 5 distinct layers | 169 |
| **Fig. 6.6** Bright Field Image of C2971 focusing on TD, with overall image inserted also. Different TDs are seen running through the SiGe layer | 170 |
| **Fig. 6.7** TEM image of C2972 indicating the TDs present throughout the Layers | 171 |
| **Fig. 6.8** Sample C2971 EELS Si profile going from bulk to cap | 172 |
| **Fig. 6.9** EELS Germanium Profile moving from bulk to cap | 172 |
| **Fig. 6.10** Si (K edge) Profile map for C2972 | 173 |
| **Fig. 6.11** EELs Ge Map moving from cap to bulk | 173 |
| **Fig. 6.12** (a) Raman Wavenumber v's Pore Size<br>(b) Raman FWHM V's Pore Size | 175 |
| **Fig. 7.1** (a) Surface view; and<br>(b) Cross section A-A' of the polycrystalline silicon microvalve | 183 |
| **Fig. 7.2** (a) Optical photograph of an array of valves fabricated on a silicon substrate; and<br>(b)SEM image of a microvalve after the sacrificial oxide has been removed in concentrated HF | 184 |
| **Fig. 7.3** ZYGO Surface profiling scan | 185 |
| **Fig. 7.4** The results plotted from ZYGO measurements used for stress and strain calculation of the deposited polysilicon material | 186 |
| **Fig. 7.5** (a) Raman shifts for MEM structure,<br>(b) Related shifts grouped together | 187 |
| **Fig. 7.6** The MEM structure with Raman colour coded information displayed | 188 |

# List of Tables


| | | |
|---|---|---|
| **Table 2.1.** | Polarisation selection rules for back scattering from a (001) and (110) surface. | 45 |
| **Table 3.1** | Growth parameters of S1, S2 and S3 | 69 |
| **Table 3.2** | Growth steps of strained silicon (S1) with step-graded buffer SiGe | 69 |
| **Table 3.3** | Growth steps of strained silicon (S6) with step-graded buffer SiGe | 75 |
| **Table 3.4** | Growth parameters of strained silicon | 76 |
| **Table 3.5** | Stress and strain in strained-Si using Raman and Moiré techniques | 81 |
| **Table 4.1** | EDS Compositional Analysis of Sample 1654 | 112 |
| **Table 4.2** | Raman Measurements for samples 1653 and 1654 | 123 |
| **Table 4.3** | XRD Analysis | 126 |
| **Table 5.1** | Equations without Strain | 138 |
| **Table 5.2** | Equations with Strain | 139 |
| **Table 5.3** | ANOVA Table | 156 |
| **Table 5.4** | Validation of Model | 158 |
| **Table 6.1** | Raman Spectra Measurements | 174 |
| **Table 6.2** | Summary of Calculations | 174 |
| **Appendix:** | | |
| **Table 1** | Sample Peak Positions | 195 |
| **Table 2** | Ge Content values using equations without strain factor | 196 |
| **Table 3** | Ge content values using equations with strain factor | 197 |
| **Table 4** | Data for X1-X8 following Cleaning/Mining | 198 |
| **Table 5** | Data for XGE1-XGE8 following Cleaning/Mining | 199 |
| **Table 6** | Reduced Dataset for Multifactor Analysis | 200 |

# Acronyms and Abbreviations

| | |
|---|---|
| AFM | Atomic Force Microscopy |
| ANOVA | Analysis Of Variance |
| CCD | Charge Coupled Device |
| CMOS | Complimentary Metal Oxide SemiConductor |
| CMP | Chemical Mechanical Polishing |
| CVD | Chemical Vapour Deposition |
| DRAM | Dynamic Random Access Memory |
| EELS | Electron Energy Loss Spectroscopy |
| EDS | Energy Dispersive Spectroscopy |
| FWHM | Full Width Half Maximum |
| Ge | Germanium |
| GIF | Gatan Imaging Filter |
| GUI | Graphical user Interface |
| HBT | Heterojunction Bipolar Transistor |
| HH | Heavy Hole |
| HREM | High Resolution Electron Microscope |
| LAN | Local Area Network |
| LH | Light Hole |
| LO | Longitudinal Optical |
| LPCVD | Low Pressure Chemical Vapour Deposition |
| MBE | Molecular Beam Epitaxy |
| MCM | Multi Chip Module |

| | |
|---|---|
| MD | Misfit Dislocation |
| MEMS | Micro-Electro-Mechanical-Systems |
| MF | Moiré Fringe |
| MIPS | Million Instructions Per Second |
| MODFET | Modulation Doped Field Effect Transistor |
| MOSFET | Metal Oxide Field Effect Transistor |
| MPU | Microprocessor Units |
| PC | Personal Computer |
| QW | Quantum Well |
| RMS | Root Mean Squared |
| RF | Radio Frequency |
| Si | Silicon |
| SIMS | Secondary Ion Mass Spectrometry |
| SO | Split Off |
| SOC | System On Chip |
| Si QW | Silicon Quantum Well |
| SE | Spectroscopic Ellipsometry |
| TD | Threading Dislocation |
| TEM | Transmission Electron Microscope |
| TO | Transverse Optical |
| VBA | Visual Basic for Applications |
| XRD | X-Ray Diffraction |
| ZLP | Zero Loss Peak |

# Author's Publications

**Refereed Journal Publications:**

1. **J. McCarthy**, S. Bhattacharya, T. S. Perova, R. A. Moore, H. Gamble, B. M. Armstrong*, Composition and Stress Analysis in Si Structures Using Micro-Raman Spectroscopy, *The Journal of Scanning Microscopies* VOL. 26, 235–239 (2004)

2. C.K. Maiti, S.K. Samanta, S. Chatterjee, G.K. Dalapati, S. Bhattacharya, B.M. Armstrong, H.S. Gamble, **J. McCarthy,** T.S. Perova., and R.A. Moore, Determination of band offsets in strained-Si heterolayers, *Thin Solid Films*, 462-463, pp. 80-84 (Sept. 2004).

3. **J. McCarthy**, S. Bhattacharya, E.Ni Mhuircheartaigh, T. S. Perova, R. A. Moore, H. Gamble, B. M. Armstrong, Composition and Stress Analysis in Strained Silicon, *Journal of Postgraduate Research* Trinity College, pp156 – 159 (2004)

4. **J.McCarthy**, R.A.Moore, Optical Engineering for Children – a Structured Approach, *European Journal of Engineering Education*, Vol. 31, 6, pp741-747(Dec. 2006)

5. **J. McCarthy**, S.Bhattacharya, T.S. Perova, R.A. Moore, H.Gamble, B.M.Armstrong, Investigation of Moire and Moire-like fringes in Strained Si, *Journal of Materials Science and Technology*, 2006 (In press)

6. **J.McCarthy**, G.Audoit, T.Perova, R.A.Moore, J. Holmes, M. Morris, Micro-Raman analysis of quantum confined crystalline germanium nanowire arrays, *British Journal of Non-Destructive Testing*, (2006), (In press)

7. **J. McCarthy**, E. Ni Mhuircheartaigh, K. Lyutovitch, T.S. Perova, R.A. Moore, W. Blau, Strained Silicon Quantum Wells : A Spectroscopical Analysis , *European Physical Journal – Applied Physics* 2006 (submitted)

8. **J.McCarthy**, A.Macakarel, R.A. Moore, Combined Test Coverage Analysis at Board Level, *IEEE Journal of Design and Test of Computers*, 2006 (submitted)
9. **J. McCarthy**, K.Lyutovitch, T.S. Perova, R.A. Moore, Analysis of novel growth techniques in relation to strain and dislocation distributions in Ge p-n photo-diodes, *J.Mater.Sci. Eng. B* (in preparation).

10. **J. McCarthy**, S. Bhattacharya, T.S. Perova, R.A. Moore, F. Meyer, H. Gamble, and B. M. Armstrong, Composition and Stress Analysis in Si Structures using Micro-Raman Spectroscopy, *J. Nanoscience and Nanotechnology* (Submitted).

11. **J.McCarthy,** T.O'Suilleabhain, R.A.Moore, Statistical Analysis of suitability of experimental equations for thin SiGe buffer layers, *Applied Physics Letters* (In Preparation)

**Referred Conference Proceedings:**

12. **J. McCarthy**, S. Bhattacharya, T.S. Perova, R.A. Moore, F. Meyer, H. Gamble, and B. M. Armstrong, Composition and stress analysis in Si structures using micro-Raman spectroscopy, *Irish Microscopical Society Conference*, 4-6 September 2003, Cork, Ireland, (oral presentation).

13. S. Bhattacharya Sekhar, Samanta Santanu K. Chatterjee Somenath, **McCarthy John**, Armstrong B.M., Gamble H.S., Maiti C.K., Perova T.S., Moore R.A., Fundamentals of Novel Oxide/Semiconductor Interfaces, *MRS Fall Conference*, November 2003.

14. S. Bhattacharya, **J. McCarthy**, B.M. Armstrong, H.S. Gamble, G.K. Dalapati, S. Das, C.K. Maiti, T.S. Perova, R.A. Moore, Gate Dielectrics on Strained-Ge Layers on Si1-xGex/Si Virtual Substrates, *International Workshop on Gate Insulator* 2003, November 6-7, 2003, Tokyo, Japan.

15. S. Bhattacharya, S.K. Santanu, S. Chatterjee, **J. McCarthy**, B.M. Armstrong, H.S. Gamble, C.K. Maiti, T.S. Perova, R.A. Moore, High-k ZrO2 Gate dielectric on Strained-Si, *MRS Fall Meeting*, December 1-4, 2003, p. 131 (E3.22).

16. S. Bhattacharya, S.K. Samanta, S. Chatterjee, **J. McCarthy**, B.M. Armstrong, H.S. Gamble, C.K. Maiti, T. Perova and R.A. Moore, Conduction Mechanism in High-k ZrO2 Gate Dielectric Films on strained-Ge Layers, *2003 International Semiconductor Device Research Symposium (ISDRS)*, December 10-12, 2003, University of Maryland, US., (oral presentation).

17. S. Bhattacharya, **J. McCarthy**, B. M. Armstrong, H. S. Gamble, C. K. Maiti, T. Perova and R.A. Moore, Deposition of Strained Ge Layers on Si1-xGex/Si Virtual Substrates, *4th International Conference on Computers and Devices for Communication*, CODEC-04, January 1-3 2004, Kolkata, India, (oral presentation).

18. **J.McCarthy**, S. Bhattacharya, T.S. Perova, R.A. Moore, F. Meyer, H. Gamble, and B. M. Armstrong, Composition and stress analysis in Si structures using micro-Raman spectroscopy, *SPIE International Conference - Photonics Europe*, 26-30 April 2004, Strasbourg France, (accepted as an oral presentation).

19. M. F. Bain, P. Baine, D. W. McNeill, G. Srinivasan, N. Yankovic, **J. McCarthy**, R.A. Moore, B. M. Armstrong and H. S. Gamble, Fabrication and Characterisation of SOI Substrates Incorporating Thermal Vias, NATO ARW: *Science and Technology of Semiconductor On-insulator structures devices operating in a harsh environment*, 25-29 April, 2004, Kyiv, Ukraine.

20. S. Chakraborty, S.K. Samanta, S. Bhattacharya, **J. McCarthy,** B.M. Armstrong, H.S. Gamble, G.K. Dalapati, S. Das, T.S. Perova, R.A. Moore C.K. Maiti, Electrical properties of high-k Ta2O5 gate dielectrics on strained Ge-rich layers, Proceedings of the International Conference on Microelectronics, v 24 II, Proceedings - 2004 *24th International Conference on Microelectronics*, MIEL 2004, 2004, p 483-486

21. S. Das, S. Chakraborty, S. Bhattacharya, M. Bain, **J. McCarthy,** B.M. Armstrong, H.S. Gamble, G.K. Dalapati, S.K. Samanta, T.S. Perova, R.A. Moore; C.K. Maiti, Rapid thermal oxidation of Ge-rich strained layers, Proceedings of the International Conference on Microelectronics, v 24 II, Proceedings - 2004 *24th International Conference on Microelectronics*, MIEL 2004, 2004, pp. 479-482

22. S. Bhattacharya, **J. McCarthy,** B.M. Armstrong, H.S. Gamble, G.K. Dalapati, S. Das, S. Chakraborty, C.K. Maiti, T.S. Perova, R.A. Moore, Electrical properties of high-k ZrO2 gate dielectrics on strained ge-rich layers, Proceedings of the International Conference on Microelectronics, v 24 I, Proceedings - 2004 *24th International Conference on Microelectronics*, MIEL, NIS, Serbia and Montenegro, 16-19$^{th}$ May 2004, pp. 405-407

23. S. Bhattacharya, S.K. Samanta, S. Chatterjee, **J. McCarthy**, B.M. Armstrong, H.S. Gamble, C. K. Maiti, T.S. Perova and R.A. Moore, High-k $ZrO_2$ gate dielectric on strained-Si, *MRS Proceedings*, June 2004 (in press).

24. **J. McCarthy**, S. Bhattacharya, T.S. Perova, R.A. Moore, H. Gamble, and B. M. Armstrong, Composition and stress analysis in Si/SiGe structures, *Proceedings of IEEE 1st International Conference*, Acapulko, Mexico, September 8-10, 2004, pp. 226-230. IEEE Catalog Number: 04EX865, ISBN: 0-7803-8532-2 ©2004 IEEE.

25. **J.McCarthy**, R.A. Moore, Maximum Impact Flow for Optics Teaching, Conference on Education and Training in Optics and Photonics, *ETOP Marseilles* (Oral presentation accepted), 2005

26. **J. McCarthy**, E. Ni Mhuircheartaigh, K. Lyutovitch, T.S. Perova, R.A. Moore, W. Blau, Spectroscopical Analyis of Strained Silicon Quantum Wells, *Opto-Ireland* 2005, 3-5 April 2005, Dublin, Ireland, (accepted Oral Presentation).

27. **J. McCarthy**, S.Bhattacharya, T.S. Perova, R.A. Moore, H.Gamble, B.M.Armstrong, Investigation of Moire and Moire-like fringes in Strained Si and the comparative determination of strain using Moire and Raman techniques *International Conference on. Materials-Energy-Design MED06*. Dublin Institute of Technology, Ireland. 14th – 17th March 2006

# Preface

Silicon has been the material of choice in the semiconductor industry for over forty years. However, limitations with this material are now being encountered and the search is taking place to find the choice material for the next forty years and beyond. Several materials have been suggested with silicon germanium (SiGe) seen as the most suitable. This is based on minimal overhead costs in terms of adjusting existing fabrication facilities due to its compatibility with Si, as well as its stable structure and its adjustable band-gap.

In order to exploit the inherent advantages of such a material over its conventional counterpart, several new structures and devices are developed. These new structures include but are not limited to, strained Si, Ge p-n photodiodes, strained Si quantum wells, and micro-electro-mechanical-systems (MEMS). These devices, with the exception of MEMS, all use an underlying SiGe buffer layer to provide either a suitable lattice mismatch for resulting strain in the top layers, or the suppression of dislocations that result from the unavoidable lattice mismatch that exists between Si and Ge.

It is envisaged that single chip solutions using monolithic integration will pave the way for future enhancements of these same novel structures. Thick graded SiGe layers, with Ge content increasing from 0% to a nominal amount, usually ~20%, are at present the most common type of layers within the developing structures. As new devices are manufactured to exploit the materials used in their growth, the thickness of the layers used poses questions in terms of integration and suitability for large scale manufacture. The thicker the material used, the greater the cost of manufacture. In line with this, the associated growth procedures now focus on developing thin films with low defect density. The challenge exists to grow the structures outlined above using optimum growth techniques.

It is also clear that in line with a reduction in size of these layers, the tools and methodologies of characterisation must also be optimised. No one spectroscopic technique is sufficient for the overall characterization of any one structure as parameters

such as threading dislocation, interface diffusion, strain and stress etc. all have to be evaluated. Therefore, the use of several independent, but complementary techniques, are required for analysis of any single structure. Raman techniques, which focus on the interaction and scattering of an incident phonon on a material, is suitable for compositional and stress analysis. This is due to the well developed library of phonon frequencies associated with periodic elements and their alloys. In line with this, the suitability of such techniques in terms of thin layers poses difficulties for researchers. The use of a Transmission Electron Microscope (TEM), and its derivatives, such as Electron Loss Spectroscopy (EELS) and Energy Dispersive Spectra (EDS) have the ability to both qualify and quantify the characterisation of materials in terms of structure and composition.

As several tools are used in the analysis of a single structure, the issue of managing and accessing such dispersed data quickly and efficiently becomes more obvious. The development of a web based, Microsoft compatible, interactive Graphical User Interface (GUI) is perhaps the best solution. This allows several researchers to access and maintain a database of several different source files.

# Chapter One

# Si/SiGe heterostructures

## 1.1 Introduction

As customer driven technology advances, so too does the need for similar developments in the underlying materials. From strained Si transistors, which offer increased speed with no cost or area overhead, to frictionless MEMs devices, the scale of both advancement and expectation in this area is phenomenal.

If steel was the raw material for the 20$^{th}$ century, silicon is for the 21$^{st}$ century [1]. Silicon, the raw material of the microprocessor, powers the Internet and today's economy, running everything from digital phones and PCs to stock markets and spacecraft while enabling today's information rich, converged, digital world.

But if silicon technology's past has been dramatic, its future promises to be even more spectacular and far reaching [2]. This work focuses on emerging technologies, primarily those which incorporate a SiGe (Silicon Germanium) buffer layer, analysing important characteristics such as threading dislocations, misfits, and strain fields. From this, one can then begin to get a better understanding of what occurs at both the micro and nanometer level.

## 1.2 Moore's Law

Gordon Moore, one of the founders of Intel, observed that innovations in technology would allow a doubling of the number of transistors in a given space every year (in an update article in 1975, Moore adjusted the rate to every two years to account for the growing complexity of chips), and that the speed of those transistors would increase [3]. What is less well known is that Moore also stated that manufacturing costs would dramatically drop as the technology advanced. A graphical representation of Moore's

Law can be seen in Fig.1.1 where the number of transistors and MIPS (Millions Instructions Per Second) are plotted as a function of years.

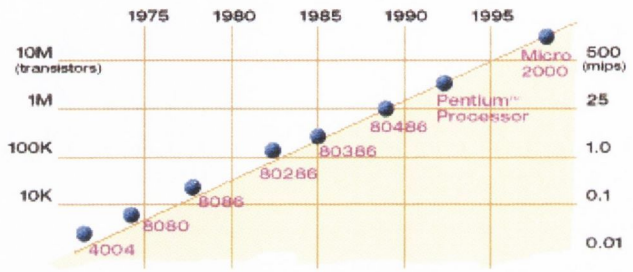


**Fig.1.1** A graphical representation of Moore's Law [1]

Moore's prediction, now popularly known as Moore's Law, had some startling implications, predicting that computing technology would increase in value at the same time it would actually decrease in cost. This was an unusual idea at the time, since, in a typical industry, building a faster, better widget with twice the functionality also usually means doubling the widget's cost. However, in the case of solid-state electronics, the opposite is true: each time transistor size shrinks, integrated circuits (ICs) become cheaper and perform better.

There are those in the industry that have long believed that the decreasing of transistor sizes would be more and more difficult because, though as transistors shrink in size the power they consume is reduced (they scale in voltage), their associated leakage current (the continued flow of current even when transistors are "off") increases. The more transistors there are on a chip, the more power is consumed. In addition, as transistor density and speed increase, the power consumed by the chip as a whole increases also and generates more heat. Thus, the efficiency of cooling techniques must also improve. It is felt that the physical limits of atomic structures for scaling transistors are now being reached, while growth concerns, such as strain manipulation as well as misfit and threading dislocations, must also be overcome. This issue, as well as other factors, creates a significant and continuous challenge for the entire silicon industry.

In response to that challenge, this thesis pursues research into both conventional and unconventional technologies that have the potential to enable the next evolutionary step in computing. This includes introducing many new and exciting technologies and innovations in materials, growth techniques and spectroscopical characterisation.

## 1.3 Tomorrow's Technologies Today

In order to make real the predictions made under Moore's Law, a typical approach involves the research and development of new process technologies and materials as part of a long term vision. Every aspect, including both variable and manufacturing issues associated with new materials must be examined. From conventional Complimentary Metal Oxide Semiconductor (CMOS) processes to research in unconventional materials, such as strained silicon and Ge P-N photodiodes etc., the key challenge is the understanding of the basic principles behind the introduction of new materials to the market place. We have now entered an age in which a majority of households employ a data connection to the home, being most typically a phone based modem installed in a personal computer (PC). Such data access is quickly becoming universal, but this consumer level connection is for now generally narrow (nominally 56 Kb/s), and thus several orders of magnitude inferior to the performance of local area networks (LANs) available in today's commercial environments (typically 16–100 Mb/s). Equally limiting, this consumer based data application is for the most part fixed, tethered by a wired phone installation not dissimilar to that in use almost a century ago [4].

In the near future, one can expect significant enhancements in the mobility, performance, and associated value (decreased cost for function) of data centric consumer applications. As services based upon the availability of bandwidth are already being developed, the implications for the data infrastructure, and specifically for the technology supporting it, must be examined [5]. Similarly, the processing cost for a finished 200mm silicon wafer is about $1000, which comes to several cents per square millimetre of silicon. In developing products for the communications marketplace, one requires only a fraction of the wafer capacity of a cost-effective 1500 wafer start-per-day fabricator, since high volume communication dice are relatively compact. Furthermore, commonality and

shared process steps with an underlying high volume CMOS technology enable dramatic savings in both tooling and production costs. Therefore, it is important that, wherever possible, manufacturing steps common to CMOS processing are used, and to share in the economy of scale leading to its reduced cost structure. In terms of emerging mixed-signal technologies (those that combine both analogue and digital functionality), the metric against which it must be measured is its achievement of performance requirements within the wired and wireless network segments while maintaining the economic constraints associated with the consumer marketplace [6].

## 1.4 Silicon Germanium

In the mid 1980s, a SiGe (Silicon Germanium) device program was initiated at IBM to extend silicon based electronics to levels of performance and to circuit topography implementations previously not feasible in a silicon based technology [6 – 9]. Very high levels of performance in SiGe devices and circuits are obtained through modification of the transistor's band structure rather than by device miniaturisation, thereby enabling the use of a low cost silicon based approach. Launched originally to address the needs of high end computing, the program was refocused in 1990 to look at devices for the rapidly developing communications area.

Since then, SiGe has evolved from a research material to now accounting for a small but significant percentage of manufactured semiconductor devices. This percentage is predicted to increase substantially as SiGe begins to be incorporated into CMOS technology in order to substantially improve performance. It is the development of Si/SiGe heterostructures and the associated band and strain engineering which gives improved conventional microelectronic device performance along with allowing new concepts to be explored. Strategies Unlimited have predicted that the wireless and digital SiGe market will reach $1.8 billion by 2008. For example, SiGe bipolar technology is one of the most attractive candidates for the emerging field of broadband wireless services. It (SiGe) combines cost and integration advantages with the potential to fulfil the technical specification and manufacturing capabilities of standard silicon technologies. Therefore,

it is of primary interest to investigate the realisation of key building blocks as a precondition for the monolithic integration of complete systems [10]. Central to this work is the need to appreciate the fundamental issues associated with SiGe, as this is the building block for the materials mentioned below. Already many SiGe products are available on the market in numerous applications and the market predictions are for an enormous growth in products.

The work reported here focuses on several materials of interest, namely:

1. Strained silicon on a SiGe buffer layer;
2. Ge P-N photodiodes;
3. Silicon Quantum Wells;
4. Micro-Electro-Mechanical-Systems (MEMS).

The majority of these materials contain a SiGe buffer layer, which has significant impact on the overall characterisation of the material in question. Fig. 1.2 outlines a typical structure of the materials under investigation, showing in this case, a strained Si layer deposited on a SiGe buffer layer.

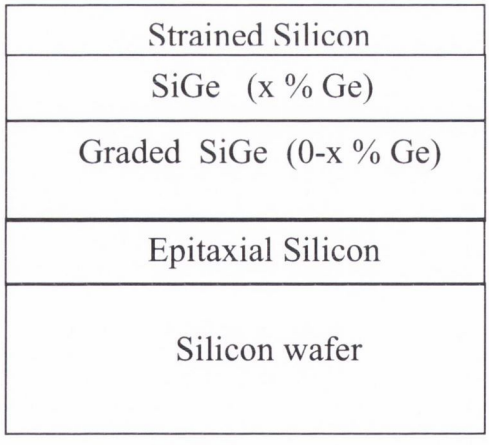


**Fig. 1.2** Schematic of strained Si on SiGe buffer layer

Fig. 1.3 shows the main technologies in semiconductors, with microprocessing units (MPUs) and dynamic random access memory (DRAM) plotted as a function of time along with the total semiconductor and electronic product sales. The advent and drive of

SiGe technology has been used to develop bandgap and strain engineering on a silicon wafer with the hope of improving some of the mediocre properties of silicon while retaining the mature and cheap fabrication processes. With the advent of the SiGe heterojunction bipolar transistor (HBT) [11-12] and the first sales in 1998, the market for SiGe devices in the radio frequency (rf) market has increased over time and is predicted to increase at 30% per annum in the future [13-14] (Fig. 1.3). Much of this increase is predicted to be in rf markets where higher cost III–V materials have previously dominated. CMOS, however, is dominant in semiconductor products in general. If SiGe can be integrated into such areas then the sales of SiGe devices will also include a share of the MPU market and the sales would be increased substantially to tens of billions of US dollars per annum.

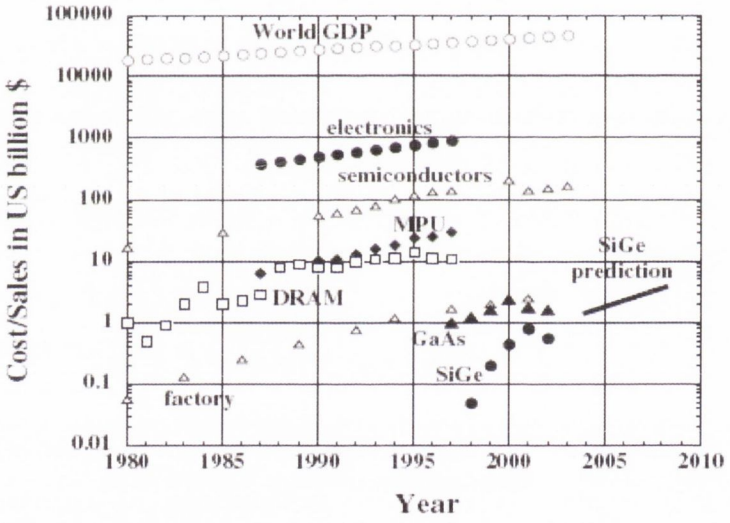


**Fig. 1.3** The economics of the semiconductor market as a function of year [10].

In early 2000, Motorola became the first in the industry to qualify the SiGe heterojunction bipolar technology (HBT) bipolar CMOS(BiCMOS) process. A year later, it introduced a general purpose, low noise amplifier with selectable current. Other applications based around SiGe material developed include fibre-optic drivers for optical networking, bluetooth, as well as short range wireless data transmission. A number of other companies, such as Texas Instruments, have also been very proactive in the incorporation of SiGe bipolar CMOS technology, as can be been in Fig. 1.4.

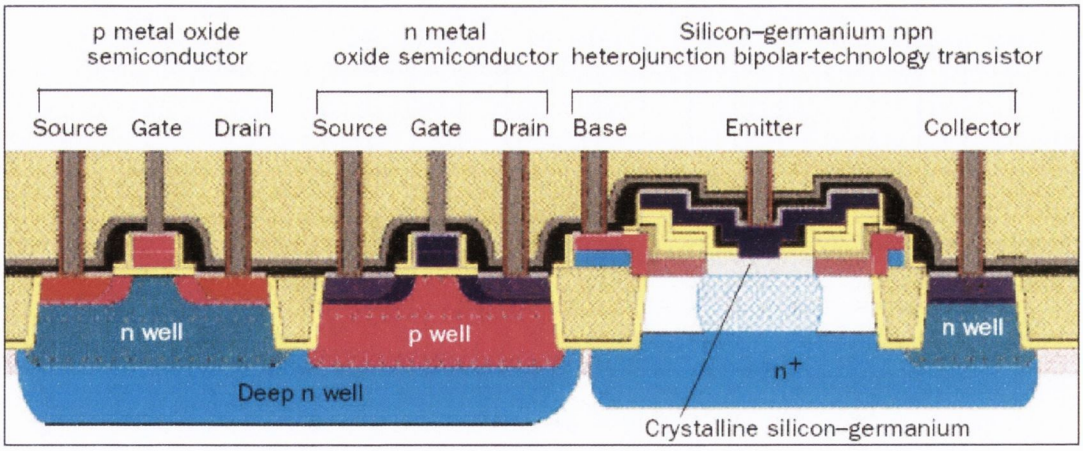


**Fig. 1.4** Cross section of the Texas Instruments SiGe bipolar CMOS integrated circuit showing where the SiGe is placed in the transistor

The use of SiGe devices allows many new functions to be added onto a Si chip potentially reducing cost and power along with increasing speed and yield. For some applications it may be preferable to have 2 or 3 chips as a cheaper solution, all bonded inside a multi-chip module (MCM), as shown in Fig. 1.5

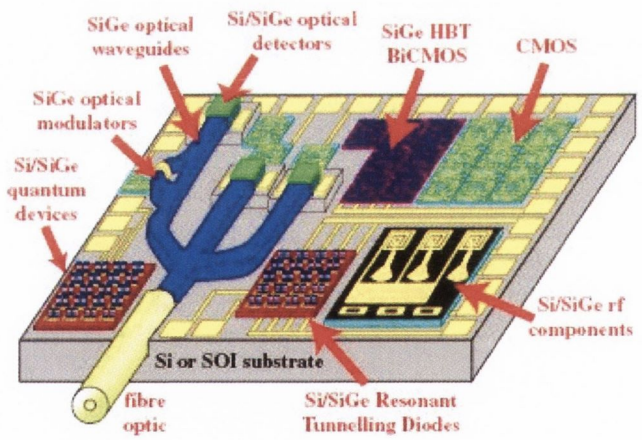


**Fig. 1.5** Schematic of system-on-a-chip (SOC) solution utilising several SiGe based technologies [10].

### 1.4.1 Strain and Lattice Constant

The lattice constant of Germanium is 4.2% larger than that of silicon [15]. Applying Vergard's law, the lattice constant of relaxed or bulk $Si_{1-x}Ge_x$ films, with $x$ between 0 and 1, is almost linear, although small variations to this have been measured. An approximation accurate to about $10^{-4}$ nm is given by [16]:

$$a_{Si_{1-x}Ge_x} = 0.5431 + 0.01992x + 0.0002733x^2 \qquad (1.1)$$

Douglas J. Paul [10] has provided an excellent review of the SiGe lattice structure, the main points of which are outlined below. Fig. 1.6 shows a schematic diagram of various layer interactions depending on the order in which the layer is deposited. Fig. 1.6(a) depicts a bulk lattice constant of a thin $Si_{1-x}Ge_x$ film to be grown on top of a thin bulk silicon layer, whereas Fig.1.6(c) shows the schematic diagram for a bulk Si film to be grown on top of a bulk $Si_{1-y}Ge_y$ film. If a thin $Si_{1-x}Ge_x$ film is grown on top of a $Si_{1-y}Ge_y$ film then for $x > y$ the top layer is compressively strained (Fig. 1.6(*b*)) while for $x < y$ the layer is tensile strained (Fig. 1.6(*d*)).

In both cases the strain is in the plane of the layer ($\varepsilon_x = \varepsilon_y = \varepsilon_{\parallel}$) but this strain also produces $\varepsilon_{\perp}$, a perpendicular strain, resulting in a tetragonal distortion to the lattice (Fig. 1.6(*b*)). In isotropic elasticity theory the strains are related by Poisson ratio, $v$, through

$$\varepsilon_{\perp} = \frac{-2v}{1-v}\varepsilon_{\parallel} \qquad (1.2)$$

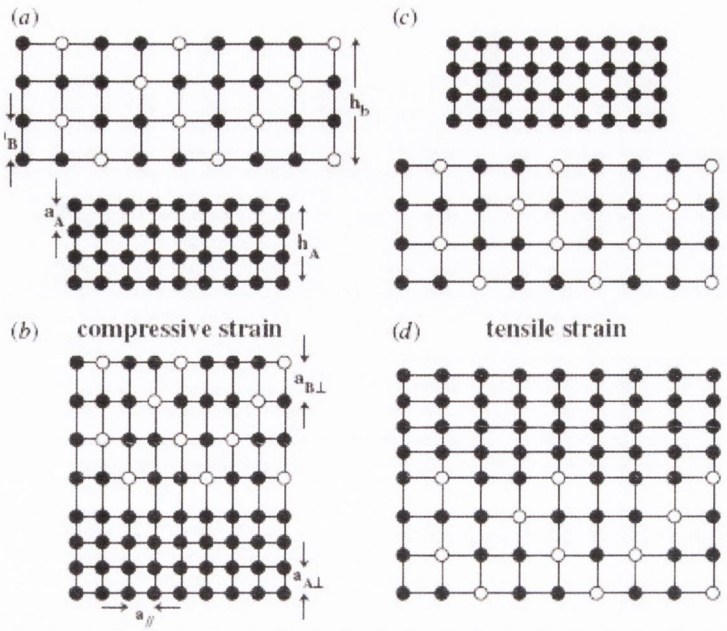


**Fig. 1.6** Schematic of lattice constant interaction of various deposited films [10].

With SiGe deposited on a Si bulk substrate, the Si remains in the cubic structure, with a lattice constant of $a_{si}$ = 5.43Å. The SiGe layer is compressed parallel to the interface to match the Si lattice constant a in the plane, $a_{//}$ = 5.43Å. For SiGe deposited on bulk Si, with respective thickness of $h_{SiGe}$ and $h_{Si}$ respectively, the parallel lattice constant is calculated using the equation:

$$a_{//} = \left(a_{Si}G_{Si}h_{Si} + a_{SiGe}G_{SiGe}h_{SiGe}\right)/\left(G_{Si}h_{Si} + G_{SiGe}h_{SiGe}\right) \qquad (1.3)$$

and

$$a_{\perp} = a_i\left[1 - D^i\left(a_{//}/a_i - 1\right)\right] \qquad (1.4)$$

where i denotes the materials, SiGe or Si, $a_i$ denotes the equilibrium lattice constants and $G_i$ is the shear modulus, and D is a constant that depends on the elastic constants $c_{11}$ and $c_{12}$. The ratio of $a_{//}$ and $a_{\perp}$ to the unstrained lattice constants determines the strain components parallel and perpendicular to the interface:

$$\varepsilon_{i//} = \left(a_{//}/a_i - 1\right) \qquad (1.5a)$$

$$\varepsilon_{i\perp} = \left(a_{i\perp}/a_i - 1\right) \qquad (1.5b)$$

As can be seen, the value of $a_{//}$ is determined by the lattice constant of the substrate used.

Most SiGe structures designed for modern electronics have only one or two strained layers grown on top of either a bulk silicon wafer or a relaxed SiGe virtual substrate which is substantially thicker than the deposited epitaxial layers. If the misfit between the epilayer and the substrate is sufficiently small, the first atomic layers grown on the substrate will be strained and latticed matched to the substrate. In this case, a coherent heterointerface will form, where the strained layer is forced to have the substrate's in-plane lattice constant and again the epilayer becomes tetragonally distorted.

### 1.4.2 Critical Thickness

As the thickness of the epitaxial layer is increased, there exists a maximum thickness, called the critical thickness, $h_c$, above which it will require too much energy to elastically strain additional heterolayers in coherence with the substrate [17]. Defects, termed misfit dislocations, act to relieve the strain present in the epitaxial film. The dislocations are typically $a/2\langle 110\rangle 60^0$ type for the SiGe system. The epitaxial layer relaxes and the defects interact with the electrical, optical and thermal properties of the material, typically degrading the performance of devices.

Well defined interface conditions require a conservation of the in-plane lattice constant, i.e. pseudomorphic (or coherent) growth on a substrate of the active layers whose lattice parameter has been properly adjusted. Hence, in order to exploit 'strain engineering' for the tailoring of the band structure both the strain defining substrate and the pseudomorphic heterolayers have to be realised. Bulk $Si_{1-x}Ge_x$ can be ruled out as a substrate, both because of the inherent problems of pulling homogeneous $Si_{1-x}Ge_x$ crystals, and because such substrates would jeopardise the main advantage of the Si/SiGe heterosystem, namely its compatibility with existing silicon technologies. It is therefore preferable to employ Si substrates and provide strain adjustment by means of a relaxed, intermediate $Si_{1-x}Ge_x$ buffer layer. Occasionally, this combination is referred to as a

*virtual substrate*. As mentioned earlier, for relaxed buffers as well as for pseudomorphic layers the most relevant material parameter is the critical thickness. Films thinner than $h_c$ cannot relax, because the elastic energy stored in such a homogeneously strained layer is lower than the elastic energy associated with the local distortion around a misfit dislocation. Above $h_c$ misfit dislocations become energetically favourable and provide partial strain relaxation of the film, the degree of which increases with increasing layer thickness. Under non equilibrium conditions a metastable thickness range between $h_c$ and an apparent critical thickness $h_{c_app}$ exists, in which the nucleation and propagation of misfit dislocations is kinetically suppressed [18-19]. The value of $h_{c_app}$ depends strongly on the growth temperature, but also on the nucleation sites and mechanisms available in the actual growth environment.

A number of models have been developed to predict the critical thickness of the strained epitaxial layer with the equation describing critical thickness being reduced to [17, 20]:

$$h_c \cong \left(\frac{0.55}{x}\right)\ln(10h_c) \qquad (1.6)$$

Low temperature epitaxy techniques, such as molecular beam epitaxy (MBE) or the different variants of low temperature chemical vapour deposition (CVD), can significantly extend the range of useful layer thicknesses. This is shown in Fig. 1.7, where for $Si_{1-x}Ge_x$ on Si substrates, the equilibrium critical thickness $h_c$ and experimental values grown by MBE at 550 $^0$C are plotted as a function of $x$. Although reasonable film thicknesses appear feasible even at a higher lattice mismatch, one has to keep in mind that metastable layers may partly relax upon subsequent heat treatments.

The three phases labelled 'stable', 'metastable', and 'relaxed' in Fig. 1.7 mark the limitations of strain engineering in a SiGe material system. The amount of strain present in a layer is linked to the critical thickness of the layer [21-22]. Therefore, for increasing Ge composition within an active layer, there is a resulting increase in strain and a corresponding reduction in the critical thickness.

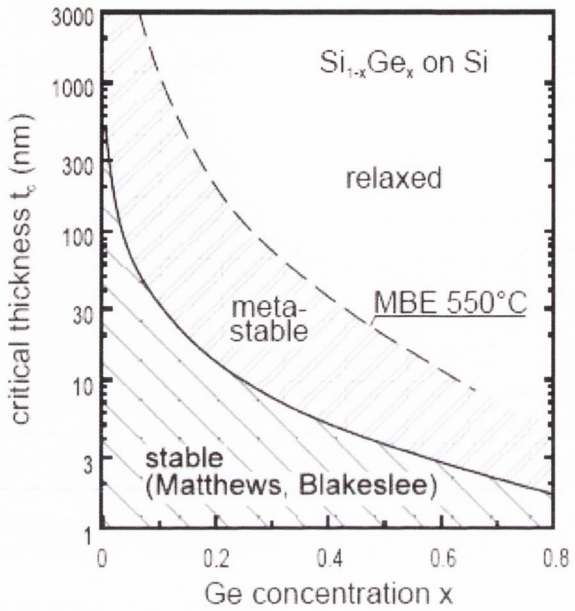


**Fig. 1.7** A plot of critical thickness against composition for $Si_{1-x}Ge_x$ on Si. The lower curve gives the theoretical limit in thermal equilibrium [20], whereas the upper (experimental) curve is for a metastable layer grown at 550 $^0$C by MBE [15].

Another area of interest in the growth of SiGe layers is the analysis of the impact of threading and misfit dislocations on the structure under investigation. Misfit dislocations are independent, thermally activated processes in the initial stages of strain relief when the nucleation's centre density N(t), is low ($<10^4$ cm$^{-1}$). The nucleation rate for misfit dislocations is represented by [23]:

$$\frac{\partial N(t)}{\partial t} = 0.7x10^5 N_o \left(\tau_{eff}\right)^{2.5} \exp\left[-\left(\frac{2.5}{k_B T}\right)\right] \qquad (1.7)$$

where $\tau$ is the effective stress, $N_o$ is the density of incipient nucleation centres for dislocations at t =0, $k_B$ is Boltzmann's constant , and $T$ is temperature. The significance of threading dislocations in the growth of various structures will become evident later in this work.

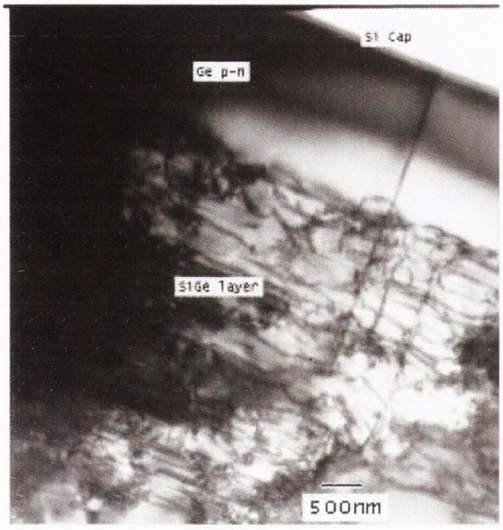


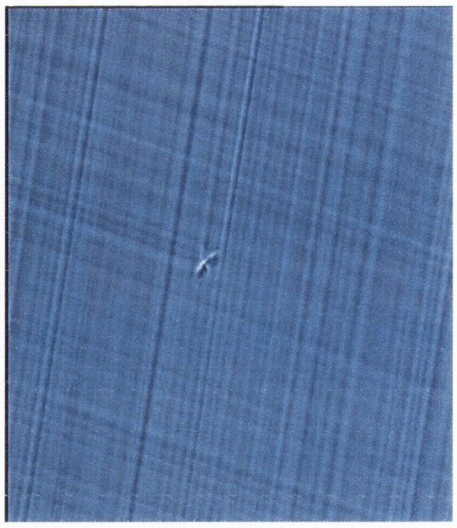

**Fig. 1.8** (a) TEM image of Ge P-N photodiodes (b) Surface micrograph showing crosshatch pattern

The growth of buffer layers such as the relaxed graded SiGe layer generally result in a dislocation structure with long misfit segments and low threading dislocation density. However, when grading to high Ge concentration, deep trenches form as shown by the cross hatch pattern of Fig. 1.8. If threading dislocations are prevented from moving by interacting with surfaces, or other dislocations, they effectively are removed from the strain relieving process. Therefore, locked dislocations have a negative impact on strain relief. This is investigated in more detail at a later stage.

### 1.4.3 Strain Relaxed SiGe Buffer Layers

Friedrich Schaffler [15] has written an informative review of SiGe buffer layers, a synopsis of which is now reflected upon. The simplest way of implementing a strain adjusting buffer layer is the growth of a constant composition SiGe layer with a thickness exceeding $h_c$ by a large enough margin to allow a reasonably high degree of strain relaxation [24]. However, such buffer layers are associated with $10^9$ to $10^{11}$ threading dislocations per $cm^2$ penetrating through the buffer, and ending at the respective growth front [25-26]. A major reason for these unacceptably high densities lies in the step like strain variation at the interface between the substrate and a constant composition buffer,

which leads to an efficient confinement of the misfit dislocations to the (001) interface plane. For this orientation two equivalent networks of strain relaxing misfit dislocations exist, which are defined by the intersection of the {111} glide planes with the (001) interface plane, resulting in line vectors along the [110] and [1$\bar{1}$0] directions. Misfit accumulation in the interface plane causes substantial interactions between the two networks that can impede and even arrest the propagation of individual misfit dislocations.

As a consequence, rather short misfit segments develop, which are associated with a high density of threading dislocations, because either end of a misfit segment has to be connected to a free surface via a threading dislocation. The only way to reduce the density of threading dislocations is by extending the misfit segment lengths. In the ideal case, these will run all the way across the substrate, until they finally reach a lateral crystal surface at the rim of the wafer, where they can no longer affect the active layers to be grown on top of the buffer. In order to approach such a situation, three conditions have to be fulfilled:

(i) The growth (or annealing) temperatures have to be sufficiently high to allow a fast enough misfit dislocation propagation in relation to the growth rate;

(ii) The density of pinning centres or arresting misfit interactions has to be low enough to promote long misfit segments and

(iii) Nucleation and multiplication mechanisms for dislocations are required, but the associated activation energies should be higher than the activation energy associated with propagation in order to prevent the introduction of many short misfit segments.

Since at Ge content greater than 10% none of these conditions can be fulfilled in a constant composition buffer, alternative ways have been proposed to overcome the problems associated with misfit pinning by dislocation interaction [27]. The most successful approach at present employs a linear Ge gradient throughout an initial buffer layer B1, followed by a second, relaxed, layer, B2, throughout which the final composition of B1 is kept constant [28–30].

Relaxed SiGe alloys deposited on Si substrates can be the bridge that brings SiGe metal oxide semiconductor field effect transistors (MOSFETs), SiGe modulation doped field effect transistors (MODFETs), and III-V device technology to a Si based platform. Such technology offers great commercial promise since these advanced technologies can be manufactured in Si process lines and equipment, drastically lowering their cost. In addition, advanced technologies can be used to complement existing and dense Si CMOS circuits, breathing new functionality into Si circuits as they approach maturity. To obtain high mobility electrons in a strained Si cap layer, the implementation of a relaxed graded SiGe buffer layer is necessary to lower the threading dislocation density and achieve high electron and hole mobilities [31-32].

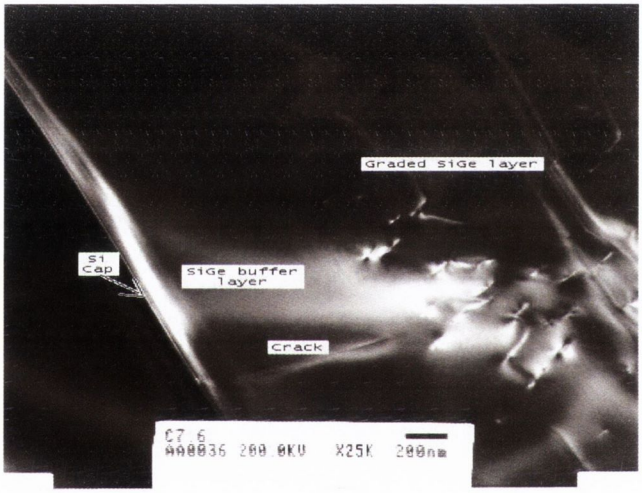


**Fig. 1.9** TEM image of strained Si cap on relaxed SiGe buffer layer(B2), grown on SiGe graded layer(B1)

The advantages of this concept are obvious: the misfit dislocations are distributed over the thickness of B1 rather than being crowded into the interface plane. This strongly reduces dislocation interactions, allowing most of the dislocations to propagate unaffected with a velocity determined by the growth temperature. An example of this is depicted in Fig. 1.9 which shows a cross sectional TEM micrograph of a strained Si layer deposited on a relaxed SiGe layer B2, beneath which lies a linearly graded SiGe buffer layer, B1. The (thermal) crack shown is due to the difference in thermal expansion of the

materials. In the last few years a significant amount of effort has been dedicated to an understanding and optimisation of graded buffers both with respect to relaxation [33–36] and surface morphology [37-38]. These two parameters are not independent of each other, because both are affected by grading rate, growth temperature, and composition, albeit in a different fashion.. While high growth temperatures are advantageous for dislocation propagation, they also support strain driven 3D growth, which leads to a rough surface morphology that may affect lithographic steps during subsequent device processing.

### 1.4.4 Morphology

The morphology of samples, such as strained Si layers, can be readily used to identify the relaxation or not of the underlying SiGe layer of constant composition. This is due to the fact that for every misfit dislocation present, a local accumulation of the double atomic surface steps results, which causes a regular crosshatch pattern, orientated along the {110} directions to appear at the surface [39,40]. Therefore, surface morphology analysis can provide an insight into the density of misfit dislocations present in the buffer layers. Multiplication mechanisms can cause a pile up of atomic surface steps as they can release on the order of 10 to 30 dislocation half-loops with identical Burgers Vector into the same {111} plane [34,36]. Later in this work, details are provided of how surface analysis can be used, in addition to other complementary techniques, to close the loop between growth and strain characterisation.

### 1.4.5 Growth Techniques

In the development of modern day electronic devices, MBE and CVD with associated subgroups, such as Low Pressure CVD (LPCVD), are, in the main, the dominant tools of choice for material deposition. There are associated advantages and drawbacks with every method used, and these are outlined briefly here. In addition, low temperature and thin film step layers, as opposed to thick film SiGe virtual substrates, are examined throughout this report as possible alternatives in the steps used to grow the various disparate devices outlined previously. This work tackles the resulting differences in terms

of threading dislocation density and strain, using a variety of complementary analytical techniques as outlined in Chapter 2.

In MBE, an atomic beam of the growth species is created by heating the raw material above its melting point using an effusion cell. The disadvantage of using electron beam sources is that the electrons themselves can create unwanted radiation in the chamber which is obviously not ideal for defect free heterolayers. CVD has a distinct advantage over MBE in terms of the number of defects present and lower background contamination. In terms of strained Si, CVD can be carried out at atmospheric pressure, and involves the pyrolysis at an elevated temperature of the precursor gas, i.e. silane.

The characterisation of the LPCVD technique used in the growth of a strained Si layer has been done with the growth/deposition of a number of epitaxial and polycrystalline silicon layers from $SiH_4$ (discussed in detail in Chapter 3). The thicknesses of grown/deposited layers were found to be in a linear relationship with time. Structures were also manufactured in both CVD and MBE chambers in order to investigate the possibility of combining both growth techniques, and this is commented on in more detail at a later stage.

### 1.4.6 Bandgap Engineering

Bandgap engineering, which is the ability to alter the energy gap of a semiconductor, has transformed the field of electronic and optoelectronic devices, particularly in the III–V materials systems. Si/SiGe heterostructures allow both bandgap and strain engineering using silicon technology. Though beyond the scope of the work reported here, it is nonetheless important to understand how the conduction band, valence band and the curvature of the bands are affected when the material's parameters are changed. A number of different papers have presented calculations on the band structure for different types of SiGe devices ranging from compressive strain [41] to complete calculations for all virtual substrate and active layers [42–45].

The basic description of a semiconductor is its bandstructure, i.e. the variation of energy $E$ with wave-vector k. The most important bands are:

*Valence band* - the last filled energy level at T=0 K

*Conduction band* - the First unfilled energy level at T=0 K

The valence band maximum is at k =0, is known as the *gamma point*. Where the conduction-band minimum also occurs at k =0, the semiconductor is said to be a *direct band* semiconductor. At non-zero k =0, the semiconductor is an *indirect-band semiconductor*.

In a semiconductor, the band gap is small enough that electrons can be moved from the orbitals in the valence band to the orbitals in the conduction band, as shown in Fig. 1. This leaves both bands partially filled, so the material can conduct electricity.

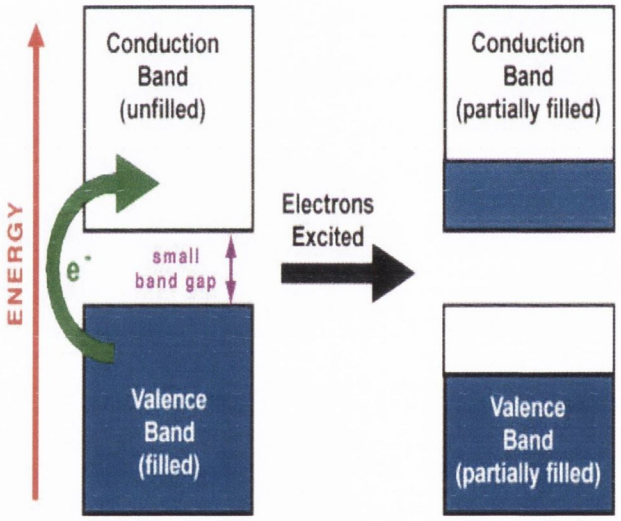


**Fig.1.10** The partial filling of a conduction band due to the excitation of electrons in the valence band [46]

The band structures of bulk (relaxed) Si and Ge are completely different. Both are indirect bandgap materials with the valence band edge at $k = 0$ consisting of degenerate light-hole (LH) and heavy-hole (HH) bands with a split-off (SO) band lower in energy. However, it is in the conduction bands that the major difference occurs. Ge has the conduction band minima at the L points of the Brillouin zone along the [111] directions with eight equivalent half valleys or four equivalent full valleys (Fig. 1.11(*a*)). Silicon, in

comparison, has the six conduction band minima about 0.85 of the way along the Δ-direction of [100] towards the zone boundary at the X points (Fig. 1.11(*b*)).

For an unstrained (100) $Si_{1-x}Ge_x$ material the bandgap is shown in Fig. 1.12. A discontinuity appears at approximately $x = 0.85$ where the conduction band changes abruptly between silicon like Δ6 minima valleys to *L* valleys. The addition of strain is also demonstrated in Fig.1.12 for compressively strained $Si_{1-x}Ge_x$ grown on relaxed Si(100) with the degeneracy of the LH and HH bands being split by the strain.

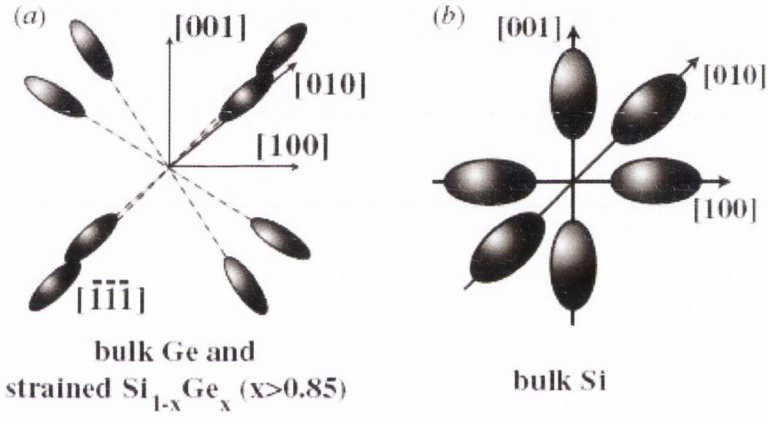


**Fig. 1.11** (*a*) The conduction band valleys of Ge along the [111] directions and (*b*) the conduction band valleys of silicon along the [100] directions [10].

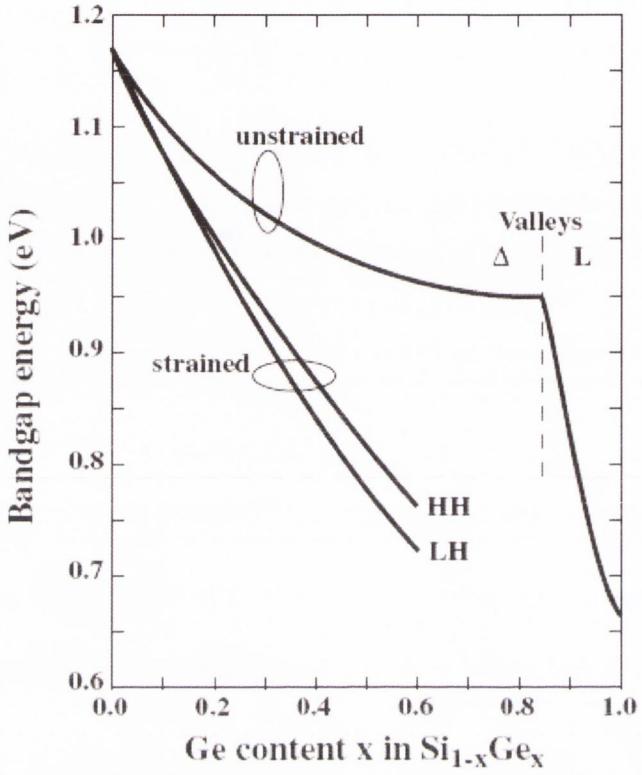


**Fig. 1.12** The bandgap in eV for strained $Si_{1-x}Ge_x$ grown on bulk silicon substrates and for unstrained $Si_{1-x}Ge_x$ [41].

In ordinary silicon, all six lobe shaped orbitals have the same energy i.e. the conduction band of silicon is six fold degenerate, so there is no preferred direction of flow. However, by stretching the lattice, the six fold degeneracy is broken, with the two out-of-plane valleys becoming preferentially occupied relative to the four in-plane valleys, as shown in Fig. 1.13. This split reduces intervalley phonon scattering in the out-of-plane valleys and reduces the effective mass, thereby increasing the mobility of the carriers [47]. This is discussed in Chapter 3 where efforts to grow strained Si structures are described in detail.

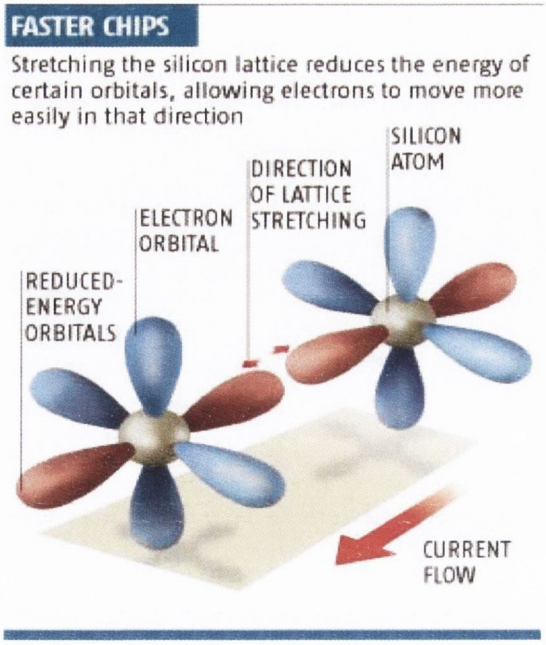


**Fig. 1.13** Orbital orientation in strained silicon [44]

## 1.5 Conclusions

For the continual advancement of technologies in line with Moore's Law, there is an inherent need for the underlying materials upon which the technology is based to improve also. To this end, several novel materials are currently being proposed, with benefits both in terms of cost and performance. This chapter has briefly outlined the different types of material that are investigated in this work, with future chapters providing a more detailed analysis.

Central to this is the need to understand the basics of SiGe as it is used as a virtual substrate in the majority of the materials presented in this work. The fundamentals associated with bandgap and strain engineering as they relate to SiGe were discussed in this chapter as well as presenting an overview of the importance of strain and lattice relationships.

Important considerations, such as optimal growth techniques and dislocation propogation were explored, while the influence of underlying defects on the surface morphology was introduced to the reader. Critical thickness, which bears an important role in the thickness of virtual substrates used in the growth of novel materials was discussed briefly, with a more detailed analysis presented in the following chapters.

**References**


1. http://www.intel.com/technology/
2. International Technology Roadmap for Semiconductors,http://www.itrs.net/
3. *Electronics*, **38**, Number 8, April 19, 1965
4. Lawrence G. Roberts, *Commun. ACM* **40,** 2 (1997)
5. R. C. Alferness, *Proceedings of the European Conference on Integrated Optics*, p. 245, 1995
6. J. Haartsen, *Ericsson Rev.* (Sweden) **75,** No. 3, 110 –117 (1998).
7. B. S. Meyerson, *Appl. Phys. Lett.* **48,** 797 (1986).
8. D. L. Harame, J. M. C. Stork, B. S. Meyerson, T. N. Nguyen, and G. J. Scilla, *IEEE Electron Device Lett.* **10,** 156 (1989).
9. G. L. Patton, D. L. Harame, J. M. C. Stork, B. S. Meyerson, G. J. Scilla, and E. Ganin, *IEEE Symposium on VLSI Technology, Digest of Technical Papers, Kyoto, Japan*, p. 95,(1989)
10. Douglas J Paul, *Semicond. Sci. Technol.* **19** (2004) R75–R108 PII: S0268-1242(04)61523-9
11. http://www.research.ibm.com/journal/rd/
12. http://www.eetimes.com/news/98/1025news/ibm.html
13. Pathfinder Research Inc. '*SiGe Advances in theMarketplace*', (2002)
14. J. Sayer '*The Market Potential of SiGe Unaxis Workshop*'(Pfaffikon), (2002)
15. F.Schaffler, *Semicond. Sci Technol.* **12**, 1515 - 1549, (1997)
16. V.T. Bublik, S.S. Gorelik, A.A. Zaitsev and A.Y. Polyakov, *Phys. Status Solidi*, **65** K79, (1974)
17. J. H. van der Merwe, *J. Appl. Phys.* **34**, 117 (1963)

18. J.C.Bean , L.C. Feldman, A.T. Fiory, S. Nakahara S and I.K. Robinson , *J. Vac. Sci. Technol. A* **2** 436, (1984)

19. H.J. Herzog, H. Jorke and E. Kasper, *J. Electrochem. Soc.* **136** 3026, (1989)

20. J. W. Matthews J W and A.E. Blakeslee, *J. Cryst. Growth* **32** 265, (1976)

21. R. People and J.C. Bean, *Appl. Phys. Lett.* **47** 322, (1985)

22. R. People and J.C. Bean, *Appl. Phys. Lett.* **49** 229, (1985)

23. D.C. Houghton, *J. Appl. Phys.* **70** 2136, (1991)

24. Herzog H-J, Jorke H, Kasper E and S.Mantl, *J. Electrochem. Soc.* **136** 3026, (1989)

25. F. LeGoues, K.Eberl and S.S. Iyer , *Appl. Phys.Lett.* **60** 2862, (1992)

26. F. Schaffler F, D. Tobben , H.J.Herzog, G. Abstreiter and B. Hollander, *Semicond. Sci. Technol.* **7** 260, (1992)

27. S. Luryi, A. Kastalski and J.C.Bean, *IEEE Trans. Electron. Dev.* **ED-31** 1135, (1984)

28. E.A. Fitzgerald, Y.H. Xie, L.M. Green, D. Brasen, A.R. Kortan J. Michel, Y.J. Mii and B.E. Weir, *Appl. Phys. Lett.* **59** 811, (1991)

29. F.K. LeGoues, B.S. Meyerson and J.F. Morar, *Phys.Rev. Lett.* **66** 2903, (1991)

30. M. Hohnisch, H.J. Herzog and F. Schaffler, *J. Crystal Growth* **157** 126, (1995)

31. B.S. Meyerson , K.J. Uram and F.K. LeGoues , *Appl. Phys Lett.* 53 2555, (1988)

32. E.A. Fitzgerald, *Appl. Phys. Lett.* 59 811, (1991)

33. M. Hohnisch, H.J. Herzog and F.Schaffler, *J. Crystal Growth* **157** 126, (1995)

34. F K LeGoues, B S Meyerson, J F Morar and P D Kirchner, *J. Appl. Phys.* **71** 4230, (1992)

35. F K LeGoues, P M Mooney and J O Chu, *Appl.Phys. Lett.* **62** 140, (1993)

36. P M Mooney, J L Jordan-Sweet, K Ismail , J O Chu, R M Feenstra and F K LeGoues, *Appl. Phys. Lett.* **67** 2373, (1995)

37. J W P Hsu, E A Fitzgerald, Y H Xie, P J Silverman and M J Cardillo, *Appl. Phys. Lett.* **61** 1293, (1992)
38. M A Lutz, R M Feenstra, F K LeGoues, P M Mooney and J O Chu, *Appl. Phys. Lett.* **66** 724, (1995)
39. P M Mooney, J L Jordan-Sweet, J O Chu and F K LeGoues, *Appl. Phys. Lett.* **66** 3642, (1995)
40. J W P Hsu, E A Fitzgerald, Y-H Xie, P J Silverman and M Cardillo, *Appl. Phys. Lett.* **61** 1293, (1992)
41. R. People, *Phys. Rev. B* **32** 1405, (1986)
42. C G Van der Walle and R M Martin, *Phys. Rev. B* **34** 5621, (1986)
43. C G Van der Walle, *Phys. Rev. B* **39** 1871, (1989)
44. M M Rieger and P Vogl . *Phys. Rev. B* **50** 8138, (1994)
45. M V Fischetti and S E Laux, *J. Appl. Phys.* **80** 2234, (1996)
46. http://www.chemistry.wustl.edu/~edudev/LabTutorials/PeriodicProperties/MetalBonding/MetalBonding.html
47. J. Barden, W. Scholckey, *Physical Review,* **80** 72-80, (1950)

# Chapter Two

# Experimental Procedures

## 2.1 Introduction

The use of SiGe in novel devices, as outlined in Chapter 1, presents many measurement challenges. Film thickness, germanium concentration, defects, lattice strain and surface roughness are all parameters that must be monitored and controlled for proper device growth. Some of these measurements must be made on ultra thin multilayer stacks, which exacerbates the challenges. This chapter presents a number of measurement techniques suitable for use on a variety of materials such as strained Si, SiGe buffer layers in Ge P-N photodiodes etc.

As already discussed in Chapter 1, a primary application for SiGe is the heterojunction bipolar transistor (HBT), which offers significant advantages over conventional Si MOSFETs for use in high speed, high frequency communications devices. To recapitulate, the SiGe HBT allows integrated circuit (IC) designers to integrate analogue, digital and radio frequency (rf) functions onto a single chip with minimal overhead on existing CMOS production methodologies [1]. HBTs use a thin (< 1000Å) multilayer stack of epitaxial Si with varying Ge concentrations and thicknesses to form the emitter region of a bipolar transistor. Compared with conventional Si layers, those with a high Ge concentration supply high mobility electrons, while the low concentration layers provide low contact resistance. This enables devices capable of gigahertz switching speeds to be developed at increasingly smaller geometries [2]. In terms of each of the epitaxial Si layers, the ability to measure accurately both Ge concentration and thickness is essential for effective process control of HBT devices. It is incumbent on the measurement tool of choice that it is capable of making independent composition and thickness measurements for each layer within any film stack. Primarily, this is because all of the layers grow during a single pass in an epi reactor and therefore one cannot make film measurements until all the layers have been formed.

Another application for SiGe is strained Si, wherein the traditional Si active device layer is replaced with a thin (< 200Å) strained Si layer deposited epitaxially on a several micron thick bed of epitaxially grown SiGe. As the lattice spacing of Si is smaller than that of SiGe, for a thin Si layer deposited on an underlying SiGe layer, its crystal lattice must be effectively stretched, or 'strained', in order to match that of SiGe. This introduction of strain into the Si lattice increases the mobility of electrons in the transistor channel, producing faster transistor switching speeds [3]. In this application, the most significant measurement parameters are the thickness of the strained Si layer and the concentration of Ge in the underlying relaxed SiGe buffered layer, which has a primary impact on the strain of the Si film [4-5]. These measurements challenge engineers because of the thinness of the strained Si layer. Also, if Ge diffusion does occur, the interface between the strained Si and SiGe layers can become indistinct, making it difficult to measure individual layer thickness.

## 2.2 Possible Methods of Analysis

The nature of this thesis requires that certain measurement techniques be used in order to provide suitable characterisation of the material under investigation. It is important that the reader is familiar from a very early stage with the tools in use and why they were chosen. This chapter discusses several possible characterisation techniques and then proceeds to explain in detail the actual tools used. In addition, the preparation steps and setup are discussed as well as some history of the various tool usages down through the years.

Secondary ion mass spectrometry (SIMS) is an offline analytical technique that can provide independent measurements of both Ge concentration and film thickness of each layer. It is an extremely accurate and sensitive technique, with a typical accuracy of within 5% for concentration measurements and 2% for depth [6-7]. SIMS is often considered to be the benchmark technique for elemental and thickness composition measurements. A typical scan, however, can take an hour or more as well as resulting in

the destruction of the device. These disadvantages make the technique highly inappropriate for production monitoring. Furthermore, SIMS suffers from measurement artefacts, such as enhanced count rates at interfaces, which can distort the true SiGe concentration profile of a multilayer film stack.

### 2.2.1 X-Ray

X-ray techniques have been used for many years to characterise semiconductor materials in a laboratory environment [8-9]. These techniques have excellent intrinsic measurement capability but historically have lacked the high throughput, small spot size, ease of use and low cost of ownership required for production monitoring. There are three main techniques associated with X-ray methods and these are: X-ray fluorescence (XRF), X-ray reflectometry (XRR) and X-ray diffraction (XRD).

XRF has been in production for more than 10 years and can be used to measure Si and Ge composition individually. The technique, however, is limited by the fact that it is only suitable in measurements of single layered unpatterned wafers. This is due to the fact that as X-rays can penetrate several microns deep into a substrate, any Ge signal that is collected from all of the layers is counted as a single, "lumped" Ge signal. XRR can be used to provide information on multilayer density, thickness and surface and interfacial roughness, both independently and simultaneously. However, XRR suffers from a poor signal-to-noise ratio as the electron density contrast between the various SiGe layers is low. This results in poor sensitivity to small changes in layer thickness. New small spot systems are becoming available, but significant challenges remain in making this technique production worthy.

Finally, XRD provides the most comprehensive information on film characteristics, since stress, thickness and Ge concentration can be theoretically extracted from diffraction spectra. Small spot systems are only now becoming available thanks to recent advances in X-ray hardware and algorithm software. Work presented in Chapter 5 outlines the benefits of using XRD as a complementary analytical technique to micro-Raman (discussed below) analysis in the measurement of strain. It also discusses how it is used

to verify the growth of the buffer layer present in the Ge P-N photodiode sample. Three sets of different XRD measurements are reported upon which, when analysed, allow one to understand the nature and characteristics of the relevant samples.

### 2.2.2 Optical Metrology

In order for a characterisation technique to be used at the manufacturing level, it is important that it is both fast and reliable, while also being non-destructive. This is necessary for incorporation into the final phases of production where samples will be used to create market ready devices. Optical metrology has the advantage of meeting the requirements outlined above for characterisation of production ready thin films. Of the various optical measurement techniques available today, Raman Spectroscopy is perhaps the most suitable for measurements relating to strain and composition while Spectroscopic Ellipsometry (SE) is another capable tool of choice. However, conventional SE systems have difficulty in achieving a high correlation (within 1%) to offline analytical techniques such as SIMS. Because of the sheer number and disparate nature of SiGe measurements, no single technology completely covers all requirements.

## 2.3 Techniques Used

Among the analytical methods that are currently available, three main measurement techniques are referred to throughout this thesis, irrespective of the material under investigation. These are:

1. Transmission Electron Microscope (TEM);
2. Micro-Raman Spectroscopy;
3. X-Ray Diffraction.

Different analytical techniques are more suitable to certain types of investigation, e.g. TEM allows one to analyse the presence of threading dislocations within heterostructures, while micro-Raman techniques allow strain measurements to take place on these same materials. By choosing these tools, complementary and independent analysis of materials can be performed.

### 2.3.1 Transmission Electron Microscope (TEM)

The Transmission Electron Microscope (TEM) uses a high energy electron beam transmitted through a very thin sample to image and analyse the microstructure of materials with near atomic scale resolution. Several research websites are dedicated to describing the operation of the TEM, including Stanford's Characterisation Library [10] and the University of Nebraska[11], the main points of which are presented below. The electrons are focused with electromagnetic lenses and the image is observed on a fluorescent screen, or recorded on film or digital camera. The electrons are accelerated to several hundred kV, giving wavelengths much smaller than that of light and X-rays: 200 kV electrons have a wavelength of 0.025Å. However, whereas the resolution of the optical microscope is limited by the wavelength of light, that of the electron microscope is limited by aberrations inherent in electromagnetic lenses, to about 1-2Å. The high-resolution mode of the microscope images the crystal lattice of a material as interference patterns between the transmitted and diffracted beams. This allows one to observe planar and line defects, grain boundaries, interfaces, etc. [12]. The Bright Field/Dark Field imaging modes of the microscope, which operate at intermediate magnification, combined with electron diffraction, are also invaluable for giving information about the morphology, crystal phases, and defects in a material. The TEM is also capable of forming a focused electron probe, as small as 2Å, which can be positioned on very fine features in the sample. This is of particular benefit for micro diffraction information or analysis of X-rays for compositional information with an energy dispersive X-ray spectroscopy (EDS) detector. The spatial resolution for this compositional analysis in TEM is very high, on the order of the probe size, because of the thinness of the sample (1000 - 2000Å). Transmission of fast electrons through the thin sample causes their inelastic scattering, i.e. energy losses of primary electrons due to the excitations of atoms of the samples [13]. The distribution of transmitted electrons as a function of energy loss is called an energy loss spectrum. Such a spectrum carries invaluable information about chemical composition of the samples as well as information about bonding, coordination and charge transfer on an atomic level. Combining the electron energy loss spectroscopy with the imaging ability of a Gatan Imaging Filter (GIF) extends the analytical power of

the TEM up to the nanoscale and allows chemical analysis of grain boundaries, thin interface layers etc.

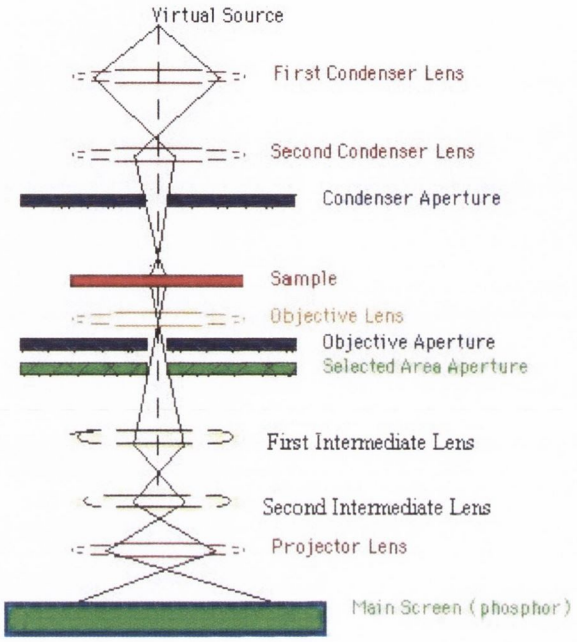


**Fig. 2.1** TEM internal diagram [11].

The "Virtual Source" at the top of Fig.2.1 represents the electron gun. The gun creates a stream of high energy monochromatic electrons. This stream is focused to a small, thin, coherent beam by the use of condenser lenses 1 and 2. The first condenser lens, as shown above, largely controls the minimum spot size while the second condenser lens affects both the diameter of the illuminated area of the specimen as well as the convergence of the beam by changing the size of the spot on the sample from a wide dispersed spot to a pinpoint beam. The condenser aperture helps to control the intensity of illumination by restricting the beam through the elimination of high angle electrons (those far from the optic axis indicated by the dotted line down the centre of Fig. 2.1). When the beam strikes the specimen it is the transmitted portion that is focused by the objective lens into an image. The objective aperture, which is placed in the back focal plane of the image, enhances the contrast by blocking out high angle diffracted electrons thereby selecting only those electrons which will contribute to the image. Using a selected area aperture, a thin metal strip with a series of holes present, one can select which part of the specimen

to obtain a diffraction pattern from. The image magnification is controlled via the strength of both the intermediate and projector lenses.

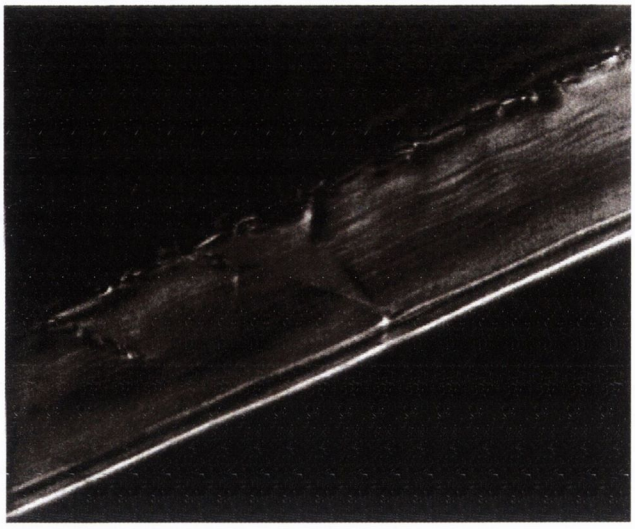

**Fig. 2.2** TEM Image of a Silicon Quantum Well

The signal strikes the phosphorous image screen and light is generated, allowing the user to see the image. The darker areas represent those portions of the sample through which fewer electrons were transmitted (these portions are thicker or denser). The lighter areas of the image represent those areas of the sample through which more electrons were transmitted (i.e. the sample is thinner or less dense at this point). Fig.2.2 shows a TEM micrograph image of a strained Si Quantum Well (QW), with the Si cap clearly shown by the bright white line, situated near the edge of the sample (or foil as it is termed), which is always the thinnest part of the TEM sample. It is important to note however, that white areas in a TEM are also influenced by the angle of tilt, which influences the distance the beam travels inside the sample, and thus the number of interactions it undergoes.

#### 2.3.1.1 Specimen Interaction

Specimen interaction is what makes Electron Microscopy possible. The energetic electrons strike the sample and various reactions can occur as shown in Fig. 2.2. The reactions noted on the top side of the diagram are utilized when examining thick or bulk

specimens (SEM) while the reactions on the bottom side are those examined in thin or foil specimens (TEM).

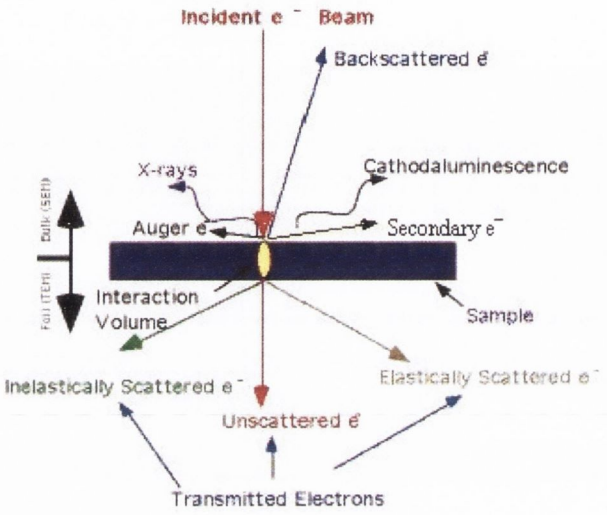


**Fig. 2.3** Specimen Interaction [11]

Interactions, as outlined in Fig. 2.2 can be broken into three separate categories, namely Inelastic, Elastic and Unscattered electrons.

#### 2.3.1.1.1 Unscattered Electrons

Electrons that do not undergo any interaction while being transmitted through a sample are termed 'Unscattered' electrons. It is to be noted that the thickness of the sample under investigation influences the number of electrons actually transmitted through the specimen, with the number of actual unscattered electrons inversely proportional to the thickness of the TEM sample. Therefore, thinner areas will appear brighter in the TEM image as more electrons are transmitted through while conversely, darker areas in the TEM image represent thicker areas that have fewer unscattered electrons.

#### 2.3.1.1.2 Elastically Scattered Electrons

Elastically scattered electrons are those electrons that interact with the sample's atoms and therefore experience a deflection from their original path but without any associated loss of energy. These scattered electrons are then transmitted through the remaining portions of the specimen. All electrons follow Bragg's Law and thus are scattered according to the equation:

$$n\lambda = 2d \sin\theta \qquad (2.1)$$

where $\lambda$ is the electron wavelength, n is an integer, $\theta$ is both the angle of reflection and incidence, and d is the crystal lattice spacing between atomic planes Electrons enter the sample normal to its surface. Incident electrons travel at the same frequency and thus possess the same wavelength and energy. It follows that electrons that are scattered by the same atomic spacing within the sample will therefore be scattered by the same angle. These electrons can then be collated to form a pattern of spots, with each spot corresponding to and identifying a particular atomic plane within the sample. This pattern can then yield information about the orientation, atomic arrangements and phases present in the area being examined.

#### 2.3.1.1.3 Inelastically Scattered Electrons

In contrast with elastically scattered electrons as described in Section 2.3.1.1.1, those electrons that lose energy through interaction with the sample's atoms are termed 'Inelastic'. The energy lost by the incident electrons is characteristic of the elements present within the sample and is unique to each bonding state present. In fact, compositional and bonding information on the specimen can be achieved through examination of the energies lost in the interaction. Bands of alternating light and dark lines that are formed by inelastic scattering interactions are termed Kakuchi bands and are related to the atomic spacing present in the specimen. Using these bands one can either 'follow' them like a roadmap to the 'real' elastically scattered electron pattern or else measure them, with their width is inversely proportional to atomic spacing.

### 2.3.1.2 Energy Dispersive X-Ray Spectroscopy (EDS)

As shown in Fig.2.3, X-rays are characteristic of the interaction of accelerated electrons with a specimen. As the wavelength of X-Rays is comparable to the size of atoms, it is obvious that they are suited to investigations at the atomic level. It is therefore useful to understand how these X-rays are generated in order to see how one might use them in the characterisation of samples'. X-rays are produced when a focused electron beam accelerated across a high voltage field bombards a solid target. As electrons collide with atoms in the target and slow down, a continuous spectrum of X-rays is emitted. The high

energy electrons eject inner shell electrons in atoms through the ionization process. In order to return the atom to its normal state, a free electron must fill the shell, i.e. an electron from a higher energy moves into the vacancy produced at the lower energy level. It is this energy difference between the contributing and vacant shell which results in an energy loss in which an X-ray photon with energy characteristic of the target material is emitted. This energy is given up in the form of electromagnetic radiation ie X-rays. Since energy levels in all elements are different, element specific, or characteristic X-rays are generated.

Energy Dispersive X-ray microanalysis uses detection equipment to measure the energy values of the characteristic X-rays generated within the electron microscope. Using semiconductor material (typically, Si/Li single crystal) to detect the X-rays and a multi-channel analyser microanalysis system converts X-ray energy into an electronic count. The accumulation of these energy counts creates a spectrum representing the chemical analysis of the sample. Therefore, while the electron microscope produces an image of the sample's topography, energy dispersive X-ray microanalysis tells the microscopist what elements are present in the sample [14]. Fig. 2.4 shows an EDS measurement recorded in a SiGe graded layer present in a Ge P-N photodiode. This is explained in more detail in Chapter 4.

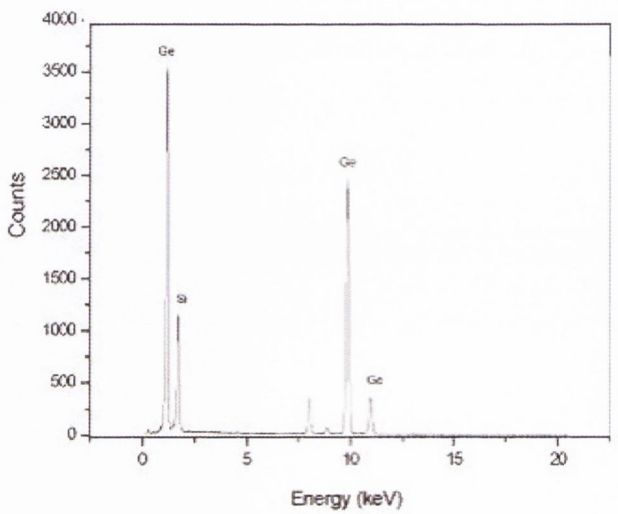


**Fig. 2.4** EDS of upper SiGe layer

### 2.3.1.3 Electron Energy Loss Spectroscopy (EELS)

Electron Energy Loss Spectroscopy (EELS) is the analysis of the energy distribution of electrons that have interacted inelastically with the specimen [15]. The transmitted beam contains inelastically scattered electrons whose energy has been decreased by amounts corresponding to characteristic absorption frequencies in the solid. As outlined earlier, these inelastic collisions carry information relating to the electron structure of the specimen atoms. Examining the spectrum of electron energies, one can reveal details of the nature of these atoms such as their bonding and nearest neighbour distributions. In order to do this, a magnetic prism spectrometer is used as an additional electromagnetic lens in TEM. A magnetic prism with a resolving power of approximately 1eV is a highly sensitive device which is sufficient to distinguish all the elements in the periodic table. Electrons that undergo different amounts of loss due to the Inelastic scattering process exit the sample at different points. This is made possible by the magnetic field of the prism which deflects the angle of the transmitted electrons through $90^0$. The EELS spectrum is a distribution of electron counts versus energy loss.

This process is exactly analogous to the dispersion of white light by a glass prism An EELS spectrum has specific features of absorption spectra, because, unlike EDS and other microanalytical techniques, EELS is concerned with detecting the primary event, namely the loss of electron energy due to an inelastic interaction and not a secondary event connected with the return of the atom to ground state.

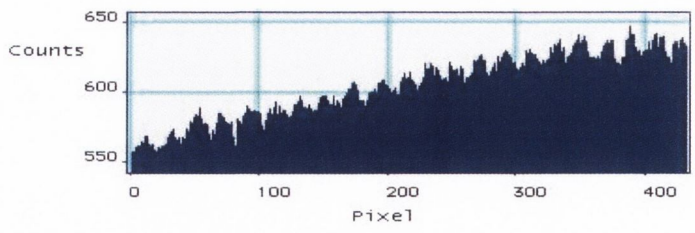


**Fig. 2.5** Si distribution across SiGe graded layer

Fig.2.5 shows an EELS spectrum taken from a strained Si structure with a relaxed graded SiGe buffer layer (from which the EELS spectrum was observed). A Gatan Imaging Filter (GIF) produces energy filtered electron images and diffraction patterns, as well as electron energy loss spectra (EELS) [16]. One of the major applications of the imaging filter is in chemical microanalysis, where the spectra provide information about the different chemical elements present, and the images show how the elements are distributed in the sample. Another important application of the GIF is improving the contrast of images and diffraction patterns by removing the contribution of elastic scattering. R.F Egerton [17], in his seminal work on EELS describes the fundamentals involved in calculating elemental maps. The following introduces some of the keys points of his work.

Different protocols are used to estimate the background image and identify the element signal to calculate the elemental map from the element enhanced image. The most common are the 'two-' and 'three-window' methods. In the two-window method, a background image is a pre-edge image that is subtracted (difference method) or divided (jump-ratio method) from the element enhanced image. The two-window method gives elemental maps with high signal-to-noise ratios because it uses only two images instead of three as in the case of the three-window-power-law method. The three-window power law method is the most conventional method for background subtraction and calculation of elemental maps. In this case, the background is estimated by a power law function $I = A.E^{-r}$, where I is the electron count, E is the energy loss and A and r are the two independent fitting parameters. To calculate the elemental map with this method, two images below and one image above the ionization edge are acquired. Background correction is done by extrapolating the background image according to the power function model. Both A and r vary within the samples as a result of variations in the thickness and composition and a separate estimation of the background image is required at each pixel. To do this, the extrapolated background is subtracted pixel by pixel from the element enhanced edge (the image above the ionization edge). The net result of this subtraction is considered the elemental map for that element [17].

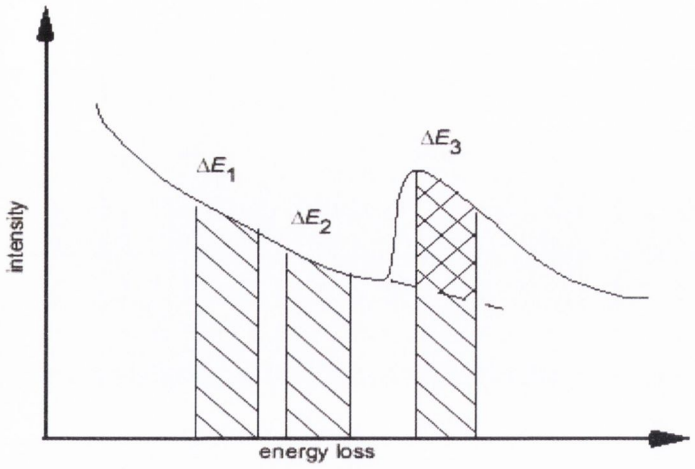


**Fig. 2.6** Schematic of three-window elemental mapping technique

### 2.3.1.4 TEM Specimen Preparation

The materials undergoing TEM analysis, whether it be EELS, EDS or HREM, have first to be prepared in such a way that electron transparent areas are present in the sample. TEM preparation is a well documented practice, with the Max Planck Institut, in which most of the TEM recorded in this work was undertaken, providing a detailed description of the process [18]. The first step in the TEM preparation is a mechanical treatment of the material, such as sawing, ultrasonic grinding or punching to give the sample a circular form with a diameter of approximately 3 mm. To prepare cross sectional specimens of, e.g., grain boundaries or hetero-phase interfaces, the formation of sandwiches of the film/substrate material is a common procedure, which is then later glued inside a ceramic or metallic tube. After sawing the tube into small disks, each disk is mechanically ground to a thickness of 100μm to 150μm. In most cases, grinding is followed by a dimpling process until the specimen thickness reaches 10μm to 50μm in the thinnest regions. The final thinning procedure is performed by $Ar^+$ ion bombardment with ion energies in the range of 100eV to 6 keV. Within this preparation step the ion thinning parameters, such as the glancing angle or the ion beam energy are varied to obtain an optimal TEM specimen quality. An additional plasma cleaning process can remove impurities on the specimen surfaces.

**Fig. 2.7** A TEM preparation desk [18]

Shown in Fig. 2.7 is a typical working desk for the mechanical preparation and thinning of the TEM samples. Each desk is equipped with a grinding/polishing machine (a), a heating plate for gluing the specimens on the used specimen holders, a dimpler (c), and a wire saw (d).

### 2.3.2 Raman Spectroscopy

From an historical perspective, it is interesting to note that Raman spectroscopy, or at least the ideas relating to it, has been around for over a hundred years. One could argue that it was the Austrian quantum physicist, A. Smekal who conceived its existence when he predicted the theoretical scattering of monochromatic radiation with change of frequency [18]. However, both Rayleigh in 1871 and Einstein some years later in 1910 had already been studying the scattering of light within various media. Up until then however, with the sole exception of certain types of scattering in the X-ray spectral region observed by Compton, no change in wavelength had been observed [19]. With this as its background, many scientists were investigating the idea relating to the inelastic scattering of light, which was first reported in Calcutta by Raman and almost simultaneously by Landsberg in Moscow in 1928 [20 -21]. It was two years later when Raman received the Nobel Prize in Physics for his discovery, which bears the name since.

### 2.3.2.1 The Raman Effect

Mechanical strain or stress may affect the frequencies of the Raman modes, and lift their degeneracy. When light is scattered from a molecule most photons are elastically scattered. The scattered photons have the same energy (frequency) and, therefore, wavelength, as the incident photons. However, a small fraction of light (approximately 1 in $10^7$ photons) is scattered at optical frequencies different from, and usually lower than, the frequency of the incident photons. The process leading to this inelastic scatter is termed the Raman effect.

Raman scattering can occur with a change in vibrational, rotational or electronic energy of a molecule. The difference in energy between the incident photon and the Raman scattered photon is equal to the energy of a vibration of the scattering molecule. A plot of intensity of scattered light versus energy difference is termed a Raman spectrum.

### 2.3.2.2 The Scattering Process

Mechanical strain or stress may affect the frequencies of the Raman modes, and lift their degeneracy. As stated, the Raman effect arises when a photon is incident on a molecule and interacts with the electric dipole of the molecule. It is a form of electronic (more accurately, vibronic) spectroscopy, although the spectrum contains vibrational frequencies. In classical terms, the interaction can be viewed as a perturbation of the molecule's electric field. In quantum mechanics the scattering is described as an excitation to a virtual state lower in energy than a real electronic transition with nearly coincident de-excitation and a change in vibrational energy. The scattering event occurs in $10^{-14}$ seconds or less. The virtual state description of scattering is shown in Fig. 2.8.

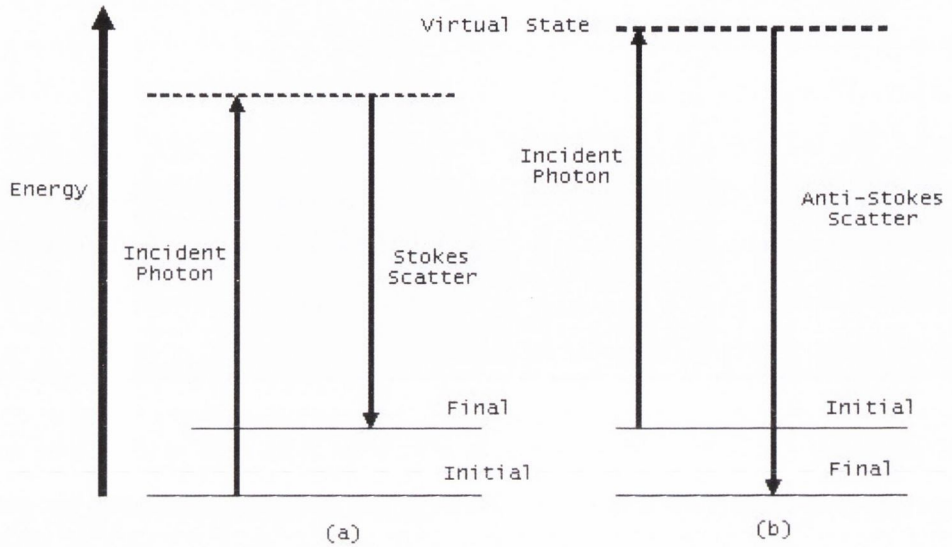


**Fig. 2.8** Energy level diagram for Raman scattering; (a) Stokes Raman scattering (b) anti-Stokes Raman scattering

The energy difference between the incident and scattered photons is represented by the arrows of different lengths in Fig. 2.8. Numerically, the energy difference between the initial and final vibrational levels, $\bar{\nu}$, or Raman shift in wave numbers ($cm^{-1}$), is calculated through the equation:

$$\bar{\nu} = \frac{1}{\lambda_{Incident}} - \frac{1}{\lambda_{Scattered}} \qquad (2.2)$$

in which $\lambda_{incident}$ and $\lambda_{scattered}$ are the wavelengths (in cm) of the incident and Raman scattered photons, respectively. The vibrational energy is ultimately dissipated as heat. Because of the low intensity of Raman scattering, the heat dissipation does not cause a measurable temperature rise in a material. At room temperature the thermal population of vibrational excited states is low, although not zero. Therefore, the initial state is the ground state, and the scattered photon will have lower energy (longer wavelength) than the exciting photon. This Stokes shifted scatter is what is usually observed in Raman spectroscopy. The energy decrease or increase from the excitation is directly related to the vibrational energy spacing in the ground electronic state of the molecule and therefore the wavenumber of the Stokes and anti-Stokes lines are a direct measure of the

vibrational energies of the molecule. Fig. 2.8(a) depicts Raman Stokes scattering. A small fraction of the molecules is in vibrationally excited states. Raman scattering from vibrationally excited molecules leaves the molecule in the ground state. The scattered photon appears at higher energy, as shown in Fig. 2.8(b). Note that the anti-Stokes line is much less intense than the Stokes line. This occurs because the anti-Stokes line is due only to molecules that are vibrationally excited prior to irradiation. Therefore in Raman spectroscopy it is more usual that only the more intense Stokes line is normally measured. However, an anti-Stokes spectrum can be used in the case where the Stokes spectrum is not directly observable, or where a measure of temperature is required, which correlates to the ratio of anti-Stokes to Stokes intensity.

#### 2.3.2.3 Raman Selection Rules and Intensities

Mechanical strain or stress may affect the frequencies of the Raman modes, and lift their degeneracy. Raman scattering can be used to measure the Ge composition, x, in thin strained alloys with an absolute accuracy of $\pm 0.015\%$. The strain, $\varepsilon$, which is the deviation of the lattice constant from its relaxed state ($=\Delta l/l$, where l is the relaxed lattice) can be measured with an absolute accuracy of $\pm 0.0025\%$. This sensitivity in micro-Raman spectroscopy scattering arises from the fact that the spectrum of a $Si_{1-x}Ge_x$ layer provides at least three different, independent ways of measuring $x$ and $\varepsilon$. In the absence of strain, the first order Stokes Raman spectrum of diamond type materials exhibits a single peak which corresponds to the $q = 0$ triply degenerate optical phonons. The Raman wavenumber of the (stress free) Si peak is 520 $cm^{-1}$.

Ingrid De Wolf, in her topical review of Micro-Raman spectroscopy [22], presents a detailed summary of the underlying mathematical basis for Raman scattering. It is worth at this stage introducing some of this analysis so the reader might gain a greater understanding of the concepts involved. The vibrations of a crystal are described, not in terms of the vibrations of individual atoms, but in terms of collective motions in the form of waves, called lattice vibrations. Each possible vibration $j$ of the lattice is characterized by a wavevector $q_j$ and a frequency $\omega_j$.

The vibration amplitude, at position r, is given by

$$Q_j = A_j \exp[\pm i(q_j \cdot r - \omega_j t)] \tag{2.3}$$

where $Q_j$ is the normal coordinate of the vibration [23,24] and $A_j$ is a constant. Such a quantized lattice vibration is called a normal mode or a phonon. These lattice vibrations may cause a variation in the electrical susceptibility of the crystal, which can give rise to 'Raman scattering'. A *classical way* to explain Raman scattering is the following. When monochromatic light of frequency $\omega_i$ is incident on a crystal in a direction $k_i$, the associated electric field $E$ will induce at position $r$ an electric moment $P$, which is related to $E$ through

$$P = \varepsilon_0 \chi \mathrm{E} = \varepsilon_0 \chi \cdot \mathrm{E}_0 \exp\left[i\left(k_i \cdot r - \omega_i t\right)\right] \tag{2.4}$$

where $\chi$ is the susceptibility tensor, which describes the response of the crystal to the electric field. If the atoms of the sample are vibrating, the susceptibility may change as a function of these vibrations. This can be expressed by expanding $\chi$, for each normal mode of vibration $j$, in a Taylor series with respect to the normal coordinate of this vibration $Q_j$:

$$\chi = \chi_0 + \left(\frac{\partial \chi}{\partial Q_j}\right) Q_j + \left(\frac{\partial \chi}{\partial Q_j \partial Q_k}\right) Q_j Q_k + \cdots \tag{2.5}$$

which can be redefined as

$$\lambda_j = \chi_j^{1} Q_j + \chi_j^{2} Q_{jk} + \cdots \tag{2.6}$$

The first term will give rise to Rayleigh scattering, the second to first order Raman scattering, and the third to second order Raman scattering (two phonons are involved). For simplicity, we neglect the third and higher order terms.

Combining Eqns. (2.3) to (2.5) results in:

$$P = \varepsilon_0 \chi_0 \cdot \mathrm{E}_0 \exp\left[i\left(k_i \cdot r - \omega_i t\right)\right] + \varepsilon_0 \mathrm{E}_0 \left(\frac{\partial \chi}{\partial Q_j}\right) A_j \cdot \exp\left[-i\left(\omega_i \pm \omega_j\right) t\right] \exp\left[i\left(k_i \pm q_j\right) \cdot r\right] \tag{2.7}$$

From this it follows that the induced moment will reradiate light which has three distinct frequency components: $\omega_i$, which is called Rayleigh scattering, and $\omega_i + \omega_j$ and $\omega_i - \omega_j$, which are called anti-Stokes and Stokes Raman scattering respectively. This will only be observed if $\chi_j^1$ differs from zero. The scattering efficiency, *I*, depends on the polarization vector of the incident ($e_i$) scattered ($e_s$) light, and is given by

$$I = C\sum_j \left| e_i \cdot R_j \cdot e_i \right|^2 \qquad (2.8)$$

where *C* is a constant and *Rj* is the Raman tensor of the phonon *j* . The values of *Rj* are obtained from group theoretical considerations [25, 26]. They are second-rank tensors which are proportional to $\chi_j^1$, and they are used to calculate the polarization selection rules. The Raman tensors for each of the 32 crystal classes (symmetry point groups) have been derived and for silicon, there are three Raman tensors [26]. In the crystal coordinate system x = [100], y = [010] and z = [001] they are given by

$$R_x = \begin{pmatrix} 0 & 0 & 0 \\ 0 & 0 & d \\ 0 & d & 0 \end{pmatrix} \qquad R_y = \begin{pmatrix} 0 & 0 & d \\ 0 & 0 & 0 \\ d & 0 & 0 \end{pmatrix} \qquad R_z = \begin{pmatrix} 0 & d & 0 \\ d & 0 & 0 \\ 0 & 0 & 0 \end{pmatrix} \qquad (2.9)$$

For back scattering from a (001) surface, $R_x$ and $R_y$ correspond to scattering by transverse optical phonons (TO), polarized along x and y respectively, and $R_z$ corresponds to scattering by longitudinal optical phonons (LO), polarized along z. Of course, the characterization of a phonon as longitudinal or transverse depends on the surface from which scattering is observed. For back scattering from a (100) surface, Rx corresponds to the LO phonon. Table 2.1 shows which of the three modes can be observed for different polarization directions (from Eqn. (2.8)). It follows from this table that for back scattering from a (001) surface only the z polarized phonon can be observed (Rz matrix), while for back scattering from (110) (for example on a cleaved wafer), either the Rz or the Rx and Ry matrices can be involved. In the absence of stress, the corresponding three optical Raman modes of silicon have the same frequency of about $\omega_{j0} = 520$ cm$^{-1}$ (j = 1,2,3) and are degenerate. From a *quantum physical* point of view, Raman scattering involves the

destruction of a photon with frequency $\omega_i$, incident from a light source, and the creation of a photon with frequency $\omega_s$.

**Table 2.1** Polarisation selection rules for back scattering from a (001) surface or a (110) surface

| Polarization | | Visible | | |
|---|---|---|---|---|
| $e_i$ | $e_s$ | $R_x$ | $R_y$ | $R_z$ |
| Back scattering from (001) | | | | |
| (100) | (100) | — | — | — |
| (100) | (010) | — | — | x |
| (1-10) | (1-10) | — | — | x |
| (110) | (1-10) | — | — | — |
| Back scattering from (110) | | — | — | x |
| (1-10) | (001) | x | x | — |
| (1-10) | (1-10) | — | — | x |
| (001) | (001) | — | — | — |

Fig. 2.9 shows a typical Feynman diagram and the related energy levels for a first-order Stokes scattering process.

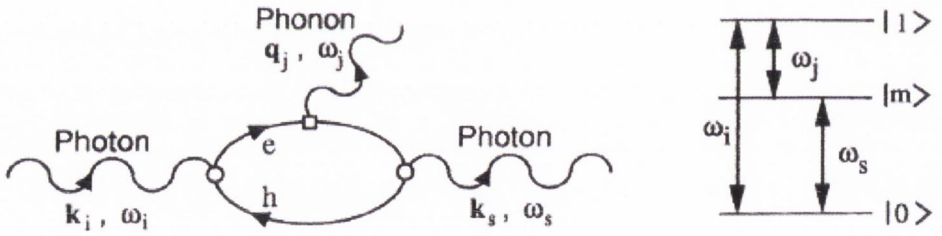


**Fig. 2.9** Feynman diagram and related energy levels for a first-order Stokes scattering process [22].

The scattering cross section can be calculated by treating this three step process using third-order perturbation theory [26]. An electron-hole pair is created through interaction of the incident photon (frequency $\omega_i$), with an electron. By this interaction, the electron goes from the ground state $|0\rangle$ to a state $|l\rangle$. By electron-phonon interaction, where a phonon of frequency $\omega_j$ is created (or annihilated in anti-Stokes), the electron goes from state $|l\rangle$ to state $|m\rangle$. By recombination of the electron–hole pair, a photon with frequency $\omega_s$ is emitted, where $\omega_s = \omega_i - \omega_j$ (for anti-Stokes it would be $\omega_s = \omega_i + \omega_j$). Because conservation of momentum is required for each intermediate step, whereas conservation of energy is required only for the overall process, both real and virtual intermediate states

are allowed. Furthermore, the three steps described above are taking place instantaneously, so the order in which they occur is not important. This results in six types of this kind of process.

#### 2.3.2.4 Effect of Stress on the Raman Modes of Silicon

Mechanical strain or stress may affect the frequencies of the Raman modes, and lift their degeneracy. One of the first papers addressing theoretically the effect of stress on the Raman modes was that by Ganesan *et al* [27]. They showed that the frequencies of the three optical modes in the presence of strain, to terms linear in the strain, can be obtained by solving the following secular equation [28, 29]:

$$\begin{vmatrix} p\varepsilon_{11}+q(\varepsilon_{22}+\varepsilon_{33})-\lambda & 2r\varepsilon_{12} & 2r\varepsilon_{13} \\ 2r\varepsilon_{12} & p\varepsilon_{22}+q(\varepsilon_{33}+\varepsilon_{11})-\lambda & 2r\varepsilon_{23} \\ 2r\varepsilon_{13} & 2r\varepsilon_{23} & p\varepsilon_{33}+q(\varepsilon_{11}+\varepsilon_{22})-\lambda \end{vmatrix} = 0 \qquad (2.10)$$

Here p, q and r are material constants, the so called phonon deformation potentials. They describe the changes in the 'spring constant' of the $q \cong 0$ optical phonons with strain and can be determined experimentally by applying external stress to the material under study [28-30]. $\varepsilon_{ij}$ is the strain tensor component. The difference between the Raman frequency of each mode in the presence of stress, $\omega_j$ (j =1,2,3), and in the absence of stress, $\omega_{j0}$, can be calculated from the eigenvalues $\lambda_j$ :

$$\lambda_j = \omega_j^{\,2} - \omega_{jo}^{\,2} \qquad (2.11)$$

or

$$\Delta\omega_j = \omega_j - \omega_{jo} \approx \frac{\lambda_j}{2\omega_{jo}} \qquad (2.12)$$

The polarisation direction of each mode, in the presence of stress, is described by the corresponding eigenvectors of the secular equation. From this it follows that the Raman frequency can be a complicated function of the strain or stress tensor components. If

uniaxial or biaxial stress is present in the sample, this function becomes very simple. For example, for uniaxial stress along the [100] direction of Si, one first calculates the strain tensor components, using Hooke's law. This gives $\varepsilon_{11} = S_{11}\sigma$, $\varepsilon_{22} = S_{12}\sigma$ and $\varepsilon_{33} = S_{13}\sigma$, where the $S_{ij}$ are the elastic compliance tensor elements of Si. Solving Eqns. 2.11 and 2.12 leads to:

$$\Delta\omega_1 = \frac{\lambda_1}{2\omega_0} = \frac{1}{2\omega_0}(pS_{11} + 2qS_{12})\sigma \tag{2.13}$$

$$\Delta\omega_2 = \frac{\lambda_2}{2\omega_0} = \frac{1}{2\omega_0}\left(pS_{12} + q\left(S_{11} + S_{12}\right)\right)\sigma \tag{2.14}$$

$$\Delta\omega_3 = \frac{\lambda_3}{2\omega_0} = \frac{1}{2\omega_0}\left(pS_{12} + q\left(S_{11} + S_{12}\right)\right)\sigma \tag{2.15}$$

The eigenvectors are not changed, which means that also the Raman tensors and the corresponding polarization vectors remain the same as without stress present. For backscattering from a (001) surface, which is the most common surface of Si wafers used in microelectronics processing, only the third Raman mode is observed, and the relation between the shift of this mode and the stress is given by the third relation in Eqn.(2.15). Using the appropriate values for p, q, r (p= $-1.85\omega_0^2$; q = $-2.31\omega_0^2$; $-0.71\omega_0^2$; $\omega_0 = 520\text{cm}^{-1}$) and $S_{ij}$ ($S_{11} = 7.68\ 10^{-12}$ Pa $^{-1}$, $S_{12} = -2.14\ 10^{-12}$ Pa $^{-1}$, $S_{44} = 12.7\ 10^{-12}$ Pa $^{-1}$), gives for crystalline Si:

$$\Delta\omega_3 / cm^{-1} = -0.0023\sigma / MPa \tag{2.16}$$

In the case of biaxial stress in the x-y plane, with stress components $\sigma_{xx}$ and $\sigma_{yy}$, this becomes

$$\Delta\omega_3 = \frac{1}{2\omega_0}\left[pS_{12} + q(S_{11} + S_{12})\right](\sigma_{xx} + \sigma_{yy}) \tag{2.17}$$

or

$$\Delta\omega_3(cm^{-1}) = -4x10^{-9}\left(\frac{\sigma_{xx} + \sigma_{yy}}{2}\right)\text{(Pa)} \tag{2.18}$$

Thus, compressive stress ($\sigma$ negative) will result in an upward shift of the Raman peak, while tensile stress ($\sigma$ positive) results in a downward shift. Whether the Raman

frequency of a certain material changes much or not with stress depends on the material parameters ($S_{11}$, p, q, r). In Si for example, according to Eqn (2.16), a uniaxial stress of 100 MPa results in a shift of only about $0.23cm^{-1}$. If high spectral resolution instrumentation is used, shifts as small as $0.02cm^{-1}$ can be detected. This means that in Si, stresses as small as about 10 MPa can be observed.

#### 2.3.2.5 Raman Spectra Measurements

Raman spectra were registered in a backscattering geometry using a micro-Raman Renishaw 1000 system equipped with a Leica microscope [31]. The excitation wavelength of 514.5nm was produced from an $Ar^+$ ion laser with a typical laser power level of ~10 mW. A filter was also used to perform measurements at reduced laser power (10% of laser intensity), in order to check the influence of laser heating on the position of the phonon lines so as to avoid in-situ laser annealing and damage to the samples. In the visible spectral range, Raman spectrometers use notch filters to cut out the signal from a very narrow range centred on the frequency corresponding to the laser radiation. The x100 magnifying objectives of the Leica microscope focuses the beam into a spot size of approximately 0.6-1μm in diameter. The scattered light from the sample passes back through the microscope's optics into the spectrometer. Raman shifted radiation is detected with a charge-coupled device (CCD) detector and a computer is used for data acquisition and curve fitting. For the majority of the samples, data were collected at 3-5 different locations on the wafer. No significant variance was observed, with average values well within experimental error limits. A relatively large number of accumulations were employed in order to achieve a high signal/noise ratio. The system is configured with a true confocal micropobe for maximum spatial resolution. An 1800 lines/mm grating was used in all measurements; this corresponds to a spectral resolution of around 2.5 $cm^{-1}$ per 3 pixels. Fig. 2.10 shows the essential elements present in a typical setup for Raman measurements.

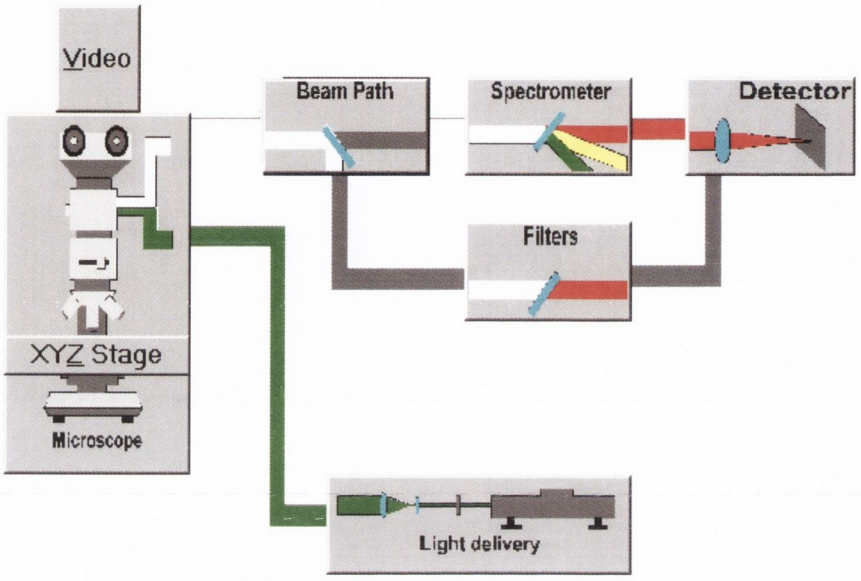


**Fig. 2.10** Schematic of Raman setup

A typical measurement would involve Raman scattered light being collected and the Stokes line analysed using Grams software. A Lorentzian curve fitting algorithm is used to determine the peak value of the scattered light from a Raman spectrum. The parameters of a Raman peak are, in no particular order:

1. peak position;
2. peak intensity;
3. integrated intensity;
4. full width at half maximum (FWHM);
5. its asymmetry.

The first order Raman spectrum of crystalline Si has a single line at about 520 $cm^{-1}$, which corresponds to longitudinal optical (LO) phonon vibrations of the Si-Si bond. However, this figure varies with ambient conditions (especially temperature), the particular spectrometer in use and the calibration method. It is a triply degenerate phonon in the sense that this frequency is the same for all phonon polarisations relative to the three crystallographic axes X [100], Y [010], Z [001]. This line has a Lorentzian shape with a linewidth of $3cm^{-1}$. The position and shape of this line is sensitive to the presence

of strain, structural defects and damage in the lattice, temperature, chemical composition and concentration of carriers.

Chapter 3 discusses in detail the use of Raman spectra in the analysis of SiGe based novel materials, but some of the more important points are introduced here. In a SiGe layer this Si-Si peak will be shifted to the low frequency side, as demonstrated in Fig. 2.11 (see the peak at 500 $cm^{-1}$), depending on Ge content (x) and stress in the layer. The other groups of phonon modes observed in the Raman spectrum in the range of 450-400$cm^{-1}$ and 240-300$cm^{-1}$, as discussed in detail in Chapter 3, are associated with the SiGe layer and belong to the Si-Ge and Ge-Ge stretching modes respectively. With a strained Si cap deposited onto a SiGe layer, we expect all these peaks to be present in the spectrum, as well as a peak indicating the presence of strained Si.

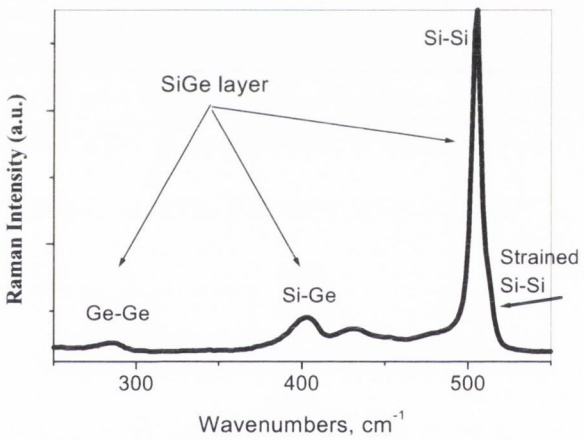


**Fig. 2.11** Typical first order Raman spectrum for a strained Si cap on a $Si_{1-x}Ge_x$ layer

### 2.3.3 X-Ray Diffraction

In X-ray diffraction (XRD), the scattering event can be described as a reflection of the beams at planes of atoms (lattice planes). Bragg's law, Eqn. 2.1, gives the relation between interplanar distance d and diffraction angle θ. A typical XRD spectrum results from measuring the diffracted intensity as a function of the diffraction angle 2θ (angle between the incident and diffracted beams) and the orientation of the sample.

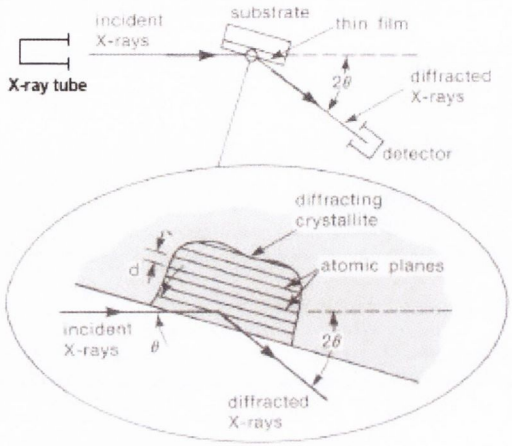


**Fig. 2.12** Schematic of setup used in XRD measurements

X-ray diffraction is a versatile, nondestructive technique used for identifying the crystalline phases present in solid materials and powders and for analyzing structural properties (such as stress, grain size, phase composition, crystal orientation, and defects) of the phases [32]. Fig. 2.12 shows a typical schematic setup used in XRD measurements. The method uses a beam of X-rays to bombard a specimen from various angles. By varying the angle of incidence, a diffraction pattern emerges that is characteristic of the sample. The pattern is identified by comparing it with an internationally recognized database containing tens of thousands of reference patterns [33].

XRD has a wide range of uses in both research and industry, i.e. it can be applied to the analysis of powders in industrial chemistry, as well as in the investigation of the atomic arrangement in metals. In this work, XRD is used as an independent method of calculating strain in novel materials. Chapter 4 discusses in more detail how XRD measurements are used to determine the value of strain present in Ge P-N photodiode structures, the results of which can then be compared and verified against expected values. In addition, XRD values are used as a benchmark in the statistical analysis of Raman compositional equations as discussed in Chapter 5. Listed below is a non-exhaustive list of the analysis made possible with XRD.

#### 2.3.3.1 Applications

1) Structural analysis. Determines the crystal structure of a material by comparing its generated diffraction patterns with reference diffraction patterns;
2) Stress measurements. Measures the strain in a sample by recording the angular shift of a given Bragg reflection as a function of angle of incidence. Strain is then used to calculate the stress;
3) Phase analysis. Determines the crystalline phases present in a sample;
4) Texture analysis. Determines the texture (orientation of the crystallites) in the sample using several diffractometer techniques. Texture can range from completely ordered to partially ordered to completely random;
5) Bulk materials to powders. Analyses bulk samples, powders, single crystals, polycrystalline materials, and thin films.

## 2.4 Conclusions

In SiGe based technology, the ability to qualify and quantify material performance and growth techniques is of primary importance. Questions relating to threading dislocations, the controlled straining of suitable layers as well as compositional analysis were all considered in this chapter, particularly from a device perspective. In line with this, several useful tools were shown to be available. This chapter discussed in detail the theory and application of such techniques in terms of their suitability to the materials under investigation, which range from strained Si quantum wells to Ge p-n photodiodes.

The transmission electron microscope (TEM) was discussed in detail within this chapter. Using a high energy electron beam transmitted through a very thin sample, it was shown to be possible to image and analyse the microstructure of materials with near atomic scale resolution. The Bright Field /Dark Field imaging modes of the microscope, which operate at intermediate magnification, were discussed with a TEM micrograph detailing the layers associated with a strained Si quantum well given as an example of the analysis possible using this technique. From this image it was apparent that such analysis can be invaluable for providing information about the morphology, crystal phases, and defects in

a material. Complementary to this discussion, the various steps in TEM sample preparation were introduced to the reader.

The various specimen interactions with an electron beam were outlined, with EDS and EELS deemed of use in the investigation of SiGe buffer layers. Both EDS and EELS spectra were presented in this chapter, from which it was apparent that both techniques can be used to investigate chemical analysis and compositional distribution across a variety of materials.

Raman scattering was introduced as a non-invasive measurement technique developed in the early 1920s. A detailed mathematical analysis of the rules and interactions associated with such a technique was presented, as well as an overview of the fundamentals involved. The suitability of such a technique to the investigation of SiGe layers was discussed, with a typical Raman spectrum presented to the reader identifying the various phonon modes present. The setup used in the measurement of Raman spectra was discussed, with the various measurable parameters such as FWHM, peak position, etc., identified. Based on the vibrational response of a material under investigation to incident light, it was clear that this technique can be used to measure both the Ge composition, $x$, as well as the strain, $\varepsilon$, in thin strained alloys.

XRD was identified as a technique that can provide comprehensive information on film characteristics. The various applications of such a technique were outlined as well as its suitability in the characterisation of SiGe layers since stress, thickness and Ge concentration can be theoretically extracted from diffraction spectra.

**References**


1. http://grouper.ieee.org/groups/802/3/10G_study/public/march99/schvan_1_0399.pdf
2. http://www.eet.com/in_focus/silicon_engineering/OEG20030822S0025
3. C.K.Maiti, L.K. Bera and S Chattopadhyay, *Semicond. Sci Technol.* **13** 1225 – 1246, (1998)
4. S.S. Iyer, J.C. Tsang, M.Copel, P.Pukite, and R.Tromp, *Appl. Phys. Lett.* **54**, 219 (1989)
5. C.G. van de Walle and R.Martin, *Phys. Rev. B* **34**, 3792 (1986)
6. 17th Annual Workshop on Secondary Ion Mass Spectrometry, May 17th- 20th 2004
7. http://www.uksaf.org/tech/sims.html
8. V. Holý, J. H. Li, G. Bauer, F. Schäffler, and H. J. Herzog, *J. Appl. Phys.* **78**, 5013 (1995).
9. J.Stangl , *Applied Physics Letters* **79**, Issue 10, pp. 1474-1476(September 3rd 2001)
10. http://www.stanford.edu/group/snl/tem.htm
11. http://www.unl.edu/CMRAcfem/temoptic.htm
12. K. Lyutovich, M. Oehme and F. Ernst, *Eur. Phys. J. Appl. Phys.* **27**, 341-344 (2004)
13. http://www.nanoscience.huji.ac.il/unit/tem_basics.htm
14. Tae-Hang Ahn, In-Seok Yeo, Tae-Kyun Kim, Moon-Sig Joo, Hyeon-Soo Kim, Joong-Jung Kim, Joong-Ho Joung, and Jin Won Park, *J. Electrochem. Soc.*, **148**, pp. G50-G54 (February 2001)
15. Royal Microscopical Society Microscopy Handbook Series 48, *Electron Loss Spectroscopy*, Rik Brydson
16. http://www.gatan.com/index.html
17. Egerton, RF. Electron energy loss spectroscopy in the electron microscope. 2nd ed. Plenum Press, New York.(1996)
18. http://www.mf.mpg.de/en/abteilungen/ruehle
19. A. Smekal, *Naturwissenschaften*, **11**, 873 (1923).

20. A. Compton, *Phys. Rev.*, **21**, 483 (1923).
21. C.V. Raman and K.S. Krishnan, *Nature*, **121**, 711 (1928).
22. I.De Wolf, *Semiconductor Science Technology*, **11** 139-154 (1996)
23. G. Landsberg and L. Mandelstam, *Naturwissenschaften*, **16**, 557 (1928).
24. P. Bruesch, 'Phonons*: Theory and Experiments. Lattice Dynamics and Models of Interatomic Forces*' (Springer Series in Solid-State Sciences 34) (Berlin: Springer), (1981)
25. M. Cardona, '*Light Scattering in Solids II*' (Topics in Applied Physics 50) ed M Cardona and G G¨untherodt (Berlin: Springer), (1982)
26. R. Loudon, *Adv. Phys.* **13** 423–80, (1964)
27. S. Ganesan , A.A. Maradudin and J. Oitmaa, *Adv. Phys.* **56** 556–94, (1970)
28. E. Anastassakis, A. Pinczuk, E. Burstein, F.H. Pollak and M. Cardona, *Solid State Commun.* **8** 133–8, (1970)
29. E. Anastassakis and E. Burstein, *J. Phys. Chem. Solids* **32**,563 570 (1971).
30. E. Anastassakis, *J. Raman Spectr.* **10**, 64 76 (1981)
31. J. McCarthy, S. Bhattacharya, T. S. Perova, R. A. Moore, H. Gamble, B. M. Armstrong, *SCANNING* **26**, 235–239 (2004)
32. http://www.nrel.gov/measurements/xray.html
33. www.icdd.com

# Chapter 3

# Investigation of Strained Silicon Using a Variety of Techniques

## 3.1 Introduction

The importance of SiGe to the ongoing development of electronic devices has been outlined in Chapter 1. The incorporation of SiGe allows bandgap manipulation and the growth of materials which have increased performance along with minimum cost overhead at the manufacturing level. Strained Si is one of these materials.

In terms of successful novel materials, it is the ability of the material to offer improvements in speed and power that will be decisive in its adoption or not in future ICs. In terms of speed, drive current is an important parameter. Drive current, which is a measure of the amount of current flowing from source to drain in a transistor, controls the switching speed of a transistor. Achieving a higher drive current will then allow a transistor to switch between its on/off states faster. This allows designers to create devices that can operate at a higher operating frequency. Strained Si is used to raise drive current in both types (N-channel and P-channel) of CMOS transistors. This is achieved by stressing (stretching) its lattice, as discussed in Chapter 1, so that both electrons and holes flow with reduced resistance in comparison with its bulk counterpart. By reducing the resistance, the transistors have a higher drive current associated with them. This gives a substantial benefit over the existing 0.13μm standard processes currently used in the industry while having a negligible impact on costs, estimated to increase by just 2%, as processing and manufacturing tools already developed for use with Si can be modified relatively easily.

For example, Intel [1] has begun the industry's first high volume manufacture of strained silicon on its new 90 nm production process. This process, needed to fabricate Intel's next-generation desktop and mobile processors, improves transistor performance by 10-25% while increasing manufacturing costs by only 2%. The first Intel® processor to be

built with this technology is a 125 million transistor desktop processor, codenamed Prescott, and a 144-million transistor mobile processor, code-named Dothan.

### 3.2 Strained Silicon Process

Strained Si on strain relaxed SiGe hetero-structures is one of the more promising candidates for expanding Si CMOS performance, due to mobility enhancement of both electrons and holes in the strained Si channel layer [2,3]. Strained Si technology enables device improvements via replacement of the bulk, cubic crystal Si substrate with a Si substrate that contains a tetragonally distorted, biaxially strained Si thin film at the surface. A strained Si layer has a different crystalline structure to that of bulk Si as its strain state reflects a change in its symmetry. It can offer the advantage of having superior electronic properties over bulk Si. In essence, this is to say that increased electron and hole mobilities in the strained Si layer means that both NMOS and PMOS transistors can have a far greater drive current capability. This increased transistor drive current can be traded off for a reduction of dynamic power consumption.

To realise high mobility devices, high quality strain relaxed SiGe buffer layers, which can introduce tensile strain into the overgrown Si, are required. Threading dislocation density has been suppressed to less than $10^5$ $cm^{-2}$ by a compositionally graded buffer method, and is now used as a template for the structure [4, 5]. The strain relaxation, however, necessarily involves the generation of misfit dislocations at the SiGe/Si substrate interface, and a resultant surface roughness with a crosshatch pattern running along the orthogonal (110) direction, which can possibly degrade the material quality and device performance. In fact, fluctuations of strained Si device properties due to the crosshatch surface have been reported, where orientation dependent oxidation of the vicinal surface was thought to be the main reason [6]. To eliminate crosshatch roughness, chemical mechanical polishing (CMP) has been employed recently, and extremely flat, relaxed SiGe with RMS roughness of 0.4 nm is now available[7].However, the inhomogeneous strain field coming from the underlying misfit dislocation may expand over the entire film [8], and is thought to degrade material properties even on CMP substrates. The correspondence between the crosshatch surface and the spatially varying strain field of a

SiGe buffer layer has been experimentally confirmed by various methods [9-11]. As outlined in Chapter 3, the conduction band of bulk Si contains six valleys at the same energy level, i.e. degeneracy. By straining the deposited Si layer through growth on a SiGe layer, the tensile strain causes this degeneracy to be split. As a result, the valleys experience what can be termed a 4-2 formation, with the two lower energy valleys at right angles to the other four in-plane valleys. As a result of this split, mobility enhancements are made possible due to the reduction in in-phonon scattering in the lower energy valleys. This increase in mobility for strained Si is shown in Fig. 3.1 [14]. Increased performance has also been observed in deep sub micron strained Si n-MOSFETs, thus demonstrating the benefits of these structures at high electric fields [15, 16]. As a result of the biaxial tensile strain of the Si layer, the valleys of the valance band are split also. This in turn increases the mobility associated with p type MOSFETs and enables the fabrication of enhanced mobility surface channel devices with performance improvements as outlined in Fig. 3.2 [17]. It is this increase in mobility for both N and P-type MOSFETS that allow strained Si devices to provide significant performance increase over bulk layers at identical gate lengths. In addition, the improvement in performance of these devices is independent of traditional Si MOSFET scaling laws and device geometries. Electron mobility in NMOS devices saturates at Ge content of 20%, and hole mobility saturates in PMOS devices at Ge content of 40% [18].

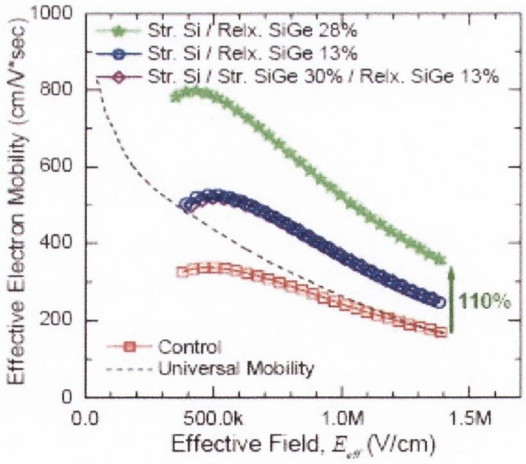


**Fig. 3.1** Effective Electron mobility v's Effective Field, for various levels of Ge in the SiGe layer [14].

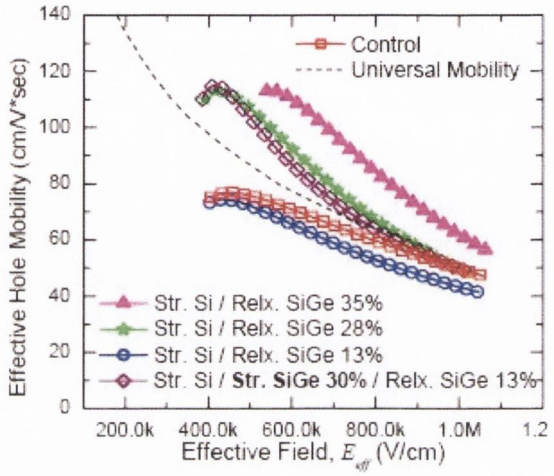


**Fig. 3.2** Effective Hole mobility v's Effective Field, for various levels of Ge concentration in SiGe layer [17].

From an engineering perspective, it is the ability to control the level of strain within the layer which makes strained Si such an attractive material of choice. In this way, the mobility and thus the operating frequency of manufactured devices can be scaled according to the strain present in the layer. This makes strained Si suitable across the engineering platform, irrespective of whether high speed mobile devices or low power wireless networks are being manufactured. For high electric field state of the art CMOS applications, the improved scalability and increased high field mobility enhancement offered by the surface channel strained Si device allows it to excel Therefore, the technological task is to grow relaxed SiGe layers with a reasonably high Ge content ($x$) and then to grow a strained Si layer on top. It is well known that due to the lattice mismatch between Si and Ge (~ 4%), a SiGe layer grown on Si without special conditions is always strained. There are a number of possible methods, but throughout this work we concentrate mainly on two possibilities to grow a relaxed SiGe layer:

1. grow a graded SiGe layer with gradual increase of the Ge content [19];
2. use a point defect introduction at the low temperature stage of the layer growth[20].

Strain relaxation is obtained through the introduction of misfit dislocations (MDs) at the interface. Important parameters to be considered at the growth stage are the degree of relaxation and density of threading dislocations (TDs) present.

### 3.3 Dislocations

It is important at this stage that the reader be familiarised by what is termed 'dislocations'. A dislocation is defined as a linear crystallographic defect, or irregularity, within a crystal structure. Dislocations are usually introduced and thought of as extra lattice planes inserted in the crystal that do not extend through all of the crystal, but end in the dislocation line. Fig 3.3 illustrates a three-dimensional view of an edge dislocation in a cubic primitive lattice. This picture shows the inserted half-plane very clearly; it serves as the quintessential illustration of what an *edge* dislocation looks like [21].

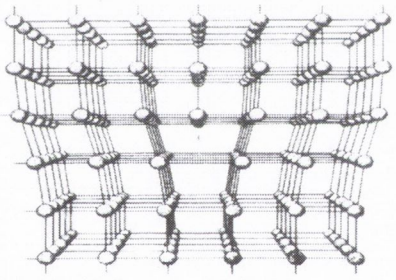

**Fig. 3.3** 3-D view of an edge dislocation [21].

The exact structure of the dislocation will be slightly different. Edge dislocations are just an extreme form of the possible dislocation structures, and in most real crystals would be split into 'partial' dislocations and look much more complicated. This linear defect, as defined above, moves along a path described by its dislocation line. It is along this line that the lattice of the material is disturbed. Some extraneous deformations may take place away from this line, but would not be considered as defects per-se. As a dislocation line describes a connection of points in time and space, the line vector $\underline{t}(x,y,z)$ describes any point along the dislocation line. As the bonds along the dislocation line are distorted, it is clear that they are not in a position of equilibrium; the dislocations will possess energy and entropy. The glide plane of a dislocation, that is to say, the area covered through the movement of the dislocation contains in itself the dislocation line vector. The movement

of a dislocation moves the whole crystal on one side of the glide plane relative to the other side. These points associated with dislocation movement are shown in Fig. 3.4, where in (a), the dislocation has been introduced into the structure, in this case through a shear stress, (b) depicts the movement of the dislocation through the crystal until finally, (c) shows the shift of the upper half of the crystal after the dislocation has emerged [22].

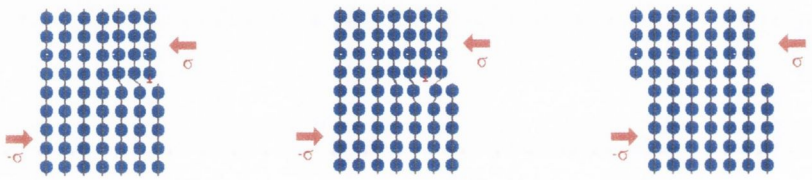


(a) (b) (c)

**Fig. 3.4** Graphic depicting the movement of a dislocation within the crystal structure [22]

### 3.3.1 Threading Dislocations

In the growth of lattice mismatched epitaxial thin films, threading dislocations (TDs) are concomitantly generated with MDs. For a wide variety of electronic and optoelectronic device applications, particularly for minority carrier devices, TDs are deleterious for physical performance. In recent years there has been a substantial experimental effort to reduce TD densities.

#### 3.3.1.1 Concept of Critical Layer Thickness and Dislocations

Critical thickness has already been introduced to the reader in Section 1.4.2 of Chapter 1. It is worthwhile at this stage to recap on some of the main points while trying to relate the thickness to the issue of dislocations etc as they relate to the growth of strained Si films on a SiGe virtual substrate.

Critical layer thickness, $h_c$, can be defined as the thickness of the epitaxial layer beyond which the strain in the film will be sufficient to give rise to defects and dislocations, leading to strain relaxation. The velocity at which a dislocation will move in a strained epitaxial film depends on the magnitude of the strain, as well as on temperature. Before the epitaxial film relaxes (i.e. before critical thickness is achieved), the film is called pseudomorphic – meaning it assumes the lattice constant of the film on which it is grown.

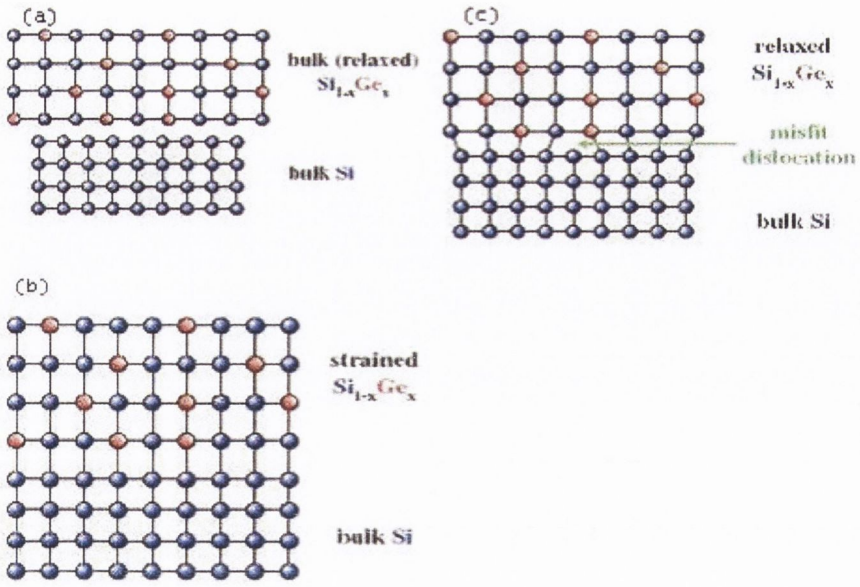


**Fig. 3.5** The concept of critical thickness for a SiGe system [23]

As can be seen in Fig. 3.5, the challenge exists to match the two layers to each other. Due to the 4.2 lattice differential between Si and Ge, every 24$^{th}$ Si atom at the interface would not be able to form a bond with a Ge atom. In turn, the mismatch between Si and SiGe films is quite challenging. Fig.3.5 (a) shows diagrammatically the difference in lattice spacing between Si and that of relaxed SiGe films. The challenge then exists to match these two layers if SiGe is to be used on top of a bulk Si substrate. Fig. 3.5 (b) shows the scenario in which the SiGe layer grown on bulk Si is thin enough so that its symmetry changes from the cubic shaped equilibrium state to a tetragonal shape, and the layer is said to be strained. Fig. 3.5 (c) outlines the introduction of misfit dislocations to relieve strain once the critical thickness has been exceeded. The fundamental quantity defining an arbitrary dislocation is its Burgers vector $\underline{b}$ [24]. Its atomistic definition follows from a Burgers circuit around the dislocation in the real crystal, which is illustrated below.

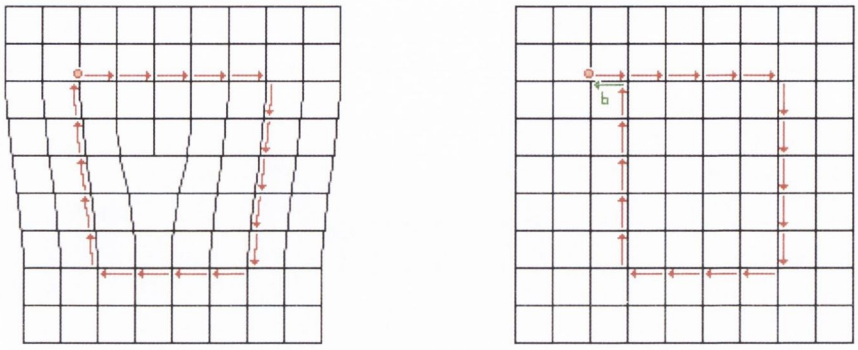

**Fig. 3.6** (a) Enclosing the lattice dislocation (b) Burger Vector b, needed to close the path [24].

As illustrated in Fig. 3.6(a), making a closed circuit that encloses the dislocation from lattice point to lattice point (later from atom to atom), one can close the chain of the base vectors which define the lattice. However, making exactly the same chain of base vectors in a perfect reference lattice, as in Fig. 3.6(b), it is seen that it cannot be closed. The special vector needed for closing the circuit in the reference crystal is by definition the Burgers vector $\underline{b}$.

The presence of a misfit dislocation network at an interface often results in a characteristic undulating morphology, known as crosshatch, of the heterostructure surface, as outlined briefly in Chapter 1. This morphology occurs in many lattice mismatched semiconductor systems including SiGe/Si and various III–V compound heterostructures [25-29]. The understanding of such a surface relief formation is important for the fabrication of low dimensional devices based on those systems which exhibit atomically smooth but mesoscopically rough surfaces and are not compatible with planar integrated circuit technologies. This is especially important for strained Si devices which in spite of their obvious advantages, in terms of increased operating speeds etc, their surface can be affected by the appearance of such a pattern. The origin of a crosshatch pattern has been shown to be linked to the dislocation density of the underlying virtual substrate [25], as discussed in Section 3.5.3.

It has been reported that in laterally uniform layers, the density of TDs present in the film can only be reduced by reacting with other TDs present in the layer [30, 31]. The two reduction reactions are:

1. annihilation, in which TDs with opposite Burgers vectors meet;
2. fusion, in which two TDs react to form a single TD [30-34].

Interaction between TDs can only occur when they meet. Motion, or to be more accurate, relative motion, between the dislocations can bring about this interaction and the resulting reduction reactions. There are several different forms of motion possible. 'Trajectory' motion, which occurs due to changes in film thickness, is a result of the associated Burgers vectors and slip planes which cause different TDs to have different directional lines. Condensation of point defects at a TD can have the added effect of creating motion, causing either positive climb vacancy condensation or negative climb interstitial condensation. A third proposed method of introducing relative motion is through the growth of a strained layer, as outlined earlier. As the film grows beyond $h_c$, misfit dislocation generation accompanies the glide motion of TDs.

### 3.4 Raman Analysis for Si/SiGe

Both the relative intensities and the frequencies of the three different first-order Raman lines in a $Si_{1-x}Ge_x$ alloy can be used to derive both Ge composition, x and strain, $\varepsilon$. The first-order spectrum of a strained $Si_{1-x}Ge_x$ alloy consists of three distinct lines whose energies and relative intensities depend on x [35] and whose energies also depend on the strain, $\varepsilon$[36]. To recapitulate Section 2.3.1 of Chapter 2, the three strong first-order lines from a $Si_{1-x}Ge_x$ layer are due to nearest neighbour Ge-Ge (~288.44 $cm^{-1}$), Ge-Si (~406.64 $cm^{-1}$), and Si-Si (~501.55 $cm^{-1}$) atomic vibrations. It has been reported in the literature that for thick layers of relaxed alloys, the Si-Si phonon frequency, $\omega_{Si}(x)$, can be related to x based on a linear extrapolation between the experimentally measured values of $\omega_{Si}$ for small and large values of x[37]:

$$\omega_{Si}(x) = 520.0 - 68x \qquad (3.1)$$

However, it can be observed that if this dependence is plotted along with previously reported experimental results one finds that Eqn. 3.1 leads to values below those recorded experimentally, i.e., to higher values of $\omega_{si}$ for $0<x<0.5$ [38]. For $0<x<0.5$, one can observe that the all the published experimental results for $\omega_{Si}(x)$ fall between Eqn.(1) and a line defined by:

$$\omega_{Si}(x) = 520.2 - 62x \qquad (3.1a)$$

Based on this, it is necessary to identify two equations of note depending on the Ge content. The small correction to Vegard's Law in the $Si_{1-x}Ge_x$ system corresponds to a decrease in the lattice constant from its linearly extrapolated value for a given value of x. The 2-3 $cm^{-1}$ difference for values of x = 0.3 between Eqns. 3.1 and 3.1a is consistent with the ~0.0073Å decrease in the lattice constant from its value at x=0.3 as determined by Vegard's Law and the published values for the Gruneisen parameters for Ge and Si [18]. Eqn. 3.1 is found to be suitable for small and large values of x. Eqn. 3.1a is of benefit for values of x near 0.3. Eqn. 3.1a is bound by the variation in Vegard's Law that results in experimental values clearly demonstrating that $\omega_{si}$ does not vary linearly with composition between x = 0 and x = 1. The experimental points of Alonso et al[41], for $0<x<0.5$, occur up to 3 $cm^{-1}$ above the linear fit in Eqn. 3.1The experimentally measured dependence of $\omega_{gs}(x)$, the Ge-Si phonon frequency, on x is described by the equation:

$$\omega_{GS}(x) = 400.5 + 14.2x \qquad (3.2)$$

for $0<x<0.5$. For such values of x, the large widths of this mode mean that all the published experimental determinations of $\omega_{gs}$ fall within $\pm 1 cm^{-1}$ of Eqn. 3.2 [37-40]. However, the reported experimental values for the compositional dependence of the frequency of the Ge-Ge line, $\omega_{ge}$, shows >3 $cm^{-1}$ differences for $0<x<0.3$. Therefore, a given Raman frequency can correspond to an unacceptably high difference in x of up to 15%, depending on which data is used. From this it is evident that the dependence of $\omega_{ge}$ on x is not known accurately enough to determine x and ε from this Raman line. The shift

in energy of the three phonon frequencies ($\omega_{si}$, $\omega_{gs}$, $\omega_{gg}$) relative to the amount of strain present in the material has been considered both theoretically and experimentally [41]. It has been found that the shift in the phonon energy is linearly related to the strain, ε, for small values of strain. Therefore, the influence of strain on Eqns. (3.1) and (3.2) can be accommodated by the addition of a simple linear term, as shown by the following equations:

$$\omega_{Si}(x) = 520.0 - 68x - 830\varepsilon \tag{3.3}$$

$$\omega_{GS}(x) = 400.5 + 12x - 575\varepsilon \tag{3.4}$$

$$\omega_{GG}(x) = 282.5 + 16x - 348\varepsilon \tag{3.5}$$

However, it has been emphasised [41] that the determination of the position of Ge-Ge band is not quite accurate for Ge content up to ~50%, so only Eqns.(3.3) and (3.4) are used to solve for Ge content and levels of strain present. As has been stated, apart from bulk Si, the other groups of phonon modes observed in the Raman spectrum in the range of 450-400cm$^{-1}$ and 240-300cm$^{-1}$ are associated with the SiGe layer and belong to the Si-Ge and Ge-Ge stretching modes respectively. With a strained Si cap deposited onto a SiGe layer, we expect all these peaks to be present in the spectrum, as well as a peak indicating the presence of strained Si.

### 3.4.1 Depth of Penetration

The presence of a Si-Si peak associated with the Si substrate (or the Si buffer layer) depends on how deeply the laser probe beam penetrates the sample during Raman measurements. The total scattered light intensity integrated from the surface to a depth *d*, $I_s$, is given by [42]

$$I_s = I_o D \int_0^d e^{-2\alpha x} dx = \frac{I_o D}{2\alpha}\left(1 - e^{-2\alpha d}\right) \tag{3.6}$$

while that from the depth d to infinity is given by

$$I_d = I_o D \int_d^\infty e^{-2\alpha x} dx = \frac{I_o D}{2\alpha}\left(e^{-2\alpha d}\right) \tag{3.7}$$

$I_o$, D and α are the incident light intensity, the Raman scattering cross section and the photoabsorption coefficient of silicon respectively. If one assumes that the penetration depth $d_p$ is given by the depth that satisfies the relationship $I_d(I_s + I_d) = 0.1$, then this depth is given by

$$d_p = 2.3/2\alpha \tag{3.8}$$

and for the SiGe layer

$$d_p(Si_{1-x}Ge_x) = (1-x)d_p(Si_{1-x}) + xd_p(Ge_x) \tag{3.9}$$

Using the literature reported values of $\alpha_{si} = 15080cm^{-1}$ and $\alpha_{Ge} = 600000cm^{-1}$ at $\lambda$=514.5 nm, we estimate $d_p(Si) \approx 763nm$ and $d_p(Ge) \approx 19.2nm$ [43]. For a SiGe layer with $x$=20%, and using Eqn. (3.9) the depth of penetration is estimated at $d_{p(Si_{0.7}Ge_{0.2})} \approx$ 614nm. Since the thickness of the SiGe layers (both constant composition and graded) is much higher than 614 nm, we can expect that no Si-Si mode associated with either the substrate or the Si buffer layer can be expected in any Raman spectrum of the samples under investigation.

### 3.4.2 Relaxation Factor

The exact position of all aforementioned peaks depends on stress (for pure Si) and on stress and Ge content (for the SiGe layer). It is well known that the LO peak of Si at $520cm^{-1}$ will shift to the low frequency side when the sample is under tensile stress and to the high frequency side when under compressive stress. Stress relaxation of the SiGe layer is calculated using the Equation [44, 45] where r is the relaxation factor, $\Delta_{exp}$ is the experimentally measured shift in Raman position, $\Delta_r$ is the maximum shift possible (70x), and $\Delta_s$ is the minimum shift possible (29.7x).

$$r = (\Delta_{exp} - \Delta_s)/(\Delta_r - \Delta_s) \qquad (3.10)$$

### 3.5 Growth and Analysis of Strained Silicon (S1, S2 and S3) Samples

Attempts were made to grow three strained silicon layers (S1, S2 and S3) with the structure shown in Fig 3.7.

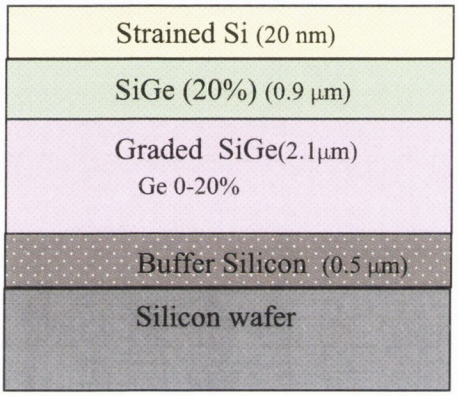


**Fig. 3.7** Structure of S1, S2 and S3

The wafers used were (111) Cinnati Epi p-type Si wafers with 2-3 μm n-type epitaxial layers. The substrates were cleaned and loaded for processing into the CVD chamber as described in Section 3.2. The differences between S1, S2 and S3 are in their graded SiGe layers. In S1, the graded SiGe layer consists of 9 steps and in S2 the same layer consists of 18 steps. In S3, the graded layer was made up of 36 steps and this can be approximated as being linearly graded. The graded buffer regions of S1, S2 and S3 are shown pictorially in Fig 3.8. The growth parameters are given in Table 3.1 and growth steps are shown in Table 3.2.

**Table 3.1** Growth parameters of S1, S2 and S3

| Wafer No. | Chamber Pressure (mbar) | Deposition Time | Thickness (nm) | Temp °C | Gas Flow (sccm) | |
|---|---|---|---|---|---|---|
| | | | | | $SiH_4$ | $GeH_4$ |
| S1 | $3.4x10^{-7}$ | 4 min buffer Si | 500 ±10 | 800 | 100 | 1-10 |
| | | 18 min graded SiGe layer (9 steps) | 2160 ±20 | | | |
| | | 7 min SiGe | 900±10 | | | |
| | | 10 sec strained Si | 20±5 | | | |
| S2 | $3.6x10^{-7}$ | As above but with 18 steps in graded SiGe layer | As Above | 800 | As Above | |
| S3 | $3.3x10^{-7}$ | As above but with 36 steps in graded SiGe layer | As Above | 800 | As Above | |

**Table 3.2** Growth steps of strained silicon (S1) with step-graded buffer SiGe.

| Step Number | Time Interval (mns) | Reactant Gases (sccm) | Grown Layer |
|---|---|---|---|
| 1 | 4 | $SiH_4(100)$ | Epitaxial silicon |
| 2 | 2 | $SiH_4(100) + GeH_4(1)$ | Graded SiGe |
| 3 | 2 | $SiH_4(100) + GeH_4(2)$ | Graded SiGe |
| 4 | 2 | $SiH_4(100) + GeH_4(3)$ | Graded SiGe |
| 5 | 2 | $SiH_4(100) + GeH_4(4)$ | Graded SiGe |
| 6 | 2 | $SiH_4(100) + GeH_4(5)$ | Graded SiGe |
| 7 | 2 | $SiH_4(100) + GeH_4(6)$ | Graded SiGe |
| 8 | 2 | $SiH_4(100) + GeH_4(7)$ | Graded SiGe |
| 9 | 2 | $SiH_4(100) + GeH_4(8)$ | Graded SiGe |
| 10 | 2 | $SiH_4(100) + GeH_4(9)$ | Graded SiGe |
| 11 | 7 | $SiH_4(100) + GeH_4(10)$ | Relaxed SiGe |
| 12 | 10 seconds | $SiH_4(100)$ | Strained silicon |

(a)

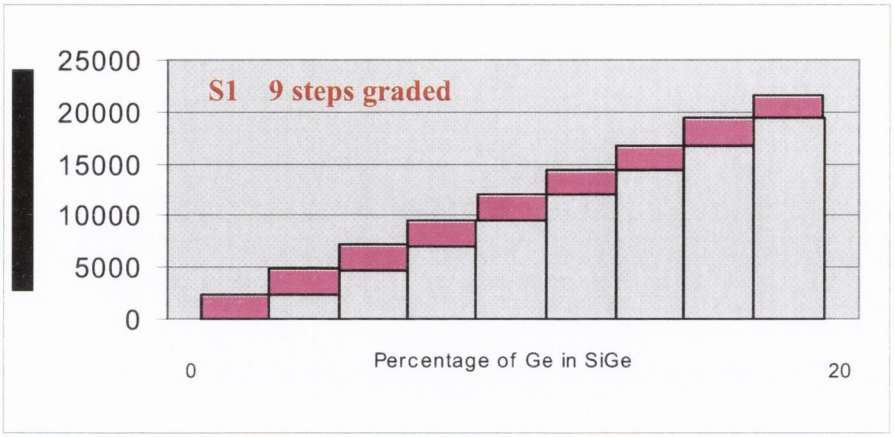


(b)

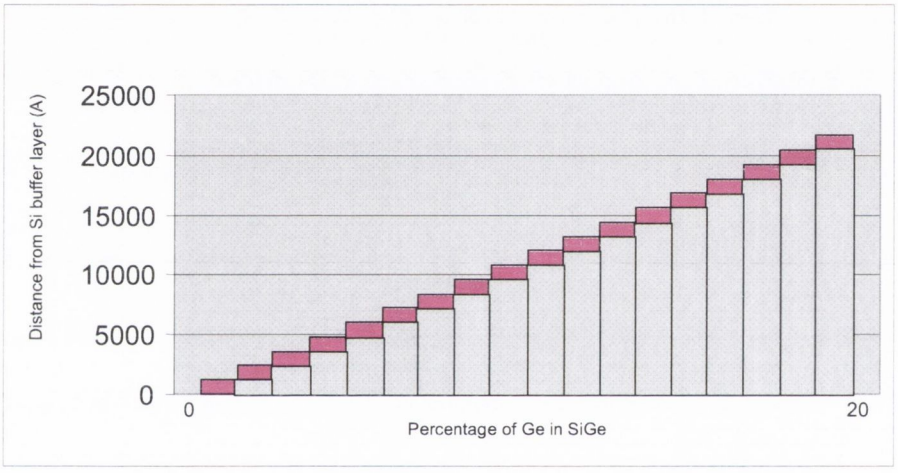


(c)

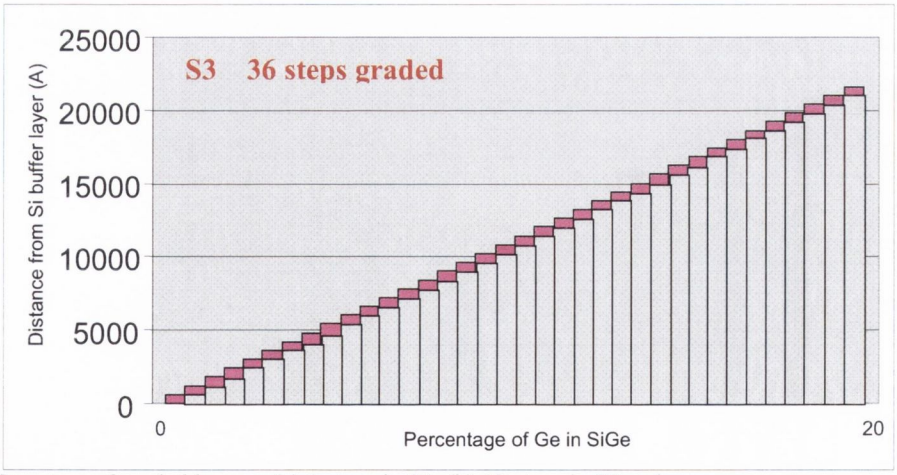


**Fig. 3.8** Structure of graded layers : (a) 9 steps in S1, (b) 18 steps in S2 and (c) 36 steps in S3. A pink rectangle represents a SiGe layer added in the graded region of buffer SiGe. The percentage of germanium in a SiGe step is constant.

### 3.5.1 Atomic Force Microscopy Analysis (AFM)

Atomic force microscopy (AFM) was used to study the topography of the strained Si layers. The AFM used was a Digital Instruments Dimension 3000 system operating in tapping mode and using Nanosensor's force modulation probes (model FESP) with pyramidal silicon tips. These probes have a typical Resonance Frequency of 75 kHz and Force Constant of 2.8 N/m. AFM images for samples S1, S2 and S3 are shown in Fig 3.9. It is observed that irrespective of the nature of grading of SiGe layer, the roughness values and defects on the surfaces of three samples appear to be very similar. The images show that the amplitude of the roughness is larger than expected.

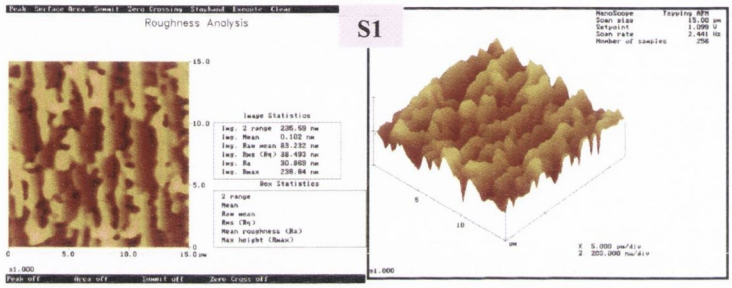


RMS Roughness 38.49 nm

RMS Roughness 37.95 nm

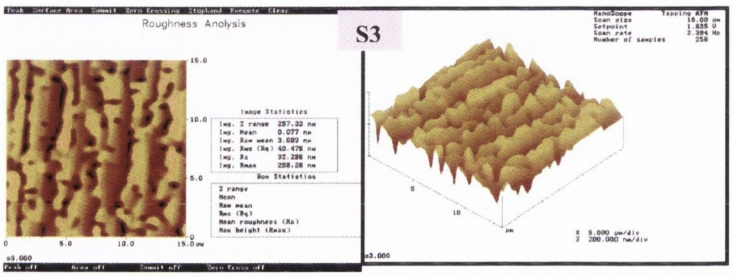


RMS Roughness 40.47 nm

**Fig 3.9** AFM images: of S1, S2 and S3

### 3.5.2 Raman Spectrum

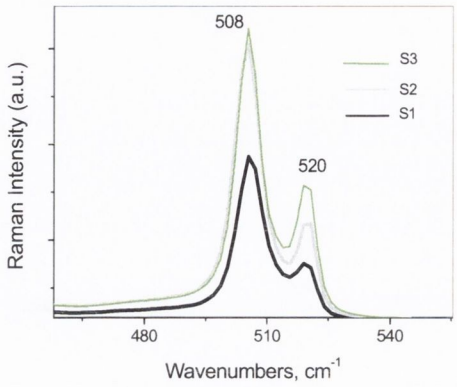


**Fig. 3.10** Raman spectra of samples S1, S2 and S3

Fig.3.10 shows the overlapping Raman spectra for samples S1, S2 and S3. As can be seen, a Si-Si peak with low intensity, which must belong to the Si cap layer for reasons discussed earlier, appears at a frequency of 520 $cm^{-1}$. This indicates the absence of any type of strain in the Si cap layer, as the phonon mode position has not been shifted. Relaxation analysis for the three samples reveals a lower than required value, close to 80%, suggesting poor relaxation mechanisms in the SiGe layers. This can be due to dislocation interaction which gives rise to a high density of shirt misfit segments. Poor control of the dislocation density within the structure can give rise to low relaxation levels which in turn impinge on the ability to manufacture strained Si cap layers.

### 3.5.3 TEM Analysis of Samples S1, S2, S3

In order to investigate further, all three samples were then analysed using TEM. A cross sectional TEM image is shown in Fig.3.11 which demonstrates the presence of threading dislocations in the upper SiGe layer due to the strain field variations associated with the buried dislocations in the graded SiGe buffer layer. Short crosshatch lines and poor morphology is also observed for the relaxed SiGe. The crosshatch surface morphology arises from lateral non-uniformities in the strain field of the misfit dislocations.

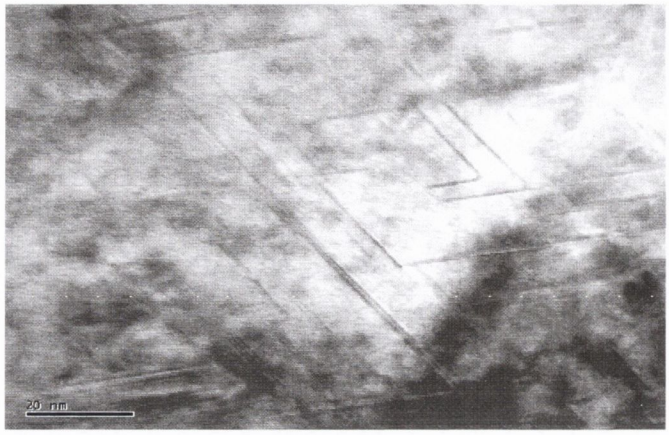


**Fig. 3.11** TEM micrograph of upper SiGe layer of sample S2.

The crystallographic orientation of the substrate affects both the morphology of the deposited film and the appearance of crystallographic defects. While smooth epitaxial films can be grown on (100) or (110) oriented silicon substrates, epitaxial growth on substrate surfaces oriented near the (111) plane results in faceted surfaces [48]. The epitaxial growth process is overall similar for the three samples S1, S2 and S3 and the nature of defects in the epitaxial layers also seems to be similar, giving nearly the same surface roughness value by AFM.

## 3.6 Virtual Substrates

A SiGe virtual substrate, as outlined in Chapter 1, Section 1.4.3, is a pre-requisite to the successful growth of a strained Si layer. Using a graded approach to the growth of the virtual substrate the number of TDs can be reduced in at least two separate ways. The initial graded layer has a lattice constant very close to that of the underlying bulk Si, due to its very low Ge composition. This means that the initial nucleation of dislocations is retarded, as it is easier to grow a near perfect interface when the difference of composition between film and substrate is small. When an initial network of dislocations is formed, there is a very high driving force for pushing the TDs all the way to the edge of the wafer. As additional dislocations are formed, and the stress thus decreases, this driving force also diminishes, so that, eventually, the threading parts should become pinned. It was pointed out by Le Goues [49], that as each new dislocation loop is formed,

and as each new thread moves towards the edge of the wafer, the grading provides 'fresh' interfaces, with few pre-existing dislocations on which a thread could become pinned. In the case of a linearly graded film, each atomic layer in the thin film needs to achieve its own lattice parameter in order to minimize the energy; thus in principle one 'layer' of dislocations is needed at each atomic plane, which in effect spreads the total dislocation network over the compositionally graded region. Consequently, at each layer, there are far fewer dislocations and thus fewer chances for a threading segment to become pinned by an intersecting phenomenon. This phenomenon is dependent upon the slope of the grading.

### 3.7 Modified Growth and Analysis of Strained Silicon Samples, S6 and S11

Since the (111) substrates provided poor results in terms of strained Si, the starting substrates were selected from high quality N type (100) Si wafers, having a resistivity of 10-20 ohm-cm. In addition, a revised structure as shown in Fig. 3.12 was used. The graded layer was increased to 3μm instead of the previous 2μm to try and ensure that the defects in the graded layer were localised at the lower part of the layer. The growth steps for relaxed SiGe and strained silicon are outlined below and shown in Table 3.3 (step graded only).

1. Epitaxial Silicon: An epitaxial silicon layer of 400 nm thickness was grown on the silicon substrate by the pyrolysis of $SiH_4$.

2. Silicon Germanium:

(i) A graded buffer SiGe layer of 3000 nm thickness with germanium concentration of 0-20% was grown over the epitaxial silicon layer by introducing $GeH_4$ to the ambient without stopping the ongoing silicon epitaxial process.

(ii) A constant composition relaxed SiGe layer of 1000 nm with constant Ge (for consistency) concentration of 20% was grown on the graded SiGe layer.

3. Strained Silicon: A 20 nm layer of strained silicon was grown on the relaxed SiGe layer

**Table 3.3** Growth steps of strained silicon with step graded buffer SiGe

| Step Number | Time Interval (mns) | Reactant Gases (sccm) | Grown Layer |
|---|---|---|---|
| 1 | 3 | $SiH_4$(100) | Epitaxial silicon |
| 2 | 3 | $SiH_4$(100) + $GeH_4$(1) | Graded SiGe |
| 3 | 3 | $SiH_4$(100) + $GeH_4$(2) | Graded SiGe |
| 4 | 3 | $SiH_4$(100) + $GeH_4$(3) | Graded SiGe |
| 5 | 3 | $SiH_4$(100) + $GeH_4$(4) | Graded SiGe |
| 6 | 3 | $SiH_4$(100) + $GeH_4$(5) | Graded SiGe |
| 7 | 3 | $SiH_4$(100) + $GeH_4$(6) | Graded SiGe |
| 8 | 3 | $SiH_4$(100) + $GeH_4$(7) | Graded SiGe |
| 9 | 3 | $SiH_4$(100) + $GeH_4$(8) | Graded SiGe |
| 10 | 3 | $SiH_4$(100) + $GeH_4$(9) | Graded SiGe |
| 11 | 10 | $SiH_4$(100) + $GeH_4$(10) | Relaxed SiGe |
| 12 | 10 seconds | $SiH_4$(100) | Strained silicon |

With the above growth steps a thin layer of strained silicon with the structure shown in Fig 3.12 was grown on wafer numbers S6 and S11. The only difference between S6 and S11 is that the graded SiGe buffer layer is step graded in S6 and is linearly graded in S11. Growth parameters are given in Table 3.4. Table 3.3 corresponds to the growth of S6 only. In the case of the linearly graded buffer SiGe growth for S11, each step of 3 minutes duration (from 2 to 10 in Table 3.3), is divided into 6 steps of 30 seconds duration and $GeH_4$ flow is increased by 0.16/0.17 sccm at the end of each 30 second step. As a result, nine step-graded SiGe becomes fifty-four step graded SiGe and this can be approximated as linearly graded SiGe. In the CVD reactor, gas flow is controlled manually and there is no automated way to increase the flow continuously with time.

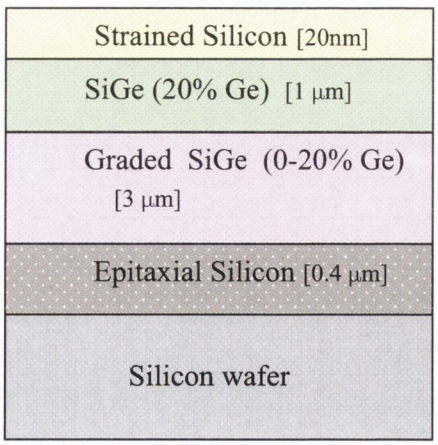


**Fig 3.12** Structure of Strained Silicon grown by CVD process

**Table 3.4** Growth parameters of strained silicon samples S6 and S11

| Wafer No. | Chamber Pressure (mbar) | Deposition Time | Thickness (nm) | Temp °C | Gas Flow (sccm) | |
|---|---|---|---|---|---|---|
| | | | | | $SiH_4$ | $GeH_4$ |
| S6 | $1.7x10^{-7}$ | 3 min buffer Si | 400 ±10 | 800 | 100 | 10 |
| | | 27 min graded SiGe layer (10 steps) | 3100 ±20 | | | |
| | | 10 min SiGe (20%) | 900±10 | | | |
| | | 10 sec strained Si | 20±5 | | | |
| S11 | $1.6x10^{-7}$ | As above but with 54 steps in graded SiGe layer | As Above | 800 | As Above | |

### 3.7.1 TEM Analysis of Strained Silicon Samples S6 and S11

TEM allows detailed analysis of the sample structure to take place, being able to identify the presence, if any, of threading dislocations as well as layer to layer interfaces.

High Resolution TEM micrographs of the heterostructures S6 and S11 are shown in Figs.3.13 to 3.16.

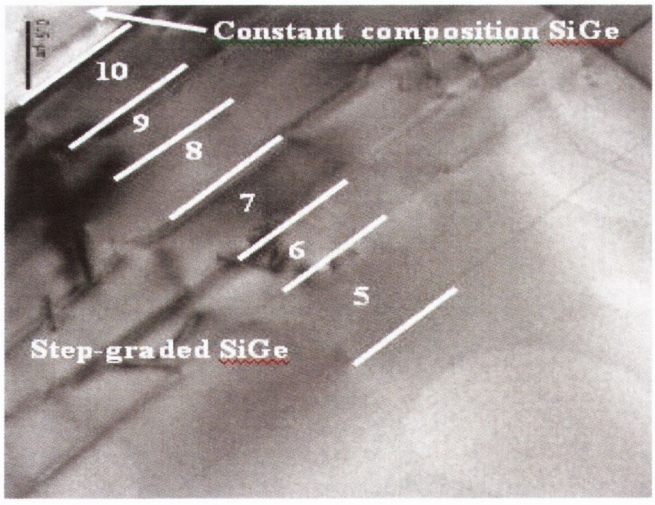


**Fig. 3.13** HR TEM micrographs of sample S6: the step graded layer. Six steps are marked with white lines

Fig. 3.13 shows the step graded SiGe layer in the sample S6. Out of nine steps in the graded SiGe layer only the top six, 10 to 5, can be seen and are marked with white lines.

It is believed that in the other three steps, 4, 3 and 2, germanium content is too low to be distinguished by TEM. The average thickness of each of the five steps, 10-6, is about 350 nm.

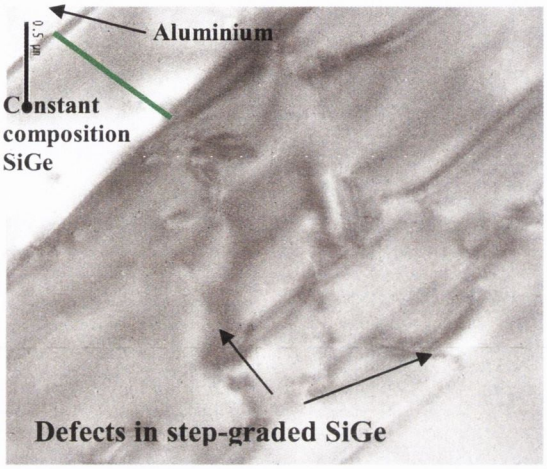


**Fig. 3.14** HR TEM micrographs of sample S6: Constant composition SiGe layer (green line), defects are clearly seen to be confined in the graded region.

Fig. 3.14 shows the constant composition SiGe layer, of about 750 nm thickness, on top of the step graded SiGe layer. It is evident from the image that the constant composition SiGe layer is almost defect free. The defects are confined in the step graded region of the SiGe layer.

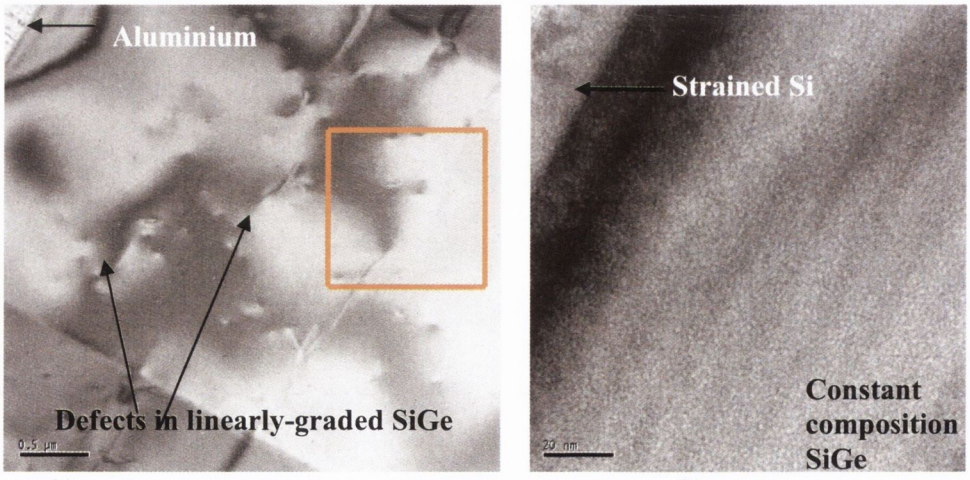


(a) (b)

**Fig 3.15** TEM images of sample S11 showing (a) defects in the linear graded SiGe region and (b) defect free upper layer of constant SiGe composition

Fig. 3.15 shows the linearly graded SiGe layer in sample S11 and no steps can be seen. The defects in the graded layer appear to be point defects. The defect density can be calculated by counting the number of point defects in a specified area. There are five point defects in the region inside the yellow square of 1 square micron area. So the defect density is found to be $5x10^8$ $cm^{-2}$. Results obtained depend on the choice of area chosen for analysis with the measured figure acting only as a rough guide to the defect density.

### 3.7.2 AFM Analysis of Samples S6 and S11

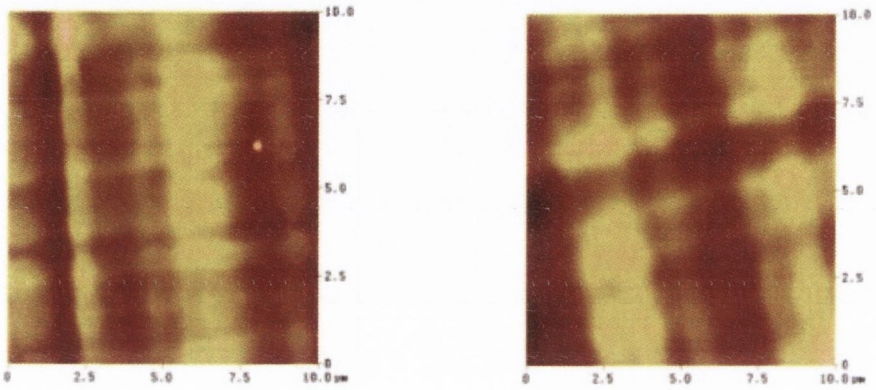


(a) (b)

**Fig 3.16** AFM images of (a) sample S6 and (b) sample S11

Fig 3.16 (a) and (b) shows the AFM images of S6 and S11 respectively. The images look much superior to those of S1, S2 and S3 (Fig 3.9). The RMS roughness values of S6 and S11 are 2.785 and 3.089 nm respectively. The crosshatched pattern is visible on both samples. The compositionally graded SiGe layer in the epitaxial sequence typically results in a rough, crosshatched surface morphology with an RMS roughness of 2-10 nm. When a thin SiGe layer is grown on silicon, the layer is pseudomorphic, i.e. in-plane lattice constants are equal and SiGe is strained. However, if the SiGe layer is thick enough, strain in the layer can be relieved by generation and multiplication of misfit dislocations. Line segments of misfit dislocation, accompanied by threading dislocations, terminate at the surface (Fig 6.15) giving rise to inhomogeneous stress fields and consequently crosshatched surface morphology [50]. So due to the relaxation of the SiGe layer, the resulting surfaces of S6 and S11 are crosshatched.

### 3.7.3 Raman Analysis

The exact position of all aforementioned peaks depends on stress (for pure Si) and on stress and Ge content (for the SiGe layer). It is well known that the LO peak of Si at $520cm^{-1}$ will shift to the low frequency side when the sample is under tensile stress and to the high frequency side when under compressive stress. Fig. 3.1 shows a Raman spectrum obtained for sample S6. The strong peak observed at $505cm^{-1}$ belongs to the Si-Si mode in the SiGe layer [44]. The shoulder observed at the high frequency side of this peak belongs to a Si-Si mode in the strained Si layer. Its intensity is much lower than that for the Si-Si peak observed at $505cm^{-1}$ due to the fact that the strained silicon layer is only 20nm thick. Therefore, most of the Raman signal originates from the SiGe layer.

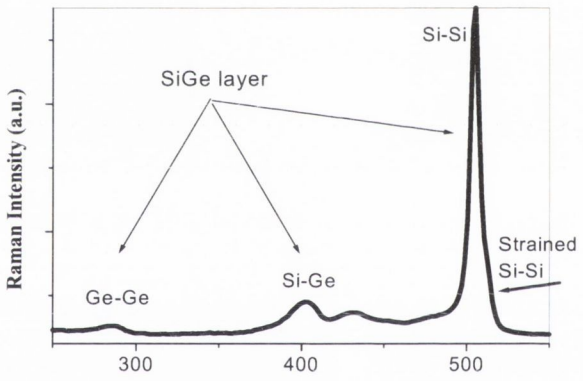


**Fig. 3.16** Raman intensity versus wave-number for strained Si on SiGe layer (sample S6).

Thus, Raman spectroscopy allows us to characterise the process and to predict indirectly the nature of surface topology and the presence of defects/threaded dislocations.

### 3.7.3.1 Ge Composition and Stress Calculation in Heterostructure Materials

In this section we discuss how the Ge content in a SiGe layer is calculated and in addition, how the magnitude of stress in a strained Si layer can be obtained.

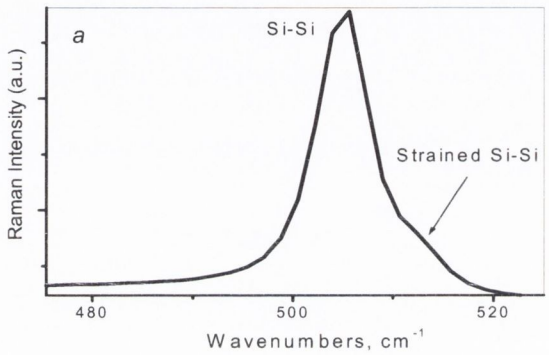


**Fig. 3.17** Raman spectrum of sample S6, focusing on the Si-Si phonon mode positions

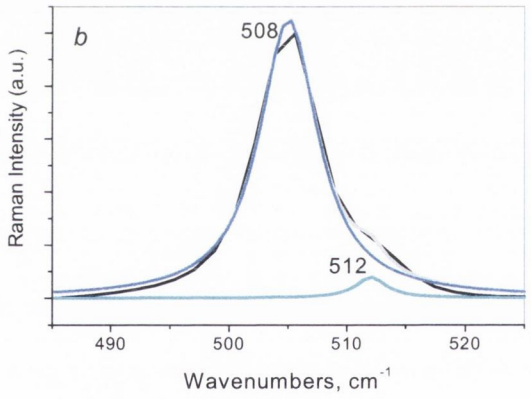


**Fig. 3.18** Raman spectrum of sample S11

Figs. 3.17 and 3.18 show Raman spectra for samples S6 and S11. As can be seen, the Si-Si band for strained Si appears as a shoulder on the more intense Si-Si band from the SiGe layer due to the overlapping of these two bands. Therefore it is necessary to perform a band fitting in order to determine the peak positions with a high degree of accuracy Fig.3.18 shows the various peaks in the Raman spectrum of sample S11 obtained from a Lorentzian curve fit. The curve for the strained Si layer can be clearly seen with a peak position at ~512cm$^{-1}$. By measuring the shift in the Raman peak position, $\Delta\omega$ (from the

unstressed Si-Si peak at 520 $cm^{-1}$) obtained for the s-Si layer, the magnitude of stress, $\sigma$ and strain, $\varepsilon$ can be estimated by using a simple equation, describing the biaxial stress in a Si lattice [51, 52]

$$\sigma_{Si} = \Delta\omega / c \tag{3.11}$$

$$\varepsilon_{Si}(\%) = (\frac{\Delta\omega}{b}) \cdot 100\% = \frac{a_{Si}^{strain} - a_{Si}}{a_{Si}} \cdot 100\% \ , \tag{3.12}$$

where c has a value of $4 \cdot 10^{-9}$ ($Pa \cdot cm^{-1}$), $b$ is the strain phonon coefficient, which was taken as 930 $cm^{-1}$ [53], $a_{Si}$ and $a_{Si}^{strain}$ are the lattice constants of relaxed and strained Si, respectively. The values of $\sigma_{Si}$ and $\varepsilon_{Si}$ are related to the elastic constants as

$$\sigma_{Si} = \frac{E_f}{1 - \nu_f} \cdot \varepsilon_{Si} \tag{3.13}$$

for a biaxial stress, where $E_f$ (130.2 GPa) is the Young's modulus for the film and $\nu_f$ (0.28) is the Poisson's ratio. The results of the measurements are recorded in Table 3.5 and are compared against results taken using Moiré fringe methods as described in Section 3.8.

**Table 3.5** Stress and strain in strained Si using Raman and Moiré Techniques

| **Sample name** | **Ge Content x(%)** | **$\Delta\omega$, $cm^{-1}$** | **$\sigma$ (GPa) (Eq.3.11)** | **$\varepsilon_{Si}$ (% ) (Eq.3.12)** | **$\varepsilon_{Si}$ (% ) from Moiré** |
|---|---|---|---|---|---|
| S6 | 21.26 | 6.72 | 1.68 | 0.723 | 0.70 |
| S11 | 22.2 | 7.29 | 1.823 | 0.784 | 0.75 |

Using Table 3.5 one can see that increasing the Ge content in the underlying SiGe layer increases the strain present in the strained Si cap layer. This correlates well with reported results which state that the strain levels measured in the Si cap increase with an associated increase in Ge composition in the SiGe buffer layer. In addition, as our results show, the use of step or linearly grown devices has little overall impact on the strain levels reported in the Si cap layer.

## 3.8 Moiré-Like Fringes

Investigation of TEM images, such as shown in Fig. 3.13 and Fig. 3.15, show the presence of lines which are very similar to those of a Moiré Fringe (MF) pattern. However, the images are from a cross sectional view of the sample and not a parallel view as is expected for fringes of this nature.

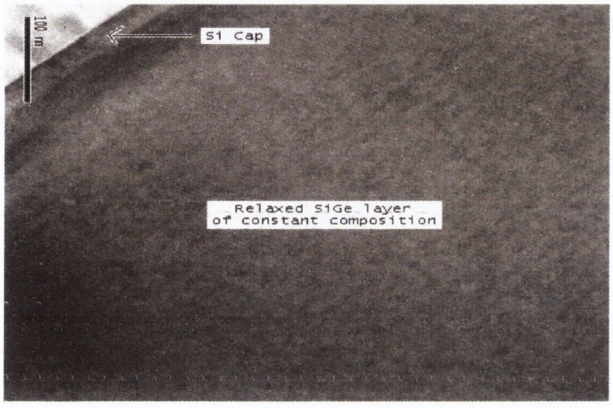


**Fig. 3.19** TEM image of Sample S6 viewed using a Philips Tecnai F20 200 kV with Field Emission Gun

Fig. 3.19 focuses on the upper layers of S6, where the defect free layer of SiGe is shown along with a series of black and white lines running parallel to the surface in the layer. Similarly, Fig. 3.20 shows the upper layer, with the black and white lines clearly more evident.

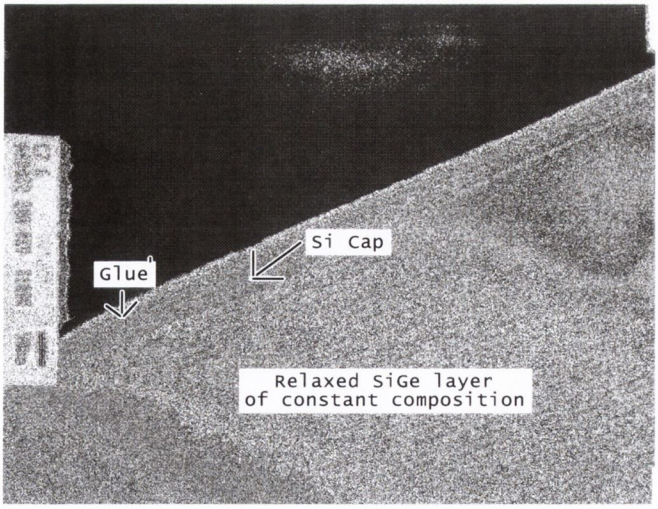


**Fig. 3.20** S6 upper layer, with lines more evident, viewed again using a Philips Tecnai F20 200 kV with Field Emission Gun

### 3.8.1 Moiré Fringes: An explanation

Moiré patterns have fascinated man for centuries. The effect was first noted in early Arabic writings when it was used to describe effects seen when weaving and the term eventually found its way into the English language by the mid $16^{th}$ century. In general, the term Moiré denotes a regular pattern in the form of a series of parallel or crossed lines. Moiré fringes arise from interference patterns that are generated when two similar grids overlap each other. The result is a series of fringe patterns that change shape as the grids are translated with respect to one another. In optics the effect arises when two gratings or grids are placed in proximity with one another with a small angle between the grating lines. Similarly, in spectroscopic investigations using TEM, Moiré fringes arise due to the overlapping of materials with similar lattice parameters. They (the fringes) can commonly be seen when viewing a set of vertical railings against another set of identical railings. One observes a pattern of bright and dark 'fringes' with a 'wavelength' that is an order, or orders, of magnitude greater than the distance of separation of the adjacent rails. The motion of these 'fringes' depends on the motion of the observer. Moiré fringes can have applications in industry and research where accurate comparisons of lattice structures are required, or for locating defects or faults in lattice structures. This is useful, as described below, in the calculation of strain present in a material. During observation of plan view TEM samples, the superimposed lattices are expected to give rise to Moiré fringes of the translational type. This is because a Moiré pattern is formed by the interference between two the regular sets of divisions of the respective lattice spacing.

## 3.9 Investigation of Moiré-Like Fringes

Unlike usual MF however, the lines shown in Figs. 3.19 and 3.20 run parallel to the surface of the material whereas MF are usually found in areas of different lattice parameters [55]. Fig. 3.21 is a Bright Field image focusing on the Si cap and the SiGe buffer layer of constant composition. The lines under investigation are clearly seen running parallel to the Si cap.

Samples for investigation were prepared at different locations, in order to rule out the introduction of such lines as a result of TEM preparations techniques, for example the tilt of a sample in the ion milling stage can give rise to overlapping lattices in TEM images. The lines from sample S6 are shown in Fig. 3.20 and match closely those identified in sample S11 as shown in Fig. 3.21. Thus, one varying parameter, preparation, was discounted as a source of the Moiré-like fringes.

**Fig. 3.21** Bright Field TEM image of sample S11 taken on a JEOL 200 with excitation voltage of 200kV and magnification of 50x.

The lines under investigation are clearly visible in Fig. 3.21. The TEM micrograph shown in Fig. 3.21 is taken from the graded SiGe layer, with misfit dislocations and half-loops present as expected. The widths of the lines are quite large and run parallel to the Si cap surface, as shown in Fig. 3.20. The spacing of the lines does not change from one layer to the next and they have no effect on the presence or absence of dislocation lines [56, 57]. To investigate this phenomenon in a CVD system, Electron Energy Loss Spectroscopy (EELS) mapping was performed using a Kedge Si map at 1839 eV, with an operating window of 60eV.The area under investigation is identified in Fig. 3.22 with the resulting elemental map shown in Fig. 3.23.

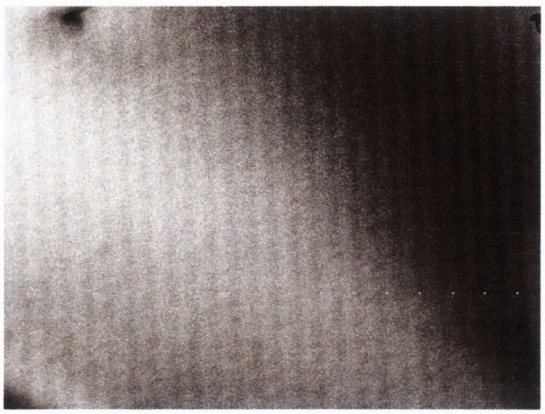

**Fig. 3.22** Gain Normalised TEM Image of the graded layer at 20x, indicating the presence of these Moiré - like Fringes.

The lines shown in Fig. 3.22 were analysed and found to be periodic and constant.

The Si EELS map of Fig. 3.23 clearly demonstrates the Si concentration varying across the material. The disparity in counts moving from left to right is indicative of the influence of the thickness of the sample on the measured data.

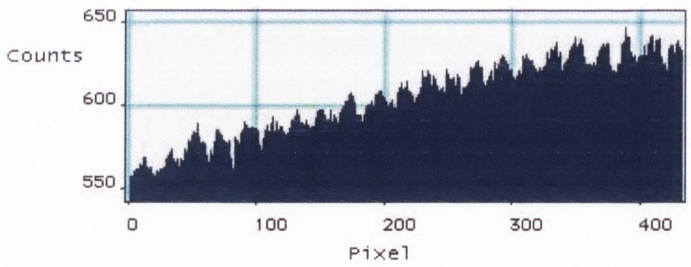


**Fig. 3.23** Si Elemental Map across S11

### 3.9.1 Influence of Sample Thickness

In order to verify this premise (thickness impacting on measurement), a thickness map was measured across the foil, and an associated colour map was generated as shown in Fig. 3.24. Variations of colour within this image indicate the disparity of thickness across the sample, with red indicating thicker areas, and blue indicating thin areas of the foil.

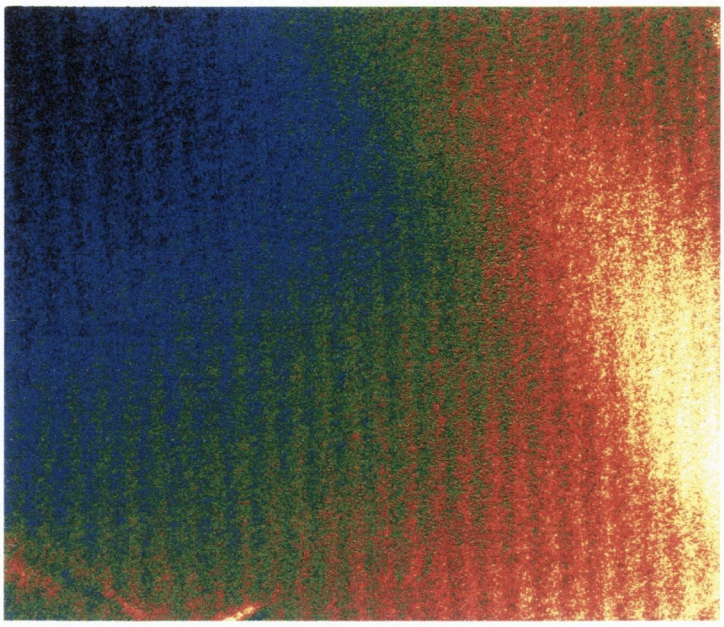

**Fig. 3.24** Colour coded thickness map for Si foil, demonstrating variation of thickness across the sample.

A thickness per wavelength (lambda) profile was developed across the same area and corresponded to an increasing thickness when moving towards the bulk. As the sample thickness increases, the probability of inelastic scattering also increases, particularly plasmon excitation, which possesses the highest cross-section of all the inelastic processes. The frequency of these independent scattering events follows a Poisson distribution and from this behaviour it can be shown that the ratio of the total intensity in the spectrum, $I_T$, to the intensity in the elastic Zero Loss Peak (ZLP), $I_{ZLP}$, gives a measure of the specimen thickness, $t$, via the formula [58]

$$t = \Lambda \ln(\frac{I_T}{I_{ZLP}}) \qquad (3.14)$$

where $\Lambda$ is the mean free path for inelastic scattering (effectively the distance travelled by the fast electron between inelastic collisions, which is of the order of 100nm at 100KeV). The accuracy of thickness determination using EELS depends critically on the value of the mean free path employed. Plasmon mean free paths and total mean free paths have been tabulated for various materials and incident beam energies (via an independent determination of sample thickness using alternative methods such as convergent beam

electron diffraction etc.). With increasing sample thickness, there is an increased probability for (single) plasmon excitation as well as an increase in the probability of multiple inelastic scattering, that is, a double or triple plasmon excitation, as well as an inner-shell ionisation event followed by a plasmon excitation. It is possible to remove this multiple inelastic scattering contribution from either the whole EELS spectrum or a particular spectral region by Fourier transform deconvolution techniques.

Once this thickness per lambda is taken into account, Si thickness is found to increase linearly when moving across the sample space towards the bulk, as shown in Fig. 3.25, with the Si count increasing from left to right, as we go deeper into the buffer layer.

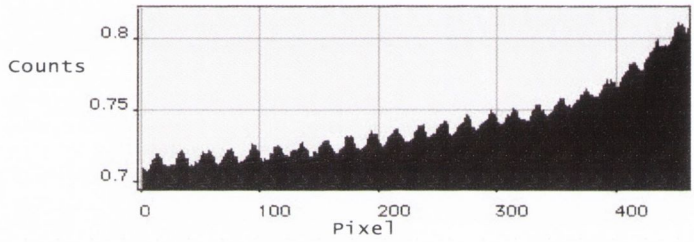


**Fig. 3.25** Elemental Silicon Map across the SiGe Buffer layer.

This regular variation in the Si content, across a buffer layer of constant composition for both Si and Ge, indicates a constant parameter fluctuation in the growth stage, such as in gas flow, which accounts for different levels of constituent materials at the micro level.

### 3.9.2 Calculation of Strain

From the EELS profile it appears that the dark and light lines map to a germanium and silicon profile respectively. It has been shown [59] that the determination of the in-plane strain is possible using the distance between occurring MFs. This calculation is independent of layer thickness and has been used to calculate strain and composition of partially relaxed SiGe layers. Fig.3.26 shows a cross sectional view of the sample. These Bright Field TEM images were taken from the HREM at 500x magnification. Real MFs are clearly visible at the interface of the Si cap and the SiGe buffer layer.

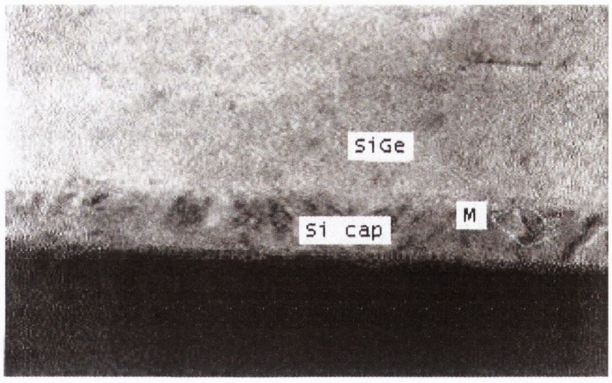


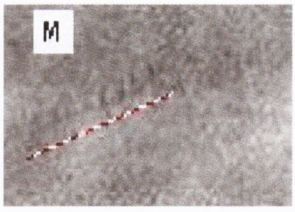


(a) (b)

**Fig.3.26** Showing the presence of 'real' Moiré fringes, indicated by the small box in (a) and shown in more detail in (b) (fringes found over the indicated dashed line)

The lattice constant $a_{//}$ can be calculated using the direction of the planes and the measured distance of the Moiré fringes from each other. Using Eqns.3.15 and 3.16 where a is the lattice constant of silicon, d represents the net plane distance of the layer and $D_{hkl}$ is the average distance between fringes, the value of the lattice constant parallel to the layer can be calculated, and thus the associated strain present in the cap.

$$d = \frac{a}{\sqrt{h^2 + k^2 + l^2}} \tag{3.15}$$

$$a_{//} = \frac{a_{Si} D_{hkl} \sqrt{h^2 + k^2 + l^2}}{\left( D_{hkl} \sqrt{h^2 + k^2 + l^2} \right) - a_{Si}} \tag{3.16}$$

Using these equations both S6 and S11 can be evaluated in terms of strain based solely on the presence of MF, the results of which are shown in Table 3.5.

## 3.10 Conclusions

Strained Si on strain relaxed SiGe heterostructures was identified as one of the promising candidates for expanding existing Si CMOS capabilities. To realise high mobility devices, high quality strain relaxed SiGe buffers were required. Various theoretical considerations, such as lattice distortion, dislocation annihilation and nucleation etc. were discussed in terms of their relevance to the growth of suitable SiGe layers. Various experimental equations relating to micro-Raman analysis were introduced to the reader, with their suitability to the various samples discussed. Limitations in this technique as imposed by the maximum possible depth of penetration were also outlined.

Efforts were described relating to the investigation of optimal growth parameters of both SiGe layers and subsequent strained Si cap layers in terms of substrate orientation and surface roughness. This chapter reported the successful growth of a strained Si cap layer, (25 nm), on a SiGe layer, with the Si cap defect free and close to expected growth thickness. The threading dislocation density in the underlying SiGe layer was calculated at extremely acceptable value of $5x10^{8}$ $cm^{-2}$, subject to experimental error. Earlier samples, S1, S2 and S3 were found to have a high degree of dislocation density due to the orientation of the wafer. AFM, TEM, and micro-Raman techniques were used to measure surface roughness and dislocation density, as well as the presence or not of strain in the Si cap respectively. This allowed for the successful growth of samples S6 and S11 following an in-depth investigation of previous unsuccessful efforts for samples S1 to S3. Sample S6 had a stress value measured at 1.68 GPa, whereas sample S11's stress was calculated at 1.82 GPa, the increase in stress relating to the extra steps of the graded layer, with these results well above reported literature values for similar Ge concentration. These measurements were made using micro-Raman techniques, which also provided a value of the Ge composition in both samples. As expected, S11 had a greater Ge composition (22%), than that of S6 (21%), as reflected in the difference in stress of the Si cap. The RMS surface roughness values of S6 and S11 are 2.785 and 3.089 nm respectively were in line with expected reported results.

Moiré like Fringes were reported in the SiGe layer and investigated using both TEM and EELS techniques. It It was identified for the very first time that variance in Si/Ge deposition rates caused the fringes to appear with closer control of the growth process suggested for future samples. A thickness map was developed across the foil sample and the importance of removing its effects from EELS spectra was outlined. Finally, as a complementary technique to micro-Raman analysis, the distance between real Moiré Fringes was used in order to calculate the lattice constant parallel to the layer. This allowed for strain measurements of the Si cap that agreed well with results measured using micro-Raman spectroscopy.

**References**


1. www.intel.com
2. S. Takagi, J. L. Hoyt, J. J. Welser, and J. F. Gibbons, *J. Appl. Phys.* **80**, 1567 (1996)
3. R. Oberhuber, G. Zandler, and P. Vogl, *Phys. Rev. B* **58**, 9941 (1998).
4. M. T. Currie, C. W. Leitz, T. A. Langdo, G. Taraschi, E. A. Fitzgerald, and D. A. Antoniadis, *J. Vac. Sci. Technol. B* **19**, 2268 (2001).
5. C. W. Leitz, M. T. Currie, M. L. Lee, Z.-Y. Cheng, D. A. Antoniadis, and E. A. Fitzgerald, *J. Appl. Phys.* **92**, 3745 (2002).
6. S. H. Olsen, A. G. O'Neill, D. J. Norris, A. G. Cullis, N. J. Woods, J. Zhang, K. Fobelets, and H. A. Kemhadjian, *Semicond. Sci. Technol.* **17**, 655 (2002).
7. K. Sawano, K. Kawaguchi, S. Koh, Y. Hirose, K. Nakagawa, T. Hattori, and Y. Shiraki, *J. Electrochem. Soc.* **150**, G376 (2003)
8. E. A. Fitzgerald, Y.-H. Xie, D. Monroe, P. J. Silverman, J. M. Kuo, A. R. Kortan, F. A. Thiel, and B. E. Weir, *J. Vac. Sci. Technol. B* **10**, 1807 (1992
9. D. E. Jones, J. P. Pelz, Y. Hong, I. S. T. Tsong, Y.-H. Xie, and P. J. Silverman, *Appl. Phys. Lett.* **69**, 3245 (1996).

10. K. Rammohan, D. H. Rich, R. S. Goldman, J. Chen, H. H. Wieder, and K. L. Kavanagh, *Appl. Phys. Lett.* **66**, 869 (1995)
11. M. H. Gray, J. W. P. Hsu, L. Giovane, and M. T. Bulsara, *Phys. Rev. Lett.* **86**, 3598 (2001).
12. R. People, *IEEE J. Quantum Electron.* **22** 1696, (1986)
13. Kasper E and Lyutovich K (ed) *Properties of Silicon Germanium and SiGe:Carbon* (London: IEE INSPEC) Chpt. 4, (2004)
14. K. Rim, *Symp. VLSI Technol.*, pp. 98–99 (2002).
15. J. Welser, J.L. Hoyt and J.F. Gibbons, *IEEE Electron Device Lett.* **15** 100, (1994)
16. J. Welser, J.L. Hoyt and J.F.Gibbons, *IEEE IEDM Tech. Dig.* 1000, (1992)
17. K. Rim, ISTDM Nagoya, Japan, January 16 – 17, 2003
18. http://www.avsusergroups.org/papers/tfug/TFUG_04_2002_Thilderkvist.pdf
19. E.A. Fitzgerald , M.T. Currie et al , *Physica Status Solidi (a)* **171** (1), 227-238 (1995)
20. E. Kasper, K.Lyutovich, *Solid State Electronics*, **48** , 1257 – 1263, (2004)
21. W. Read, W. T. Jr. *Dislocations in Crystals* ISBN 1114490660, (1953)
22. http://www.tf.uni-kiel.de/matwis/amat/def_en/kap_5/backbone/r5_1_1.html
23. D.J.Paul, **13**, no.2 February, pp 27-32, (2000)
24. D J Paul, *Semicond. Sci. Technol.* **19** R75–R108, (2004)
25. J. M. Burgers, *Proc. K. Ned. Akad. Wet.* **42**, 293–378, (1939)
26. Hsu WP, Fitzgerald E A, Xie Y H, Silverman P J, CardilloMJ, *Appl Phys Lett* **61**,1293–1295, (1992)
27. R. Beanland, M. Aindow, T.B. Joyce, P. Kidd, M. Lourenc, P.J. Goodhew, *J Cryst Growth* **149**, 1–11, (1995)
28. K. Samonji , H. Yonezu ,Y. Takagi , N. Ohshima, *J Appl Phys* **86**, 1331–1339, (1999)
29. Chen H, Li Y K, Peng S, Liu H F, Liu Y L, Huang Q, Zhou J M, Qi-Kun Xue, *Phys Rev B* **65**, 233303–(1-4), (2002)
30. A.M. Andrews, J.S. Speck, A.E. Romanov , M. Bobeth , W. Pompe , *J Appl Phys* **91**, 1933–1943, 2002

31. J. S. Speck, M. A. Brewer, G. E. Beltz, A. E. Romanov, and W. Pompe, *J. Appl. Phys.* **80**, 3808 1996.
32. A. E. Romanov, W. Pompe, G. E. Beltz, and J. S. Speck, *Appl. Phys. Lett.* **69**, 3342 1996.
33. A. E. Romanov, W. Pompe, G. Beltz, and J. S. Speck, *Phys. Status Solidi B* **198**, 599 1996.
34. A. E. Romanov, W. Pompe, G. Beltz, and J. S. Speck, *Phys. Status Solidi B* **199**, 33 1997.
35. G. E. Beltz, M. Chang, J. S. Speck, A. E. Romanov, and W. Pompe, *Philos. Mag. A* **76**, 807 1997.
36. M.A.Renucci, J.B.Renucci, and M.Kardona, *Proceedings of the 2nd International Conference on Light Scattering in Solids*, edited by M.Balkanski (Flammarion,Paris,1971),p326
37. F Cerdeira, A. Pinczuk, J. Bean, B. Batlogg, and B. A. Wilson, *Appl. Phys. Lett.* **45**, 1138 (1984).
38. M. I. Alonso, Ph.D. thesis, University of Stuttgart, Stuttgart, 1989
39. W. Byra, *Solid State Commun.* **12**, 253 (1973).
40. J.P.Dismukes, L. Ekstrom, and R.J. Paff, *J.Phys. Chem.*, **68**, 3021, (1964)
41. M.I.Alonso and K.Winer, *Phys.Rev.B*, **39,** 10056 - 10062 (1989).
42. J. C. Tsang, P. M. Mooney, F. Dacol, and J. O. Chu, *J. Appl. Phys.* **75**, 8098-8108(1994)
43. Takahashi J-I and Makino T 1998 *J.Apply.Phys.* **63** 87-91, (1998)
44. European Commission: Catalogue of optical and physical parameters 'Nostradamus' project SMT4-CT-95-2024, EC, EIR 18595. (Eds. De Wolf I, Jimenez J, Landesman J-P, Frogeri C, Braun P, Da Silva E, Calvet C). *RAMAN and Luminescence Spectroscopy for Microelectronics*, 16 (1995)
45. B. Dietrich, E. Bugiel, J.Klatt *J Appl Phys* **74**, 3177–3180 (1993)
46. C.H. Perry , F. Namavar *Solid State Communications* **88**, 613–617(1993)
47. R. Hull, J. C. Bean, and C. Beuscher, *J. Appl. Phys.* **66**, 5837 (1989)
48. A.A.Baski, S.C.Erwin, L.J.Whitman, Surface Science **69**,392, (1997)

49. F. K. LeGoues, B.S. Meyerson, and J.F Morar, *Phys. Review Letters*, **66** (22) 2903 – 2906, 1991
50. http://www.compoundsemiconductor.net/articles/magazine/8/9/1/1
51. S.A. Ringel and P.N. Grillot, *Proceedings of MRS symposium on Defects In Electronic Materials II*, 313-24 (1997).
52. T. Perova, *Proceedings E-MRS Symposium*, 2005
53. I. DeWolf, *Semicond. Sci. Technol.* **11** 139, (1996).
54. S.B. Samavedam, V.J. Taylor, J.M. Grant. J.A. Smith. P.J. Tobin, A. Dip, A.M. Phillips, and R. Liu, *J.Vac.Sci.Technol. B*, **17**, 1424, (1999)
55. J.J. Wortman and R.A. Evans, *J. Appl. Phys.*, **36**, 153, (1965)
56. D.Simon and A.Authier, *Acta Cryst.* A **24** 527, (1968)
57. F. K. LeGoues, M. Horn–Von Hoegen, M. Copel, R. M. Tromp, *Phys. Rev. B* **44**, 12894 - 12902 (1991)
58. Royal Microscopical Society Microscopy Handbook Series 48, Electron Loss Spectroscopy, Rik Brydson
59. E.Bugiel, P.Zaumseil, *Applied Physics Letters* **62** , 17, 2051-2053, 26 April 1993

# Chapter 4

# Dislocation, Composition and Strain analysis of SiGe layers within Ge P-N Photodiode structures

## 4.1 Introduction

Ge p-n photodiodes have been proposed as a suitable device for optical communications within the 1 – 1.6μm wavelength range. Due to their inherent advantages in bandwidth and noise immunity, several other applications have also been suggested for their use, including TV, Telephony and the Internet [1]. However, the implementation of such strategies necessitates a reduction in cost over existing proven technologies such as coaxial cables etc. Therefore, it is vital that the price of optical transceivers be reduced in line with present day solutions. The widespread demand for high speed data communications is driving the optical communications industry into devising more cost effective ways of meeting these demands. Monolithic integration, with its ability to combine a variety of devices such as sources/modulators to photodetectors on a single Si chip, can reduce both cost and system integration issues while increasing device capability. In addition, any proposed solution must use a material that can be readily adapted to current fabrication facilities. Epitaxial Ge is the material of choice for photodetectors due to its compatibility with Si technology and its high absorption in the near infrared [2-4]. Absorption of photons in a photodiode structure with suitable bandgap energy causes an electron to move from the valence band to the conduction band whereupon the generated carriers are then swept out of the device to provide a current [5]. Therefore, the higher the absorption rate, the higher the current. Si based optoelectronics, and photodetectors in particular, are now receiving considerable interest in both industrial and academic research [6, 7].

In terms of integration, a common approach to the fabrication of any Ge based device is the use of a fast graded SiGe buffer layer as has been suggested in Chapter 3 for strained Si. In addition, the growth of Ge layers directly on the Si substrate has also been

proposed [8, 9]. As outlined in earlier chapters, the problem with integrating Ge with Si is the lattice mismatch of ~4%. As a result, one can expect TDs to be present. Indeed, diodes that have been manufactured using such a process were found to have poor signal-to-noise ratios and an equally large dark current, both of which are related to the high density of TDs in the Ge layer.

Depending on the technique employed, the growth of a relaxed graded SiGe layer typically results in a dislocation structure which has long misfit segments and a low TD density. This was seen in Chapter 3 during the growth of strained Si structures. There are however, several challenges in growing SiGe buffers when graded to high Ge concentrations. While resolving questions relating to growth is one issue, one must also consider the paradoxical situation of maintaining a low TD density when growing a Ge epitaxial layer that greatly exceeds the pseudomorphic critical thickness, which is necessary for integration purposes [10].

## 4.2 Thin Film Virtual Substrates versus SiGe Graded Layers

In the world of electronics, Si has been the material of choice for more than 40 years due to the inherent advantages associated with it. As a result, expensive stream lined fabrication facilities have been built that focus primarily on Si and now, to a lesser degree, on those materials that offer increased functionality for limited adaptation costs. In this report, relaxed SiGe is seen as a potential material of choice, not just in terms of complementing existing CMOS devices but also as a link between separate devices all grown on a single wafer. In terms of integration costs, SiGe based technologies could then be combined on a bulk Si wafer. This means SOC solutions could offer III-V devices (i.e. a GaAs photodetector grown on a SiGe buffer layer), SiGe metal oxide semiconductor field effect transistors (MOSFETs) etc., all on a Si based platform. This combines the approach of increased functionality with reduced area for devices, in line with Moore's Law. In Fig. 4.1 the band gap of III-V materials, Si, and Ge versus lattice constant is shown [11]. What can clearly be seen is the large mismatch between Si and GaAs. It can be directly inferred from such lattice disparity that it is almost impossible to

create efficient devices that are made from abrupt GaAs on a bulk Si substrate. This is separate to the issue of thermal expansion which must also be addressed should an engineer wish to combine the two materials. Therefore, it is evident that a 'conduit' must be found that allows one to integrate the advantages of new materials with existing Si based technologies. SiGe, which is a miscible alloy, can be used to span the large lattice differential. In terms of existing Si based technologies, Chapter 3 reinforces the suitability of SiGe through the use of lattice manipulation in creating tailor made devices with increased mobility [12-16].

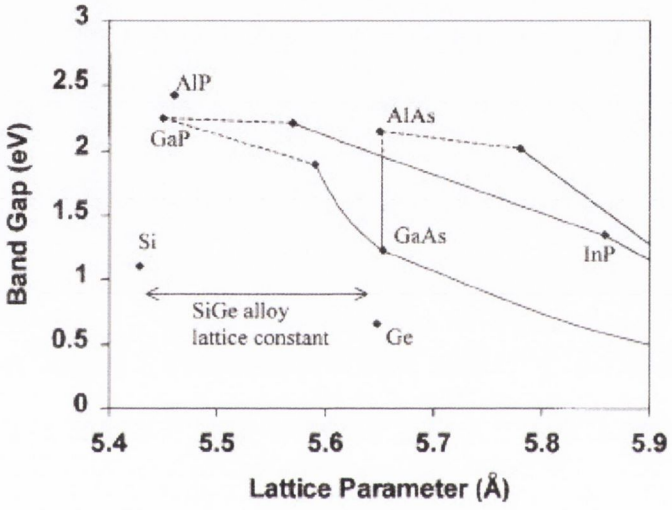


**Fig. 4.1** A map of band gap versus lattice constant for III-V alloys and Si and Ge [11].

This chapter investigates the benefits of using a graded SiGe buffer layer in the growth of Ge p-n photodiode structures as apposed to the use of a thin, abrupt virtual Ge layer. Thin virtual substrates are considered important for monolithic integration. Critical disadvantages arise with standard monolithic approaches to integration because the typical epitaxial layer structure differs between the electronic and the optoelectronic elements, making processing complicated. The potential advantages of using a thin virtual substrate are that it reduces chip count, with the potential of incrementally lower packaging costs and improved efficiency between the elements [17]. In this chapter, two different samples, 1653 and 1654, are analysed, with their corresponding structures shown in Fig. 4.2 and Fig. 4.3 respectively.

## 4.3 Sample Structure and Sample Preparation

Both sample 1653 and 1654 were grown by means of molecular beam epitaxy (MBE) on different types of virtual substrates. For technological reasons, both samples are capped by a thin Si layer (25nm). Sample 1654, as shown in Fig. 4.3 has a structure very similar to that of sample 1653, as outlined in Fig.4.2, except that a graded SiGe layer, with growth rate of 10% Ge per μm, is present. TEM characterisation of the Ge p-n photodiode structures include the analysis of the dislocation density present in the various layers, as well as using EDS and EELS spectra to quantify and qualify the structure's both in terms of elemental composition and gradient. Additional layer analysis relies on micro-Raman and XRD measurements to measure the stress levels present within the structures. Use of these tools allows for structural investigation at the atomic level.

As discussed in Chapter 3, TEM analysis allows direct comparison on the structural differences, such as the dislocation density, between one sample and another. Sample 1654 was grown on a virtual substrate with a thick graded buffer of SiGe (from Si to Ge) overgrown with a constant composition Ge layer. Chemical Vapour Deposition (CVD) was used initially, with the sample then transferred to a Molecular Beam Epitaxy (MBE) unit for the Ge p-n layers to be deposited. For sample 1653, the Ge p-n layers were grown on a thin (13 nm) Ge buffer deposited using molecular beam epitaxy (MBE). A CVD process was used in the growth of the thick graded SiGe layer due to the very slow growth rate (1nm/sec) and associated high cost of MBE. Both samples were prepared for TEM analysis in the usual way, with dimpling and ion milling.

| 25nm Si Cap ($n^+$) |
|---|
| 252nm Ge ($n^+$) |
| 378nm Ge (i) |
| 377nm Ge ($p^+$) |
| 13nm Ge (single step) |
| 150nm epi Si |
| Si Substrate |

**Fig. 4.2** Schematic Structure of Sample 1653

| 25nm Si Cap ($n^+$) |
|---|
| 245nm Ge ($n^+$) |
| 367nm Ge (i) |
| 377nm Ge ($p^+$) |
| 12nm Ge (single step) |
| 10μm graded SiGe + 2μm Ge |
| Si Substrate |

**Fig. 4.3** Schematic structure of Sample 1654

Absorption associated with a Ge p-n photodiode structure occurs in both the SiGe graded buffer layer and the overlying Ge layer. Parameters such as the density of TDs are important due to the potential adverse effect they can have on the absorption capabilities. Enhanced carrier drift velocity and higher bandwidth are associated with increasing depth of the buffer layer [10]. However, for improved integration schemes thin buffers below 100nm, such as used in sample 1653, with an associated high relaxation are developed.

## 4.4 TEM Measurements

Bright Field TEM measurements were recorded on a high resolution microscope (HREM), JEOL 4000FX, with an accelerating voltage of 400kV. The angle of rotation and tilt were adjusted to give suitable images while a diffraction aperture was inserted for maximum contrast.

## 4.5 Defect Dynamics and Structure in SiGe Graded Composition Layers

SiGe is especially suitable for studying constant strain rate experiments through composition grading. TDs, as shown in Fig. 4.4, are an inherent obstacle that must be overcome in device manufacture.

**Fig. 4.4** TDs in the SiGe buffer layer of sample 1654

At a variety of different magnifications and angles of tilt, TEM was used to analyse both samples. The advantages of such a technique are that layer interfaces, misfit dislocations and threading dislocations can all be investigated throughout the structures. As reported in the work by Fitzgerald [11], once a certain number of TDs are moving in the system during grading, enough misfit dislocations can be created to maintain a low strain state. Since graded layer growth is a continuous strain rate experiment, where the strain rate is constant, as continued grading increases the strain due to lattice mismatch, TDs continually flow to relieve the strain. Fig. 4.5 is a schematic representation of TD flow and misfit creation during relaxation.

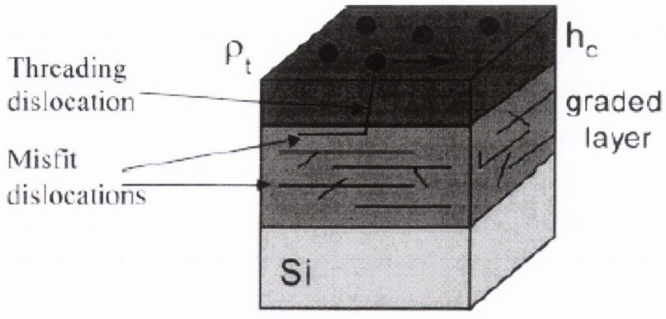


**Fig. 4.5** Schematic showing the concept of dislocation flow based on relaxed, graded SiGe data [11].

In Fig. 4.5, the top of the graded layer is strained due to a critical thickness ($h_c$) defined by the grading rate (i.e. mismatch/unit thickness). Increasing strain created by increased

Ge composition at the surface creates TD motion, as indicated by the arrow. The TD motion creates increased misfit segment length at about $h_c$ below the surface

A simple expression [19]

$$\frac{\partial \delta}{\partial t} = C\left(\delta_{eq} - \delta\right) \tag{4.1}$$

can be derived for the amount of strain relaxation versus time by realizing that the TD motion creates strain relaxation, and the velocity of the TDs is known empirically to be almost linearly dependent on strain and varies exponentially with temperature. In Eqn.4.1 $\delta$ is the amount of strain relieved by TD motion (and therefore misfit dislocation extension), $\delta_{eq}$ is the strain relief desired by equilibrium for the graded structure, and $C$ is a constant which is linearly dependent on TD density and exponentially dependent on temperature.

The Bright Field image of Fig. 4.6 shows the buffered SiGe layer used in the Ge p-n photodiode structure of sample 1654. The number of TDs present in this layer depends on their ability to move along the glide plane in such a manner as to achieve an equilibrium state. This is controlled by the rate of compositional increase within the SiGe buffer layer

**Fig. 4.6** TEM image of the SiGe buffer layer of sample 1654

## 4.6 Dislocation Density

As the movement of TDs relieves the strain present in the material, it is logical to then state that stopping TD glide in a material has a negative impact, i.e. an increase, on the TD density. This is due to the fact that in terms of strain relief, more TDs are then needed in order to compensate for the blocked dislocations. When TDs interact with other dislocations, as outlined in Chapter 3, or with other surfaces etc., they are thus removed from the strain relief mechanism. It has been shown that the increase in TD density in SiGe is due to a mechanism that arrests dislocation flow [20, 21].

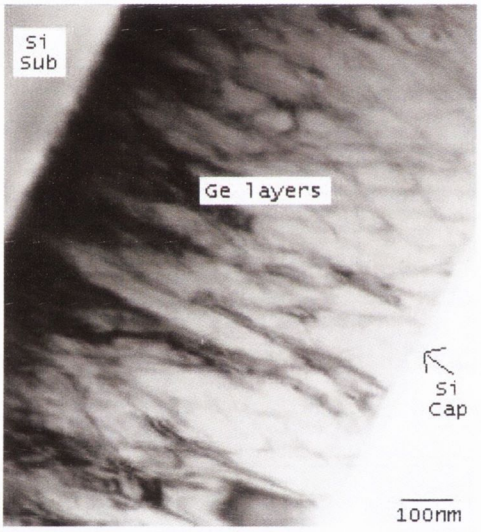


**Fig. 4.7** Sample 1653 Bright Field TEM, indicating structure of sample, taken at a magnification of 60K

A TEM image of sample 1653 is shown in Fig. 4.7. TDs dominate the material's layers, moving across the whole Ge p-n structure. The difficulty in Ge heteroepitaxy on Si stems from the previously discussed lattice mismatch. Using a thin, non-annealed Ge buffer layer, the density of TDs is extremely high as can be seen in Fig.4.7. A high TD density results in an associated high dark current value, unsuitable for photodetector operation [8]. The density of threading dislocations in sample 1653 suggests that the upper Ge layer is tending towards a state of lower relaxation than that of sample 1654 as more TDs are

working to try and relax the layer. This tendency is reflected in the higher stress value of the associated silicon cap measured using micro-Raman as discussed later.

Buried misfit dislocations can create inhomogeneous strain fields leading to surface crosshatch patterns as already discussed in Section 1.1.4 of Chapter 1 [19, 22]. It has already been identified that the blocking of TDs can lead to increased dislocation density. Surface interaction can occasionally block TD glide due to severe depressions in the crosshatch pattern, since the surface and the strain fields from the underlying misfit dislocations combine to eliminate the lateral force on the TD in this region. This is a self perpetuating situation as dislocations removed from the strain relieving mechanism due to surface interaction, can themselves interact with other TDs, thus creating a pile up of dislocations that can impact on the surface even further.

## 4.7 TEM Investigation of Graded SiGe Layers

Work in the GeSi/Si system has shown that step grading 20% Ge over 2000Å to pure Ge produces the same high dislocation density as pure Ge on Si [23]. By compositionally grading at a rate where the strain level in the structure never reaches a high value, and by growing at a high temperature, dislocation nucleation should be suppressed but relaxation from existing dislocations should be quite rapid. From our TEM images, such as the one shown in Fig. 4.8, it is clear that the mean misfit dislocation lengths are extremely long, implying that the dislocation morphology of a low mismatched system has been retained, as the Ge concentration increases.

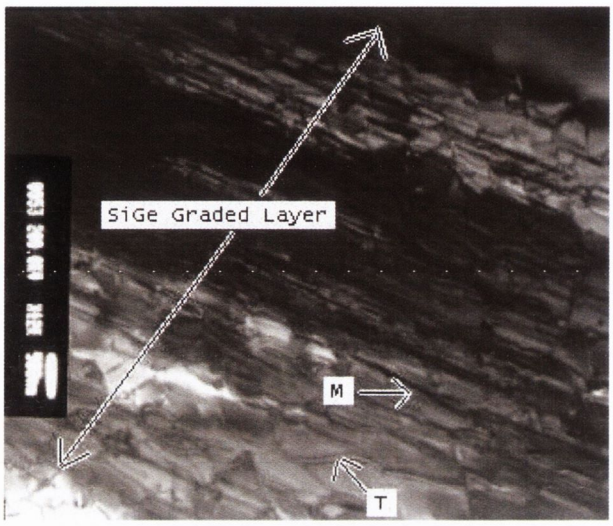


**Fig. 4.8** SiGe graded buffer layer of Sample 1654 detailing the threading (T) and misfit dislocations (M)

The graded structure not only retards new dislocation nucleations due to the low strain level, but also reduces dislocation interactions since the dislocations are distributed throughout the graded volume. Dislocation interactions indirectly nucleate additional dislocations, since the existing threading segments are prevented from further glide.

Fig. 4.9 depicts a Bright Field TEM image, showing clearly the layers present. As can be seen, dislocations are mostly confined to the graded SiGe buffer layer, thereby yielding high quality Ge layers, necessary for optimal performance of photodiodes. A low TD density in the overlying Ge layer indicates the effectiveness of the buffer layers in relieving the strain and blocking the propagation of the dislocations throughout the layer. Associated with effective strain relief through misfit dislocations is a clearly defined crosshatch pattern on the surface in (110) directions which is indicated in Fig. 4.10.

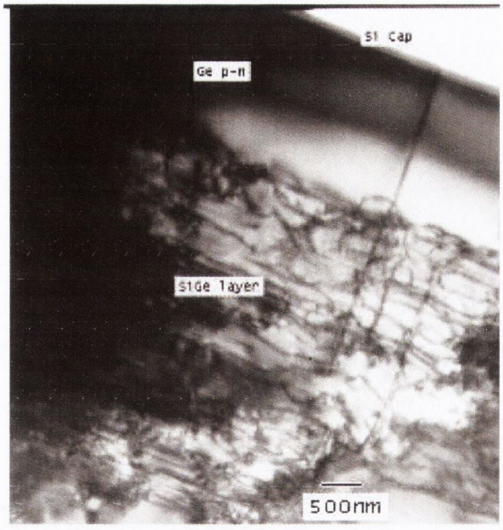


**Fig. 4.9** Bright Field TEM image of Sample 1654, at an energy of 12kV

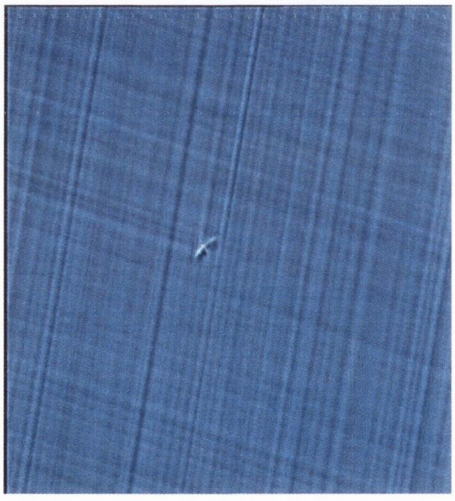

**Fig.4.10** Surface Micrograph of Sample 1654

The TEM image of Fig. 4.9 shows a line running through the Ge layers which is indicative of the resulting fallout from a thermal crack, due to the difference in thermal coefficients between the sample materials. Ge has a higher thermal coefficient of expansion than Si at both the growth temperature ($\alpha_{Si}$ = 3.55 x $10^{-6}$/K, $\alpha_{Ge}$ = 7.66 x $10^{-6}$/K at 750$^0$C) and room temperature ($\alpha_{Si}$ = 4 x $10^{-6}$/K, $\alpha_{Ge}$ = 5.7 x $10^{-6}$/K at 25$^0$C). As the graded structure is cooled down from the growth temperature to room temperature, the

Ge rich layers are tensilely strained relative to the Si rich layers, leading to the microcracking as evidenced in Figs. 4.9 and 4.11

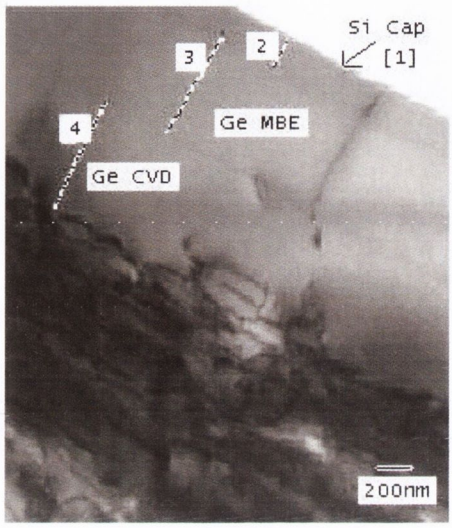


**Fig. 4.11** Bright Field TEM Image of Sample 1654 , at 20K magnification.

Changes in growth systems, CVD to MBE, are indicated in Fig. 4.11, where the TEM image can be used to directly indicate the point of transfer. Fig. 4.11 shows four distinct layers, separated with lines running parallel to the surface. These layers are:

(1) a strained Si cap layer;
(2) Sb doped Ge, with Sb included in an effort to contribute to surface smoothness;
(3) Ge deposited using MBE;
(4) Ge deposited using CVD;

As stated in Section 4.3, initial growth of the thick Ge buffer layer, (4), was performed in a CVD system, whereas layer (3) of Fig. 4.11 relates to an MBE environment. This change in growth environments causes the boundary line. The distinction between layers (2) and (3) of Fig. 4.11 is caused by the high Sb doping in the upper Ge layer. From TEM micrographs of sample 1654, the area measured differs somewhat from expected growth parameters. Using the TEM images of Fig. 4.11 and others already presented, it was found that the thick Ge buffer layer, (4), was closer to 1μm than the expected 2μm. Similarly, the widths of both layers (3) and (2) are not as expected, but to a much smaller degree. This difference is dependent on many things, such as exact boundary position etc.

As discussed earlier, the large lattice mismatch (~4%) between Ge and Si leads to the formation of a high density of misfit and associated threading dislocations when uniform Ge layers are grown on Si substrates. The SiGe buffered graded layer in sample 1654 is suitable for alleviating threading dislocations for the incorporation of Ge into the Si structure. The TEM image of sample 1653 as shown in Fig.4.12 demonstrates the presence of threading dislocations throughout the entire Ge p-n structure, all the way to the surface. Fig. 4.12 (b) is a magnified version of (a), focusing on the upper layers of sample 1653. Results are taken from the upper half of the TEM picture but can be equally applicable to the lower half also. The Bright Field TEM images of Fig. 4.12 show the high TD density associated with a large lattice mismatch. This large proportion of TDs can be readily explained. Once a TD is removed from the strain relieving process, through interaction with other surfaces or dislocations, further TDs must then be introduced to the system as it works to achieve a steady state dislocation density. In layers that attempt to relieve more than 2% mismatch, (in this case 4%), the TD density can increase substantially as compared to the desired equilibrium density. In tandem with this, the relaxation of the layer is dependent on the number of TDs present, and a high density of TD indicates that the layer itself is moving towards, but may not necessarily be in, a fully relaxed state. From this analysis, it is interesting to note the agreement between this supposition and measured micro-Raman results for both the Ge upper layer and Si cap.

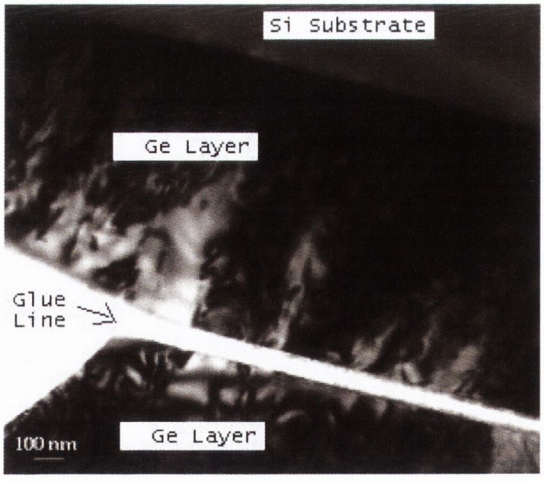


**Fig. 4.12** (a) Bright Field TEM micrograph of sample1653

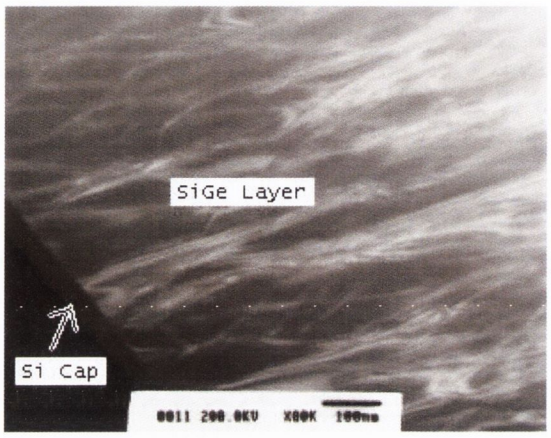


**Fig. 4.12** (b) TEM image at 200x magnification focusing on a close up of the cap area

## 4.8 Composition and Growth Gradient

The work outlined to date has established that the growth of SiGe buffer layers is a vital consideration in the development of Ge p-n photodiode structures. Threading and misfit dislocations are shown to be reduced through the use of graded SiGe layers with increasing Ge composition. Therefore, to create structures and devices with low dislocation densities, the parameters associated with the SiGe buffer layer must themselves be carefully controlled. This means that increases in Ge concentration as well as proper compositional grading must be examined from the growth stages. In the past decade qualitative and quantitative analysis of Ge p-n photodiode structures has been undertaken in order to understand the growth kinetics of the SiGe buffer layer. As outlined in Chapter 2, TEM characterization of these materials has a vital role to play in the development of new and improved devices. This section focuses on how EDS and EELS were used to determine, and subsequently optimise, the growth of the SiGe graded buffer layers.

As reported earlier, EELS is the analysis of the energy distribution of electrons that have interacted inelastically with the specimen, c.f. Chapter 2 [24]. These inelastic collisions

provide information about the electron structure of the specimen atoms, which in turn reveals details of the nature of these atoms. EDS uses detection equipment to measure the energy values of the characteristic X-rays generated within the electron microscope [25]. It is then possible to create a spectrum representing the chemical analysis of the sample under investigation. In particular, the use of EDS in calculating the gradients of Ge growth is outlined, which allows us to compare the measured results against expected values. In developing suitable EELS spectra K edge excitation is shown to be a suitable mechanism in the measurement of the Si cap layer, while thickness per wavelength ($\lambda$) spectra are explained and then subsequently used to overcome the influence of the thickness in foil samples. In addition to the work reported earlier, conventional TEM techniques are used to investigate the presence of TDs resulting from different growth techniques. Due to the large thickness (12$\mu$m) of sample 1654, it was not possible to get an EELS map across the whole of the specimen, so EDS was deemed the most suitable quantitative tool to use. Conversely, for sample 1653, EELS analysis was undertaken as SiGe compositional trends are obviously not important due to the nature of the device structure, i.e. sample 1653 uses a thin Ge layer instead of the conventional SiGe layer, and the sample size is small enough to allow a full sample scan. This is further discussed in the following section.

## 4.9 EDS Analysis

A series of EDS spectra from sample 1654 were taken at fixed intervals across the Ge p-n photodiode structure. Through a collation of these spectra it is then possible to determine the composition of relevant materials within the sample.

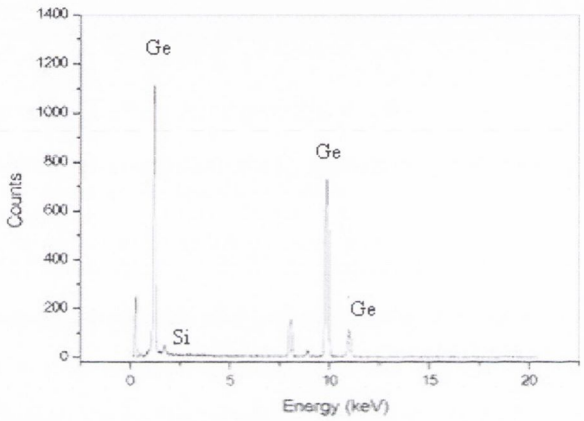


**Fig. 4.13** EDS spectrum from Si cap

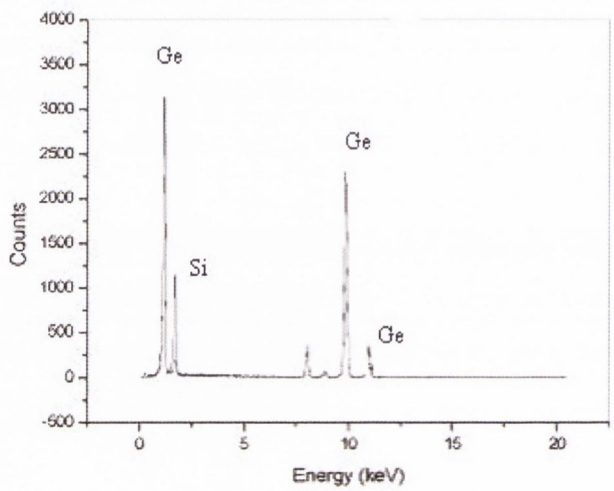


**Fig. 4.14** EDS near Ge/SiGe interface

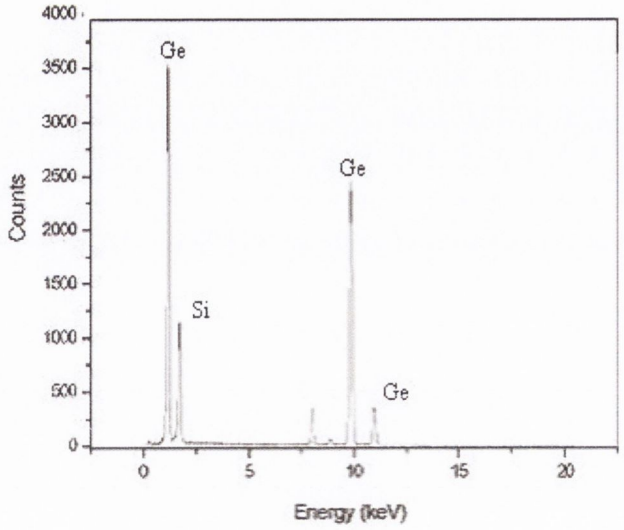


**Fig. 4.15** EDS of upper SiGe layer

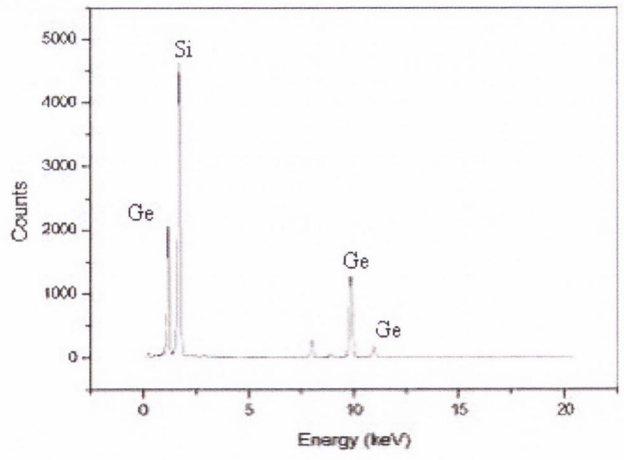


**Fig. 4.16** Spectrum in lower layers of SiGe

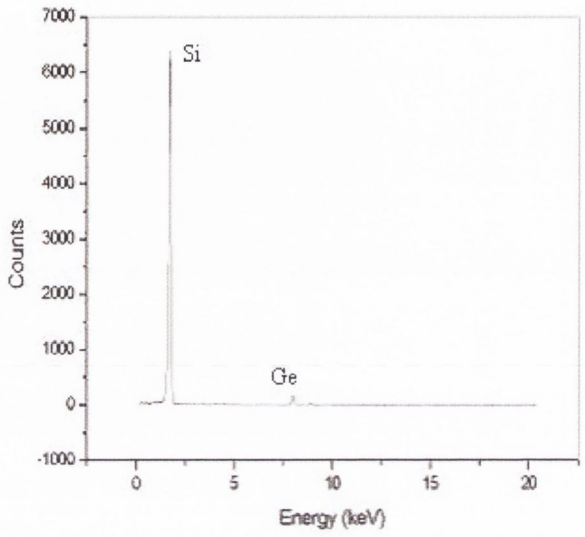


**Fig. 4.17** EDS Spectrum of sample 1654 near bulk Si.

Figs.4.13 to Fig.4.17 show quite clearly the Ge/Si distribution across different layers within the material. It is evident from Fig.4.13 that the upper Ge layer consists of 100% Ge with the detected Si peak coming from the Si cap itself. As the spot size of the EDS probe is much greater than the size of the Si cap, there will be a significant contribution from surrounding layers. This is reflected in the unexpectedly high Ge contribution visible in the spectrum. Various Ge lines in the spectra are explained by the photon energies of principal K-, L-, and M-shell emission lines. It is interesting to note that from Fig.4.13 to Fig.4.17 there is a reversal in the Ge/Si content underlying the presence of the SiGe buffer layer with the Ge composition decreasing closer to the Si bulk. Using the ratios of the intensity of the signal, the Ge/Si distribution can be calculated across the sample. The relevant compositional values achieved using EDS are outlined in Table 4.1, while the position of the associated measurements within the structure are outlined in Fig. 4.18 with the measurement points clearly numbered, 1-4, in correspondence with the position in structure as identified in Table 4.1. Sample point 5 is not identified due to large sample size.

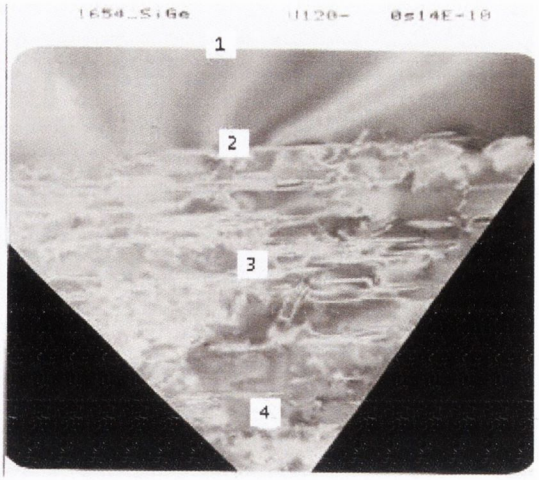


**Fig. 4.18** TEM micrograph of sample1654

**Table 4.3** EDS Compositional Analysis of Sample 1654

| Position in Fig.6 | Position in Structure | % Silicon | %Germanium |
|---|---|---|---|
| **1** | Near Silicon Cap | 91.76 | 8.74 |
| **2** | Ge/SiGe Interface | 8.38 | 91.62 |
| **3** | Upper SiGe Layer | 33.81 | 66.19 |
| **4** | Lower SiGe Layer | 80.72 | 19.28 |
| **n/a** | SiGe/Si Bulk | 99.97 | 0.03 |

Knowing the relative position on the sample from which measurements were taken, as well as the associated change in the Ge composition, it is possible to measure the gradient of Ge growth within the SiGe buffer layer. Calculations based on the above EDS spectrum yield a 12% Ge increase per 1μm, close to the expected value of 10%. It is the control of the Ge compositional increase which has a direct influence on both the threading dislocation density and the surface roughness. We have shown that using EDS

one can conclusively prove the distribution of the constituent materials across the whole of the device, as well as investigating the Ge gradient across the buffered structure.

## 4.10 EELS Analysis

Quantitative analysis of sample 1653 was performed using various EELS measurements. In EELS analysis of Si and Ge, L and K edge filtering is possible and both L and K edge filtering is available for analysis from the Si and Ge materials. Both were used initially to establish the most suitable operating environment for the sample under investigation [26]. Using the L edge Si, that is, using electrons excited from the L shell in silicon, the image shown in Fig. 4.19 was obtained. Note the roughness of the material revealed, detailing the contours present in our TEM prepared specimen of sample 1653. Switching to the K edge Si excitation gives a micrograph that is less influenced by the topographical nature of the specimen. The line presented in Fig.4.20 is the line map used for the elemental mapping necessary for the generation of the EELS spectrum [27, 28].

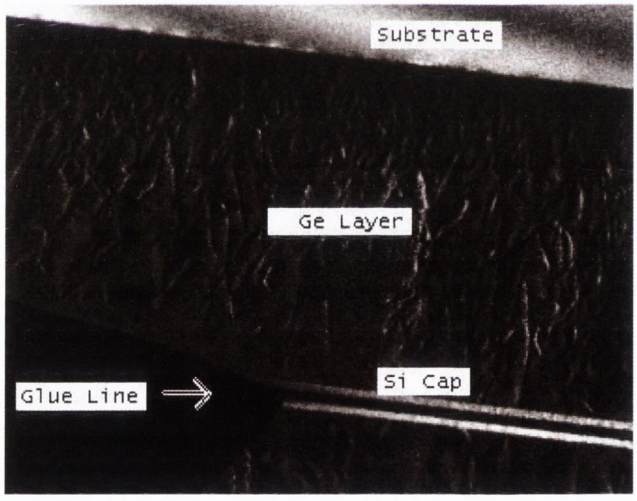


**Fig. 4.19** Sample 1653 silicon L edge map

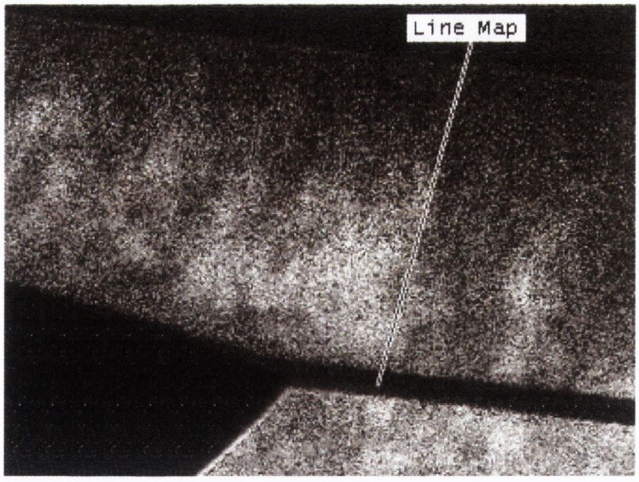


**Fig. 4.20** Sample 1653 silicon K edge map

The spectrum generated using the K edge Si excitation is shown in Fig. 4.21. The bulk Si layer is clearly seen, with a corresponding high count presence in both the bulk and the Si cap. It is interesting to note that in moving from left to right in Fig. 4.21, there is no other signal, i.e. no Si signature, otherwise present, as expected. The slight signal present is readily accountable due to noise. As the mapping reaches the Si cap, there is an observable increase in the counts for Si, indicating the presence of a Si cap layer, from which the Full Width Half Maximum (FWHM) can be used to estimate the width of the cap present. The Si cap layer thickness is calculated at 22nm, close to the expected value of 20nm. It must be noted that the double peak on the left hand side of Fig.4.21 is due to the mapping running across the glue line and coming into the presence of the Si cap at the other side of the glue line, indicated by the dashed line. This is due to the TEM preparation technique as described earlier. Conversion between pixel and nanometres is possible based on machine specifications which link the two, based on primary issues such as the magnification used, binning, etc. Using the GATAN CCD camera, at a magnification of 31.5x, a 210 pixel count corresponds to 100nm at 1x binning, whereas at 2x binning, as used in the profile generation shown in Fig. 4.21, 105 pixels correspond to 100nm. This relationship allows one to convert the measured pixel values into real physical measurements.

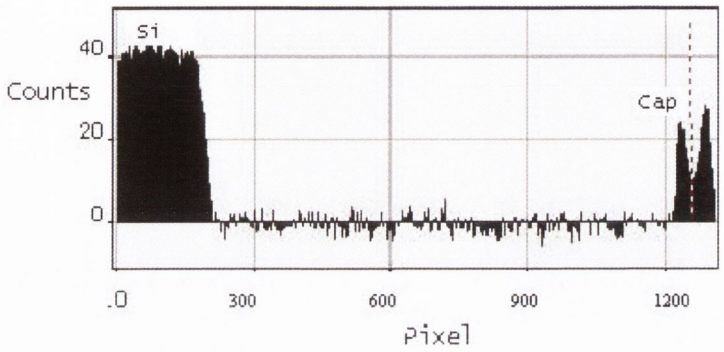


**Fig. 4.21** Profile from K edge Si spectrum moving from the bulk Si layer to cap.

From Fig. 4.20 it is clear that, compared to L edge, using the K edge excitation gives a better pattern analysis for Si, and from similar analysis the same type of excitation was chosen for Ge as well. The K edge is at 1869eV while the window used was 60eV. The spectrum obtained for Ge is shown in Fig.4.22. The line mapping in this case starts from the cap, left hand side, and moves across the p-n photodiode structure. From the spectrum an initial low count value is indicative of the presence of the Si cap. A Ge distribution across the Ge p-n layers is then observed, as expected. The shape of the distribution is quite interesting and will be accounted for in the discussion of Section 4.11.1.

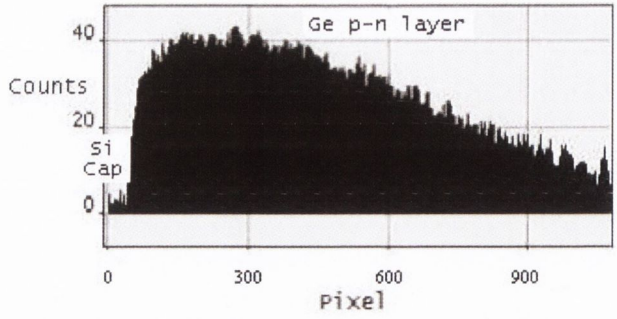


**Fig. 4.22** Ge EELS spectrum, showing Ge distribution from Si cap across Ge layers

An EELs colour map is then generated to show primarily, the presence of relevant materials, and secondary to this, the distribution of elements in the material, i.e. interstitial diffusion etc. if present can be readily identified. Fig. 4.23 shows a colour mapping, identifying the presence of both Si and Ge at the cap end.

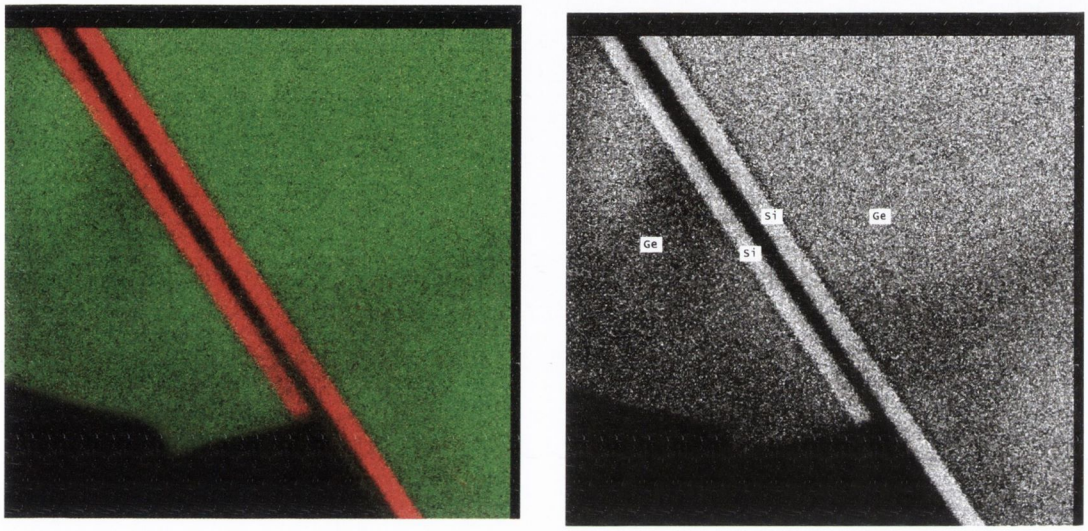


(a) (b)

**Fig.4.23** (a) EELS Colour Map, with Si in red and Ge in green, while (b) is a black and white copy of the same image with constituent elements identified.

### 4.10.1 Resolving the Effect of Foil Thickness

Elemental Mapping allows for the direct indication of materials present as well as being a tool in the analysis of diffusion etc. between layers. The black and white copy is for print purposes. As discussed in Section 3.9.1 of Chapter 3, the thickness of the TEM thin foil has a ready impact on the spectrum data obtained. The probability of multiple scattering increases in proportion to the specimen thickness and rising atomic number or density and the more multiple scatterings a sample may present, the less reliable the analysis for the element characteristic single scattering. Thus, as outlined previously, the section thickness of a specimen for acquisition of an EELS spectrum or calculation of an elemental map should be optimised for best results. Fig. 4.24 (a) shows a profile of the thickness of our foil, with Fig. 4.24(b) indicating a colour scale for the profile map. The

line across indicates the map line for the collected spectra. A thickness per wavelength expression was resolved for our foil and the resulting spectrum is shown in Fig. 4.25. As we go from our Si cap, blue, to areas of white, which correspond to the bulk Si, we move across areas of different thicknesses, thus giving us a different composition map as indicated in Fig.4.25.

(a)

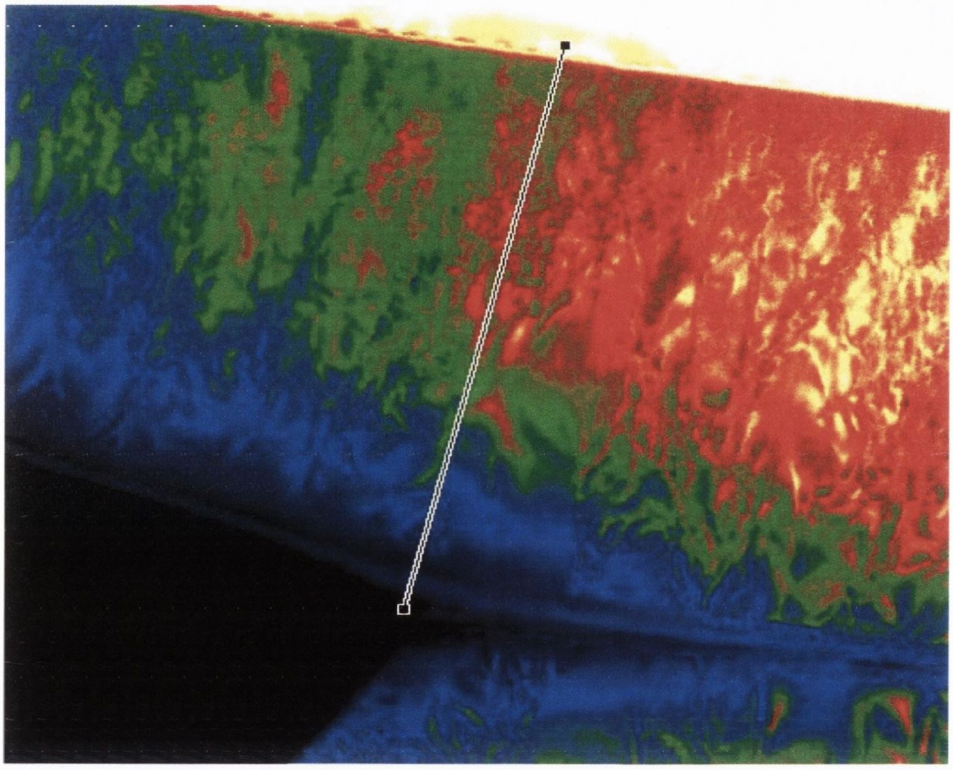

(b)

**Fig. 4.24** (a) Colour profile of thickness of the foil for sample 1653, and (b) a colour/thickness scale

If we compare Fig. 4.25 to that of our Ge mapping spectrum of Fig. 4.22 we can see that the thickness profile peaks in areas where the Ge profile is seen to tail off. Variation in the Ge content can thus be explained by the variation of thickness across the sample foil. This demonstrates that once the relationship between the thickness of foil and Ge content is resolved, the Ge composition across the Ge p-n structure is constant.

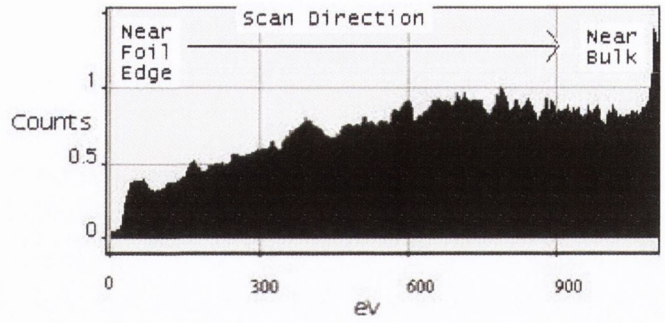


**Fig. 4.25** Thickness per wavelength spectrum for foil, showing influence of foil thickness across sample 1653

## 4.11 Strain Analysis

As outlined in earlier sections within this chapter, there is an intrinsic link between the density of TDs present in a semiconductor layer and the degree of strain in the layer. Sample 1654 demonstrated that with proper growth techniques, dislocations can be mostly confined to the graded buffer layer. With the top Ge layer exhibiting a low dislocation density, it indicates that the buffer layers are effective in relieving the strain. Therefore, it is expected that the upper Ge layers are completely relaxed which would then allow for a strained Si cap to be grown. Micro-Raman spectroscopy has already been demonstrated as a suitable tool in the measurement of strain in novel materials, and here again it is used to identify the level of strain present in the upper layers of Ge p-n photodiode structures, namely samples 1653 and 1654 respectively. In addition, XRD is employed as a complementary analytical technique to micro-Raman analysis in the measurement of strain, as well as being used to verify the growth of the buffer layer present in sample 1654.

### 4.11.1 Raman Spectroscopy

Micro-Raman spectroscopy is a technique suitable for the investigation of strain in semiconductor materials as discussed in Chapters 2 and 3. Analysis is performed based on the phonon vibration position of the relevant bonds, such as Si-Ge, Si-Si and Ge-Ge etc. In the discussion presented already, it has been shown that the depth of penetration of the laser light is a critical factor. Depth of penetration, $d_p$, as it relates to Si and Ge is measured at $d_p(Si) \approx 763nm$ and $d_p(Ge) \approx 19.2nm$ respectively, calculated from known

equations, c.f. Chapter 3, Section 3.4.1. It is clear therefore, that any information from the Raman spectrum relates solely to the upper layers. Therefore, a peak at or near 520cm$^{-1}$ will relate solely to the Si cap with a shift in wavenumber depending on the amount of stress present in the layer. Other groups of phonon modes that may be observed are associated with the SiGe layer and belong to the Si-Ge and Ge-Ge stretching modes.

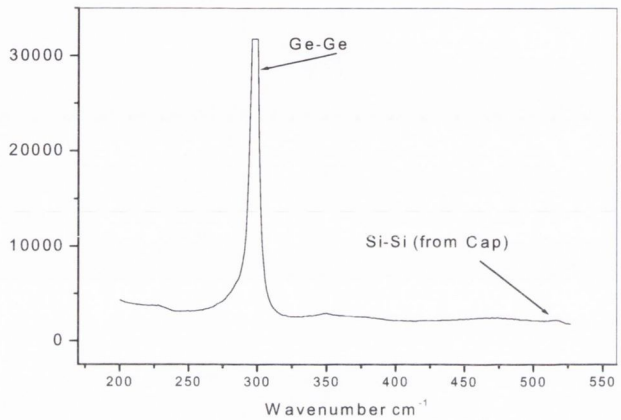


**Fig. 4.26** Raman spectrum of sample 1654

Observing Fig. 4.26, two main peaks of interest can be identified. One of these peaks sits at 300cm$^{-1}$, indicating the presence of Ge, and the other wide, soft peak sits at around 520 cm$^{-1}$ indicating the presence of the Si cap. The absence of SiGe related peaks at either 404 or 505 cm$^{-1}$ indicates in general the absence of interdiffusion between the Si cap and the Ge underlying layer. This analysis concurs with the earlier TEM micrographs which showed little or no interdiffusion between successive layers. The exact position of all aforementioned peaks depends on stress (for pure Si) and on stress and Ge content (for the SiGe layer). It is well known that the LO peak of Si at 520cm$^{-1}$ will shift to the low frequency side when the sample is under tensile stress and to the high frequency side when under compressive stress.

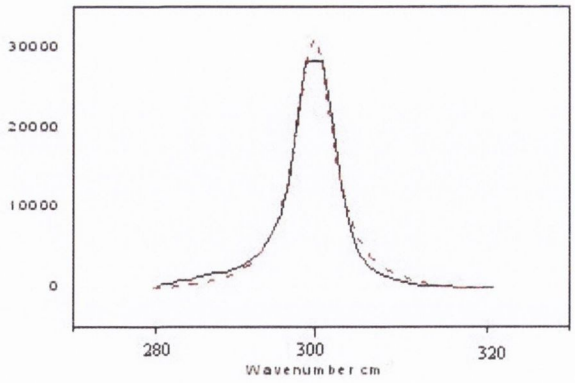


**Fig. 4.27** Ge-Ge phonon position and curve fitting (indicated by the broken line)

Fig. 4.27 and Fig. 4.28 highlight more clearly the peaks in the earlier spectrum, with an associated Lorenztian curve fit, indicated in dashed lines present also, allowing for good curve fitting parameters, such as FWHM and peak position, to be extrapolated

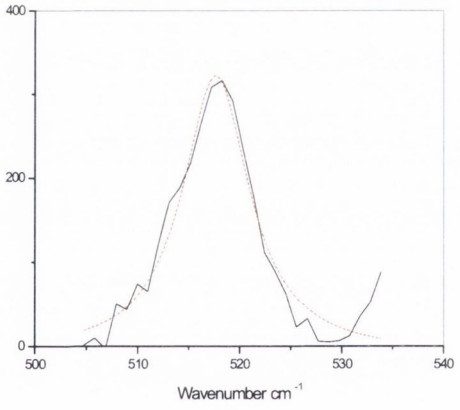


**Fig. 4.28** Si-Si phonon position, from cap, and curve fit

From the above spectra, differences in intensity between the Ge-Ge peak and the Si-Si peak can be readily observed. Peak intensity is generally directly related to the thickness of the material, but in this case, where light penetrates only to 19nm of Ge, the efficiency of Raman scattering for both Si and Ge has to taken into account. For sample 1654, the Ge spectrum exhibits a small shift from the relaxed Ge-Ge phonon position.

For calculations of the magnitude of stress ($\sigma$) present in the strained Si layer, Equation 3.11 as given in Chapter 3 is used

$$\sigma = (\Delta\omega / 4x10^{-9}) \qquad (4.2)$$

where $\Delta\omega$ is the shift of the Raman peak from the unstressed Si-Si peak position of $520cm^{-1}$. In this case, the Si cap is calculated to have a stress value measured at $1.060x10^{9}$ Pa.

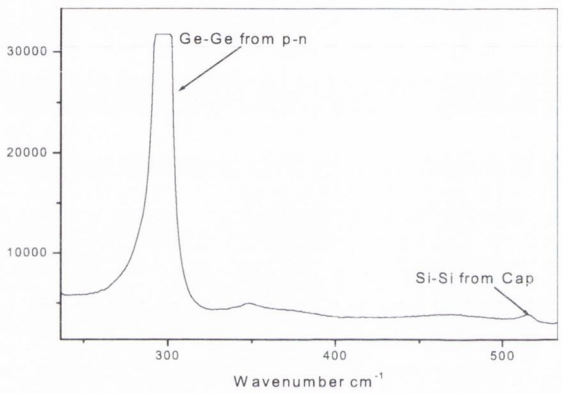


**Fig. 4.29** Raman spectrum from Sample 1653

From analysis of Fig.4.29, the Raman spectrum of sample 1653, the following conclusions can be drawn. As is the case for sample 1654, there is no interstitial diffusion present between the Si cap and the underlying Ge layers. This is proven by the absence of the well documented SiGe and Si-Si bonds associated with such a layer. Therefore, the growth process is well controlled and stops the migration of atoms between layers. Using the two indicated predominant peaks as discussed earlier, relevant information such as germanium content, and the presence of stress in the upper layers can be calculated. Fig. 4.30 and Fig. 4.31 show the Ge-Ge and Si-Si phonon spectra, again with a Lorentzian curve fit indicated in dashes. Measured peak positions and associated stress are summarised in Table 4.2.

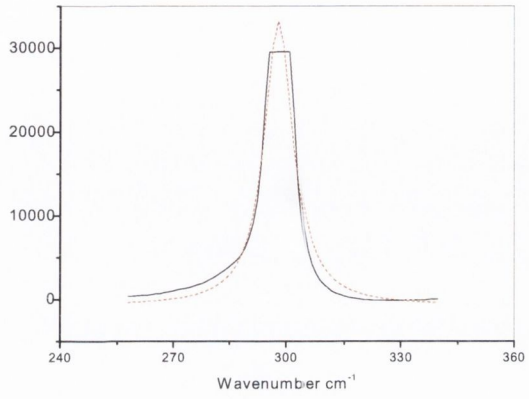


**Fig. 4.30** Ge-Ge phonon Raman spectrum

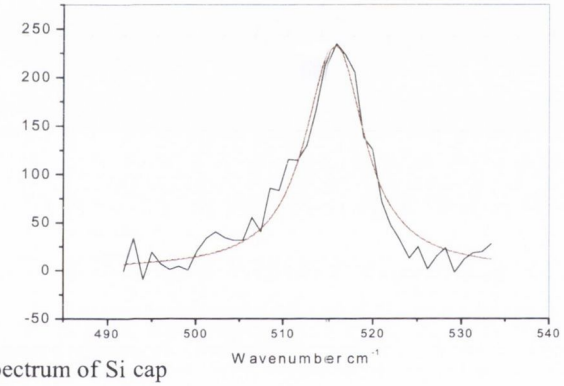


**Fig. 4.31** Si-Si Raman spectrum of Si cap

Using Eqn.(4.2) the magnitude of stress present in the Si cap is calculated at $1.060 \times 10^9$ Pa. The Ge-Ge phonon position exhibits an increased red shift relative to sample 1654, and this (marginal) increase in associated tensile stress present in the upper Ge layer reflects the influence of using a thin Ge virtual substrate as outlined earlier. On both samples the formation of a Si cap is observed. This cap has a higher level of stress in sample 1654, which can be explained following analysis of the TEM micrographs. The density of threading dislocations in sample 1653 suggests that the upper Ge layer is tending towards a state of lower relaxation than that of sample 1654 as the dislocations interact and reduce their effectiveness on the strain relieving process. Therefore, the lattice of the upper layer will not be effectively relaxed thus reducing the amount of

stretching (stress) on the upper Si cap layer. This is reflected in the lower stress value in the silicon cap of sample 1653.

**Table 4.4 Raman Measurements for samples 1653 and 1654**

| Sample Number | Ge-Ge $cm^{-1}$ | Si-Si $cm^{-1}$ | $\varepsilon_{Ge}$ (% ) (Eq.3.12) | $\Delta\sigma$ (Si) | $\sigma$(Si) |
|---|---|---|---|---|---|
| 1653 | 298.07 | 517.67 | 0.09 | 2.33 | 582.5 MPa |
| 1654 | 299.12 | 515.76 | 0.2 | 4.24 | 1060 MPa |

### 4.11.2 XRD Strain Analysis

X-Ray Diffraction (XRD) constitutes a powerful nondestructive technique for the structural analysis of crystalline and polycrystalline layers. It is based on the diffraction by the crystalline planes of a collimated beam of X-rays with wavelengths typically in the range 0.7-2Å. The XRD spectrum is usually obtained by measuring the diffracted intensity as a function of the diffraction angle $2\theta$ (angle between the incident and diffracted beams) and the orientation of the specimen. Different maxima, corresponding to the contribution of the different crystalline planes in the crystal, are obtained when constructive interference of diffracted X-rays occurs according to the Bragg's law,

$$\lambda = 2\, d \sin\theta \qquad (4.3)$$

$\lambda$ being the wavelength of the X-rays and d the spacing between the atomic planes in the crystal. The technique is extremely sensitive to variations of d determined by strain in the crystal. Strain values in the range $10^{-5}$-$10^{-6}$ units are routinely measured, and values as low as $10^{-8}$ can be detected. The penetration depth of the X rays is determined by the absorption length, which for Si has a value of 66μm at $\lambda$ = 1.54 Å.

#### 4.11.2.1 Calculation of Strain Using XRD

XRD spectra, obtained by measuring the diffracted intensity as a function of the diffraction angle $2\theta$ and the orientation of the specimen, were taken for both samples 1653 and 1654.

Three sets of different XRD measurements were performed which, when analyzed, allows one to understand the nature and characteristics of the relevant samples. Shown in Fig. 4.32 (a) and (b) are the $\omega$ scans along the $Ge_{004}$ plane, with two theta ($2\Theta$) fixed for

both sample 1653 and 1654 respectively. A perfectly epitaxial film would give a peak with zero width, but in reality, individual crystallites in the film have orientations which deviate slightly from the perfect epitaxial orientation and the resulting curve consists of a peak with a finite width, mirroring the mosaic structure of the film. The measured integral width for these samples is $0.5^{o}$ and $0.3738^{o}$ respectively, indicating a suitably acceptable sharpness of texture in the material.

(a)

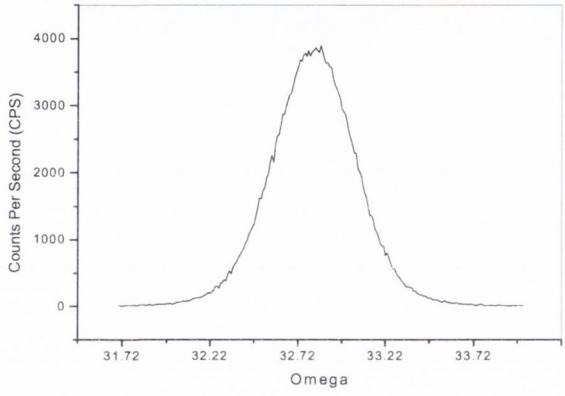


(b)

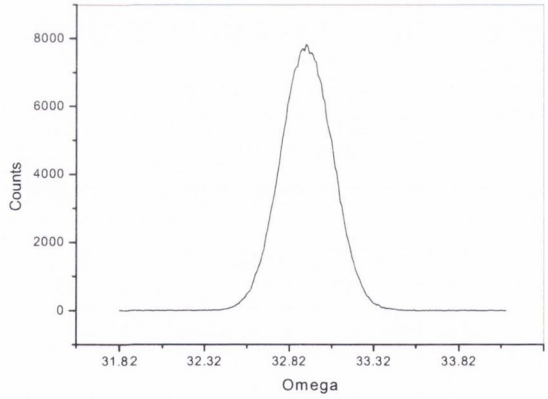


**Fig. 4.32** XRD spectra showing (a) ω scan along the $Ge_{004}$ plane for sample 1653 and (b) ω scan along the $Ge_{004}$ plane for sample1654

Similarly, Fig.4.33 (a) and (b) indicates the 2Θ scan along the $Si_{004}$ plane for both 1653 and 1654 respectively. Using these two spectra we can calculate the degree of strain present in the Si cap layer.

(a)

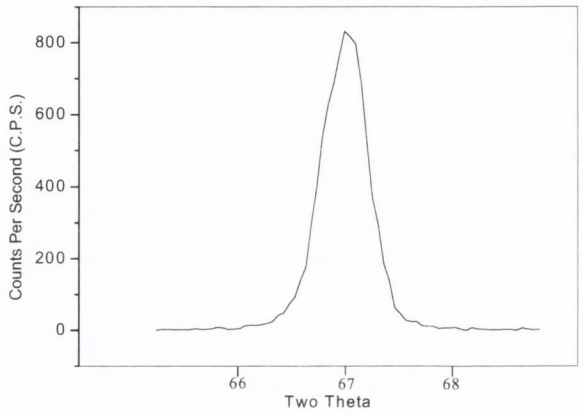


(b)

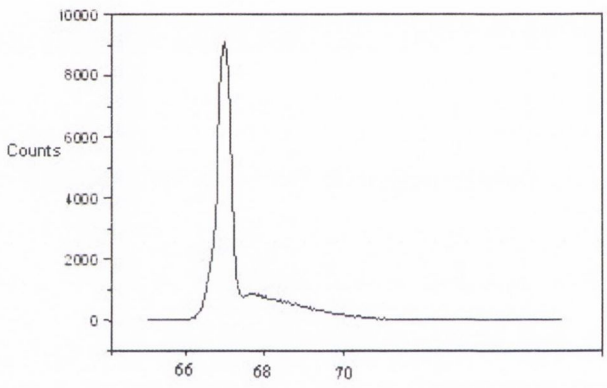


**Fig. 4.33** XRD spectra showing (a) 2 Θ scan along the $Si_{004}$ plane of sample 1653, and (b) 2 Θ scan along the $Si_{004}$ plane of 1654

From Fig. 4.33 (a) and (b) the value of 2 Θ can be readily identified. The offset value, introduced due to instrumentation error, is then calculated using a base silicon reference. Using well established values for 2 Θ as indicated in the literature, the exact value of Δ2 Θ can then be finalised as indicated in Table 4.3, where $2\Theta_{off}$ is the offset introduced due to instrumentation error, $2\Theta_{cor}$ is the corrected value of 2 theta after the offset has been removed and $2\Theta_{ref}$ is the journal based references for two theta [29].

**Table 4.3** XRD Analysis

| SAMPLE | $2\Theta$ | $2\Theta_{off}$ | $2\Theta_{cor}$ | $2\Theta_{ref}$ | $\Delta 2\Theta$ |
|---|---|---|---|---|---|
| **1653** | 67.108 | 0.028 | 67.080 | 67.013 | 0.067 |
| **1654** | 67.172 | 0.036 | 67.136 | 67.013 | 0.123 |

Using the values outlined in Table 4.3 and Eqns.4.3 and 4.4 shown below, the value of strain in the respective samples can be calculated:

$$(\Delta d)/(d) = \epsilon = (-\cot \Theta)(\Delta\Theta) \qquad (4.4)$$

For sample 1653, strain = $9 \times 10^{-4}$ and is measured at $1.62 \times 10^{-3}$ for sample 1654, which is in good agreement with previously stated results as detailed in Table 4.2, where both samples exhibited a slight red shift in Raman spectra.

### 4.12 XRD Structure Analysis

Using suitable XRD spectra, such as coupled two theta scans, it is possible to identify the layers present within the structure. Coupled two theta scans for samples 1653 and 1654 are presented in Fig. 4.34 (a) and (b) respectively. The buffered layer of SiGe, which has already been shown using other characterisation techniques, such as EDS, is clearly identified. In Fig. 4.34(b), the Ge peak is indicated and represents 100% Ge content. The gradual fall off from this peak to the higher (Si) peak at the right hand side, demonstrates the decreasing Ge content in a SiGe buffer layer. Sample 1653 does not have a similar spectrum, indicating only the single 100% Ge step underneath the Ge p-n photodiode structure.

(a)

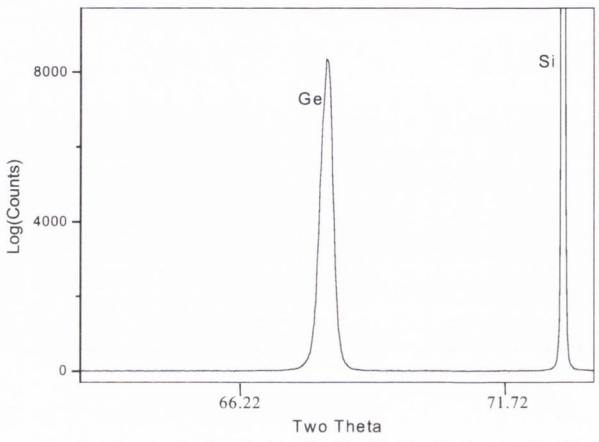


(b)

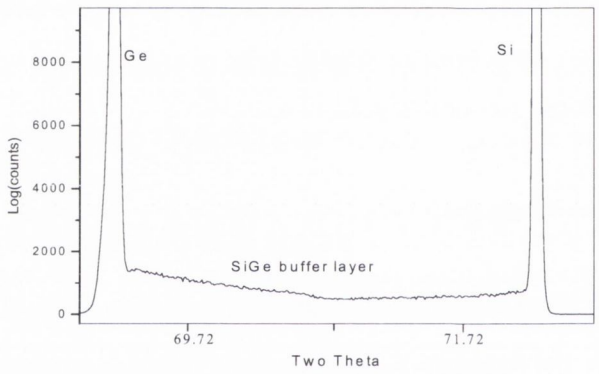


**Fig. 4.34** Coupled 2 Θ scan (a) for sample 1653 and (b) for sample 1654

It must be noted that the tops of the peaks are not visible in the spectra shown due to limitations placed on the y axis count value.

## 4.13 Conclusion

The importance of a SiGe graded layer in the fabrication of Ge p-n photodiode structures has been confirmed in this chapter using a variety of techniques, including TEM, EELS, EDS, micro-Raman analysis and XRD. Excellent confinement of the dislocations to the threading layer was achieved using a graded SiGe layer. It was clear from Bright Field TEM images that the threading dislocations differed dramatically from one specimen to another and that the SiGe graded layer present in sample 1654 is a necessary step, thus far, in the suppression of threading dislocations that occur due to lattice mismatch. In contrast, the use of a thin Ge layer as a virtual substrate has shown that due to the high TD density present throughout sample 1653, the search for a suitable technology for monolithic integration must continue.

It has been shown that using EDS one can conclusively prove the distribution of the constituent materials across the whole of the device, as well as investigating the Ge gradient across the buffered structure. In terms of the SiGe graded layer, calculations based on EDS spectra yielded a 12% Ge increase per μm, close to the expected value of 10%. We have shown that the Si cap thickness can be directly measured and that EDS profiles are suitable for composition analysis across such a thick material.

In addition, using EELS one can measure the thickness of the layers within a structure which can then be corroborated against any other complementary technique such as TEM, while also giving an indication of Ge and Si distribution across the layers present. It was also found that K edge excitation gives a better pattern analysis for both Si and Ge over L edge excitation as it was less influenced by the morphology of the sample. An EELs colour map was generated to show primarily, the presence of relevant materials, and secondary to this, the distribution of elements in the material, and that no interstitial diffusion could be readily identified. It was shown that the section thickness of a specimen for acquisition of an electron energy loss spectrum or calculation of an elemental map must be optimised for best results.

Complementary to the EELS analysis, micro-Raman spectra revealed no interstitial diffusion present between the Si cap and the underlying Ge layers. This was proven by the absence of the well documented SiGe and Si-Si bonds associated with such a layer. Therefore, the growth process was perfectly controlled and stopped the migration of atoms between layers. Using the two indicated predominant peaks as discussed earlier, relevant information such as Ge content, and the presence of stress in the upper layers was calculated. On both samples the formation of a Si cap was observed. For the first time, stress levels associated with Ge p-n photodiodes were investigated, with a noticeable level of stress present in the cap, with the value ranging from 585MPa to 1060MPa. The Si cap had a lower level of stress in sample 1653, which is related to the observed misfit dislocations in the TEM micrographs. The density of threading dislocations in sample 1653 suggested that the upper Ge layer was tending towards a state of lower relaxation than that of sample 1654, as was proven conclusively by the Raman measurements. This proves that not only must the density of dislocations be considered but also the stress imparted onto the Si cap.

XRD was used to verify the structure of the SiGe layer present in sample 1654 as well as the increase in Ge composition per step within the layer. The exceptional accuracy of XRD in the calculation of relatively low levels of strain was confirmed in this chapter. XRD was employed as a complementary analytical technique to micro-Raman analysis in the measurement of strain with calculated values from XRD of 0.09 and 0.16% for samples 1653 and 1654 respectively corresponding well to the values taken from independent Raman analysis. This demonstrates the usefulness of using both techniques in the characterisation of such materials.

**References**


1. L. Colace, G. Masini, and G. Assanto, *Appl. Phys. Letters* **76** 10 1231-1231 (2000)
2. A. Cutolo, M. Iodice, P. Spirito, and L. Zeni, *J. Lightwave Technol.* **15**, 505 (1997)
3. A. DeRossi, G. Masini, and G. Assanto, *IEEE Photonics Technol. Lett.* **11**, 194 (1999)
4. L. Colace, G. Masini, and G. Assanto, *IEEE J. Quantum Electron.* **35**, 1843 (1999)
5. http://ece-www.colorado.edu/~bart/book/book/chapter4/ch4_6.htm
6. L. T. Canham, T. I. Cox, A. Loni, and A. J. Simons, *Appl. Surf. Sci.*, **102**, 436–441, Aug. 1996.
7. L. C. Kimerling, *Appl. Surf. Sci.*, **159**, pp. 8–13, (June 2000)
8. S. Luyri, A. Kastalsky and J. C. Bean, *IEEE Trans. Electron Dev.* **31**, 1135 (1984).
9. P. Sutter, U. Kafader and H. von Kanel, *Solar Energy Materials and Solar Cells*, **31**, 541 (1994).
10. Oh Jungwoo, Joe C. Campbell, Shawn G. Thomas, Sushil Bharatan, Rainer Thoma, Craig Jasper, Robert E. Jones, and Tom E. Zirkle, *IEEE Journal of Quantum Electronics*, **38** , 1238 -1241, (September 2002)
11. E.A. Fitzgerald, M.T. Currie, S.B. Samavedam, T.A. Langdo, G. Taraschi, V. Yang, C.W.Leitz, M.T. Bulsara, *Phys. Stat. Sol. (a)* **171**, 227 (1999)
12. G. Abstreiter, H. Brugger, T. Wolf, H. Jorke, and H.J. Herzog, *Phys. Rev. Lett.* **54**, 2441 (1985)
13. Y.H. Xie, E.A. Fitzgerald, D. Monroe, P.J. Silverman, and G.P. Watson, *J. Appl. Phys.* **73**, 8364 (1993).
14. Y.-J. Mii, Y.-H. Xie, E.A. Fitzgerald, D. Monroe, F.A. Thiel, B.E. Weir, and L.C. Feldman, *Appl. Phys. Lett.* **59**, 1611 (1991)

15. E.A. Fitzgerald, Y.-H. Xie, M.L. Green, D. Brasen, A.R. Kortan, J. Michel, Y.-J. Mii, and B. E. Weir, *Appl. Phys. Lett.* **59**, 811 (1991)
16. F. Schaffler, D. Tobben, H.J. Herzog, G. Abstreiter, and B. Hollander, *Semicond. Sci. Tech.* **7**, 260 (1992)
17. D J Paul, *Semicond. Sci. Technol.* **19** R75–R108, (2004)
18. E.A. Fitzgerald, *Annu. Rev. Mater. Sci.* **25**, 417 (1995).
19. E.A. Fitzgerald, Y.-H. Xie, D. Monroe, P.J. Silverman, J.-M. Kuo, A.R. Kortan, F.A. Thiel, B.E. Weir, and L.C. Feldman, *J. Vac. Sci. Technol. B* **10**, 1807 (1992)
20. S.B. Samavedam and E.A. Fitzgerald, *J. Appl. Phys.* **81**, 3108 (1997)
21. E.A. Fitzgerald and S.B. Samavedam, *Thin Solid Films* **294**, 3 (1997)
22. E.A. Fitzgerald, P.D. Kirchner, G.D. Pettit, J.M. Woodall, and D.G. Ast, *J. Appl. Phys.* **63**, 693 (1988)
23. J. M. Baribeau, T. E. Jackman, D. C. Houghton, P. Maigne, and M. W. Denhoff, *J. Appl. Phys.* **63**, 5738 ( 1988)
24. Royal Microscopical Society Microscopy Handbook Series **48**, '*Electron Loss Spectroscopy*', Rik Brydson
25. Tae-Hang Ahn, In-Seok Yeo, Tae-Kyun Kim, Moon-Sig Joo, Hyeon-Soo Kim, Joong-Jung Kim, Joong-Ho Joung, and Jin Won Park, *J. Electrochem. Soc.*, **148**, G50-G54 (February 2001),
26. T. Walter, C.J.Humpries, A.G Cullis, *Applied Physics Letters*, **71**, 809-811, August 11, 1997
27. http://dmseg5.cwru.edu/Groups/Ernst/Courses/EMSE-512-S05/Pages/transparencies/EMSE-512-03.pdf
28. R.F. Egerton, '*Electron energy loss spectroscopy in the electron microscope.*' 2nd ed. Plenum Press, New York.(1996)
29. P.Lampard, Max Planck Institut fur Metallforschung, Stuttgart, Germany

# Chapter 5

# Interface Development and Dataset Analysis

## 5.1 Introduction

Data Management is of critical importance within a wide variety of sectors [1]. It is critical to be able to retrieve data of interest from multiple distributed heterogeneous data sources in a timely manner, and precisely enough to be able effectively to separate them from the distracting noise of irrelevant, unreliable or insignificant data. The control and observation of test data and results are primary metrics within self contained and proper data management techniques. While datasets can explode exponentially over time, the ability to contain these results and extract trends etc is a time consuming and often confusing aspect of research [2]. There are a variety of search engines, citation indices etc., which are important to scientific research, but there is no tool that allows the integration of results from a wide variety of significantly different datasets on the one platform. In this chapter details are given of the development of an interactive Graphical User Interface (GUI) that allows for seamless integration of new datasets and, at a higher level, allows for easy interaction between the user (scientist, student, researcher etc) and the information data sheets. This GUI was developed using Visual Basic for Applications which is part of the Microsoft Office tools suite and is bound to the Microsoft Excel platform [3]. In parallel, statistical analysis was performed on existing datasets relating to thin SiGe films. Equations already introduced in Chapter 3 are investigated here using XRD as a reference benchmark [4-6]. Data trends across the set are observed and a new equation used to calculate Ge composition is proposed. This equation provides a corrected value of Ge concentration, (x), based on the correlation that exists between Raman and XRD results. This is applicable to both experimental results and data mapping to existing equations. This work is important from a sense of understanding the impact of parameters, such as thickness, on Ge compositional analysis, as well as providing the scientific community with a more robust formula for Ge calculation.

## 5.2 Visual Basic for Applications (VBA)

Microsoft Visual Basic for Applications (VBA) is part of the Microsoft Visual Basic family that also includes the Microsoft Visual Basic development system (Learning Edition, Professional Edition, and Enterprise Edition) and Visual Basic Scripting Edition (VBScript) [3]. VBA is an embeddable programming environment designed to enable developers to build custom solutions using the full power of Microsoft Visual Basic. Developers using applications that host VBA can automate and extend the application functionality, shortening the development cycle of custom solutions.

## 5.3 Graphical User Interface (GUI)

The GUI consists of several linked userforms which are themselves part of underlying Excel spreadsheets. The interface developed is very intuitive with the user prompted for direction as well as information throughout. Links to detailed databases provide a seamless and non-obtrusive way of manipulating data.

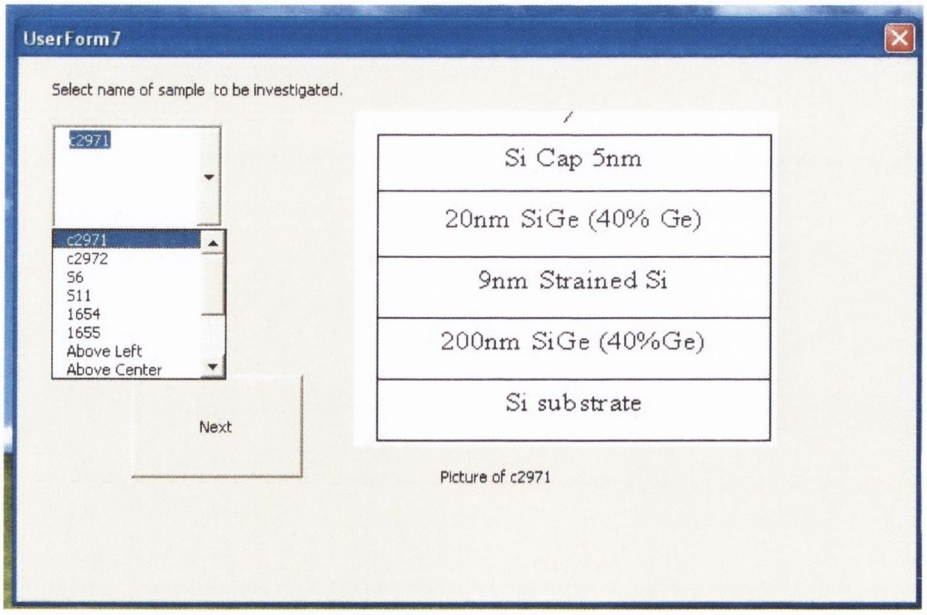


**Fig. 5.1** Introductory Userform

The GUI was developed based on the increased need for accessible and useful data. Researchers need to be able to track data and find information in a quick and seamless fashion, for example analysing the TEM and micro-Raman spectra associated with a strained Si sample. This package allows one to navigate through a variety of sources in order to provide a complete and comprehensive analysis of samples. Fig.5.1 shows the GUI developed to allow the user to choose the sample which is to be investigated. Selecting the sample name on the scroll bar causes the associated structure to appear, as shown. Using the mouse button, pressing the "Next" button allows the user to move into the next level of the programme. Fig.5.2 shown below details the different methods of investigation possible. Raman, TEM or EELS data analysis is possible with the user choosing the required method. The "Next" button has the same functionality as before, and the "Back" button allows the user to move to the previous working userform.

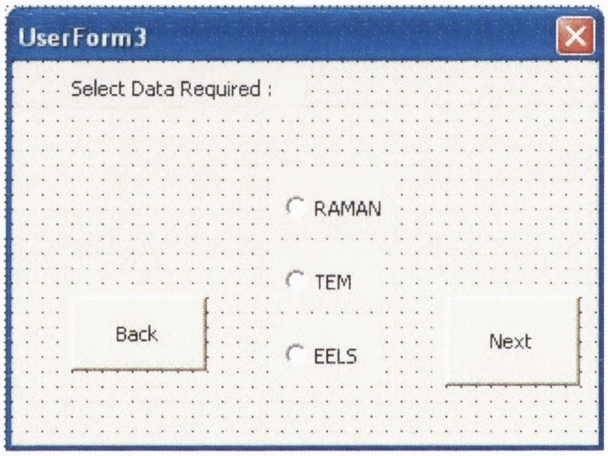


**Fig. 5.2** Different methods of analysis possible using the VBA GUI

Depending on the choice made, different userforms appear. In the case of TEM, the next userform, as shown in Fig.5.3, contains a scroll bar allowing a library of TEM images to appear. These TEM Bright Field images contain information such as tilt and magnification for the sample chosen. The GUI automatically directs the correct images to appear without having to waste time searching various directories.

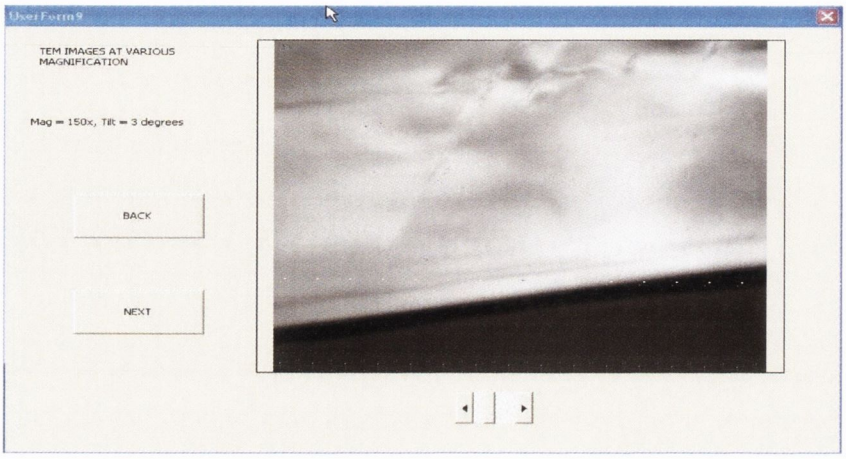


**Fig. 5.3** Form showing TEM images

Similarly, should EELS be chosen as the research of choice, the relevant EELS images for the sample under investigation will be displayed in the userform as shown in Fig. 5.4. Selection of Germanium (Ge) or Silicon (Si) analysis, using the K edge as described in Chapter 4, changes the image displayed.

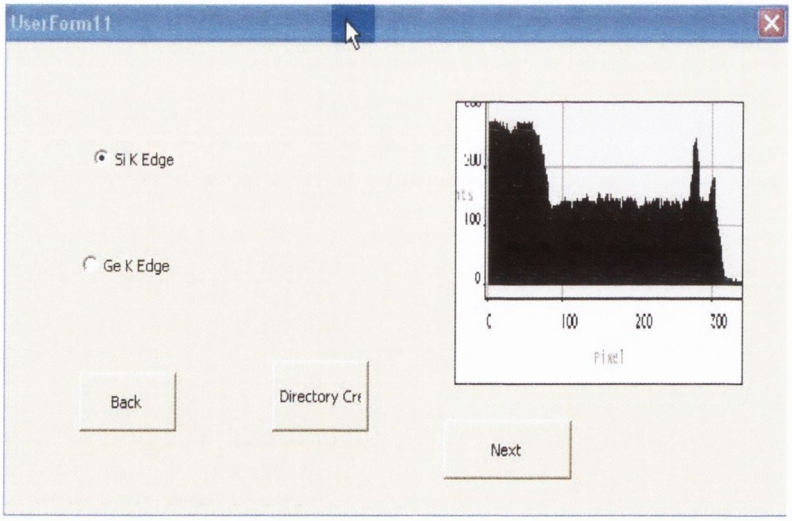


**Fig. 5.4** Userform showing EELS data displayed on request

In addition to TEM and EELS analysis, micro-Raman spectra, as well as calculations relating to the Ge content, are provided also. Strain coefficients along with explanations

of the various labels used in formulae are shown by the GUI. This is done in order to allow the user to maximise the benefits of such an interactive tool. Following the initial choice of sample to be investigated, the associated spectrum is displayed, see for example Fig. 5.5. In order to call the spectrum to the form, it is simply a matter of depressing the "Spectrum" button. Similarly, depressing the "Formula Used" button brings one to the next userform where relevant equations are detailed, as shown in Fig. 5.6. Parameters present in this equation are indicated in Fig. 5.7 where the user can scroll through all coefficients used and the associated explanation will appear on the screen.

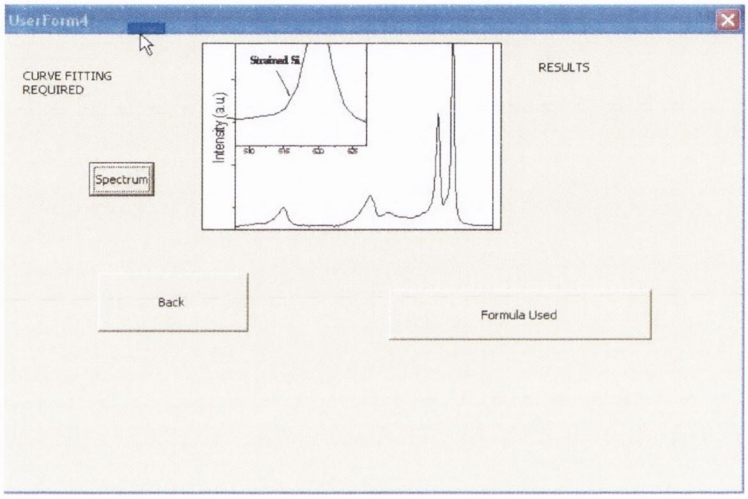


**Fig. 5.5** Userform depicting the relevant Raman spectrum

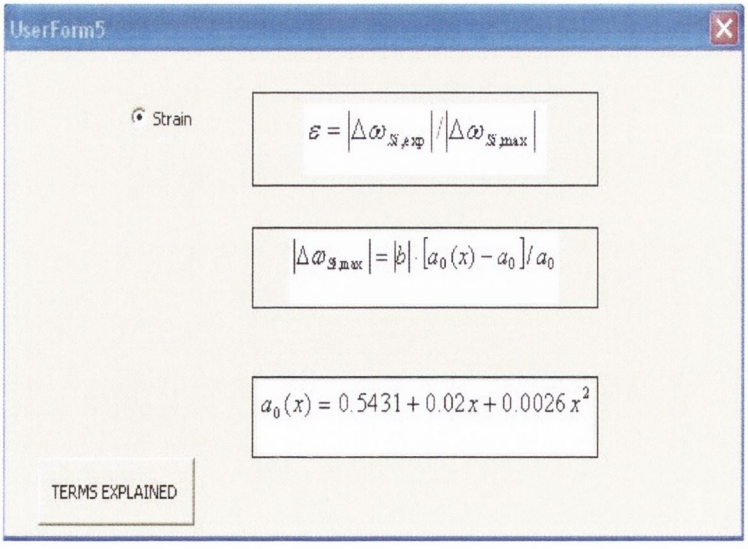


**Fig. 5.6** Equations relating to the calculation of strain

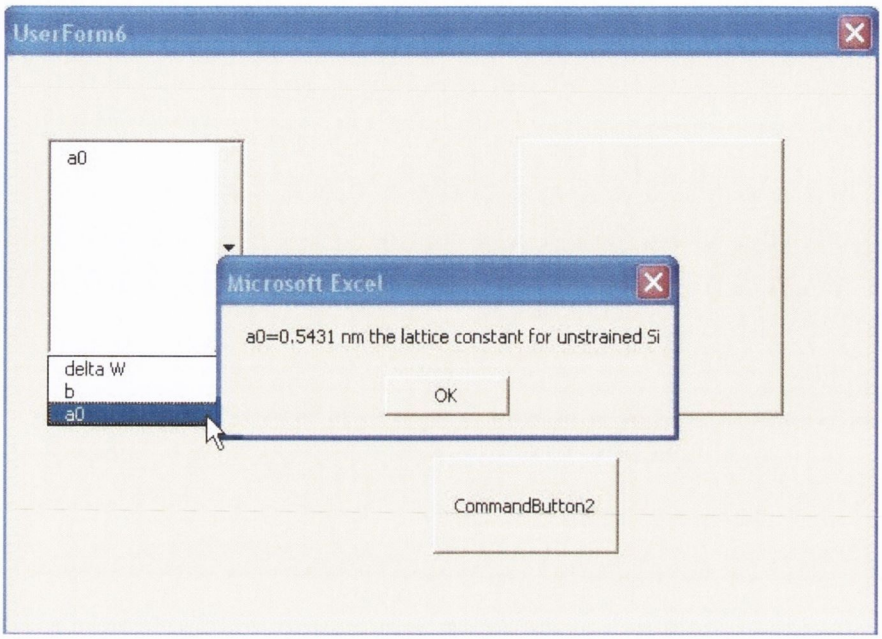


**Fig. 5.7** Explanation of terms presented in equations

## 5.4 Datasets

Various sets of data have been collected for thin film SiGe buffer layers, distinguished by differences in thickness and Ge concentration. These datasets are stored in Excel spreadsheets and are analysed in VBA using equations presented in the literature which either include or ignore the impact of strain in the calculation of Ge content. Independent XRD measurements have also been recorded in order to allow proper comparison between estimated and real Ge concentration measurements.

Table 1 of Appendix I, outlines the important peak positions associated with a SiGe buffer layer, as discussed earlier in Chapter 3. The tables are not included here but are placed in the appendices for the reader's convenience. In addition, thickness of buffer and XRD values are also recorded. Substituting peak position into the relevant equations values as outlined in Tables 5.1 and 5.2, allow for the calculation of the associated Ge concentration.

**Table 5.1** Equations without Strain

| | | |
|---|---|---|
| *X1* | *Alonso* | $\omega_{SS}(x) = 520 - 68x$ |
| *X2* | *Brya* | $\omega_{SS}(x) = 520 - 66.7x$ |
| *X3* | *Tsang* | $\omega_{SS}(x) = 520.2 - 62x$ |
| *X4* | *Shin* | $\omega_{SS}(x) = 521.2 - 67.91x$ |
| *X5* | *Olivares* | $\omega_{GS}(x) = 400.5 + 12x$ |
| *X6* | *Tsang* | $\omega_{GS}(x) = 400.5 + 14.2x$ |
| *X7* | *Alonso* | $\omega_{GG}(x) = 282.5 + 16x$ |
| *X8* | *Shin* | $\omega_{GG}(x) = 282.8 + 19.37x$ |

Using the equations outlined, the values X1-X8, which represent the Ge concentration within the sample, are calculated. These variables are then used within the VBA program to allow comparison and data trend extraction.

$$\mathbf{X1} = \left(520 - \omega_{SS}(x)\right) \Big/ 68 \tag{5.1}$$

$$\mathbf{X2} = \left(520 - \omega_{SS}(x)\right) \Big/ 68 \tag{5.2}$$

$$\mathbf{X3} = \left(520 - \omega_{SS}(x)\right) \Big/ 62 \tag{5.3}$$

$$\mathbf{X4} = \left(521.2 - \omega_{SS}(x)\right) \Big/ 67.91 \tag{5.4}$$

$$\mathbf{X5} = \left(\omega_{Gg}(x) - 282.5\right) \Big/ 16 \tag{5.5}$$

$$\mathbf{X6} = \left(\omega_{GS}(x) - 400.5\right) \Big/ 14.2 \tag{5.6}$$

$$\mathbf{X7} = \left(\omega_{GG}(x) - 282.5\right) \Big/ 16 \tag{5.7}$$

$$\mathbf{X8} = \left(\omega_{GG}(x) - 280.8\right) \Big/ 19.73 \tag{5.8}$$

Similarly, for analysis that takes into account the presence of strain, the equations as outlined in Table 5.2, are used. In this case a linear combination of equations is necessary in order to generate the Ge concentration variables XGE1 to XGE8, which themselves are then used within the VBA programme.

**Table 5.2** Equations with Strain

| | | |
|---|---|---|
| *1* | *Alonso* | $\omega_{SS}(x) = 520.2 - 62x - 830\varepsilon$ |
| *2* | *Brya* | $\omega_{SS}(x) = 520 - 66.7x - 830\varepsilon$ |
| *3* | *Tsang* | $\omega_{SS}(x) = 520.2 - 62x - 830\varepsilon$ |
| *4* | *Olivares* | $\omega_{GG}(x) = 282.5 + 16x - 384\varepsilon$ |
| *5* | *Tsang* | $\omega_{GS}(x) = 400.5 + 14.2x - 575\varepsilon$ |
| *6* | *Alonso* | $\omega_{GG}(x) = 282.5 + 16x - 384\varepsilon$ |

Suitable combination of relevant equations makes possible the calculation of the Ge concentration across the samples using the various sample peak positions

$$\mathbf{XGE1} = \left(\left(\omega_{GG}(x) - 282.5\right) + 0.6678\left(400.5 - \omega_{GS}(x)\right)\right)/7.986 \qquad (5.9)$$

Combining Eq.1 and Eq.4

$$\mathbf{XGE2} = \left(\left(\omega_{GS}(x) - 400.5\right) - 0.6928\left(\omega_{SS}(x) - 520\right)\right)/57.154 \qquad (5.10)$$

Combining Eq.2 and Eq.4

$$\mathbf{XGE3} = \left(\left(\omega_{GS}(x) - 400.5\right) - 0.6928\left(\omega_{SS}(x) - 520\right)\right)/60.41 \qquad (5.11)$$

Combining Eq.3 and Eq.4

$$\mathbf{XGE4} = \left(\left(\omega_{GS}(x) - 400.5\right) - 0.6928\left(\omega_{SS}(x) - 520\right)\right)/59.11 \qquad (5.12)$$

Combining Eq.1 and Eq.5

$$\mathbf{XGE5} = \left(\left(\omega_{GS}(x) - 400.5\right) - 0.6928\left(\omega_{SS}(x) - 520\right)\right)/54.954 \qquad (5.13)$$

Combining Eq.2 and Eq.5

$$\mathbf{XGE6} = \left(\left(\omega_{GS}(x) - 400.5\right) - 0.6928\left(\omega_{SS}(x) - 520\right)\right)/58.21 \qquad (5.14)$$

Combining Eq.3 and Eq.5

$$\mathbf{XGE7} = \left(\left(\omega_{GG}(x) - 282.5\right) + 0.6678\left(400.5 - \omega_{GS}(x)\right)\right)/6.517 \qquad (5.15)$$

Combining Eq.4 and Eq.6

**XGE8** = $\left(\left(\omega_{GG}(x)-282.5\right)+0.6678\left(400.5-\omega_{GS}(x)\right)\right)/7.986$ (5.16)

Combining Eq.5 and Eq.6

Tables 2 and 3 in Appendix 1 highlight the calculations of Ge using Equations 1 to 16, with the XRD measurement present also. These tables are calculated within the VBA programme.

## 5.5 VBA Raman Analysis

As outlined previously, the calculation of Ge content (x) is possible using Equations 5.1-5.8 or 5.9 to 5.16, depending on whether strain, ε, is considered or not. The VBA utility recognises this and allows the user to select which set of equations. are to be used, as outlined in Fig. 5.8.

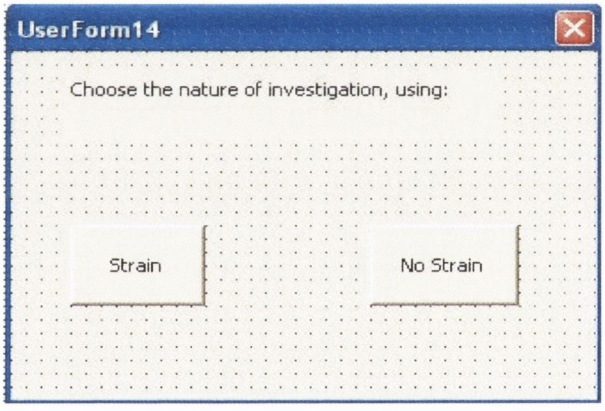


**Fig. 5.8** Interactive userform allowing user to choose which method of analysis to use

Choosing "Strain", Fig. 5.9 illustrates the userform that is next displayed. This userform shows the various equation combinations possible, with the user being afforded the possibility of understanding the combinations of equations possible, as well as their association to the relevant researcher. This userform does not perform any calculations but is merely an interactive tool applied to educating the user. The resulting equation is then shown in blue on the userform.

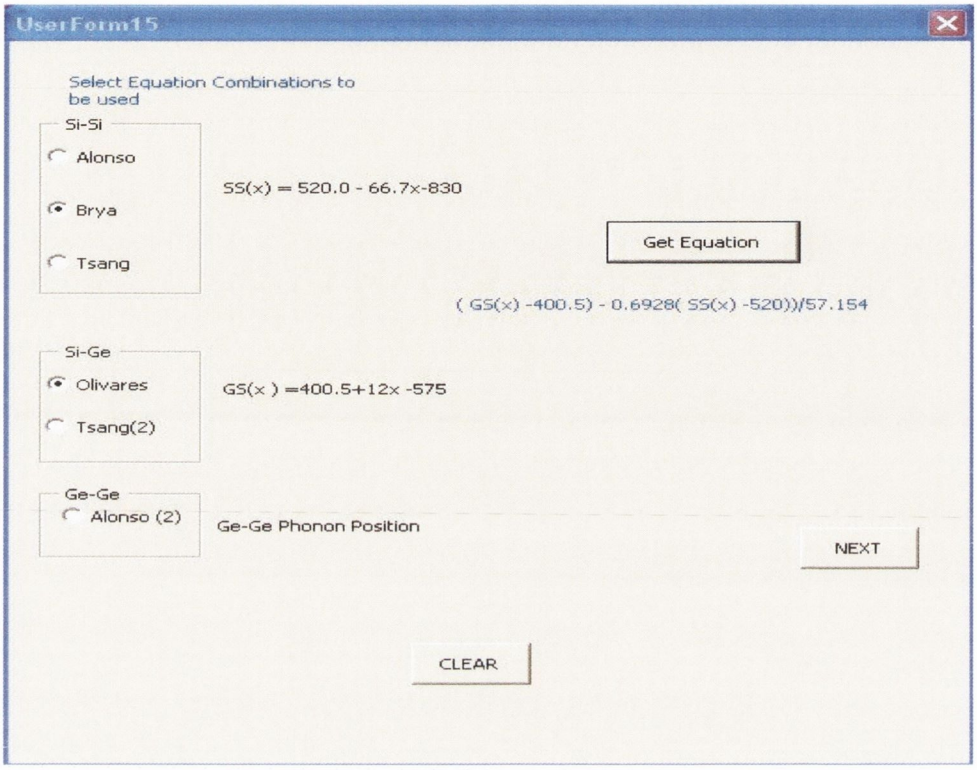


**Fig. 5.9** Userform15 showing the combination of different equations

As has been demonstrated, the purpose of the VBA utility is both to educate the user and to perform detailed analysis of underlying information recorded from a variety of sources. In line with this, Fig. 5.10 shows a userform where the user is informed of the various combinations possible, i.e. reflecting Eqns. 5.9 to 5.16 presented earlier. Additionally, the various terms used in the equations can be selected for user clarification. In this case, the button GG is depressed with an associated message box appearing defining the term GG used in the listed equations.

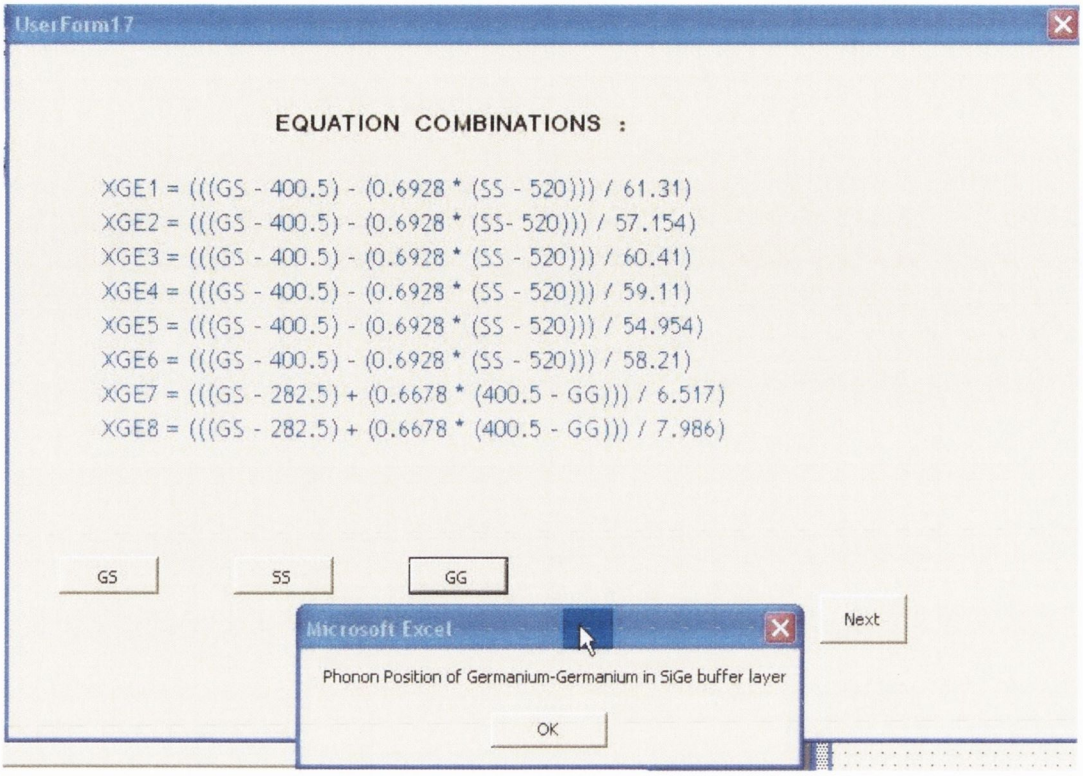


**Fig. 5.10** List of all Strain related equation combinations – with user prompted information box

In terms of mathematical analysis, the Ge content is the primary parameter investigated. Using the dataset presented in Table 1 of Appendix I, it is possible to investigate the value of Ge using the different equation sets, all the time using the XRD recorded value as the reference value. This allows one to investigate both Ge content as well as deviation away from exact values (XRD) within the dataset. Userform19, as shown in Fig. 5.11, illustrates the value of Ge calculated across the whole dataset using Eqn. 5.9 as the equation of choice. Similarly, the user can select Eqns. 5.10 to 5.16 and recalculate the Ge value across the dataset based on the peak positions of the recorded Raman spectrum. In essence, the GUI is creating and extracting information as presented earlier in Table 5 in Appendix I in an interactive way, plotting the calculated values while at the same time creating an Excel spreadsheet for further investigation, should it be required.

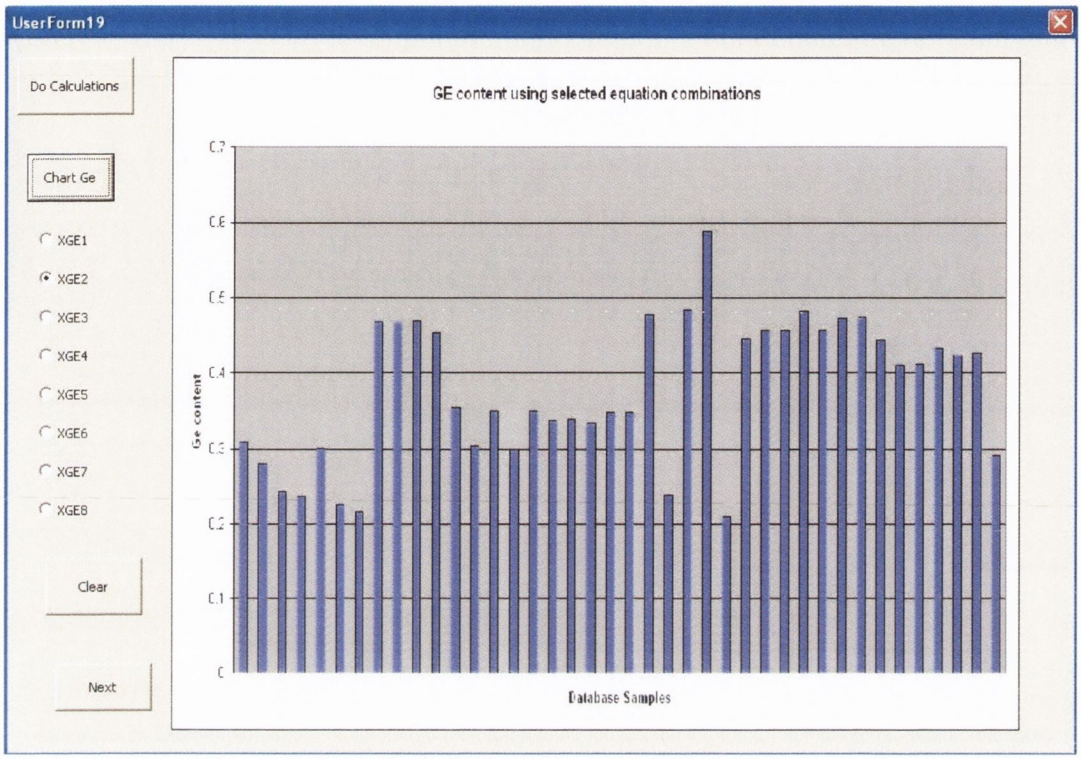


**Fig. 5.11** Userform illustrating the variation of Ge content using Eqn.5.10

Pressing the "Chart Ge" button for varying equations, allows the user to see the variations in Ge value across the sample set. The charts associated with these calculations are automatically displayed in the userform. Similarly, the deviation away from the reference value is calculated and displayed, as shown in Fig. 5.12. This allows the user to see the ability of the relevant equations to track the correct value across a variety of thicknesses for a fixed equation. Again, the deviation can be examined in terms of the equation used in userform19.

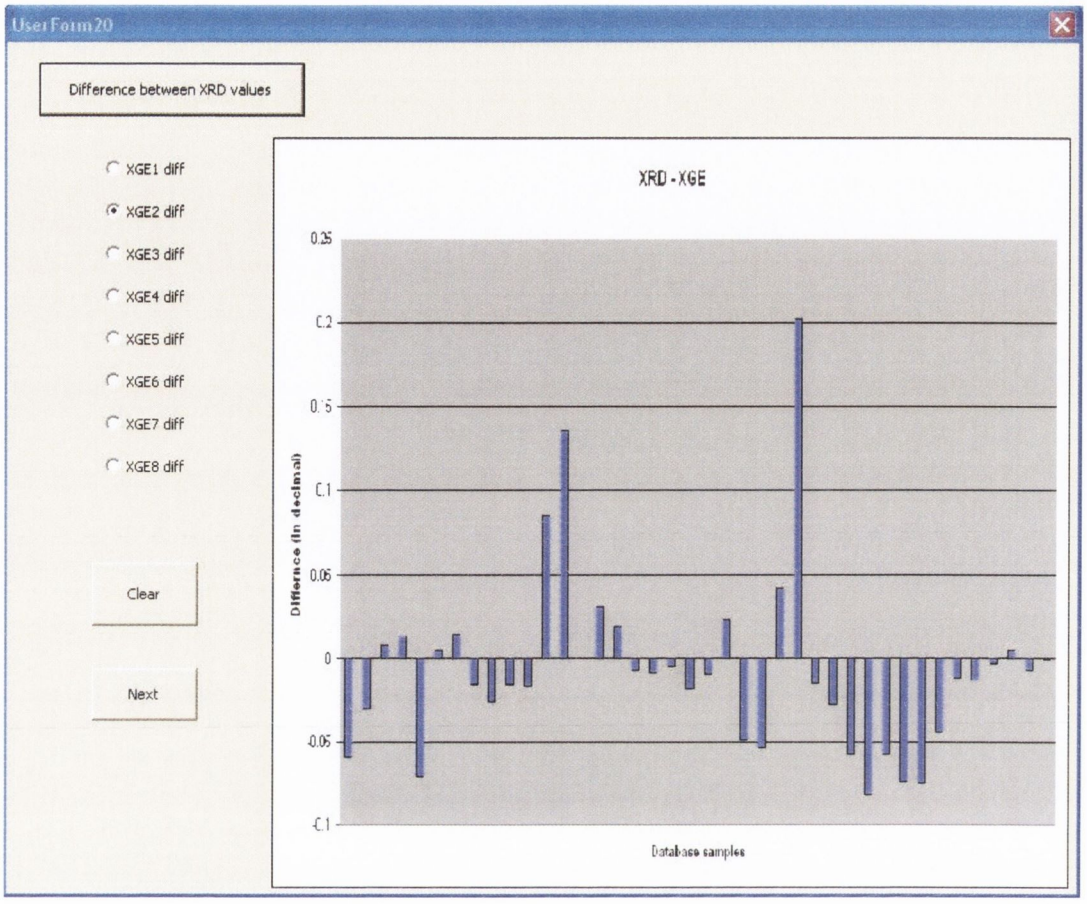


**Fig. 5.12** Userform illustrating the deviation of the Ge value away from the XRD calculated value

From the various userforms presented thus far, it is quite conceivable that more detailed information, relating to particular samples, would be required. Individual samples can be investigated in terms of previously presented parameters, such as Ge content relating to equation choice, as well as associated deviation from the XRD reference value. Fig.5.13 shows the variation in Ge content for sample 773 depending on which equation is selected. The eight points plotted correspond to the eight different equations possible based on the combinations explained earlier. The pink line is a constant line reflecting the XRD value and thereby allowing the user to see the deviation on a sample by sample and equation by equation basis.

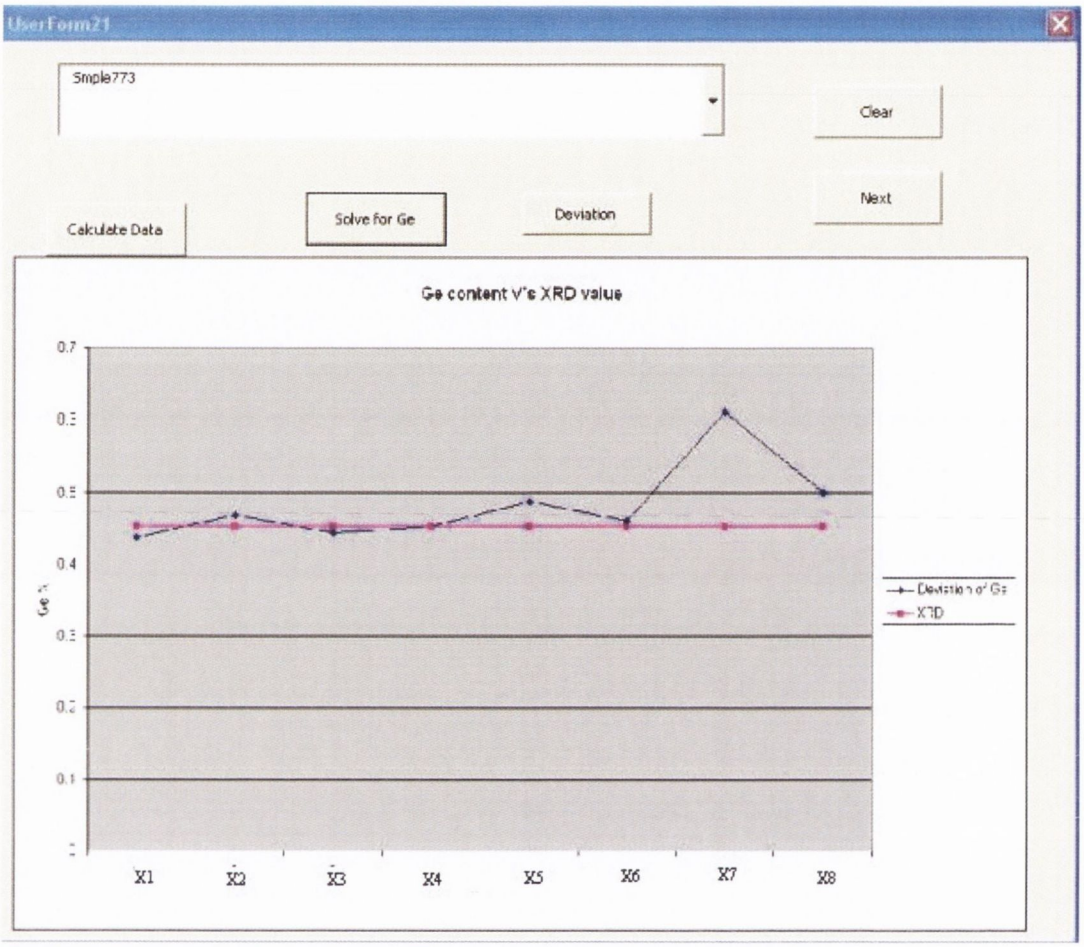


**Fig. 5.13** Sample 773's Ge content and XRD mapped against results for Eqns X1-X8

In order to evaluate the effectiveness of the various equations, it is important also to examine trends that may occur due to the thickness of the sample under investigation. In this way it may be possible to modify equations based on thickness parameters. Fig.5.14 shows the GUI used to browse Ge content and deviation based on a sample set thickness.

(a)

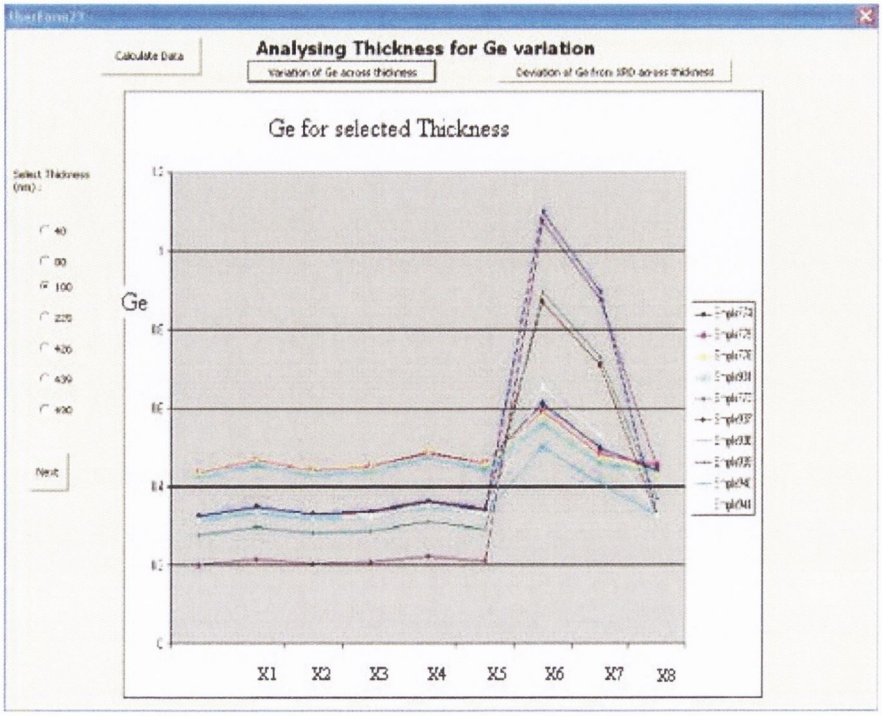


(b)

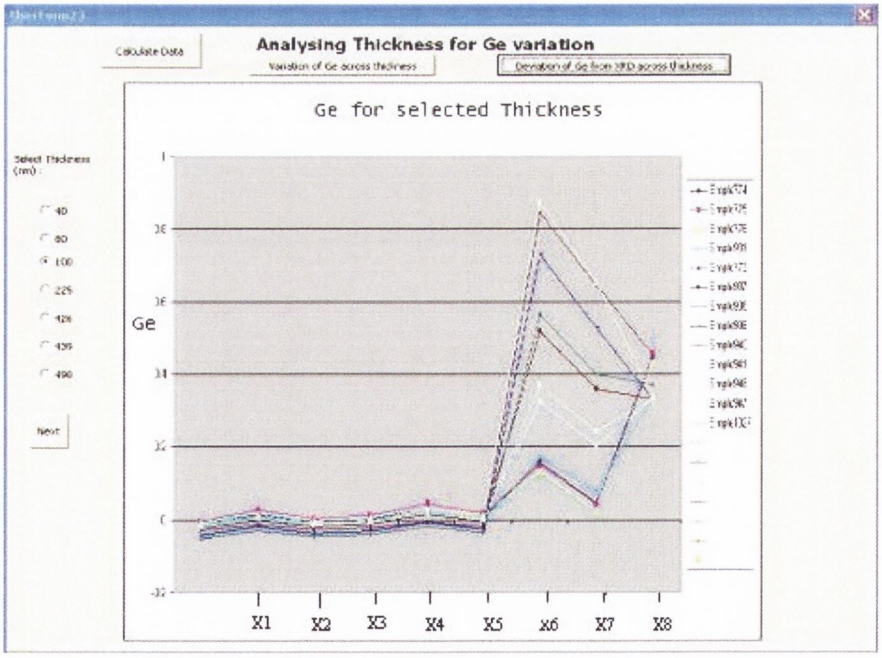


**Fig. 5.14** (a) Ge variation vs Eqns.X1-X8 (b) Deviation across samples with common thickness vs X1-X8

Fig. 5.14(a) illustrates the variation of Ge content, x, across a sample set with a common thickness, in this case 100nm, while (b) shows the deviation being displayed on the same form. The user can select which analysis is made with the associated graph being linked to the active userform. As was shown in Fig. 5.8, the user is allowed the choice of making analysis based on the incorporation or not of strain in the relevant equations. The GUI illustrated thus far is based on the "Strain" box being selected in Fig. 5.8. Similar interfaces exist if "No Strain" had been chosen, with the primary difference being the equation used in the calculation of Ge content and deviation, as explained earlier.

Fig.5.15 illustrates the userform displayed when calculations that remove the influence of strain are used. This userform is very similar to the one shown already in Fig.5.9. All subsequent interfaces are identical to those shown already, with the underlying spreadsheets reflecting the new equations used.

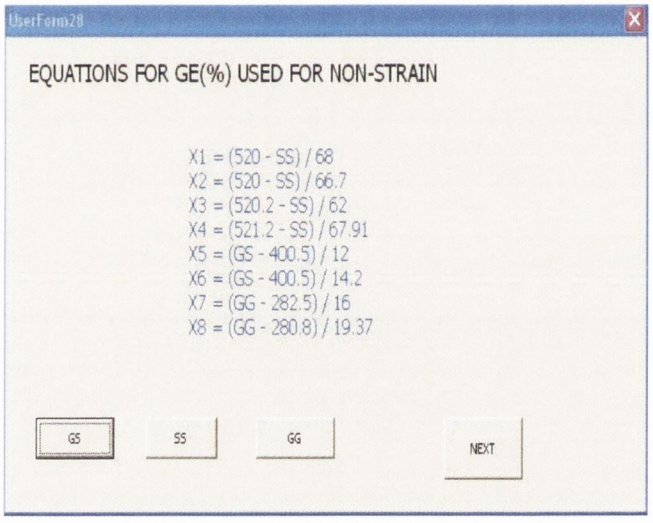


**Fig. 5.15** Userform illustrating the equations used in the absence of strain

The code for the GUI is to be found in the attached CD.

## 5.6 Statistical Analysis

Thin film SiGe buffer layers are not as rigorous in their agreement with earlier equations as thick film buffer layers are. This section identifies modification to the calculated Ge concentration that are necessary in order to move the value closer to independent, and more trustworthy XRD results. As mentioned briefly in the introduction, the dataset of Table 1 in Appendix 1 was subjected to a rigorous statistical analysis using the following flow:

1. Data Mining and Cleaning
2. Single Factor Analysis
3. Multi Factor Analysis

This method is standard in relation to large sets of data and was used with the intention of determining the possibility or not of generating a new equation for Ge compositional measurements.

### 5.6.1 Data Cleaning and Mining

Data cleaning and mining is standard practice in statistical analysis [7]. It involves the manipulation of data into a truer subset, where erroneous measurements or incomplete values are removed from the original profile. This allows results to move towards a steady state and not be influenced by the injection of false values. Table 4 of Appendix 1 shows the modified dataset, with rows having been removed for various reasons, namely:

1. Incomplete data;
2. Widely varying Ge values across the row;
3. Ge values calculated to be greater than 100%.

Data cleaning is typically done in several stages, but because of the relatively small dataset available, only 1 pass is necessary. Data mining is the investigation of available data and the subsequent detection and correction of untrustworthy values. In terms of detection, proper mining procedure involves the correlation of individual cell values within the range of the majority of values. Should issues arise, analysis is necessary to investigate whether spikes or unusual pattern behaviour results from inclusion. Logical checking, such as when Ge is great than 100%, is another step in the cleaning process.

### 5.6.2 Single Factor Analysis

Factor analysis is a mathematical tool which can be used to examine a wide range of datasets [8]. Each value of X (from X1 to X8), as well as thickness, is compared to the benchmark figure generated through XRD. From these graphs it can be deduced whether or not readings (X1-X8) provide additional, independent information. From this, the best datasets are found in which it is felt the plots add some information and help to show trends from which new information can be gleaned.

One can summarise the correlation between two variables in a scatter plot. A regression line is then drawn, which in essence is a line drawn through a scatterplot of two variables. From this trendline the R squared value can be calculated. The R-squared value is the fraction of the variance (not 'variation') in the data that is explained by a regression. The percentage of variance in the dependent variable can be expressed by:

$$R^2 = 1 - \left[\frac{SSError}{SSTotal}\right] = \frac{SSTotal - SSError}{SSTotal} = \frac{SSregression}{SSTotal} \qquad (5.17)$$

Assuming "SS" = Sum Squared error, and that "SS(Total)" means the variance in the data. Shown in Figs. 5.16 to 5.23 is the linear regression for each individual equation, and the associated R squared value and the best fit linear regression equation. This equation describes the adjustments that must be made to the values of X in order for it to more closely match the independently verified XRD value.

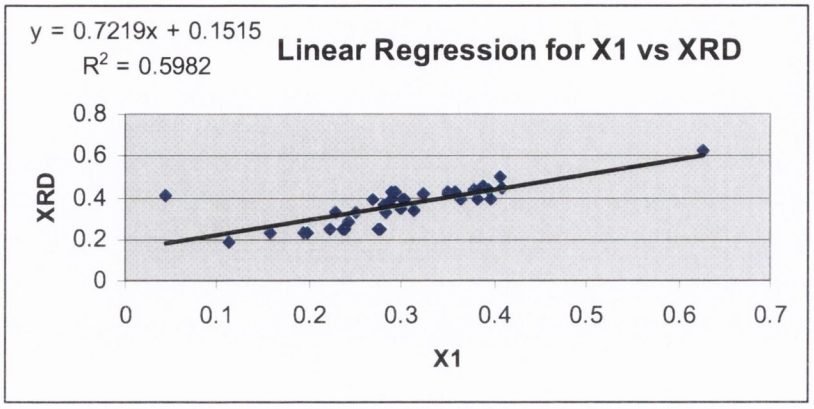


**Fig.5.16** X1 vs XRD with trendline and R squared values shown

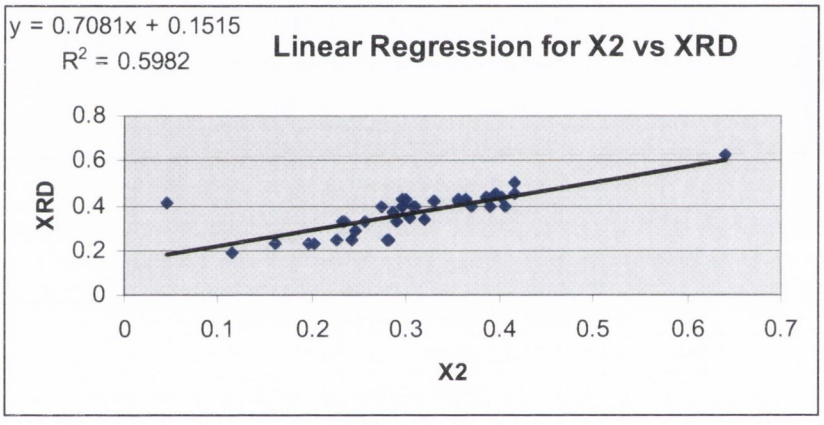


**Fig.5.17** X2 vs XRD with trendline and R squared values shown

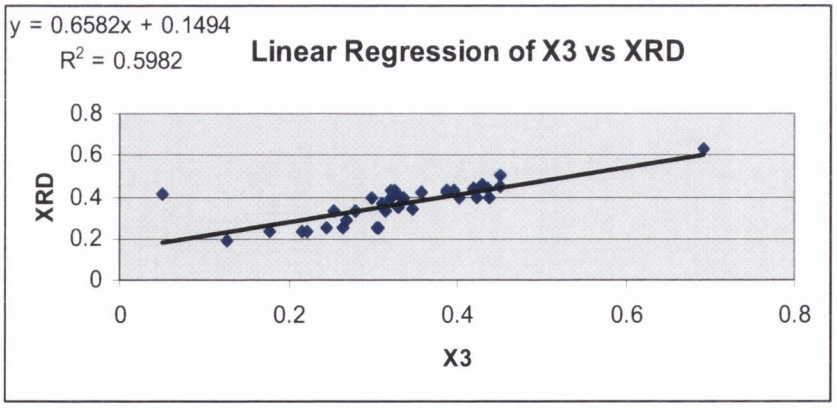


**Fig.5.18** X3 vs XRD with trendline and R squared values shown

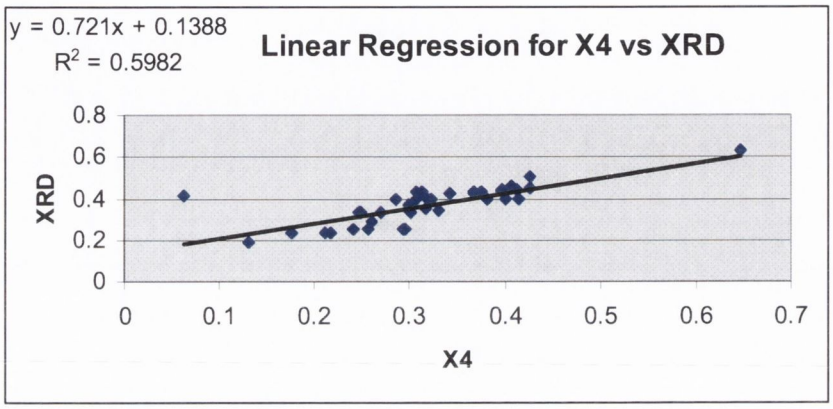


**Fig.5.19** X4 vs XRD with trendline and R squared values shown

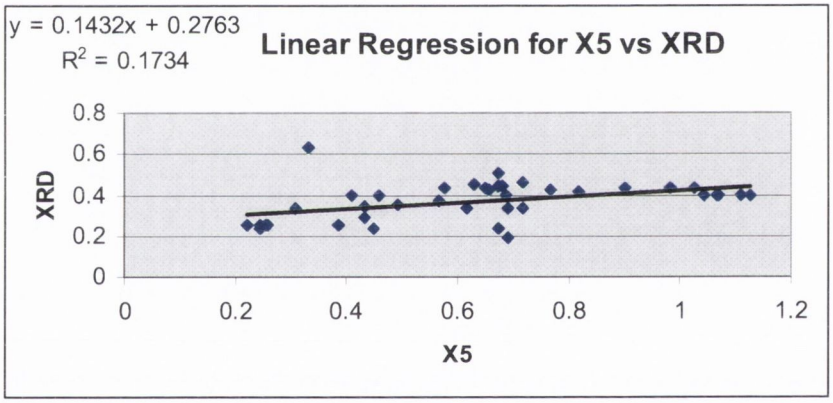


**Fig.5.20** X5 vs XRD with trendline and R squared values shown

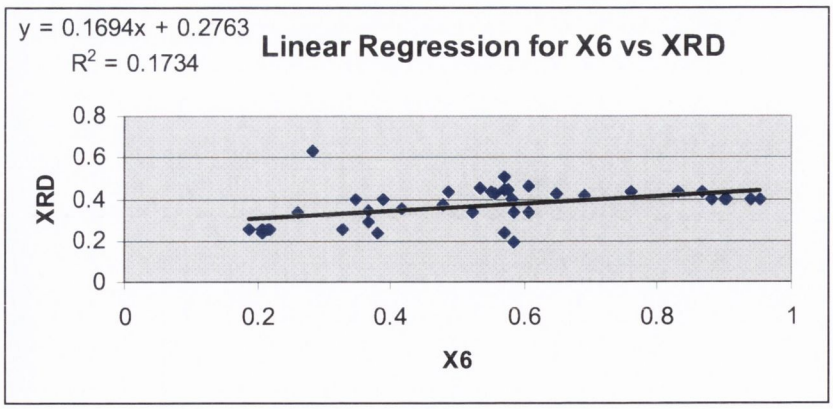


**Fig.5.21** X6 vs XRD with trendline and R squared values shown

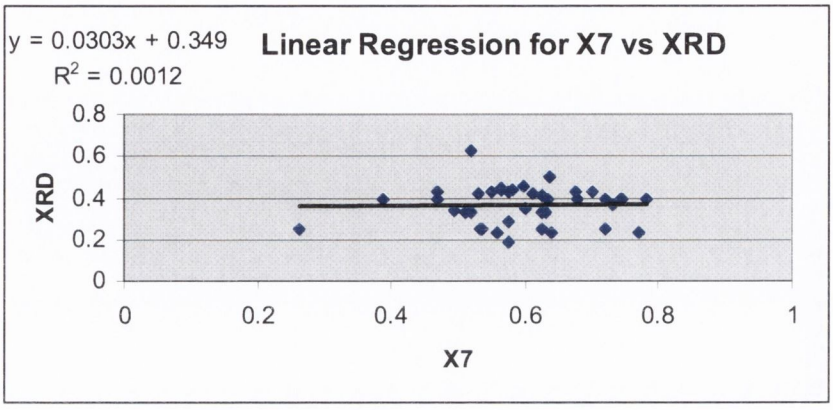


**Fig.5.22** X7 vs XRD with trendline and R squared values shown

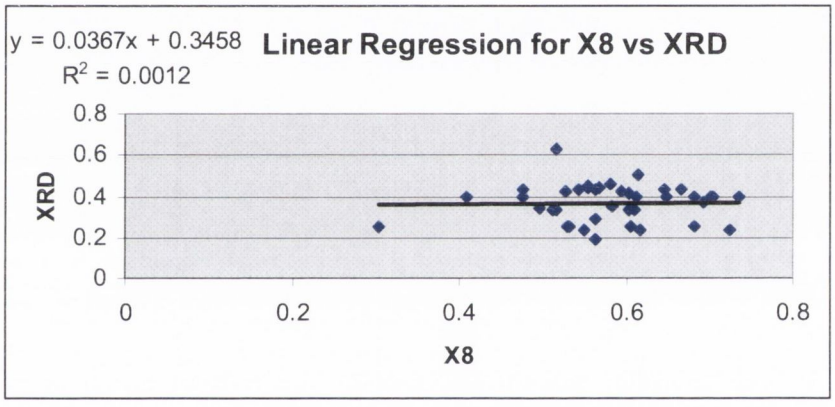


**Fig.5.23** X8 vs XRD with trendline and R squared values shown

From analysis of the various graphs, a trend within the datasets is highlighted. As repetitious data cannot be used in order to extract more information of trends with the dataset, the graphs for X2 to X4 can all be presumed to be represented by the graph of X1. This is due to the similar nature of the linear regression trendline, but also by the R squared value which remains unchanged from one sample to the next. The equation for X5 is seen to change, with an associated variation of the R squared value, as is expected, based on the fact that the phonon positions used to calculate X5 and X6 differ from those used for X1 to X4. The R squared value of X7 and X8, calculated on the position of the Ge-Ge phonon position is very weak. This suggests that there is a weak relationship between X7, X8 and XRD. Therefore, this evidence signifies that X7 and X8 are poor

predictors of the XRD value. As X1 and X5 are shown to contribute information relating to the fitting of measured values of XRD, these datasets are combined, as well as thickness, in Section 5.1.2 in the determination of an overall equation.

### 5.6.3 XGE Data Analysis

Similar to the analysis performed in the earlier section, the dataset relating to those equations that included the influence of strain, that is XGE1 to XGE 8 were investigated. Data cleaning and mining was carried out as before with Table 5 in Appendix 1 showing the result of this analysis. Linear regression was performed as before with a subset of the more important graphs presented below.

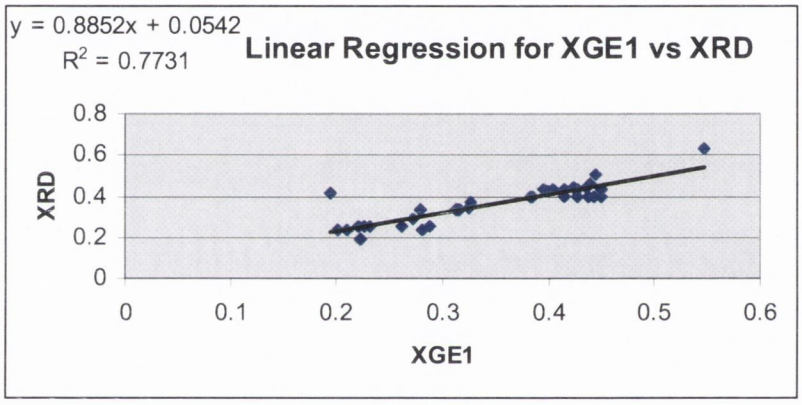


**Fig.5.24** XGE1 vs XRD with trendline and R squared values shown

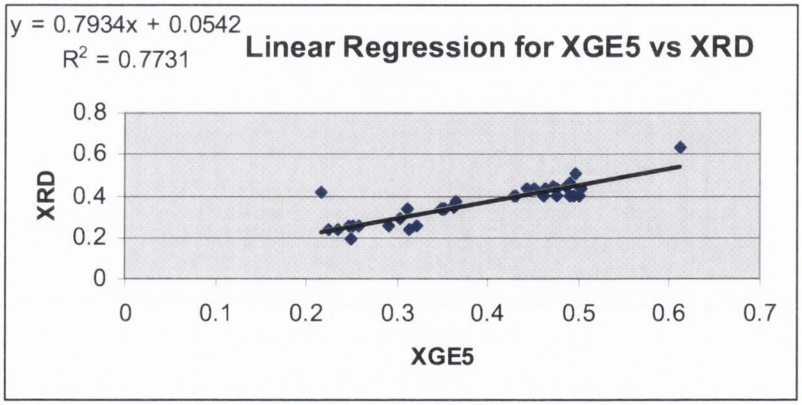


**Fig.5.25** XGE5 vs XRD with trendline and R squared values shown

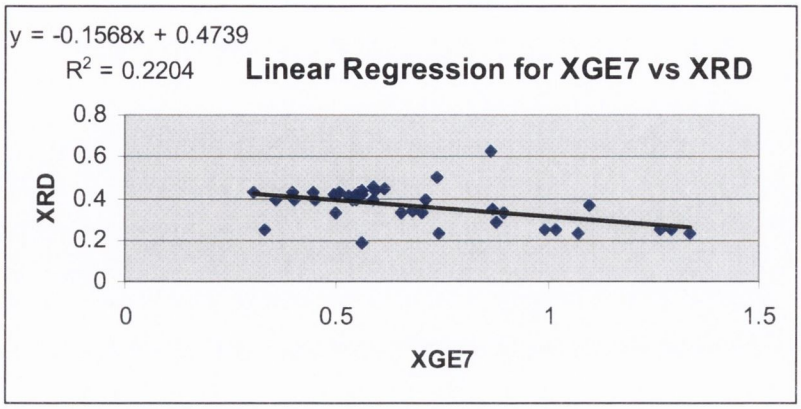


**Fig.5.26** XGE7 vs XRD with trendline and R squared values shown

Fig. 5.25, which shows the regression test for equation XGE5 was chosen as a representative of equations XGE1 to XGE 6, as the reader is now familiar with the procedure. In comparison with results obtained for X5, the regression test reveals no additional impact on the data retrieved from XGE1 analysis, as shown in Fig.5.24, and therefore can be discounted as it is but a subset of the XGE1 data. Analysis of the trendline introduced in Fig.5.26 for XGE7 shows that the results are counter productive as the line is of opposite slope to that of XGE1. As mentioned earlier, data from XGE7 and XGE8 are known to be unreliable so their influence is ignored for the sake of this investigation. Therefore, from limited data, an equation that takes the influence of strain into account and that best fits the XRD results is described by:

$$0.8852x + 0.0542 \qquad (5.18)$$

with an R squared value of 0.7731 (for XGE1). It should be noted that there is an associated variation in the multiplication factor depending on equation source used. This is possibly due to the limited data available and the limited influence of the other five equations on the single factor analysis.

### 5.6.4 Multi Factor Analysis

Following the single factor stage, multi factor analysis is necessary in order to analyse the complementary factors as a single unit [9]. A new dataset has to be generated to take into account the outcome from the single factor analysis. This dataset is shown in Table 5 of Appendix 1, where X1 and X5 are included for reasons presented already. The thickness variable is included so that its impact can be analysed in terms of its contribution to the calculated Ge percentage.

ANOVA (Analysis Of Variance) is a statistical model described by the equation:

$$x_{ij} = \mu_i + \varepsilon_{ij} \tag{5.19}$$

where $x_{ij}$ stands for the value of the response measurement at the $j^{th}$ observation under the $i^{th}$ treatment. The term $\varepsilon_{ij}$ is assumed to be a normal random variable with mean zero and standard deviation $\sigma$ for all measurements. This expression means that an observed response measurement comes from an overall average group, $\mu_i$ plus or minus some random error $\varepsilon$. It is widely accepted that the ANOVA procedure derives from the work of Fisher[10].The table currently used when obtaining output from the ANOVA procedure is quite similar to the original, which consisted of the following four columns:

1. Sources of variation
2. Degrees of freedom
3. Sums of squares
4. Mean squares

The addition of the F-statistic into a fifth column and the corresponding p-values into a sixth column is now common practice [11]. The ANOVA model is outlined below in Table 5.3 as taken from an Excel spreadsheet, with the results included.

**Table 5.3** ANOVA Table

**Multiple Regression Results**

| | Intercept | X1 | X5 | Thickness |
|---|---|---|---|---|
| ***b*** | **0.0679** | **0.70074** | **0.1398** | **9E-06** |
| ***s(b)*** | 0.03533 | 0.08279 | 0.0321 | 7E-05 |
| ***p-value*** | **0.0639** | **0.0000** | **0.0001** | **0.8948** |

**ANOVA Table**

| **Source** | **SS** | **df** | **MS** | ***F*** | $F_{Critical}$ | ***p*-value** |
|---|---|---|---|---|---|---|
| Regn. | 0.19028 | 3 | 0.0634 | 29.574 | 2.9113 | 0.0000 |
| Error | 0.06648 | 31 | 0.0021 | | | |
| Total | 0.25676 | 34 | | | | |

| | | | |
|---|---|---|---|
| | | *s* | 0.0463 |
| $R^2$ | 0.7411 | Adjusted $R^2$ | 0.716 |

### 5.6.4.1 ANOVA Table Explanation

From the ANOVA Table 5.3, the equation that bests describes the ability to modify the X value results to give the appropriate Ge value as measured using XRD is:

$$0.0679 + 0.7004\ X1 + 0.1398\ X5 \qquad (5.20)$$

as described in the first line of the table. Thickness, with a p-value recorded at 0.89 shows that its influence can be ignored in terms of influencing the Ge calculations, as the p-value represents the probability, out of 1, that a term is insignificant. The R-squared value, as outlined earlier, describes how well the curve fits the data, i.e., how much the variance in XRD is explained by our model. With an R-squared value of 0.7411, we can be relatively confident based on the small sample set that our model is good and the equation can be trusted. When the sum of squares (SS) is divided by the degrees of freedom (df), it yields the sample variance. The ANOVA procedure seeks to decompose the total sample variance into the corresponding sources of variation. The value of 0.25676 is referred to as the total sum of squares and is merely the numerator in the familiar formula for the sample variance:

$$s^2 = \frac{\sum_{i=1}^{n}(x_i - x)^2}{n-1} \qquad (5.21)$$

There are 35 resulting values from the experiment and the corresponding degrees of freedom in the ANOVA table is 34, one less than the total number of observations. When the sum of squares is divided by the degrees of freedom, it yields the sample variance. The sums of squares for the input variable effect is 0.19028. Therefore, roughly 70% of the total variation is explained by this effect. Note that this fraction (0,19028/0.25676 = 74%) is used here as the $R^2$ value. This value is a comment on factors that have not been taken into account during the analysis, such as possible variations in:

1. Temperature
2. Growth conditions (MBE/CVD)
3. Data collection limitations

From the table, it is imperative to consider not only the individual sums of squares, but also the amount of information used to obtain the degrees of freedom. The sums of squares for the X values (X1 and X5) and the residual error are weighted by the degrees of freedom in order to obtain a valid comparison. The comparison is illustrated in the column of results in the mean square column (MS) where the sums of squares are divided by the appropriate degrees of freedom. A large ratio of the mean squares (the F-statistic) implies that the amount of variation explained by X1 and X5 is large in comparison with the residual error. For this example the F-statistic is 29.74, with an associated p-value of 0.000.

## 5.7 Validation of Model

It is necessary to take a random selection of input variables, i.e. X1 and X5, in order to justify the proposed equation. The results of such feedback are shown below in Table 5.4.

**Table 5.4** Validation of Model

| Sample Name | Raman Value (using X1) | Raman Value (using X5) | New Equation Value | XRD Value |
|---|---|---|---|---|
| 759 | 0.15868 | 0.45 | 0.24 | 0.23 |
| 760 | 0.19897 | 0.24417 | 0.24 | 0.23 |
| 773 | 0.40779 | 0.63083 | 0.44 | 0.453 |
| 774 | 0.39368 | 0.68083 | 0.438 | 0.441 |
| 936 | 0.29853 | 0.49167 | 0.3457 | 0.35 |
| 1308 | 0.39706 | 0.40833 | 0.403 | 0.4 |
| 1316 | 0.35 | 0.65833 | 0.405 | 0.42 |

As can be seen, results from the new equation map closely those XRD values selected for comparison. Variations in the exact nature of the value from the new equation is dependent on the small sample set used in its generation, as well as limiting factors such as only X1 and X8 contributing to the multiple regression. However, it is clearly evident that the new Ge calculated values are much more closely aligned to exact XRD values than has previously been possible using equations based on thick SiGe buffer layers.

## 5.8 Conclusions

The importance of proper data management techniques was a key factor in the work reported in this chapter. The development of an interactive GUI, developed using VBA, was shown to provide for seamless integration of various aspects of research associated with a single sample. TEM, EELS and micro-Raman results were all readily accessible in an informative and interactive way. Through this technique, it was possible to build a

library of datasets which can be readily accessed by the researcher through a drop down menu. In addition, Excel analysis of Ge composition was made possible. As VBA is linked to an underlying dataset, it was shown that information could be plotted on the GUI that allowed for a more uncluttered investigation of samples. In addition, the calculations themselves were analysed on a sample by sample basis. The inclusion of strain as a determining factor in the calculation of Ge composition was also investigated. The patentable and potentially commercially viable GUI was developed to allow users to interact with data dependent on the inclusion of strain or not in micro-Raman analysis. XRD results were used as a benchmark for comparative purposes, which allowed one to investigate the pertinent deviation between calculated and actual results. This deviation was then plotted for a range of samples with similar thickness, allowing for a quick intuitive review of sample behaviour.

Thin film SiGe buffer layers were examined in terms of their relationship with experimental equations developed for thick layered SiGe buffer layers. The procedure used was based on any correlation that existed between Raman and XRD values examined under linear regression. For the very first time, a new equation:

$$0.0679 + 0.7004\ X1 + 0.1398\ X5$$

was proposed to provide a more accurate measure of Ge concentration in thin SiGe layers, based on previously defined micro-Raman experimental equations developed for thick SiGe layers. This has potentially huge significance in the ability to quantify more accurately the elemental concentration in thin layers suitable for monolithic integration. In terms of statistical certainty, the suggested equation was subjected to a validation procedure using 7 randomly selected samples with an average accuracy of ~98%. Future work would include these and other variable parameters.

In addition, what has been conclusively shown is that sample thickness has no bearing on the accuracy of equations used in the calculation of Ge content. Equations defined as giving solutions identified as XGE1 to XGE8 were also investigated and a linear fit analysis revealed a more suitable equation in terms of XRD values. A more thorough analysis of this work is to be pursued under an Enterprise Ireland 'Proof Of Concept'

grant. Results reported in this chapter have proven to be extremely important for thin film buffer layers as it has been clearly shown that results obtained from equations developed for bulk layers must be modified to produce a more accurate value for Ge concentration.

**References**


1. 1. Z. Lacroix and T. Critchlov, '*Bioinformatics: Managing Scientific Data*', Morgan Kaufmann, (2003)
2. The French National Institute for Research in Computer Science and Control, INRIA, ATLAS : *Complex data management in distributed systems*
3. http://msdn.microsoft.com/isv/technology/vba/default.aspx
4. M.A.Renucci, J.B.Renucci, and M.Kardona, *Light Scattering in Solids*, edited by M.Balkanski, Flammarion,Paris,p326, (1971)
5. M.I.Alonso and K.Winer, *Phys.Rev.B*, **39**, 10056 - 10062 (1989).
6. J. C. Tsang, P. M. Mooney, F. Dacol, and J. O. Chu, *J. Appl. Phys.* **75**, pp. 8098-8108(1994)
7. Paolo Giudici, '*Applied Data Mining: Statistical Methods for Business and Industry (Statistics in Practice)*', ISBN 0-470-84679-8, Wiley , 2003
8. Harry Harman, '*Modern Factor Analysis*', University of Chicago Press, ISBN 0226316521, 1976
9. http://ocw.mit.edu/NR/rdonlyres/Sloan-School-of-Management/15-062Data-MiningSpring2003
10. R.A. Fisher, '*Statistical Methods for Research Workers*', published in Edinburgh by Oliver and Boyd, (1925)
11. H.R. Lindman, '*Analysis of variance in complex experimental designs*'. San Francisco: W. H. Freeman & Co, (1974)

# Chapter 6

# Strained Si Quantum Wells

## 6.1 Introduction

The future of devices made at the nanoscale is promising. The ability to harness the benefits of such structures provides an opportunity for new and as yet unknown possibilities in a variety of disciplines. Advances made to date in conventional Si based platforms may have to be updated or completely revised when considering nanomaterials. In many ways this is reminiscent of solid state physics research in around 1950. Scientists are making gains in understanding the fundamental properties of these new systems; simultaneously they are making laboratory demonstrations of possible technological spin-offs [1]. Research is still essentially at the embryonic stage, with significant potential for development in both the academic and industrial sphere. Some nanoscale technologies however are already beginning to permeate into the marketplace. For example, semiconductor lasers used in CD players and in fibre optic communication systems contain nanoscale structures called quantum wells [2]. These quantum structures have led to low cost and improved product performance.

In order to realise devices such as quantum wells or Ge nanowires, new and varied methods of growth and fabrication are currently being investigated due to the constraints of working at this geometrically challenging scale. Because of the associated reduction in size, it is envisaged that nanodevices will offer greater functionality and less power usage as compared with current products. Working at the nanoscale level may lead to unprecedented products in electronics, biotechnology, medicine, transportation, national security and other fields [3]. In line with such possibilities, this chapter focuses on strained silicon quantum wells. The structure is analysed in terms of both composition and strain using a variety of spectroscopical tools.

## 6.2 Strained Silicon Quantum Wells

In recent years Si/Ge quantum heterostructures have attracted considerable attention due to extensive progress in the growth technology, the considerable improvement in heterostructure quality, and their potential compatibility with the silicon based electronic industry needs. Quantum wells are emerging as a new and exciting material in the area of thermal and sensing applications. Using a Si/SiGe quantum well, their exists an easy route to integration, the importance of which is discussed in detail in Chapter 4, as well as potential for far-infrared detection (>20μm) [4]. In line with this, it is important that such a material is understood in terms of optimum growth conditions as well as the associated impact on dislocation density. This provides the motivation behind the research reported here on strained Si QWs.

Two main features characterise the SiGe semiconductor material system.
The first feature is the indirect energy gap of both Si and Ge. The second one is the distribution of the band-gap energy difference between the two materials, which takes place mostly within the valence bands [5, 6]. Thus, in a typical SiGe/Si heterostructure interface the bottom indirect conduction bands from both sides of the interface are nearly aligned, and the valence bands are considerably offset.

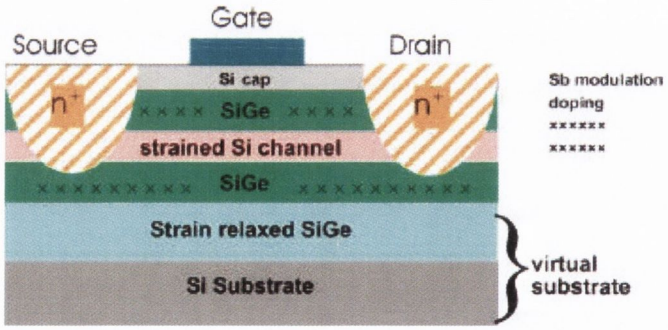


**Fig. 6.1** Schematic cross-section of an nMODFET structure (xxx identifies areas of Sb modulation doping) [5].

A quantum well is a semiconductor structure in which an electron is sandwiched between two barriers so that its motion is confined to two dimensions. Fig.6.1 illustrates an nMODFET device with the active structure containing a buried strained Si channel which

acts as a quantum well for electrons, inserted between two modulation doped relaxed SiGe layers [7, 8]. While this work investigates the different growth strategies possible for QWs, it is useful that some background information is provided as to what exactly a quantum well is and how it operates. Several websites and tutorials exist, and a brief synopsis of one [9] presented below.

As Frensley states [10], if one makes a heterostructure with sufficiently thin layers, quantum interference effects begin to appear prominently in the motion of the electrons. The simplest structure in which these may be observed is a quantum well, which simply consists of a thin layer of a narrower-gap semiconductor between thicker layers of a wider-gap material [11]. The band profile then shows a ``rectangular well,'' as illustrated in Fig. 6.2.

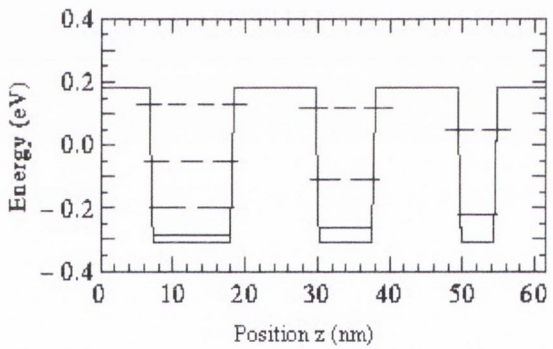


**Fig. 6.2** Energy-band profile of a structure containing three quantum wells, showing the confined states in each well [12].

The gaps in the lines indicating the confined state energies show the locations of nodes of the corresponding wavefunctions.

The electron wavefunctions in such a well consist of a series of standing waves, such as might be found in a resonant cavity in acoustic, optical or microwave technologies. The energy separation between these stationary states is enhanced by the small effective mass of electrons in the conduction bands of direct-gap semiconductors. With advanced epitaxial techniques, the potential profile of the quantum well need not be rectangular. Because the band-edge energy is usually linear in the composition, the conducation and

valence energy level will follow the functional form of the composition. The quantum states in two parabolic wells are illustrated in Fig. 6.3.

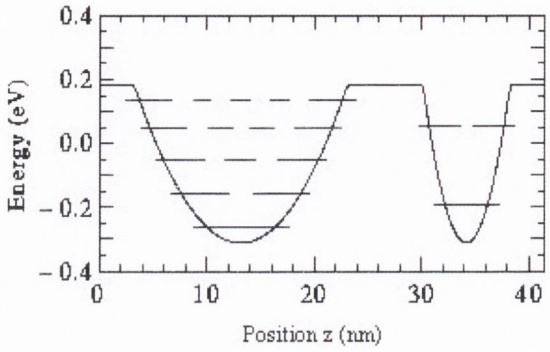


**Fig. 6.3** Energy band profile of a structure containing two parabolic quantum wells [13]

In a quantum well, the SiGe region with a smaller energy gap is where the light is generated due to radiative recombination of the injected carriers; thus it is called the active region. Other pairs of semiconductors may be used, but all require a smaller energy gap active region with larger energy gap cladding layers. Also, to prevent non-radiative recombination at the heterojunction interphases, the active layer and the cladding layers must have the same lattice constant. Electric current travels through the layers in the form of moving negatively charged electrons and positively charged holes. The middle layer acts as a pit, called a quantum well, which the electrons either overshoot or fall into. When an electron falls into a hole, it gives up energy in the form of a photon, a bundle, or quantum or light. A photon vibrates with a frequency equal to its energy divided by a number called Planck's constant. According to the laws of quantum mechanics that govern the emission of photons, electrons in an object can emit photons that have only certain special amounts of energy. Furthermore the number of possible amounts of energy and the amounts themselves given up by electrons as they fall into an object depend upon the size of the object. In other words, the smaller the size of the object, the smaller the number of possible energies.

The enhanced performances with tensile strained Si layers are associated with increased electron confinement at the heterointerface between Si and SiGe and to the splitting of the degeneracy of the conduction valleys. The enhanced carrier mobility in tensile

strained Si channel layers allows the development of high performance MOSFETS. These structures have been developed through the use of MBE and UHV–CVD systems [14-18]. This chapter investigates strained silicon quantum wells (SSQWs) on top of thin, abrupt virtual substrates. Thin virtual substrates are considered important in terms of monolithic integration. The virtual substrate consists of a silicon substrate and a strain relaxed SiGe buffer (SRB). Important parameters to be considered include the degree of relaxation present as well as the threading dislocation (TD) density.

## 6.3 Sample Growth

Two samples, C2971 and C2972, were grown at the University of Stuttgart in collaboration with E. Kasper and K. Lyutovich, in order to investigate the impact of using either a thin, low temperature virtual substrate on a Si buffer or a step like SiGe layer in the growth of a Strained Si Quantum Well (SSQW). The impact of different growth techniques can be seen in terms of the TD density present throughout either device. Both samples had a rather high Ge content (40%) which can lead to potential stress values of up to 6 GPa.

| Si Cap 5nm |
|---|
| 20nm SiGe (40% Ge) |
| 9nm Strained Si |
| 200nm SiGe (40%Ge) |
| Si substrate |

(a) Structure schematic for C2971

| Si cap 5nm |
|---|
| 20nm SiGe (40% Ge) |
| 9nm strained Si QW |
| 200nm SiGe (40% Ge) |
| LTVS 160 $^{O}$C (15+25) nm |
| Si substrate |

(b) Structure schematic for C2972

**Fig. 6.4**

Sample C2972 has an extremely thin (40nm) low temperature virtual substrate (LTVS) with the SSQW sandwiched between SiGe barriers of constant composition, as detailed in Fig. 6.4(b). Sample C2971, on the other hand, contains a SiGe layer with no LTVS present, as shown in Fig. 6.4(a). For technological reasons, both structures are capped by a thin Si layer (5nm). Molecular Beam Epitaxy (MBE) was used in the growth of the two distinct samples. It must be noted that for sample C2972 the growth was interrupted, with

the wafer being removed and cleaned again after the initial 200nm SiGe layer, with Ge composition of 40%, having been deposited. This was done to investigate the transfer of virtual substrates to other processing groups. Both samples C2971 and C2972 were prepared for TEM analysis in the usual way, with dimpling and ion milling.

As discussed earlier, a Si quantum well nominally consists of three or more different planar layers on a silicon substrate in which the doping and/or the germanium content are varied [19]. The top four thin 'active layers', as shown in Fig. 6.4(b), are:

1. the undoped silicon capping layer;
2. a $Si_x Ge_{1-x}$ supply layer (this layer is generally called the supply layer);
3. the strained silicon well;
4. an underlying $Si_{1-x} Ge_x$ layer.

The supply layer acquires this name, as a higher channel occupation and a related threshold voltage shift can be achieved by doping this layer. The well itself is formed by the conduction band offset in tensile strained silicon as compared with the $Si_{1-x}Ge_x$ [20,21].This allows electrons to be separated from their ionised dopant atoms and collected.

The tensile strain is produced by the virtual substrate present in both samples, with sample C2971 utilising the underlying barrier layer as the virtual substrate. For $Si_xGe_{1-x}$ /Si virtual substrates to be effective in the growth of materials such as SSQWs, it is important that they first meet the essential requirements, as detailed in earlier chapters and summarised by Kasper et al([6]), such as:

1. high Ge content causing a corresponding strain in the Si channel;
2. high degree of strain relaxation which provides lattice constants equivalent to the composition and stable device parameters during and after the processing, as expressed by:

$$a_{SiGe} / a_{Si} = (1 + fR) \qquad (6.1)$$

where a is the lattice constant, f is the mismatch, and R is the degree of relaxation;

3. smooth surface with low roughness as well as low defect density preventing electron scattering in the overgrown channel and making the processing reliable;
4. low thickness, a desired parameter for easy integration with other devices in ICs as well as for better heat dissipation in the devices and for less energy consumption during the buffer layer production.

In order to overcome these problems and to enable the fabrication of ultra thin, highly relaxed, device quality SiGe buffers with a high Ge content, an approach has been developed that intentionally introduces point defects. This follows on from earlier work by Kasper and Lyutovich [22], the fundamental principles of which are explained here. It is expected that point defects introduced in the metastable SiGe layer will initiate strain relaxation using misfit dislocations. This work focuses on developing this technique further using point defect generation through a two stage low temperature process and then comparing the results, using a variety of techniques, against a sample grown using a more traditional method. A high super saturation of point defects will lead to their condensation and to the formation of prismatic dislocation loops, mostly near the interface. Furthermore, interaction between point defects and dislocations will support the climbing of dislocations and, in this way, increase the probability of the annihilation of threading dislocations with opposite Burgers vectors. Point defects can be introduced into the layers in different ways–growth at low temperatures, ion bombardment, surfactant mediated growth, etc. [23]. The thickness of the first part of the buffer layer with the high point defect supersaturation should exceed the equilibrium critical thickness, given by the Matthews–Blakesley curve [24] for the corresponding SiGe composition, and lie in the area of metastability. At the second stage, growth continues without point defect introduction until the total layer thickness slightly exceeds the non-equilibrium critical thickness [25]. At this stage, point defects should promote both early onset and high degree of strain relaxation. Point defects also interact with arising dislocations and may contribute to the formation of a layer with a smooth surface morphology and lower defect density. The main function of the first growth stage is to serve for the generation of

necessary point defects and to accumulate them in the layer. The generation of point defects is carried out by reduction of the growth temperature to a very low one. Decreased nucleus mobility at very low temperature growth causes a high super saturation of point defects during layer formation [23]. The growth temperature is already reduced during the deposition of a Si buffer and reaches the given value at the beginning of the SiGe growth. The first growth stage of SiGe with very low temperature runs until the equilibrium critical thickness for the chosen composition is exceeded.

## 6.4 TEM Investigation

At a variety of different magnifications and angles of tilt, TEM was used to analyse both samples. Using this technique, layer interfaces, misfit dislocations and threading dislocations throughout the structures were investigated. Fig. 6.5 shows a Bright Field TEM image of sample C2971, showing the distinct layers present. A low TD density is clearly present in the SiGe layers with a small number of MDs found at the SiGe/ Si substrate interface. Subsequent TEM images at a variety of tilt angles revealed similar results.

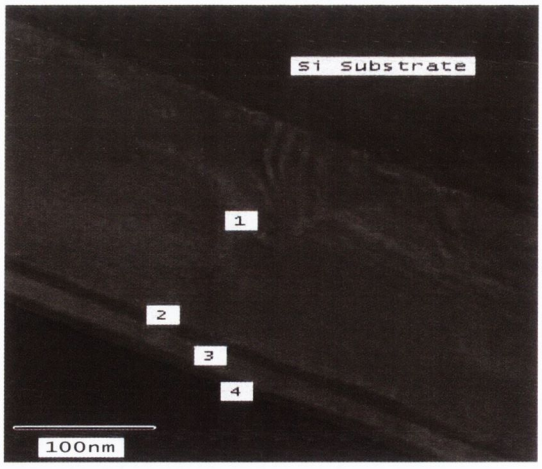


**Fig. 6.5** Bright Field C2971 TEM image, with 5 distinct layers: Silicon Substrate, (1) 200nm SiGe layer, Ge 40%, (2) 9nm Strained Si, (3)20nm SiGe (40%), (4) 5nm Si cap.

Though TDs are present in the SiGe layer, their density is low, with terminations either in the prepared TEM foil, as indicated in Fig.6.6 by TD1 or in the SiQW, as shown by TD2. This TEM image is in marked contrast to the Bright Field image for sample C2972 as shown in Fig. 6.7 which highlights the high threading dislocation density running from the Si/SiGe interface all through the structure. The contrast in TEM imagery is due to sample growth, with sample C2972 using a 40nm thick LTVS, while C2971 does not. In the case of C2972, the TD density is very high, moving from the interface of the Si bulk right across the layers. Various points are marked off along the micrograph of Fig. 6.7 and can be explained as follows. In the growth of sample C2972, two MBE setups were used. After the very low temperature growth stage and with a total thickness of 200nm in the initial MBE system, the wafer was unloaded and given an additional pre-epitaxial cleaning. The sample was then loaded into the second MBE setup, where a SiGe layer was overgrown with the final QW structure. Line 2 in this image is the boundary caused by this reloading. Line 1 is due to the epitaxial cleaning stage. The strained Si QW is located at point no. 3 while the cap is found at point no. 4.

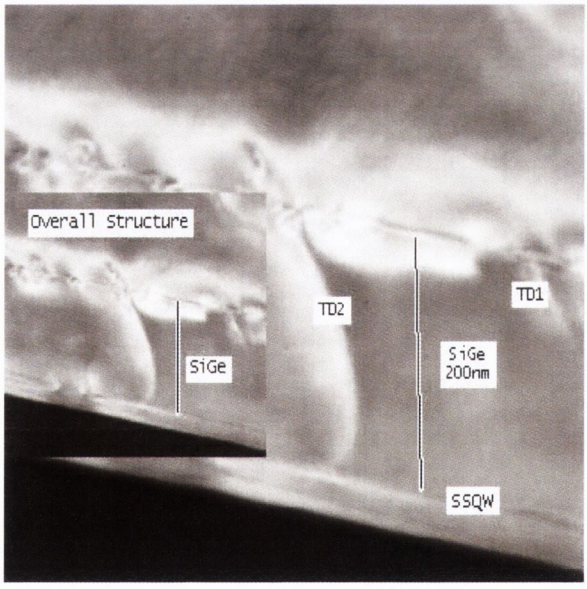


**Fig. 6.6** Bright Field Image of C2971 focusing on TD, with overall image inserted also. Different TDs are seen running through the SiGe layer.

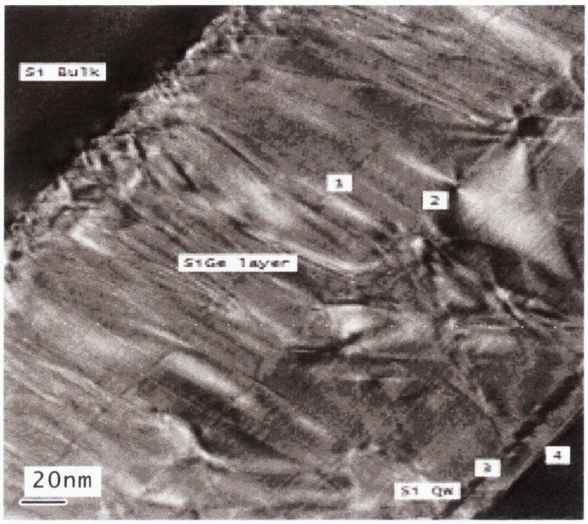


**Fig. 6.7** TEM image of C2972 indicating the TDs present throughout the layers

The TEM image of C2972 shown in Fig. 6.7 clearly shows the high density of threading dislocations present in the material. TDs dominate the material layers due to the high stress caused by LTVS stage in wafer growth.

## 6.5 EELS Analysis

Using EELS mapping it is possible to determine the compositional map of the material as well as the percentage of materials present using a 'ratio of counts' technique. However, in order for this approach to be suitable, the TEM foil thickness should be constant. The disparity in counts moving from left to right in Fig. 6.8 is indicative of the influence of the foil thickness on the measured data. As detailed in Chapter 4, a thickness per wavelength scan is run which, when taken into account allows percentage compositional values to be calculated. In EELS, both L and K edge filtering is possible for Si and Ge materials. Both were used initially to establish the most suitable operating environment for the samples under investigation. However, switching to the K edge Si excitation gives us a clearer picture that is less influenced by the topographical nature of the specimen. The K edge is at 1869eV while the window used was 60eV. Similarly, for Ge, K edge mapping was performed.

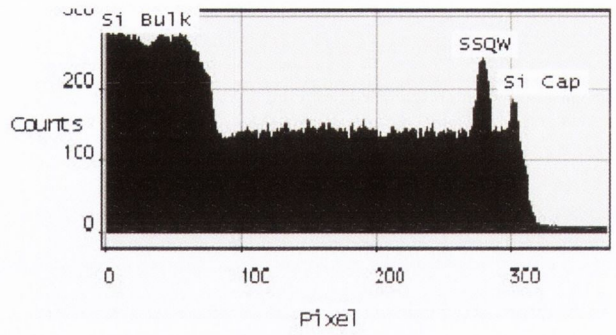


**Fig. 6.8** Sample C2971 EELS Si profile going from bulk to cap.

The elemental profile map of Fig. 6.8 is performed moving across the sample from the bulk to the top layer. As indicated, the count value on the left side of the image corresponds to bulk Si, while the decrease in the count value while mapping across the SiGe layer corresponds to a reduction in Si levels, where a Si content of 60% is recorded, in line with expected values. The two peaks on the right hand side of Fig. 6.8 are indicative of the Si well and Si cap respectively. The valley between these peaks corresponds to the presence of the 20nm SiGe layer with Ge composition of ~40%.

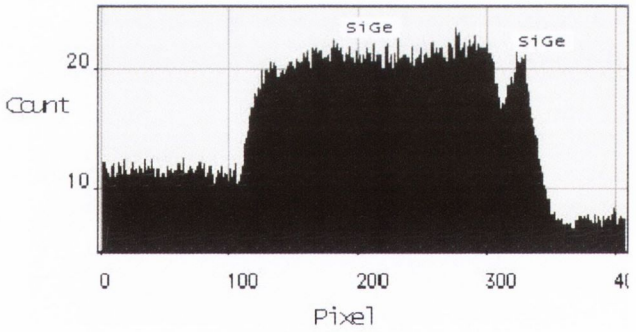


**Fig. 6.9** EELS Germanium Profile moving from bulk to cap.

Similarly for Ge compositional analysis an EELS profile was developed, as shown in Fig. 6.9. The profile is a raw profile map ignoring the influences of thickness but once again a clear pattern emerges. Moving from the bulk area, the Ge profile increases (as expected) as the mapping moves across the SiGe layer, and reduces again when the Si QW is encountered (at pixel = 300 approx). The top SiGe layer is clearly present as indicated by the peak after the QW. Conversion of data from pixel into actual real dimensions is a

straightforward process. The actual thickness of the layers is in good agreement with the nominal one. Again, this information is cross-checked and verified using HREM.

Similarly, for sample C2972 an EELS map was developed that allows us to determine the materials present, as well as indicating both size and compositional ratios. A K edge filter was used for both Si and Ge profile mapping and the results are interpreted below. Fig. 6.10 shows a Si profile map of C2972, moving from the Si cap into the bulk, in contrast to the setup used for C2971.

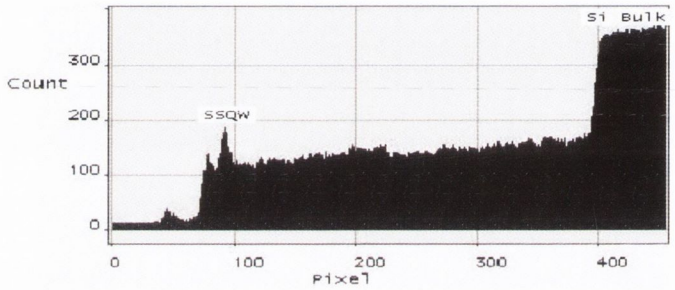


**Fig. 6.10** Si (K edge) Profile map for C2972.

Moving from left to right in Fig. 6.10, two distinct peaks indicating the Si cap and SSQW, as well as the dominant feature of the bulk are noted. The composition of layers in between these peaks is determined using an EELS Ge profile map, shown in Fig. 6.11.

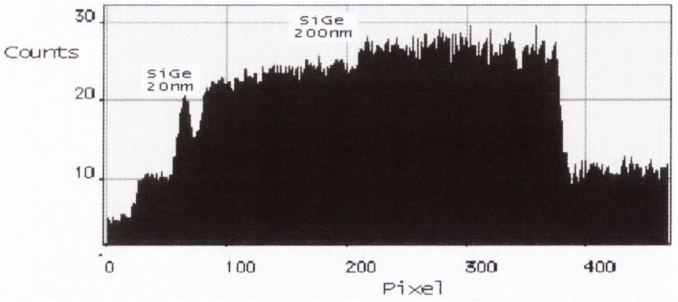


**Fig. 6.11** EELS Ge map, moving from cap to bulk.

Noise peaks and thickness influences are subsequently removed to give accurate data readings. The determination of sample composition is clearly evident from the EELs profile maps. Following image filtering to remove the spurious effects of foil thickness

and measurement noise, the various layers widths were calculated, as detailed in Section 4.10 of Chapter 4. The Si cap of both samples was measured at 6nm, in very good agreement with the expected 5nm width, while the QW was measured at 10nm for sample C2971 and at 11nm for sample C2972, again in good agreement with expected values. The slight variation in measurements is accounted for in parts due to the difficulty in clearly identifying the exact position of the interface between the layers. Similarly, the SiGe layer widths present within the sample were found to be in good agreement with expected results.

Thus, the SSQWs have been analysed in terms of their respective thicknesses, TD density, and composition. These parameters are critical in the growth of application based quantum wells. What is to be noted is that the novel growth technique is at this stage unrefined due to the high density of dislocations that permeate through the sample. Future work will look at investigating different growth temperatures as well as different thicknesses. However, for the two samples investigated, it is important to try and understand how the low temperature layer influences the relaxation levels. This is done using micro-Raman measurements to calculate both relaxation levels, as well as providing independent confirmation of Ge content.

## 6.6 Micro-Raman Spectroscopy

From equations presented in Chapter 2, and using $x$=0.4, it can be estimated that the laser light will penetrate through the four active layers of the samples. Raman spectra, as shown in Fig. 6.12, underscore this estimation, with all peaks associated with relevant layers present. The Si-Si peak at 520cm$^{-1}$, corresponding to the substrate, is more pronounced in sample C2971 due to the difference in structure of the layers beneath the Si QW. However, the intensity of this peak for sample C2972 is significantly smaller than can be expected from the presence of the additional 40 nm thick $Si_{0.6}Ge_{0.4}$ layer. It is believed that this is due to the high density of dislocations found in C2972 which causes additional loss of light within the sample.

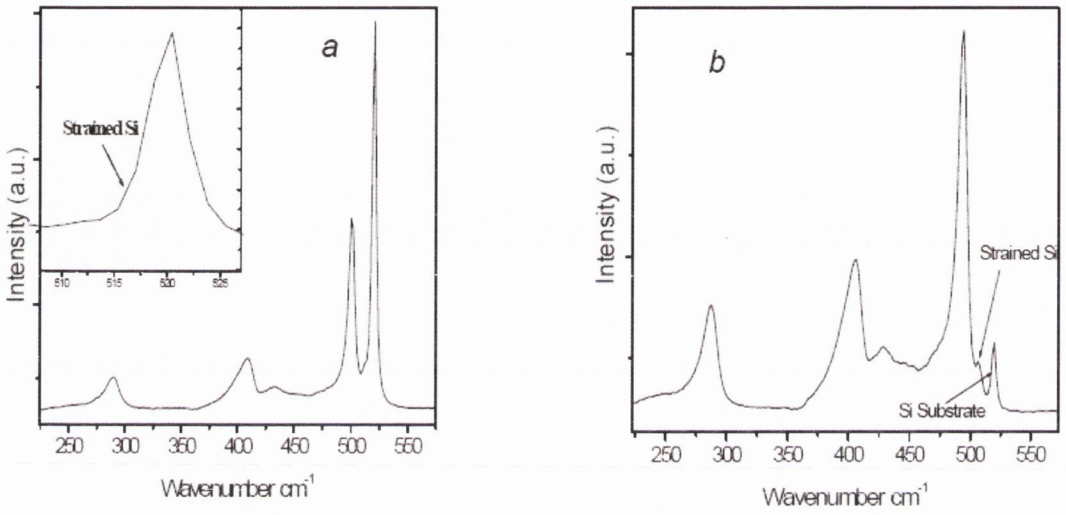


**Fig.6.12** Raman spectra of Sample (a) C2971 and (b) C2972

Analysis of these sandwich type structures using Raman spectroscopy is not trivial due to the reciprocal influence of neighbouring layers. Careful curve fitting and the making of certain assumptions is necessary in order to extract relevant information. In particular, it must be assumed that the major contribution to the phonon lines from the SiGe layer originates from the $Si_{0.6}Ge_{0.4}$ layer beneath the Si QW, since the thickness of this layer is much greater than the thickness of all other SiGe layers in the structure. A similar approach is follower with regard to the Si QW layer which is nearly twice as large as the strained Si cap layer. Stress,$\sigma$, in the Si cap was estimated from the position of Si-Si phonon mode using the expressions outlined earlier in this work and stated once more for the reader's convenience:

$$\sigma=\Delta\omega/4x10^{9}\ \text{Pa}, \tag{6.2}$$

while strain, $\varepsilon$, was determined by the following very good estimation:

$$\varepsilon = \left|\Delta\omega_{Si,\exp}\right| / \left|\Delta\omega_{Si,\max}\right| \tag{6.3}$$

and

$$\left|\Delta\omega_{Si,\max}\right| = |b| \cdot [a_0(x) - a_0] / a_0 \tag{6.3}$$

$$a_0(x) = 0.5431 + 0.02x + 0.0026x^2 \tag{6.5}$$

where $\Delta\omega_{Si,exp}$, is the measured Raman shift, b=930 $cm^{-1}$ the strain-phonon coefficient and $a_0$=0.5431 nm the lattice constant for unstrained Si. The relaxation factor, R, is calculated from the equation:

$$R = \frac{\Delta\omega - 29.7 \cdot x}{70 \cdot x - 29.7 \cdot x} \tag{6.6}$$

The results of measurements made from both the Raman spectra and the equations listed above are outlined in Tables 6.1 and 6.2.

**Table 6.1** Raman Spectra Measurements

| Sample | $\omega_{Si}$ substr. | $\omega_{Si\text{-}Si}$ | $\omega_{Si\text{-}Ge}$ | $\omega_{Ge\text{-}Ge}$ | Correction | $\omega_{Si\text{-}SiCor}$ | $\omega_{Si\text{-}GeCor}$ | $\omega_{Ge\text{-}GeCor}$ |
|---|---|---|---|---|---|---|---|---|
| C2971 | 520.078 | 500.342 | 408.59 | 289.369 | -0.078 | 500.42 | 408.668 | 289.447 |
| C2972 | 520.055 | 495.405 | 405.78 | 286.863 | -0.055 | 495.46 | 405.835 | 286.918 |

**Table 6.2** Summary of Calculations

| Samples | $\omega_{Si}$ of top layer | $\Delta\omega_{Si}$ | Strain, $\varepsilon_{si}$ | Ge content, x | Relaxation, R | stress σ, [GPa] |
|---|---|---|---|---|---|---|
| C2971 | 512.71 | 7.29 | 0.00784 | 0.38025 | 0.541 | 1.82 |
| C2972 | 507.9 | 12.1 | 0.01301 | 0.39081 | 0.821 | 3.03 |

In agreement with both EELS analysis and expected results, the Ge content is measured at ~40% for both samples. In terms of the SiGe layers, the analysis shows an essential difference in the degree of relaxation, r, associated with the relevant samples. Sample C2972, which was fabricated using a very low temperature SiGe buffer is much more relaxed with relaxation measured at ~82%, while for C2971 the degree of relaxation is calculated at ~54%. In addition, simple estimations of the Si-Si linewidth ($\Delta\nu$) for both samples show a linewidth value of 9 $cm^{-1}$ for sample C2972 and 6.3 $cm^{-1}$ for sample C2971. This is in good agreement with previously published work which found that an increase in the relaxation factor for a SiGe buffer layer can be identified by an associated increase in linewidth. From this (low relaxation factor) it can be concluded that the

growth temperatures employed for point defect introduction were too low which accounts for the high density of dislocations identified through TEM.

## 6.7 Conclusions

Two strained Si quantum well (Si QW) samples, C2971 and C2972, were grown in order to investigate the impact of using either a thin, low temperature virtual substrate on a Si buffer in comparison with the use of a single step SiGe layer. Both growth techniques were novel in that the use of a graded SiGe layer was avoided and that the layer thicknesses within the sample were very thin. The impact of different growth techniques can be seen in terms of the TD density present throughout either device. Using Bright Field TEM techniques, it was clearly shown that TDs dominate the material layers of a Si QW grown using a LTVS stage due to the high levels of stress it introduces.

Reported for the very first time was the successful growth of a QW, sample C2971, using a single step SiGe buffer layer of 40%. Sample C2971 was shown to have a defect density very much in line with traditional SiQWs grown using the more conventional graded SiGe buffer layer approach. A nominal amount of defects were present, which strongly suggests the suitability of this structure for the manufacture of device orientated SiQWs. This is important in the integration of thin film devices. The importance of temperature control in the growth of novel materials, such as strained Si QWs was illustrated through the TEM images of sample C2972. Amorphisation of the first stage was quickly followed by re-crystallisation which leads to the high density of TDs evident throughout the layers. In marked contrast, various TEM images already presented have shown that the use of a single step SiGe layer is more conducive to the growth of QWs.

Complementary micro-Raman analysis provides an insight into the stress levels present throughout both materials. An exceptional stress value of 1.8GPa was recorded for sample C2971, exceeding previously reported values which were achieved using the conventional graded layer approach. Conversely, sample C2972 displays unsurpassed strain levels in the Si cap which relate to the dislocation structure existing underneath. Future work would plan to resolve this conflict as well as achieving a narrow optimum

growth temperature range for the low temperature virtual substrate. In line with discussion presented earlier and in good agreement with reported behaviour, increasing Raman linewidths were matched to an associated increase in the relaxation factor of the layer.

Through the use of EELS, one was provided with information such as thickness and elemental distribution in relation to the individual layers present, such as the Si cap, the SiGe buffer layer as well as the Si QW itself, all of which were found to be in close agreement with expected growth widths. In addition, EELS analysis provided a quantitative measurement of the elements present that was in good agreement with Raman analysis, i.e. a Ge content of ~40% was estimated. As discussed in earlier chapters, it was conclusively shown that using the K edge Si excitation gave a resulting image that was influenced to a lesser extent by the topographical nature of the specimen.

**References**


1. http://www.owlnet.rice.edu/~phys533/

2. http://www.cmu.edu/corporate/news/2005/0405_nano_center.html

3. Technical Insights 'Nanoelectronics: Markets; Applications; and Technology Developments',http://www.theinfoshop.com/study/ti12887_nanoelectronics_toc.html

4. http://www.ecs.soton.ac.uk/research/projects/QWIPS/

5. E. Kasper, K. Lyutovich, editors. Properties of Silicon Germanium and SiGe:Carbon. *EMIS Datareviews Series*. London:INSPEC; 2000

6. E.Kasper, K.Lyutovich, , *Solid State Electronics* **48** (2004) 1257 – 1263

7. M. Ensico-Aguilar, N. Zerounian, F. Aniel, T. Hackbarth, H.J. Herzog, K. Lyutovich, 33rd *European Microwave Conference* 2003, GaAs-Session.

8. T. Hackbarth T, M. Zeuner M, U. Konig, *Comp Semicond* **8** 45-47, 2002;

9. http://www.skepticfiles.org/silly/laserqak.htm

10. W. R. Frensley and N. G. Einspruch editors *Heterostructures and Quantum Devices*, A volume of *VLSI Electronics: Microstructure Science*. (Academic Press, San Diego, 1194) ISBN 0-12-234124-4],

11. R. Dingle, in ``Festkörperprobleme/Advances in Solid State Physics," (H.J. Queisser, ed.), Vol. 15, p. 21, Vieweg, Braunschweig, 1975

12. http://www.utdallas.edu/~frensley/technical/hetphys/hetphys.html

13. C. Miller, D. A. Kleinman and A. C. Gossard, Phys. Rev. B29, 7085 (1984).

14. J M Fernandez, A. Matsumura A, X M Zhang, M H Xie, L. Hart, J. Zhang, B.A. Joyce and T J Thornton, *J. Mater. Sci.: Mater. Electron.* **6** 330, (1995)

15. F. Schäffler, *Semicond.Sci. Technol.* **12** 1515, (1997)

16. K. Lyutovich , E. Kasper ,F. Ernst ,M. Bauer, M. Oehme, *Mat. Sci. Eng.* **B71** 14, (2000)

17. F.K. Legoues, B.S. Meyerson and J.F. Morar, *Phys. Rev. Lett.* **66** 2903, (1991)

18. K. Ismail, M. Arafa, K L Saenger, J O Chu and B S Meyerson, *Appl. Phys. Lett.* **66** 1077, (1995)

19. M J Rack, T J Thornton, D K Ferry, Jeff Roberts and Richard Westhoff, *Semicond. Sci. Technol.* **15** 291–296 (2000)

20. F. Stern and S.E. Laux, *Appl. Phys. Lett.* **61** 1110, (1992)

21. E. Kasper, *Appl. Surf. Sci* **102** pp 189-193, (1996)

22. E. Kasper, K. Lyutovich , , *Solid State Electronics*; **48**, 1257–1263, (2004)

23. K. Lyutovich K, M. Bauer, E. Kasper, H.J. Herzog, T. Perova , R Maurice , *Mater Sci Eng B*; **89**: 341–5, (2002)

24. J.W. Matthews, A.E. Blakeslee, S. Mader, *Thin Solid Films* **33**: 253–66, (1976)

25. R. People, J.C. Bean, *Appl Phys Lett*, **47**: 322–324, (1985)

# Chapter 7

# Microvalve MEMS

## 7.1 Introduction

The work presented so far in this thesis has dealt with analysing Si based structures, such as strained Si QWs in terms of structure and stress using a variety of characterisation techniques. However, the most important benefit of such materials, outside of improved performance etc, probably relates to a very non-engineering parameter; their size. Nanoelectronics, and in this regard, quantumelectronics as well, will have a significant impact on the semiconductor industry. Electronic related items such as memory devices, storage devices, as well as display and communication devices will all be affected by the migration to a smaller scale. The integration of devices at the micro or even nanolevel is a challenge that is being faced through the advent of N/MEMS. Nano/Micro-Electro-Mechanical-Systems (N/MEMS) is the integration of different elements such as mechanical elements, sensors, actuators, and electronics all on a common silicon substrate through the utilization of microfabrication technology. The electronic devices are fabricated using integrated circuit (IC) process sequences, while the micromechanical components are fabricated using compatible 'micromachining' processes that selectively etch away parts of the silicon wafer or add new structural layers to form the mechanical and electromechanical devices. MEMS and nanotechnology are expected to play a leading role in the development of technology in this millennium [1]. Progress of research and development in these areas depends on strong integration of multidisciplinary areas that include Physics, Chemistry, Biology, Medicine and Engineering [2]. This section focuses on introducing the concept of MEMs and the characterisation of a MEM device using a variety of techniques.

## 7.2 Significance of MEMs

MEMS promises to revolutionise nearly every product category by bringing together silicon based microelectronics with micromachining technology, thereby making possible the realisation of complete systems on a single chip. MEMS is an enabling technology allowing the development of smart products by augmenting the computational ability of microelectronics, such as those discussed in Chapters 3 to 6, with the perception and control capabilities of microsensors and microactuators [3]. Since MEMS devices are manufactured using batch fabrication techniques similar to integrated circuits, unprecedented levels of functionality, reliability, and sophistication can be placed on a small silicon chip at a relatively low cost [4]. The nature of MEMS technology and its diversity makes it a potentially far more pervasive technology than even integrated circuit microchips, although time will tell. So far, very few commercial applications exist. Some that are presently on the market are pressure sensors and collision detectors (used for air bag deployment). However, there is a vast amount of research attempting to make different types of MEMS devices available for commercial use.

## 7.3 Reliability Assessment

The current state of MEMS reliability assessment is disjointed and limited. There is no cohesive effort or centre that deals solely with the reliability of microstuctures and microsystems [5]. In terms of manufacturing devices on a large scale, the industry is hampered by the lack of information available on reliability data (in terms of temperature, voltage etc.) between foundries and actual devices. The creation of libraries and templates for error free manufacture is as a result impacted upon and the collection of definitive statistical results for accurate risk assessment has not been obtained. This section aims to outline the benefits of reliable Raman analysis in the verification of MEM devices. Although industry addresses reliability issues as they are highlighted, this process is somewhat ad-hoc and many industries simply lack the resources (time, expertise, facilities) to do a comprehensive reliability assessment of their products.

However, some reliability issues have begun to be addressed at various universities. For example, the mechanical properties of polysilicon (strain, Young's modulus, and fracture strength) have been characterised in air on a custom built test setup [6]. The phenomenon of surface micromachined polysilicon layers sticking to the substrate after release etching ('stiction') has been studied and attempts to combat stiction include self assembled monolayers and the use of lasers [7,8]. In this chapter, an array of valves fabricated using a combination of surface and bulk micromachining techniques are investigated. The structures are analysed using a variety of methods including Scanning Electron Microscope (SEM), Focus Ion Beam system (FIBs), ZYGO surface profiling instrumentation as well as Raman Spectroscopy. Stress in the polycrystalline silicon beam can be calculated from the ZYGO measurement results and then compared against the noninvasive technique of micro-Raman Spectroscopy.

## 7.4 Structure

The structure of a passive microvalve is presented in Fig. 7.1. The valve is comprised of a silicon substrate with an etched aperture to form the inlet for gas or liquid. A surface micromachined polycrystalline silicon movable plate is located at the centre above the inlet hole. Depending on its position, the plate will either enable or restrict the flow. The movable plate is supported by four flexible polycrystalline silicon arms attached to the silicon substrate.

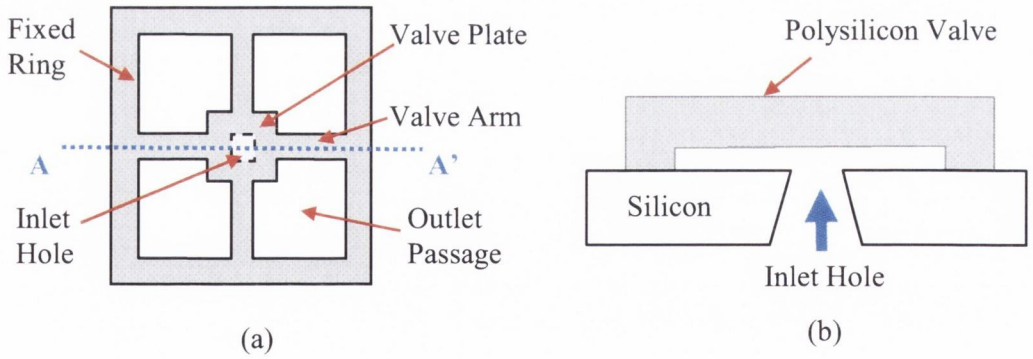


**Fig. 7.1** (a) Surface view (b) Cross section A-A' of the polycrystalline silicon microvalve

## 7.5 Microvalve Formation

The valve is fabricated utilising surface micromachining methods by depositing a layer of polycrystalline silicon and patterning to form the movable plate and its four flexible supporting arms. The inlet hole of the valve will be produced by bulk etching of the silicon substrate in potassium hydroxide (KOH) solution. An array of microvalves, as indicated in Fig. 7.2, with different dimensions of movable plate and supporting arms is fabricated using these techniques.

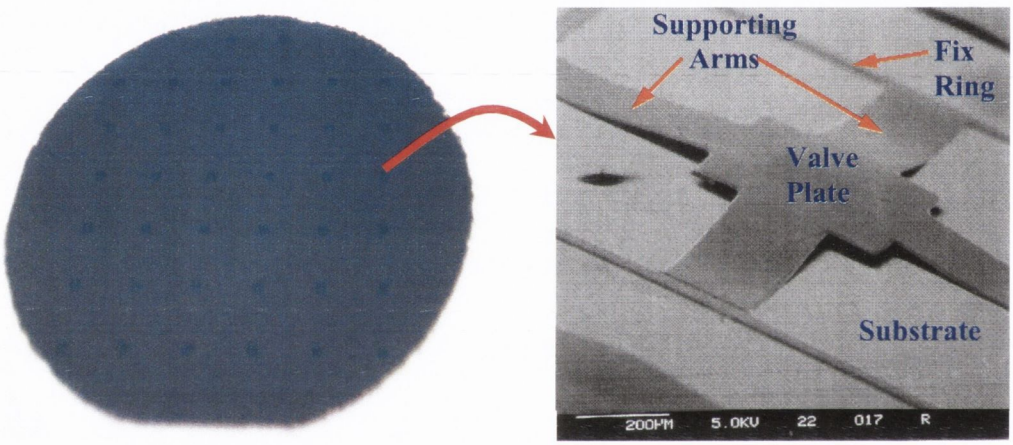


(a) (b)

**Fig. 7.2** (a) Optical photograph of an array of valves fabricated on a silicon substrate; and (b) SEM image of a microvalve after the sacrificial oxide has been removed in concentrated HF.

## 7.6 Results and Discussions

A Raman spectrum of pure c-Si is a Lorentzian shape peak centred at $520cm^{-1}$ , with a full width at half maximum (FHWM) of $3cm^{-1}$. For polycrystalline silicon it is found that the position and the FHWM of its Raman peak depends on the amount of residual stress in the material, the grain size as well as the density of intergrain defects. All samples have shown a grain size that is larger than 100nm, which enables one to exclude any red shift of the first order optical phonon Raman line due to phonon confinement. It is vitally important, due to the nature of polycrystalline Si, that power be kept to a minimum in

Raman measurements as heating effects on polycrystalline Si can give incorrect Raman results.

A ZYGO surface profile scan of the fabricated microvalve is presented in Fig.7.3. The ZYGO system uses non contact scanning white light interferometry to acquire ultrahigh vertical resolution images with 0.1nm resolution [9]. The result shows that the polysilicon valve plate and supporting arms were properly released, with the centre plate resting above the substrate. Valve plate deflection of 17.8 μm was obtained from the ZYGO data. This deflection is due to stress in the polysilicon layer that was deposited at 620 °C. This stress measured on the valve plate is found to be in tensile stress, as is expected from ZYGO plot of Fig. 7.3; this is in contrast to the compressive nature of the polycrystalline wafer, which pushed the valve plate up on release giving a tensile strained plate. Using micro-Raman spectroscopical techniques, one can investigate the stress present in the released valve and legs, and compare directly to the more crude results obtained from the ZYGO plot.

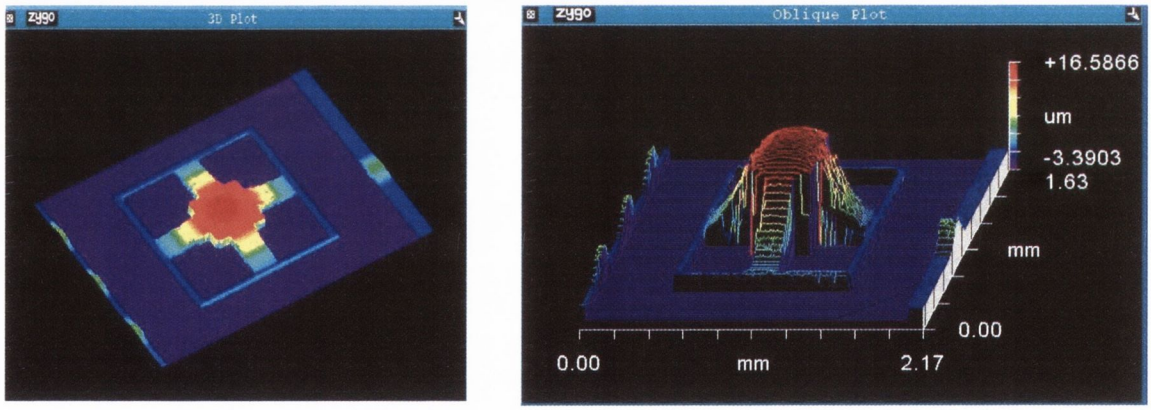


**Fig. 7.3** ZYGO Surface profiling scan.

## 7.7 Stress and Strain Calculation of MEM

The stress in the polysilicon material deposited at 620°C, can be calculated from the data obtained from ZYGO surface profile measurements. Fig. 7.4 shows the plot from ZYGO (points in red) for a relaxed (zero applied pressure) membrane microvalve with

dimensions of 400 μm square plate, 300 x 200 μm supporting arms and 100 μm square inlet hole (valve B). The original results were adjusted, with spikes and measurement errors compensated to obtain a relatively smooth curve (points in blue shown in Fig.7.4). The deflected curve can be broken into small linear increments δl, which are equally spaced in length. The actual length ($L + \Delta L$) is equal to the summation of all the small increments ($\Sigma\delta l$). Hence, the strain ($\varepsilon$) and stress ($\sigma$) of the polysilicon material is given by:

$$Strain,\ \varepsilon = \frac{(L+\Delta L)-L}{L} \tag{7.1}$$

$$Stress,\ \sigma = E \cdot \varepsilon \tag{7.2}$$

where E is the Young's Modulus of the material (130.2 GPa for polysilicon) [10].

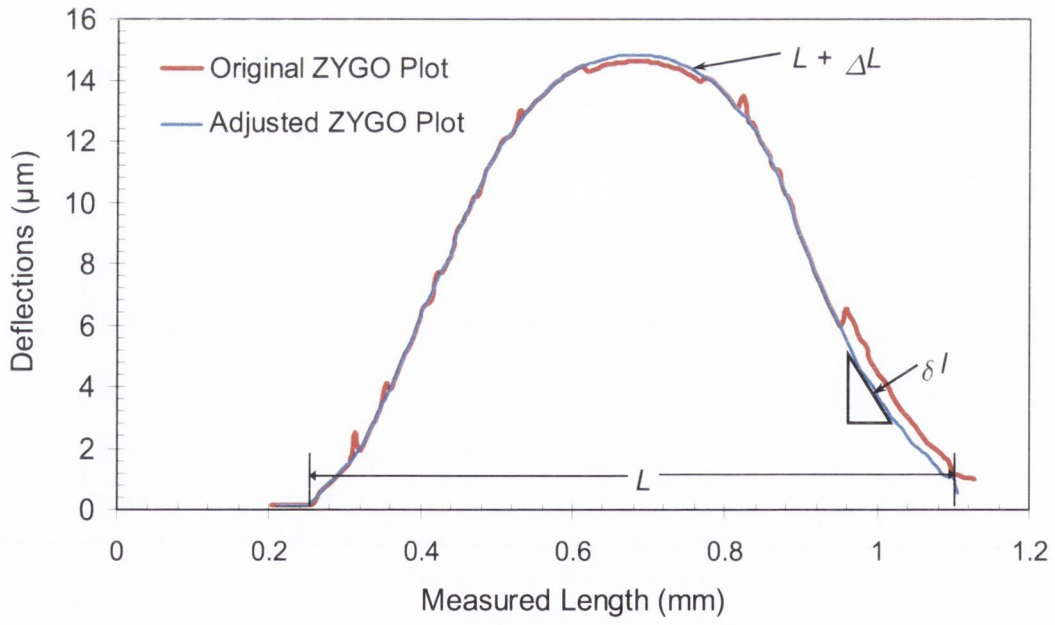


**Fig. 7.4** The results plotted from ZYGO measurements used for stress and strain calculation of the deposited polysilicon material.

From the unadjusted ZYGO plot, the tensile stress of the polysilicon valve is approximately 130 MPa.

## 7.8 Raman Measurements

As an extremely reliable and non invasive stress measurement tool, Raman spectroscopy can be used to map stress across a structure, thus giving a clearer picture of the impact of the various steps involved in the process in terms of their relationship with measured stress. Fig. 7.5 gives the Raman wavenumber values taken from a line scan across the MEM structure. A line scan is an accumulation of various Raman spectra taken at fixed intervals apart.

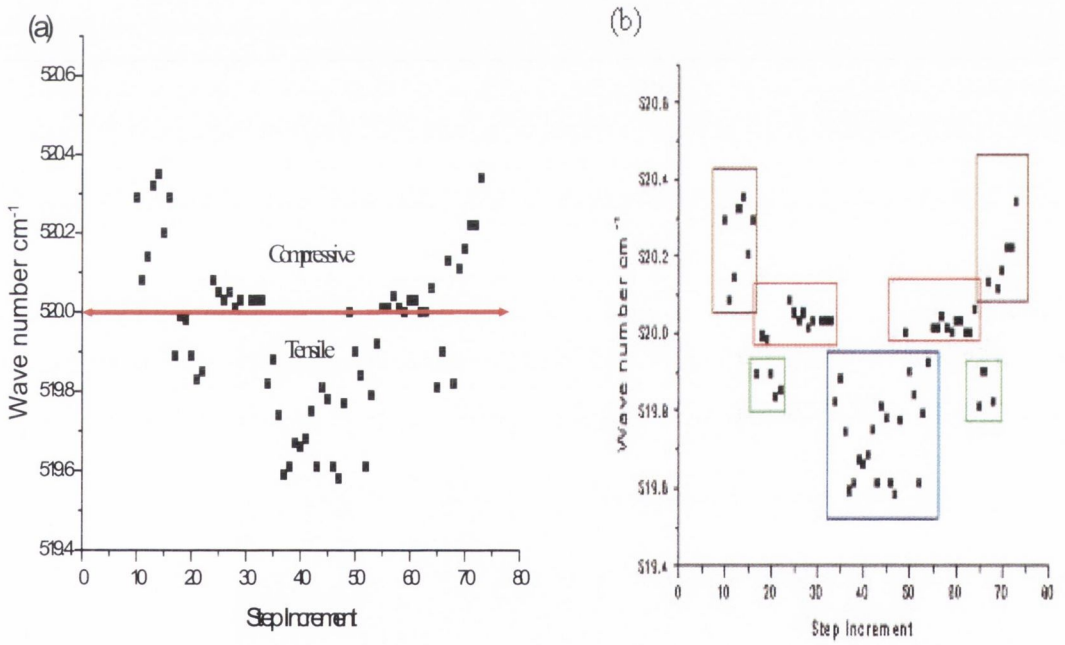


**Fig. 7.5** (a) Raman shifts for MEM structure (b) Related shifts grouped together

Depending on the location of the light on the MEM structure, different levels and natures, of stress are recorded. Related levels of stress can be grouped together in order to facilitate the understanding of gathered measurements. Fig.7.5 (a) shows the raw

measurements for the MEM structure and the shifts in wavenumber related to the degree and type of stress present. Measured Raman shifts above the $520cm^{-1}$ reference value for stress free silicon represent compressive stress while a shift below $520cm^{-1}$ represents a tensile stress [11-13]. It has been shown that Raman microscopy can be used as a nondestructive technique for the immediate characterisation of MEMs, and more specifically, for the investigation of the amount and type of stress present in these devices [14-16]. Fig. 7.5 (b) relates 4 main areas of the MEM valve structure with the recorded Raman data, namely:

1. Brown, **BR**, the polycrystalline wafer;
2. Green, **G**, interface of structure with wafer;
3. Red, **R**, oxide;
4. Blue, **B**, the actual MEM device itself.

Close examination of these groups provides much information about the manufacturing techniques and the resultant structure. On release, as can be see from Fig. 7.3 of the ZYGO plots, the valve is in a 'hill' shape, and thus, a tensile strain is expected in this region, independent of the material used. Raman measurements confirm this hypothesis by a negative shift in the wavenumber position of the Raman spectrum, with stress levels in the range of 0 – 100 MPA.

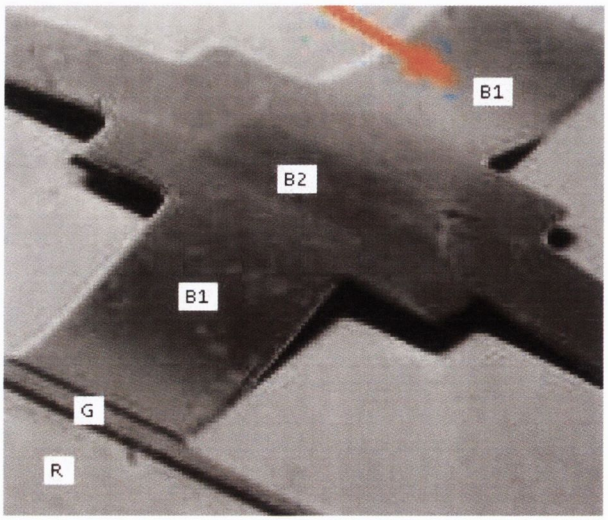


**Fig. 7.6** The MEM structure with Raman colour coded information displayed

From Fig. 7.5 and using the associated letters **B, G, R** as outlined above as they apply to the different grouped areas recorded from the various Raman spectra, Fig. 7.6 shows how they apply directly to the valve of Fig.7.2. The compressive area corresponding to the brown box of the Raman spectrum is not shown here but is to be found to the left of the red area on the wafer itself. Section B, indicating Blue, is divided into two subsections, B1 and B2, in order to indicate the variation of tensile strain across the valve. Stress across the valve increases, in general, going towards the middle, B2, where it then begins to reduce in magnitude near the leg of the valve, B1

However, when analysing the Raman spectrum of Fig.7.5, and particularly the blue grouped section, the following can be identified. Within three 20μm increments, i.e. 60μm, there is a shift in the wavenumber from 519.8 $cm^{-1}$ to 519.9 $cm^{-1}$ and down to 519.6$cm^{-1}$. This corresponds to a wavenumber adjustment of 0.4 $cm^{-1}$, which gives an overall Raman stress variation of 100MPa. Therefore, the maximum range of stress calculated for the central valve is seen in the first 15mm. However, rather than experiencing a stress plateau and a subsequent linear decrease, as would be expected from the ZYGO plot and the interferometry scans of Fig.7.3, the stress is seen to fluctuate within this 0-100MPa range for the whole of the central valve. Several subsequent line scan measurements reveal a 50MPa variation, while quite small in terms of stress (a 0.1$cm^{-1}$ deviation in wavenumber gives a stress of 25MPa), reveal a fluctuation in stress that is unexpected. Experimental error is comparable to the change in wavenumber for line scan variation, but this was eliminated as an impact factor due to the large number of scans taken at different positions over the central valve which revealed exactly the same behaviour. Therefore, stress variation is due to the nature of the device itself, and though while minimal, must be accounted for in datasheets and subsequent usage of the device. Stress variations in a central valve can, in the long term, lead to device failure if the fluctuation is unacceptably high. However, in the case of these particular devices under investigation, the variation, as stated above, is in line with Raman experimental error so is relatively small. This allows acceptable stress variation associated with different grouped devices to be tabulated at the manufacturing site. For example, the future manufacture of

such MEM devices would be validated against an established library of acceptable metrics measured from the Raman spectra, including stress variation, before a device is released to the market. This allows for close control of both overall stress variation as well as detailed verification of acceptable local stress levels.

## 7.9 Conclusions

Micro-Electro-Mechanical-Systems (MEMS) were introduced to the reader, with a variety of potential applications outlined. A MEM valve was investigated using two separate techniques in terms of its surface profile and the associated stress levels. The importance of these measurements relates to the ability to apply such techniques at the manufacturing level in order to create standard, repeatable structures.

Micro-Raman was shown to provide a method of structure analysis as variations in stress across a structure give an insight into the topography of the device. This was confirmed through the use of non contact scanning white light interferometry and dedicated profiling software which showed the valve to have increasing stress when analysing from arm to valve. Line scan Raman spectra were recorded with stress levels found to vary from 0-100MPa depending on the position of the valve under investigation.

Measured stress levels increase going across the valve legs to the centre plate, peak at the middle and then fall once more when moving to the other leg. This is in general agreement with expected results based on the ZYGO plot. Variations between measured results can be in part explained by the difficulty in choosing the most accurate value of Young's modulus available. However, what can be readily seen is that Raman spectra can be used to provide information relating to the surface of a MEM, such as a raised centre valve, whilst in turn being used to calculate the variation of stress across the device. This is of fundamental importance in order to calculate variations in process parameters across batch devices.

In terms of the Raman spectra, grouped Raman results on the central valve reveal a strong variation in stress values. This indicates manufacturing limitations in the strict control of

stress levels. Detailed analysis of the central valve revealed a stress variation of 100MPa in general as well as a similar deviation across a 60μm area. This showed unusual high stress values over 140μm from the centre of the valve, the suggested point of maximum stress. Experimental error was discounted as the source of such variation due to the number of scans performed and the exact replication of behaviour in each scan. This confirmed the suitability of Raman spectra for building a detailed analysis of stress at both the general and more importantly, the micro level. This allows for development of allowable Raman stress templates for future devices which would have to be considered prior to release of the device.

What micro-Raman analysis demonstrated was the ability to develop a set of acceptable templates, a 'golden set', which can then be used to establish a library of various metrics against which other devices can be compared. Development of such a library helps in the future characterisation of similar products while at the same time develops information regarding the growth process itself. These sets of data can then be accessed in the software package outlined in Chapter 5. This enables a developer/researcher to retrieve all relevant parameters, i.e. shape, general stress profile or even detailed stress analysis, instantaneously.

**References**


1. International Conference on MEMS and Nanotechnology (ICMN '06) Hotel Pan Pacific, Kuala Lumpur, Malaysia - 14-15th March 2006

2. Mihail C Roco, William S Bainbridge '*Societal Implications of Nanoscience and Nanotechnology*', Kluwer Academic Publishers, (2001)

3. Integrated Sensing Systems, Inc. (ISSYS), http://www.mems-issys.com/html/technology.html

4. M.A. Huff ,Position Paper: MEMS Manufacturing The MEMS Exchange, http://www.eas.asu.edu/~nsf2000/Table_of_Contents/MH.pdf

5. R. A. Lawton, G. Lin, J. Wellman, L. M. Phinney, J. Uribe, E. Griffith, I. De Wolf, A. Bear, F. Fifi, E. Lawrence, Jet Propulsion Laboratory, California, http://parts.jpl.nasa.gov/docs/Lawton3.pdf,

6. W. Sharpe, J. Yuan, R. Edwards, *J. Microelectromechanical Systems*, vol. 6, no. 3, pp. 193 - 199, September 1997.

7. R. Maboudian, R. T. Howe, *J. Vac. Sci Technology B.*, vol. 15, no. 1, pp. 1 - 20, Jan/Feb 1997.

8. K. Fushinobu, L. M. Phinney, Y. Kurosaki, C. L. Tien,, *Numerical Heat Transfer, Part A (Applications),* **26**, pp. 345 - 357, Sept. 1999.

9. http://www.zygo.com/?/products/nv6000/

10. J.J. Wortman and R.A. Evans, J. Appl. Phys., **36**, 153, (1965)

11. M. J. Pelletier, *Analytical Applications of Raman Spectroscopy*. Oxford, U.K.: Blackwell Science, 1999.

12. R. Loudon, *Adv. Phys.*, vol. **13**, pp. 423–482, 1964.

13. E. Anastassakis, A. Pinczuk, E. Burstein, F. H. Pollack, and M. Cardona, *Solid State Commun.*, vol. **8**, pp. 133–138, (1970)

14. V.T. Srikar „*Journal of Micromechanical Systems*, **12**, NO. 6, ( December 2003)

15. H. Mahfoz-Kotb, *Thin Solid Films* **427**, 422-426, (2003)

16. L.A.Starman, J. Lott, *Sensors and Actuator*s **104**, 107-116, (2003)

# Chapter 8

# Conclusions and Suggestions for Future Work

## 8.1 Conclusions

Many advances in consumer electronics relate to the associated advances that have been made in the underlying materials upon which the technology is based. From both a consumer and an engineering perspective, the need for research into new materials is therefore obvious. While commercial motivation exists to create materials that offer advantages in terms of speed and performance, etc, the requirement to have future materials based around existing manufacturing capabilities is as important. This allows new devices and applications to be developed which enhance the cost savings that are already present for Si based components. In this respect, SiGe heterosystems are a natural choice. Both Si and Ge are group IV elements which, when mixed together, form a similar diamond formation as their constituent parts.

In line with this, the work reported here covered a variety of novel materials all of which, excepting MEMS, have a SiGe layer. The materials investigated were:

1. Strained Si;
2. Ge p-n photodiode structure;
3. Thin Film SiGe buffer layers;
4. Si Quantum Wells;
5. MEMS.

A strained Si cap grown on a relaxed SiGe buffer layer was successfully grown, with stress levels of 1.8GPa exceeding previously reported stress levels in the literature. Moiré-Like Fringes were analysed for the first time using cross-sectional TEM images, with hitherto unexplained patterns accounted for using EELS analysis of the various samples. Raman spectroscopy was shown to be of benefit in the growth feedback process

in tandem with TEM for predicting the morphology of Si cap layers grown on a SiGe layer with excessive dislocation density.

A strained Si quantum well was successfully grown without the presence of a thick SiGe graded layer. Dislocations were comparable to those in traditional techniques, with only minimal dislocations permeating the layers. This result highlights the benefit of such an approach. Devices manufactured without the traditional SiGe graded layer are obviously less expensive due to reduction of manufacturing costs. Monolithic integration, which depends on thin layered devices on a single wafer, is most suitable to such an approach. The successful integration of thin layered devices onto a single wafer can in turn play a significant role in the development of System On Chip (SOC) solutions. This would reduce cost and noise while increasing device performance In parallel, the use of a low temperature virtual substrate was investigated, with dislocations introduced using point defects found to propagate and permeate through all the layers. This approach was successfully investigated using Raman techniques, which is not a trivial matter, with relaxation analysis successfully demonstrating the use of a non-optimum temperature in the growth stage. This was confirmed through exhaustive TEM analysis of dislocation behaviour within the layer, with high dislocation interaction resulting from slow dislocation propagation along the glide plane due to the use of a temperature which was too low. Novel characterisation techniques, such as EELS, stressed the need for complementary analysis of such complicated structure. Layer thicknesses and compositional values were verified to be in good agreement with micro-Raman results.

Using linear and multiple regression statistical techniques and algorithms, a unique approach was taken in the investigation of the suitability of equations developed for thick layered SiGe buffer layers for use with thin SiGe layers. Through the use of an appropriate dataset, Ge content was measured using a variety of micro-Raman based experimentally evolved equations, as well as using XRD as an independent benchmark technique in order to verify the Raman calculations. Using the statistical methods outlined above, the Raman values for Ge composition were mapped to the XRD values. Confidence levels were measured for such an approach and an original, new equation was

proposed for use on existing micro-Raman data. Data were subsequently fed back into the equation with remarkable accuracy achieved relative to the XRD values. This is important for thin film buffer layers as it has been shown that results obtained from equations developed for bulk layers must be modified to produce a more accurate value for Ge concentration. It was reported here for the first time that the thickness of a thin layer sample had no bearing in calculating Ge content when using the experimental equations outlined in the chapter. This is highly significant in terms of its contribution to the understanding of compositional variation in relation to phonon activity when using micro-Raman analysis.

In good agreement with reported results, the impact of foil thickness was shown to be a significant factor in the EELS analysis of Ge p-n photodiode structures. Taking this into account, the successful growth of a Ge p-n photodiode with a graded SiGe layer was demonstrated. Dislocations were successfully confined to the SiGe layer without the need for external polishing or high temperature annealing steps, in contrast to work reported elsewhere. In addition, successful growth of a structure combining hitherto independent techniques, CVD and MBE, was demonstrated. The use of a thin Ge buffer layer instead of a thick SiGe graded layer was investigated, with dislocation density found to propagate throughout the material. This approach, in terms of removing costly and time consuming layers from a structure is something that is considered briefly in the next section, where future work ideas are discussed. For the first time, stress levels of a deposited cap on the Ge p-n photodiode structures were investigated, with results showing that though the values are small, stress levels are not to be ignored. In addition, Raman analysis once more proved itself beneficial in the complementary analysis of defects within a structure with relaxation levels directly linked to the amount of dislocation interaction present in the underlying layers.

Using micro-Raman techniques, it was shown that accurate verification of various devices is possible in terms of stress deviation. MEM valves were successfully created with a deflection value due to tensile stress confirmed by both white light interferometry and Raman spectroscopy. Micro-Raman allowed for the detailed analysis of stress

distributions and showed that the central plate of the valve is itself prone to fluctuations in stress values. This is of more benefit than the general information offered by the ZYGO plots. Using this technique, it would enable manufacturing sites to develop libraries of stress variation for every element of the device, and not just the general variation.

## 8.2 Future Work

It is important that once structures can be successfully grown, such as those identified in this work, the next logical step is the creation of a device containing such a structure, that would allow for analysis in terms of operation speed, mobility enhancement, absorption current etc.

Strained Si devices offer the advantage of a significant increase in mobilities, for both holes and electrons, and it is important that this is verified in terms of the structure that was manufactured in Chapter 3. Similarly for both Ge p-n photodiode and strained Si structures described in Chapters 4 and 6 respectively, it is of obvious interest to the scientific community to investigate and parameterise devices based on the structures outlined. In addition, the investigation into the optimum operating temperature for the addition of low temperature thin virtual substrates must continue as it is believed that this can offer great advantages in terms of integration and dislocation control. As Raman spectroscopy has been proven to be a successful tool in the analysis of MEMS for stress distribution, it is clearly obvious that future MEMS should be manufactured and subjected to such treatment. This allows a library of stress levels for various MEMS devices to be developed, which is necessary for the commercialisation of such a product.

As a new equation was suggested in terms of modification of Raman results in order to align more closely with their XRD counterparts, it is important that this equation be rigorously tested. In line with such work, the creation of a greater database allows the equation to be modified if necessary to take into account any extra information that may be included in such work.

In relation to library development and database management, it is interesting to note that Chapter 5, with the development of a software GUI, possesses the greatest potential of all in terms of commercialisation and marketing. This software tool is Microsoft compatible, and therefore can be integrated in any existing computer solutions available. The development using Visual Basic for Applications (VBA) supports Excel spreadsheets which enhances the capability of the tool. The key advantage to this GUI is that it is independent of data sources (Raman, TEM, EELS), and can be created on a network of computers to allow access from different researchers, even concurrently. It is envisaged that an application will be made to Enterprise Ireland for funding from the 'Proof of Concept' fund in order to further develop the tool and explore any avenues for commercialisation.

# Appendix I

**Table 1** Sample Peak Positions

| Sample | Si-Si Sub | Si-Si | Si-Ge | Ge-Ge | SiGe Buffer Thickness(nm) | %Ge XRD |
|---|---|---|---|---|---|---|
| 745 | 519.96 | 501.19 | 405.13 | 294.01 | 80 | 0.25 |
| 746 | 519.96 | 501.28 | 403.54 | 286.68 | 80 | 0.25 |
| 753 | 519.79 | 503.86 | 403.17 | 292.53 | - | 0.25 |
| 755 | 519.83 | 504.93 | 403.6 | 291.05 | - | 0.25 |
| 756 | 519.81 | 503.82 | 403.42 | 291.09 | - | 0.25 |
| 758 | 519.93 | 506.84 | 408.6 | 292.73 | 80 | 0.23 |
| 759 | 519.95 | 509.21 | 405.9 | 294.83 | 80 | 0.23 |
| 760 | 519.87 | 506.47 | 403.43 | 291.45 | 80 | 0.23 |
| 773 | 521.01 | 492.27 | 408.07 | 291.54 | 100 | 0.453 |
| 774 | 521.37 | 493.23 | 408.67 | 291.81 | 100 | 0.441 |
| 775 | 521.06 | 493.56 | 409.11 | 292.07 | 100 | 0.455 |
| 776 | 521.01 | 494.23 | 408.59 | 291.55 | 100 | 0.437 |
| 931 | 520.1 | 508.1 | 412.5 | 295.5 | - | - |
| 935 | 520.1 | 500.1 | 404.1 | 290.1 | - | - |
| 936 | 519.9 | 499.7 | 406.4 | 292.1 | 80 | 0.35 |
| 937 | 520 | 500.7 | 404.2 | 290.8 | 80 | 0.33 |
| 938 | 520.1 | 500.9 | 407.3 | 294.2 | 80 | 0.37 |
| 939 | 520.1 | 502.9 | 407.9 | 290.7 | 80 | 0.33 |
| 940 | 519.9 | 504.5 | 409.1 | 292.5 | 80 | 0.33 |
| 941 | 520.1 | 504.4 | 408.8 | 292.6 | 80 | 0.33 |
| 946 | 520.3 | 505 | 410 | 296.7 | 80 | - |
| 947 | 520.5 | 498.7 | 405.7 | 290.4 | 80 | 0.34 |
| 1027 | 520.2 | 492.3 | 408.6 | 292.7 | - | 0.5 |
| 1193 | - | - | 399.3 | 294.6 | - | 1 |
| 1199 | 520.7 | 512.3 | 408.8 | 291.7 | 490 | 0.19 |
| 1200 | 520 | 495.7 | 411.3 | 291.7 | 426 | 0.43 |
| 1202 | - | 477.3 | 404.5 | 290.8 | 439 | 0.63 |
| 1298 | 522.4 | 517 | 410.3 | 292.5 | 40 | 0.41 |
| 1299 | 519.9 | 500.3 | 412.3 | 293.7 | 40 | 0.43 |
| 1300 | 519.9 | 500 | 412.8 | 293.3 | 40 | 0.43 |
| 1301 | 520.3 | 500.3 | 413 | 294.4 | 40 | 0.4 |
| 1302 | 520 | 499.49 | 413.83 | 294.01 | 40 | 0.4 |
| 1303 | 520.36 | 501.75 | 414.02 | 295.03 | 40 | 0.4 |
| 1304 | 519.98 | 499.32 | 413.28 | 293.37 | 40 | 0.4 |
| 1305 | 520.21 | 499.32 | 413.32 | 294.45 | 40 | 0.4 |
| 1306 | 520.03 | 495.27 | 408.75 | 292.65 | 40 | 0.4 |
| 1307 | 520.2 | 494 | 406 | 290 | 40 | 0.4 |
| 1308 | 520 | 493 | 405.4 | 288.7 | 225 | 0.4 |
| 1312 | 520 | 494.2 | 407.4 | 290 | 225 | 0.43 |

| | | | | | | |
|---|---|---|---|---|---|---|
| 1314 | 519.9 | 496.2 | 408.3 | 291.3 | 225 | 0.43 |
| 1316 | 520 | 496.2 | 408.4 | 291 | 225 | 0.42 |
| 1317 | 520.2 | 503.5 | 405.7 | 291.7 | 225 | 0.29 |
| 1318 | 520.2 | 498 | 409.7 | 292.3 | 225 | 0.42 |

**Table 2** Ge Content values using equations without strain factor

| Sample | X1 | X2 | X3 | X4 | X5 | X6 | X7 | X8 | XRD |
|---|---|---|---|---|---|---|---|---|---|
| 745 | 0.27662 | 0.28201 | 0.30661 | 0.29465 | 0.38583 | 0.32606 | 0.71937 | 0.68198 | 0.25 |
| 746 | 0.27529 | 0.28066 | 0.30516 | 0.29333 | 0.25333 | 0.21408 | 0.26125 | 0.30356 | 0.25 |
| 753 | 0.23735 | 0.24198 | 0.26355 | 0.25534 | 0.2225 | 0.18803 | 0.62687 | 0.60558 | 0.25 |
| 755 | 0.22162 | 0.22594 | 0.24629 | 0.23958 | 0.25833 | 0.21831 | 0.53438 | 0.52917 | 0.25 |
| 756 | 0.23794 | 0.24258 | 0.26419 | 0.25593 | 0.24333 | 0.20563 | 0.53687 | 0.53123 | 0.25 |
| 758 | 0.19353 | 0.1973 | 0.21548 | 0.21146 | 0.675 | 0.57042 | 0.63938 | 0.6159 | 0.23 |
| 759 | 0.15868 | 0.16177 | 0.17726 | 0.17656 | 0.45 | 0.38028 | 0.77062 | 0.72432 | 0.23 |
| 760 | 0.19897 | 0.20285 | 0.22145 | 0.2169 | 0.24417 | 0.20634 | 0.55937 | 0.54982 | 0.23 |
| 773 | 0.40779 | 0.41574 | 0.45048 | 0.42601 | 0.63083 | 0.5331 | 0.565 | 0.55447 | 0.453 |
| 774 | 0.39368 | 0.40135 | 0.435 | 0.41187 | 0.68083 | 0.57535 | 0.58188 | 0.5684 | 0.441 |
| 775 | 0.38882 | 0.3964 | 0.42968 | 0.40701 | 0.7175 | 0.60634 | 0.59812 | 0.58183 | 0.455 |
| 776 | 0.37897 | 0.38636 | 0.41887 | 0.39714 | 0.67417 | 0.56972 | 0.56563 | 0.55498 | 0.437 |
| 931 | 0.175 | 0.17841 | 0.19516 | 0.1929 | 1 | 0.84507 | 0.8125 | 0.75891 | - |
| 935 | 0.29265 | 0.29835 | 0.32419 | 0.31071 | 0.3 | 0.25352 | 0.475 | 0.48012 | - |
| 936 | 0.29853 | 0.30435 | 0.33065 | 0.3166 | 0.49167 | 0.41549 | 0.6 | 0.58338 | 0.35 |
| 937 | 0.28382 | 0.28936 | 0.31452 | 0.30187 | 0.30833 | 0.26056 | 0.51875 | 0.51626 | 0.33 |
| 938 | 0.28088 | 0.28636 | 0.31129 | 0.29893 | 0.56667 | 0.47887 | 0.73125 | 0.69179 | 0.37 |
| 939 | 0.25147 | 0.25637 | 0.27903 | 0.26947 | 0.61667 | 0.52113 | 0.5125 | 0.5111 | 0.33 |
| 940 | 0.22794 | 0.23238 | 0.25323 | 0.24591 | 0.71667 | 0.60563 | 0.625 | 0.60403 | 0.33 |
| 941 | 0.22941 | 0.23388 | 0.25484 | 0.24739 | 0.69167 | 0.58451 | 0.63125 | 0.60919 | 0.33 |
| 946 | 0.22059 | 0.22489 | 0.24516 | 0.23855 | 0.79167 | 0.66901 | 0.8875 | 0.82086 | - |
| 947 | 0.31324 | 0.31934 | 0.34677 | 0.33132 | 0.43333 | 0.3662 | 0.49375 | 0.49561 | 0.34 |
| 1027 | 0.40735 | 0.41529 | 0.45 | 0.42556 | 0.675 | 0.57042 | 0.6375 | 0.61435 | 0.5 |
| 1193 | -- | -- | -- | -- | -0.1 | -0.0845 | 0.75625 | 0.71244 | 1 |
| 1199 | 0.11324 | 0.11544 | 0.12742 | 0.13106 | 0.69167 | 0.58451 | 0.575 | 0.56273 | 0.19 |
| 1200 | 0.35735 | 0.36432 | 0.39516 | 0.3755 | 0.9 | 0.76056 | 0.575 | 0.56273 | 0.43 |
| 1202 | 0.62794 | 0.64018 | 0.69194 | 0.64644 | 0.33333 | 0.28169 | 0.51875 | 0.51626 | 0.63 |
| 1298 | 0.04412 | 0.04498 | 0.05161 | 0.06185 | 0.81667 | 0.69014 | 0.625 | 0.60403 | 0.41 |
| 1299 | 0.28971 | 0.29535 | 0.32097 | 0.30776 | 0.98333 | 0.83099 | 0.7 | 0.66598 | 0.43 |
| 1300 | 0.29412 | 0.29985 | 0.32581 | 0.31218 | 1.025 | 0.8662 | 0.675 | 0.64533 | 0.43 |
| 1301 | 0.28971 | 0.29535 | 0.32097 | 0.30776 | 1.04167 | 0.88028 | 0.74375 | 0.70212 | 0.4 |
| 1302 | 0.30162 | 0.3075 | 0.33403 | 0.31969 | 1.11083 | 0.93873 | 0.71937 | 0.68198 | 0.4 |
| 1303 | 0.26838 | 0.27361 | 0.29758 | 0.28641 | 1.12667 | 0.95211 | 0.78312 | 0.73464 | 0.4 |
| 1304 | 0.30412 | 0.31004 | 0.33677 | 0.32219 | 1.065 | 0.9 | 0.67938 | 0.64894 | 0.4 |
| 1305 | 0.30412 | 0.31004 | 0.33677 | 0.32219 | 1.06833 | 0.90282 | 0.74687 | 0.7047 | 0.4 |
| 1306 | 0.36368 | 0.37076 | 0.4021 | 0.38183 | 0.6875 | 0.58099 | 0.63437 | 0.61177 | 0.4 |

| | | | | | | | | | |
|---|---|---|---|---|---|---|---|---|---|
| 1307 | 0.38235 | 0.38981 | 0.42258 | 0.40053 | 0.45833 | 0.38732 | 0.46875 | 0.47496 | 0.4 |
| 1308 | 0.39706 | 0.4048 | 0.43871 | 0.41526 | 0.40833 | 0.34507 | 0.3875 | 0.40785 | 0.4 |
| 1312 | 0.37941 | 0.38681 | 0.41935 | 0.39759 | 0.575 | 0.48592 | 0.46875 | 0.47496 | 0.43 |
| 1314 | 0.35 | 0.35682 | 0.3871 | 0.36813 | 0.65 | 0.5493 | 0.55 | 0.54208 | 0.43 |
| 1316 | 0.35 | 0.35682 | 0.3871 | 0.36813 | 0.65833 | 0.55634 | 0.53125 | 0.52659 | 0.42 |
| 1317 | 0.24265 | 0.24738 | 0.26935 | 0.26064 | 0.43333 | 0.3662 | 0.575 | 0.56273 | 0.29 |
| 1318 | 0.32353 | 0.32984 | 0.35806 | 0.34163 | 0.76667 | 0.64789 | 0.6125 | 0.5937 | 0.42 |

**Table 3** Ge content values using equations with strain factor

| Sample | XGE1 | XGE2 | XGE3 | XGE4 | XGE5 | XGE6 | XGE7 | XGE8 | XRD |
|---|---|---|---|---|---|---|---|---|---|
| 745 | 0.28807 | 0.30902 | 0.29236 | 0.29879 | 0.32139 | 0.30341 | 1.29171 | 1.05411 | 0.25 |
| 746 | 0.26112 | 0.28011 | 0.26501 | 0.27084 | 0.29132 | 0.27503 | 0.32989 | 0.26921 | 0.25 |
| 753 | 0.22593 | 0.24236 | 0.2293 | 0.23434 | 0.25206 | 0.23796 | 1.26546 | 1.03268 | 0.25 |
| 755 | 0.22085 | 0.23691 | 0.22414 | 0.22907 | 0.2464 | 0.23261 | 0.99429 | 0.8114 | 0.25 |
| 756 | 0.23046 | 0.24722 | 0.23389 | 0.23904 | 0.25712 | 0.24273 | 1.01888 | 0.83146 | 0.25 |
| 758 | 0.28082 | 0.30124 | 0.28501 | 0.29127 | 0.3133 | 0.29578 | 0.73973 | 0.60366 | 0.23 |
| 759 | 0.21 | 0.22527 | 0.21313 | 0.21782 | 0.23429 | 0.22119 | 1.33863 | 1.0924 | 0.23 |
| 760 | 0.20068 | 0.21527 | 0.20367 | 0.20815 | 0.22389 | 0.21137 | 1.07309 | 0.8757 | 0.23 |
| 773 | 0.43682 | 0.46858 | 0.44333 | 0.45308 | 0.48734 | 0.46008 | 0.61144 | 0.49897 | 0.453 |
| 774 | 0.43576 | 0.46744 | 0.44225 | 0.45198 | 0.48616 | 0.45896 | 0.59139 | 0.4826 | 0.441 |
| 775 | 0.4392 | 0.47114 | 0.44575 | 0.45555 | 0.49 | 0.46259 | 0.5862 | 0.47837 | 0.455 |
| 776 | 0.42315 | 0.45392 | 0.42946 | 0.4389 | 0.47209 | 0.44569 | 0.55969 | 0.45674 | 0.437 |
| 931 | 0.3302 | 0.35421 | 0.33512 | 0.34249 | 0.36839 | 0.34778 | 0.76514 | 0.62439 | - |
| 935 | 0.28359 | 0.30421 | 0.28781 | 0.29414 | 0.31639 | 0.29869 | 0.79729 | 0.65063 | - |
| 936 | 0.32562 | 0.3493 | 0.33047 | 0.33774 | 0.36328 | 0.34296 | 0.86849 | 0.70874 | 0.35 |
| 937 | 0.27844 | 0.29868 | 0.28259 | 0.2888 | 0.31064 | 0.29327 | 0.89445 | 0.72992 | 0.33 |
| 938 | 0.32674 | 0.3505 | 0.33161 | 0.3389 | 0.36453 | 0.34414 | 1.09851 | 0.89644 | 0.37 |
| 939 | 0.31393 | 0.33675 | 0.3186 | 0.32561 | 0.35024 | 0.33065 | 0.49997 | 0.408 | 0.33 |
| 940 | 0.31542 | 0.33836 | 0.32012 | 0.32716 | 0.3519 | 0.33222 | 0.6532 | 0.53305 | 0.33 |
| 941 | 0.31166 | 0.33432 | 0.3163 | 0.32326 | 0.3477 | 0.32825 | 0.69929 | 0.57066 | 0.33 |
| 946 | 0.32445 | 0.34804 | 0.32928 | 0.33653 | 0.36198 | 0.34173 | 1.20545 | 0.98371 | - |
| 947 | 0.3255 | 0.34917 | 0.33035 | 0.33762 | 0.36315 | 0.34284 | 0.67937 | 0.5544 | 0.34 |
| 1027 | 0.44512 | 0.47749 | 0.45176 | 0.46169 | 0.49661 | 0.46883 | 0.73513 | 0.5999 | 0.5 |
| 1193 | -- | -- | -- | -- | -- | -- | 1.97965 | 1.6155 | 1 |
| 1199 | 0.22239 | 0.23856 | 0.2257 | 0.23066 | 0.24811 | 0.23423 | 0.56119 | 0.45796 | 0.19 |
| 1200 | 0.45074 | 0.48352 | 0.45746 | 0.46752 | 0.50288 | 0.47475 | 0.30501 | 0.24891 | 0.43 |
| 1202 | 0.54775 | 0.58758 | 0.55591 | 0.56814 | 0.6111 | 0.57692 | 0.86371 | 0.70483 | 0.63 |
| 1298 | 0.19374 | 0.20783 | 0.19663 | 0.20095 | 0.21615 | 0.20406 | 0.53024 | 0.4327 | 0.41 |
| 1299 | 0.41507 | 0.44526 | 0.42126 | 0.43052 | 0.46308 | 0.43718 | 0.50943 | 0.41572 | 0.43 |
| 1300 | 0.42662 | 0.45764 | 0.43297 | 0.4425 | 0.47596 | 0.44934 | 0.39682 | 0.32382 | 0.43 |
| 1301 | 0.42649 | 0.4575 | 0.43284 | 0.44236 | 0.47582 | 0.4492 | 0.54511 | 0.44484 | 0.4 |
| 1302 | 0.44918 | 0.48184 | 0.45587 | 0.4659 | 0.50113 | 0.4731 | 0.40022 | 0.3266 | 0.4 |

| | | | | | | | | | |
|---|---|---|---|---|---|---|---|---|---|
| 1303 | 0.42674 | 0.45777 | 0.4331 | 0.44263 | 0.4761 | 0.44947 | 0.53726 | 0.43844 | 0.4 |
| 1304 | 0.44213 | 0.47428 | 0.44872 | 0.45859 | 0.49327 | 0.46568 | 0.35837 | 0.29245 | 0.4 |
| 1305 | 0.4384 | 0.47028 | 0.44493 | 0.45472 | 0.48911 | 0.46175 | 0.35837 | 0.29245 | 0.4 |
| 1306 | 0.41401 | 0.44411 | 0.42018 | 0.42942 | 0.46189 | 0.43606 | 0.71208 | 0.5811 | 0.4 |
| 1307 | 0.38351 | 0.41139 | 0.38922 | 0.39778 | 0.42786 | 0.40393 | 0.58725 | 0.47923 | 0.4 |
| 1308 | 0.38502 | 0.41302 | 0.39076 | 0.39935 | 0.42955 | 0.40552 | 0.44925 | 0.36661 | 0.4 |
| 1312 | 0.40408 | 0.43346 | 0.4101 | 0.41912 | 0.45082 | 0.4256 | 0.44379 | 0.36216 | 0.43 |
| 1314 | 0.39616 | 0.42497 | 0.40206 | 0.41091 | 0.44198 | 0.41726 | 0.55104 | 0.44968 | 0.43 |
| 1316 | 0.39779 | 0.42672 | 0.40372 | 0.4126 | 0.4438 | 0.41898 | 0.49476 | 0.40375 | 0.42 |
| 1317 | 0.27126 | 0.29099 | 0.27531 | 0.28136 | 0.30264 | 0.28571 | 0.87885 | 0.71719 | 0.29 |
| 1318 | 0.39866 | 0.42764 | 0.4046 | 0.41349 | 0.44476 | 0.41989 | 0.56103 | 0.45783 | 0.42 |
| | | | | | | | | | |

**Table 4** Data for X1-X8 following Cleaning/Mining

| Sample | X1 | X2 | X3 | X4 | X5 | X6 | X7 | X8 | XRD |
|---|---|---|---|---|---|---|---|---|---|
| 745 | 0.27662 | 0.28201 | 0.30661 | 0.29465 | 0.38583 | 0.32606 | 0.71937 | 0.68198 | 0.25 |
| 746 | 0.27529 | 0.28066 | 0.30516 | 0.29333 | 0.25333 | 0.21408 | 0.26125 | 0.30356 | 0.25 |
| 758 | 0.19353 | 0.1973 | 0.21548 | 0.21146 | 0.675 | 0.57042 | 0.63938 | 0.6159 | 0.23 |
| 759 | 0.15868 | 0.16177 | 0.17726 | 0.17656 | 0.45 | 0.38028 | 0.77062 | 0.72432 | 0.23 |
| 760 | 0.19897 | 0.20285 | 0.22145 | 0.2169 | 0.24417 | 0.20634 | 0.55937 | 0.54982 | 0.23 |
| 773 | 0.40779 | 0.41574 | 0.45048 | 0.42601 | 0.63083 | 0.5331 | 0.565 | 0.55447 | 0.453 |
| 774 | 0.39368 | 0.40135 | 0.435 | 0.41187 | 0.68083 | 0.57535 | 0.58188 | 0.5684 | 0.441 |
| 775 | 0.38882 | 0.3964 | 0.42968 | 0.40701 | 0.7175 | 0.60634 | 0.59812 | 0.58183 | 0.455 |
| 776 | 0.37897 | 0.38636 | 0.41887 | 0.39714 | 0.67417 | 0.56972 | 0.56563 | 0.55498 | 0.437 |
| 936 | 0.29853 | 0.30435 | 0.33065 | 0.3166 | 0.49167 | 0.41549 | 0.6 | 0.58338 | 0.35 |
| 937 | 0.28382 | 0.28936 | 0.31452 | 0.30187 | 0.30833 | 0.26056 | 0.51875 | 0.51626 | 0.33 |
| 938 | 0.28088 | 0.28636 | 0.31129 | 0.29893 | 0.56667 | 0.47887 | 0.73125 | 0.69179 | 0.37 |
| 939 | 0.25147 | 0.25637 | 0.27903 | 0.26947 | 0.61667 | 0.52113 | 0.5125 | 0.5111 | 0.33 |
| 940 | 0.22794 | 0.23238 | 0.25323 | 0.24591 | 0.71667 | 0.60563 | 0.625 | 0.60403 | 0.33 |
| 941 | 0.22941 | 0.23388 | 0.25484 | 0.24739 | 0.69167 | 0.58451 | 0.63125 | 0.60919 | 0.33 |
| 947 | 0.31324 | 0.31934 | 0.34677 | 0.33132 | 0.43333 | 0.3662 | 0.49375 | 0.49561 | 0.34 |
| 1199 | 0.11324 | 0.11544 | 0.12742 | 0.13106 | 0.69167 | 0.58451 | 0.575 | 0.56273 | 0.19 |
| 1200 | 0.35735 | 0.36432 | 0.39516 | 0.3755 | 0.9 | 0.76056 | 0.575 | 0.56273 | 0.43 |
| 1202 | 0.62794 | 0.64018 | 0.69194 | 0.64644 | 0.33333 | 0.28169 | 0.51875 | 0.51626 | 0.63 |
| 1298 | 0.04412 | 0.04498 | 0.05161 | 0.06185 | 0.81667 | 0.69014 | 0.625 | 0.60403 | 0.41 |
| 1299 | 0.28971 | 0.29535 | 0.32097 | 0.30776 | 0.98333 | 0.83099 | 0.7 | 0.66598 | 0.43 |
| 1300 | 0.29412 | 0.29985 | 0.32581 | 0.31218 | 1.025 | 0.8662 | 0.675 | 0.64533 | 0.43 |
| 1301 | 0.28971 | 0.29535 | 0.32097 | 0.30776 | 1.04167 | 0.88028 | 0.74375 | 0.70212 | 0.4 |
| 1302 | 0.30162 | 0.3075 | 0.33403 | 0.31969 | 1.11083 | 0.93873 | 0.71937 | 0.68198 | 0.4 |
| 1303 | 0.26838 | 0.27361 | 0.29758 | 0.28641 | 1.12667 | 0.95211 | 0.78312 | 0.73464 | 0.4 |
| 1304 | 0.30412 | 0.31004 | 0.33677 | 0.32219 | 1.065 | 0.9 | 0.67938 | 0.64894 | 0.4 |
| 1305 | 0.30412 | 0.31004 | 0.33677 | 0.32219 | 1.06833 | 0.90282 | 0.74687 | 0.7047 | 0.4 |
| 1306 | 0.36368 | 0.37076 | 0.4021 | 0.38183 | 0.6875 | 0.58099 | 0.63437 | 0.61177 | 0.4 |

| | | | | | | | | | |
|---|---|---|---|---|---|---|---|---|---|
| 1307 | 0.38235 | 0.38981 | 0.42258 | 0.40053 | 0.45833 | 0.38732 | 0.46875 | 0.47496 | 0.4 |
| 1308 | 0.39706 | 0.4048 | 0.43871 | 0.41526 | 0.40833 | 0.34507 | 0.3875 | 0.40785 | 0.4 |
| 1312 | 0.37941 | 0.38681 | 0.41935 | 0.39759 | 0.575 | 0.48592 | 0.46875 | 0.47496 | 0.43 |
| 1314 | 0.35 | 0.35682 | 0.3871 | 0.36813 | 0.65 | 0.5493 | 0.55 | 0.54208 | 0.43 |
| 1316 | 0.35 | 0.35682 | 0.3871 | 0.36813 | 0.65833 | 0.55634 | 0.53125 | 0.52659 | 0.42 |
| 1317 | 0.24265 | 0.24738 | 0.26935 | 0.26064 | 0.43333 | 0.3662 | 0.575 | 0.56273 | 0.29 |
| 1318 | 0.32353 | 0.32984 | 0.35806 | 0.34163 | 0.76667 | 0.64789 | 0.6125 | 0.5937 | 0.42 |

**Table 5** Data for XGE1-XGE8 following Cleaning/Mining

| Sample | XGE1 | XGE2 | XGE3 | XGE4 | XGE5 | XGE6 | XGE7 | XGE8 | XRD |
|---|---|---|---|---|---|---|---|---|---|
| 745 | 0.28807 | 0.30902 | 0.29236 | 0.29879 | 0.32139 | 0.30341 | 1.29171 | 1.05411 | 0.25 |
| 746 | 0.26112 | 0.28011 | 0.26501 | 0.27084 | 0.29132 | 0.27503 | 0.32989 | 0.26921 | 0.25 |
| 753 | 0.22593 | 0.24236 | 0.2293 | 0.23434 | 0.25206 | 0.23796 | 1.26546 | 1.03268 | 0.25 |
| 755 | 0.22085 | 0.23691 | 0.22414 | 0.22907 | 0.2464 | 0.23261 | 0.99429 | 0.8114 | 0.25 |
| 756 | 0.23046 | 0.24722 | 0.23389 | 0.23904 | 0.25712 | 0.24273 | 1.01888 | 0.83146 | 0.25 |
| 758 | 0.28082 | 0.30124 | 0.28501 | 0.29127 | 0.3133 | 0.29578 | 0.73973 | 0.60366 | 0.23 |
| 759 | 0.21 | 0.22527 | 0.21313 | 0.21782 | 0.23429 | 0.22119 | 1.33863 | 1.0924 | 0.23 |
| 760 | 0.20068 | 0.21527 | 0.20367 | 0.20815 | 0.22389 | 0.21137 | 1.07309 | 0.8757 | 0.23 |
| 773 | 0.43682 | 0.46858 | 0.44333 | 0.45308 | 0.48734 | 0.46008 | 0.61144 | 0.49897 | 0.453 |
| 774 | 0.43576 | 0.46744 | 0.44225 | 0.45198 | 0.48616 | 0.45896 | 0.59139 | 0.4826 | 0.441 |
| 775 | 0.4392 | 0.47114 | 0.44575 | 0.45555 | 0.49 | 0.46259 | 0.5862 | 0.47837 | 0.455 |
| 776 | 0.42315 | 0.45392 | 0.42946 | 0.4389 | 0.47209 | 0.44569 | 0.55969 | 0.45674 | 0.437 |
| 936 | 0.32562 | 0.3493 | 0.33047 | 0.33774 | 0.36328 | 0.34296 | 0.86849 | 0.70874 | 0.35 |
| 937 | 0.27844 | 0.29868 | 0.28259 | 0.2888 | 0.31064 | 0.29327 | 0.89445 | 0.72992 | 0.33 |
| 938 | 0.32674 | 0.3505 | 0.33161 | 0.3389 | 0.36453 | 0.34414 | 1.09851 | 0.89644 | 0.37 |
| 939 | 0.31393 | 0.33675 | 0.3186 | 0.32561 | 0.35024 | 0.33065 | 0.49997 | 0.408 | 0.33 |
| 940 | 0.31542 | 0.33836 | 0.32012 | 0.32716 | 0.3519 | 0.33222 | 0.6532 | 0.53305 | 0.33 |
| 941 | 0.31166 | 0.33432 | 0.3163 | 0.32326 | 0.3477 | 0.32825 | 0.69929 | 0.57066 | 0.33 |
| 947 | 0.3255 | 0.34917 | 0.33035 | 0.33762 | 0.36315 | 0.34284 | 0.67937 | 0.5544 | 0.34 |
| 1027 | 0.44512 | 0.47749 | 0.45176 | 0.46169 | 0.49661 | 0.46883 | 0.73513 | 0.5999 | 0.5 |
| 1199 | 0.22239 | 0.23856 | 0.2257 | 0.23066 | 0.24811 | 0.23423 | 0.56119 | 0.45796 | 0.19 |
| 1200 | 0.45074 | 0.48352 | 0.45746 | 0.46752 | 0.50288 | 0.47475 | 0.30501 | 0.24891 | 0.43 |
| 1202 | 0.54775 | 0.58758 | 0.55591 | 0.56814 | 0.6111 | 0.57692 | 0.86371 | 0.70483 | 0.63 |
| 1298 | 0.19374 | 0.20783 | 0.19663 | 0.20095 | 0.21615 | 0.20406 | 0.53024 | 0.4327 | 0.41 |
| 1299 | 0.41507 | 0.44526 | 0.42126 | 0.43052 | 0.46308 | 0.43718 | 0.50943 | 0.41572 | 0.43 |

| | | | | | | | | | |
|---|---|---|---|---|---|---|---|---|---|
| 1300 | 0.42662 | 0.45764 | 0.43297 | 0.4425 | 0.47596 | 0.44934 | 0.39682 | 0.32382 | 0.43 |
| 1301 | 0.42649 | 0.4575 | 0.43284 | 0.44236 | 0.47582 | 0.4492 | 0.54511 | 0.44484 | 0.4 |
| 1302 | 0.44918 | 0.48184 | 0.45587 | 0.4659 | 0.50113 | 0.4731 | 0.40022 | 0.3266 | 0.4 |
| 1303 | 0.42674 | 0.45777 | 0.4331 | 0.44263 | 0.4761 | 0.44947 | 0.53726 | 0.43844 | 0.4 |
| 1304 | 0.44213 | 0.47428 | 0.44872 | 0.45859 | 0.49327 | 0.46568 | 0.35837 | 0.29245 | 0.4 |
| 1305 | 0.4384 | 0.47028 | 0.44493 | 0.45472 | 0.48911 | 0.46175 | 0.35837 | 0.29245 | 0.4 |
| 1306 | 0.41401 | 0.44411 | 0.42018 | 0.42942 | 0.46189 | 0.43606 | 0.71208 | 0.5811 | 0.4 |
| 1307 | 0.38351 | 0.41139 | 0.38922 | 0.39778 | 0.42786 | 0.40393 | 0.58725 | 0.47923 | 0.4 |
| 1308 | 0.38502 | 0.41302 | 0.39076 | 0.39935 | 0.42955 | 0.40552 | 0.44925 | 0.36661 | 0.4 |
| 1312 | 0.40408 | 0.43346 | 0.4101 | 0.41912 | 0.45082 | 0.4256 | 0.44379 | 0.36216 | 0.43 |
| 1314 | 0.39616 | 0.42497 | 0.40206 | 0.41091 | 0.44198 | 0.41726 | 0.55104 | 0.44968 | 0.43 |
| 1316 | 0.39779 | 0.42672 | 0.40372 | 0.4126 | 0.4438 | 0.41898 | 0.49476 | 0.40375 | 0.42 |
| 1317 | 0.27126 | 0.29099 | 0.27531 | 0.28136 | 0.30264 | 0.28571 | 0.87885 | 0.71719 | 0.29 |
| 1318 | 0.39866 | 0.42764 | 0.4046 | 0.41349 | 0.44476 | 0.41989 | 0.56103 | 0.45783 | 0.42 |

**Table 6** Reduced Dataset for Multifactor analysis

| XRD | X1 | X5 | Thickness |
|---|---|---|---|
| 0.25 | 0.27662 | 0.38583 | 80 |
| 0.25 | 0.27529 | 0.25333 | 80 |
| 0.23 | 0.19353 | 0.675 | 80 |
| 0.23 | 0.15868 | 0.45 | 80 |
| 0.23 | 0.19897 | 0.24417 | 80 |
| 0.453 | 0.40779 | 0.63083 | 100 |
| 0.441 | 0.39368 | 0.68083 | 100 |
| 0.455 | 0.38882 | 0.7175 | 100 |
| 0.437 | 0.37897 | 0.67417 | 100 |
| 0.35 | 0.29853 | 0.49167 | 80 |
| 0.33 | 0.28382 | 0.30833 | 80 |
| 0.37 | 0.28088 | 0.56667 | 80 |
| 0.33 | 0.25147 | 0.61667 | 80 |
| 0.33 | 0.22794 | 0.71667 | 80 |
| 0.33 | 0.22941 | 0.69167 | 80 |
| 0.34 | 0.31324 | 0.43333 | 80 |
| 0.19 | 0.11324 | 0.69167 | 490 |
| 0.43 | 0.35735 | 0.9 | 426 |
| 0.63 | 0.62794 | 0.33333 | 439 |
| 0.41 | 0.04412 | 0.81667 | 40 |
| 0.43 | 0.28971 | 0.98333 | 40 |
| 0.43 | 0.29412 | 1.025 | 40 |
| 0.4 | 0.28971 | 1.04167 | 40 |
| 0.4 | 0.30162 | 1.11083 | 40 |
| 0.4 | 0.26838 | 1.12667 | 40 |
| 0.4 | 0.30412 | 1.065 | 40 |

| | | | |
|---|---|---|---|
| 0.4 | 0.30412 | 1.06833 | 40 |
| 0.4 | 0.36368 | 0.6875 | 40 |
| 0.4 | 0.38235 | 0.45833 | 40 |
| 0.4 | 0.39706 | 0.40833 | 225 |
| 0.43 | 0.37941 | 0.575 | 225 |
| 0.43 | 0.35 | 0.65 | 225 |
| 0.42 | 0.35 | 0.65833 | 225 |
| 0.29 | 0.24265 | 0.43333 | 225 |
| 0.42 | 0.32353 | 0.76667 | 225 |

# Appendix II

**An example of the code developed:**

UserForm23

```
Private Sub CommandButton1_Click()

Dim E_STAR(100) As Single
Dim C_STAR(100) As Single
Dim G_STAR(100) As Single
Dim F_STAR(100) As Single
Dim A_STAR(100) As Single
Dim XRD(100) As Single
Dim count As Integer
Dim try As Integer
Dim XGE1(100) As Single
Dim XGE2(100) As Single
Dim XGE3(100) As Single
Dim XGE4(100) As Single
Dim XGE5(100) As Single
Dim XGE6(100) As Single
Dim XGE7(100) As Single
Dim XGE8(100) As Single

Sheets("Sheet1").Select
'Sheets.Add.Name = "Sheet11"
count = 1
For try = 1 To 60
    A_STAR(try) = Application.Sum(Range("A" & try).Resize(, 1))
    C_STAR(try) = Application.Sum(Range("C" & try).Resize(, 1))
    E_STAR(try) = Application.Sum(Range("D" & try).Resize(, 1))
    G_STAR(try) = Application.Sum(Range("E" & try).Resize(, 1))
    F_STAR(try) = Application.Sum(Range("F" & try).Resize(, 1))
    XRD(try) = Application.Sum(Range("G" & try).Resize(, 1))

  ' MsgBox F_STAR(try)


    XGE1(try) = (((E_STAR(try) - 400.5) - (0.6928 * (C_STAR(try) - 520))) / 61.31)
    XGE2(try) = (((E_STAR(try) - 400.5) - (0.6928 * (C_STAR(try) - 520))) / 57.154)
    XGE3(try) = (((E_STAR(try) - 400.5) - (0.6928 * (C_STAR(try) - 520))) / 60.41)
    XGE4(try) = (((E_STAR(try) - 400.5) - (0.6928 * (C_STAR(try) - 520))) / 59.11)
    XGE5(try) = (((E_STAR(try) - 400.5) - (0.6928 * (C_STAR(try) - 520))) / 54.954)
    XGE6(try) = (((E_STAR(try) - 400.5) - (0.6928 * (C_STAR(try) - 520))) / 58.21)
    XGE7(try) = (((G_STAR(try) - 282.5) + (0.6678 * (400.5 - E_STAR(try)))) / 6.517)
```

```
    XGE8(try) = (((G_STAR(try) - 282.5) + (0.6678 * (400.5 - E_STAR(try)))) / 7.986)

If OptionButton1 = True Then
  If F_STAR(try) = 40 Then
      Sheets("Sheet11").Range("A1").Offset(count).Value =
Sheets("Sheet1").Range("A1").Offset(try).Value
      Sheets("Sheet11").Range("B1").Offset(count).Value = XGE1(try)
      Sheets("Sheet11").Range("C1").Offset(count).Value = XGE2(try)
      Sheets("Sheet11").Range("D1").Offset(count).Value = XGE3(try)
      Sheets("Sheet11").Range("E1").Offset(count).Value = XGE4(try)
      Sheets("Sheet11").Range("F1").Offset(count).Value = XGE5(try)
      Sheets("Sheet11").Range("G1").Offset(count).Value = XGE6(try)
      Sheets("Sheet11").Range("H1").Offset(count).Value = XGE7(try)
      Sheets("Sheet11").Range("I1").Offset(count).Value = XGE8(try)

      Sheets("Sheet11").Range("J1").Offset(count).Value =
Sheets("Sheet1").Range("G1").Offset(try).Value
      Sheets("Sheet11").Range("A1000").Offset(count).Value =
Sheets("Sheet1").Range("A1").Offset(try).Value
      Sheets("Sheet11").Range("B1000").Offset(count).Value = XGE1(try) - XRD(try)
      Sheets("Sheet11").Range("C1000").Offset(count).Value = XGE2(try) - XRD(try)
      Sheets("Sheet11").Range("D1000").Offset(count).Value = XGE3(try) - XRD(try)
      Sheets("Sheet11").Range("E1000").Offset(count).Value = XGE4(try) - XRD(try)
      Sheets("Sheet11").Range("F1000").Offset(count).Value = XGE5(try) - XRD(try)
      Sheets("Sheet11").Range("G1000").Offset(count).Value = XGE6(try) - XRD(try)
      Sheets("Sheet11").Range("H1000").Offset(count).Value = XGE7(try) - XRD(try)
      Sheets("Sheet11").Range("I1000").Offset(count).Value = XGE8(try) - XRD(try)
      Sheets("Sheet11").Range("J1000").Offset(count).Value =
Sheets("Sheet1").Range("G1").Offset(try).Value


      count = count + 1
   End If

End If

If OptionButton2 = True Then
  If F_STAR(try) = 80 Then
      Sheets("Sheet11").Range("A1").Offset(count).Value =
Sheets("Sheet1").Range("A1").Offset(try).Value
      Sheets("Sheet11").Range("B1").Offset(count).Value = XGE1(try)
      Sheets("Sheet11").Range("C1").Offset(count).Value = XGE2(try)
      Sheets("Sheet11").Range("D1").Offset(count).Value = XGE3(try)
      Sheets("Sheet11").Range("E1").Offset(count).Value = XGE4(try)
      Sheets("Sheet11").Range("F1").Offset(count).Value = XGE5(try)
      Sheets("Sheet11").Range("G1").Offset(count).Value = XGE6(try)
```

```
        Sheets("Sheet11").Range("H1").Offset(count).Value = XGE7(try)
        Sheets("Sheet11").Range("I1").Offset(count).Value = XGE8(try)

        Sheets("Sheet11").Range("J1").Offset(count).Value =
Sheets("Sheet1").Range("G1").Offset(try).Value

        Sheets("Sheet11").Range("A1000").Offset(count).Value =
Sheets("Sheet1").Range("A1").Offset(try).Value
        Sheets("Sheet11").Range("B1000").Offset(count).Value = XGE1(try) - XRD(try)
        Sheets("Sheet11").Range("C1000").Offset(count).Value = XGE2(try) - XRD(try)
        Sheets("Sheet11").Range("D1000").Offset(count).Value = XGE3(try) - XRD(try)
        Sheets("Sheet11").Range("E1000").Offset(count).Value = XGE4(try) - XRD(try)
        Sheets("Sheet11").Range("F1000").Offset(count).Value = XGE5(try) - XRD(try)
        Sheets("Sheet11").Range("G1000").Offset(count).Value = XGE6(try) - XRD(try)
        Sheets("Sheet11").Range("H1000").Offset(count).Value = XGE7(try) - XRD(try)
        Sheets("Sheet11").Range("I1000").Offset(count).Value = XGE8(try) - XRD(try)
        Sheets("Sheet11").Range("J1000").Offset(count).Value =
Sheets("Sheet1").Range("G1").Offset(try).Value

      count = count + 1
    End If
End If
If OptionButton3 = True Then
   If F_STAR(try) = 100 Then
        Sheets("Sheet11").Range("A1").Offset(count).Value =
Sheets("Sheet1").Range("A1").Offset(try).Value
        Sheets("Sheet11").Range("B1").Offset(count).Value = XGE1(try)
        Sheets("Sheet11").Range("C1").Offset(count).Value = XGE2(try)
        Sheets("Sheet11").Range("D1").Offset(count).Value = XGE3(try)
        Sheets("Sheet11").Range("E1").Offset(count).Value = XGE4(try)
        Sheets("Sheet11").Range("F1").Offset(count).Value = XGE5(try)
        Sheets("Sheet11").Range("G1").Offset(count).Value = XGE6(try)
        Sheets("Sheet11").Range("H1").Offset(count).Value = XGE7(try)
        Sheets("Sheet11").Range("I1").Offset(count).Value = XGE8(try)

        Sheets("Sheet11").Range("J1").Offset(count).Value =
Sheets("Sheet1").Range("G1").Offset(try).Value

        Sheets("Sheet11").Range("A1000").Offset(count).Value =
Sheets("Sheet1").Range("A1").Offset(try).Value
        Sheets("Sheet11").Range("B1000").Offset(count).Value = XGE1(try) - XRD(try)
        Sheets("Sheet11").Range("C1000").Offset(count).Value = XGE2(try) - XRD(try)
        Sheets("Sheet11").Range("D1000").Offset(count).Value = XGE3(try) - XRD(try)
        Sheets("Sheet11").Range("E1000").Offset(count).Value = XGE4(try) - XRD(try)
        Sheets("Sheet11").Range("F1000").Offset(count).Value = XGE5(try) - XRD(try)
        Sheets("Sheet11").Range("G1000").Offset(count).Value = XGE6(try) - XRD(try)
```

```
        Sheets("Sheet11").Range("H1000").Offset(count).Value = XGE7(try) - XRD(try)
        Sheets("Sheet11").Range("I1000").Offset(count).Value = XGE8(try) - XRD(try)
        Sheets("Sheet11").Range("J1000").Offset(count).Value =
Sheets("Sheet1").Range("G1").Offset(try).Value


        count = count + 1
    End If
 End If
If OptionButton4 = True Then
   If F_STAR(try) = 225 Then
        Sheets("Sheet11").Range("A1").Offset(count).Value =
Sheets("Sheet1").Range("A1").Offset(try).Value
        Sheets("Sheet11").Range("B1").Offset(count).Value = XGE1(try)
        Sheets("Sheet11").Range("C1").Offset(count).Value = XGE2(try)
        Sheets("Sheet11").Range("D1").Offset(count).Value = XGE3(try)
        Sheets("Sheet11").Range("E1").Offset(count).Value = XGE4(try)
        Sheets("Sheet11").Range("F1").Offset(count).Value = XGE5(try)
        Sheets("Sheet11").Range("G1").Offset(count).Value = XGE6(try)
        Sheets("Sheet11").Range("H1").Offset(count).Value = XGE7(try)
        Sheets("Sheet11").Range("I1").Offset(count).Value = XGE8(try)

        Sheets("Sheet11").Range("J1").Offset(count).Value =
Sheets("Sheet1").Range("G1").Offset(try).Value

        Sheets("Sheet11").Range("A1000").Offset(count).Value =
Sheets("Sheet1").Range("A1").Offset(try).Value
        Sheets("Sheet11").Range("B1000").Offset(count).Value = XGE1(try) - XRD(try)
        Sheets("Sheet11").Range("C1000").Offset(count).Value = XGE2(try) - XRD(try)
        Sheets("Sheet11").Range("D1000").Offset(count).Value = XGE3(try) - XRD(try)
        Sheets("Sheet11").Range("E1000").Offset(count).Value = XGE4(try) - XRD(try)
        Sheets("Sheet11").Range("F1000").Offset(count).Value = XGE5(try) - XRD(try)
        Sheets("Sheet11").Range("G1000").Offset(count).Value = XGE6(try) - XRD(try)
        Sheets("Sheet11").Range("H1000").Offset(count).Value = XGE7(try) - XRD(try)
        Sheets("Sheet11").Range("I1000").Offset(count).Value = XGE8(try) - XRD(try)
        Sheets("Sheet11").Range("J1000").Offset(count).Value =
Sheets("Sheet1").Range("G1").Offset(try).Value

        count = count + 1
    End If
 End If
If OptionButton5 = True Then
   If F_STAR(try) = 426 Then
   MsgBox "426"
        Sheets("Sheet11").Range("A1").Offset(count).Value =
Sheets("Sheet1").Range("A1").Offset(try).Value
```

```
        Sheets("Sheet11").Range("B1").Offset(count).Value = XGE1(try)
        Sheets("Sheet11").Range("C1").Offset(count).Value = XGE2(try)
        Sheets("Sheet11").Range("D1").Offset(count).Value = XGE3(try)
        Sheets("Sheet11").Range("E1").Offset(count).Value = XGE4(try)
        Sheets("Sheet11").Range("F1").Offset(count).Value = XGE5(try)
        Sheets("Sheet11").Range("G1").Offset(count).Value = XGE6(try)
        Sheets("Sheet11").Range("H1").Offset(count).Value = XGE7(try)
        Sheets("Sheet11").Range("I1").Offset(count).Value = XGE8(try)
        Sheets("Sheet11").Range("J1").Offset(count).Value =
Sheets("Sheet1").Range("G1").Offset(try).Value

        Sheets("Sheet11").Range("A1000").Offset(count).Value =
Sheets("Sheet1").Range("A1").Offset(try).Value
        Sheets("Sheet11").Range("B1000").Offset(count).Value = XGE1(try) - XRD(try)
        Sheets("Sheet11").Range("C1000").Offset(count).Value = XGE2(try) - XRD(try)
        Sheets("Sheet11").Range("D1000").Offset(count).Value = XGE3(try) - XRD(try)
        Sheets("Sheet11").Range("E1000").Offset(count).Value = XGE4(try) - XRD(try)
        Sheets("Sheet11").Range("F1000").Offset(count).Value = XGE5(try) - XRD(try)
        Sheets("Sheet11").Range("G1000").Offset(count).Value = XGE6(try) - XRD(try)
        Sheets("Sheet11").Range("H1000").Offset(count).Value = XGE7(try) - XRD(try)
        Sheets("Sheet11").Range("I1000").Offset(count).Value = XGE8(try) - XRD(try)
        Sheets("Sheet11").Range("J1000").Offset(count).Value =
Sheets("Sheet1").Range("G1").Offset(try).Value

        count = count + 1
    End If
End If

If OptionButton6 = True Then
   If F_STAR(try) = 439 Then
        Sheets("Sheet11").Range("A1").Offset(count).Value =
Sheets("Sheet1").Range("A1").Offset(try).Value
        Sheets("Sheet11").Range("B1").Offset(count).Value = XGE1(try)
        Sheets("Sheet11").Range("C1").Offset(count).Value = XGE2(try)
        Sheets("Sheet11").Range("D1").Offset(count).Value = XGE3(try)
        Sheets("Sheet11").Range("E1").Offset(count).Value = XGE4(try)
        Sheets("Sheet11").Range("F1").Offset(count).Value = XGE5(try)
        Sheets("Sheet11").Range("G1").Offset(count).Value = XGE6(try)
        Sheets("Sheet11").Range("H1").Offset(count).Value = XGE7(try)
        Sheets("Sheet11").Range("I1").Offset(count).Value = XGE8(try)
        Sheets("Sheet11").Range("J1").Offset(count).Value =
Sheets("Sheet1").Range("G1").Offset(try).Value

        Sheets("Sheet11").Range("A1000").Offset(count).Value =
Sheets("Sheet1").Range("A1").Offset(try).Value
        Sheets("Sheet11").Range("B1000").Offset(count).Value = XGE1(try) - XRD(try)
```

```
        Sheets("Sheet11").Range("C1000").Offset(count).Value = XGE2(try) - XRD(try)
        Sheets("Sheet11").Range("D1000").Offset(count).Value = XGE3(try) - XRD(try)
        Sheets("Sheet11").Range("E1000").Offset(count).Value = XGE4(try) - XRD(try)
        Sheets("Sheet11").Range("F1000").Offset(count).Value = XGE5(try) - XRD(try)
        Sheets("Sheet11").Range("G1000").Offset(count).Value = XGE6(try) - XRD(try)
        Sheets("Sheet11").Range("H1000").Offset(count).Value = XGE7(try) - XRD(try)
        Sheets("Sheet11").Range("I1000").Offset(count).Value = XGE8(try) - XRD(try)
        Sheets("Sheet11").Range("J1000").Offset(count).Value =
Sheets("Sheet1").Range("G1").Offset(try).Value
      count = count + 1
    End If
End If

If OptionButton7 = True Then
   If F_STAR(try) = 490 Then
        Sheets("Sheet11").Range("A1").Offset(count).Value =
Sheets("Sheet1").Range("A1").Offset(try).Value
        Sheets("Sheet11").Range("B1").Offset(count).Value = XGE1(try)
        Sheets("Sheet11").Range("C1").Offset(count).Value = XGE2(try)
        Sheets("Sheet11").Range("D1").Offset(count).Value = XGE3(try)
        Sheets("Sheet11").Range("E1").Offset(count).Value = XGE4(try)
        Sheets("Sheet11").Range("F1").Offset(count).Value = XGE5(try)
        Sheets("Sheet11").Range("G1").Offset(count).Value = XGE6(try)
        Sheets("Sheet11").Range("H1").Offset(count).Value = XGE7(try)
        Sheets("Sheet11").Range("I1").Offset(count).Value = XGE8(try)

        Sheets("Sheet11").Range("A1000").Offset(count).Value =
Sheets("Sheet1").Range("A1").Offset(try).Value
        Sheets("Sheet11").Range("B1000").Offset(count).Value = XGE1(try) - XRD(try)
        Sheets("Sheet11").Range("C1000").Offset(count).Value = XGE2(try) - XRD(try)
        Sheets("Sheet11").Range("D1000").Offset(count).Value = XGE3(try) - XRD(try)
        Sheets("Sheet11").Range("E1000").Offset(count).Value = XGE4(try) - XRD(try)
        Sheets("Sheet11").Range("F1000").Offset(count).Value = XGE5(try) - XRD(try)
        Sheets("Sheet11").Range("G1000").Offset(count).Value = XGE6(try) - XRD(try)
        Sheets("Sheet11").Range("H1000").Offset(count).Value = XGE7(try) - XRD(try)
        Sheets("Sheet11").Range("I1000").Offset(count).Value = XGE8(try) - XRD(try)
        Sheets("Sheet11").Range("J1000").Offset(count).Value =
Sheets("Sheet1").Range("G1").Offset(try).Value
        count = count + 1
    End If
End If



Next
```

```
MsgBox "Done"
End Sub

Private Sub CommandButton2_Click()
  Charts.Add
   ActiveChart.ChartType = xlLineMarkers
   ActiveChart.SetSourceData Source:=Sheets("Sheet11").Range("A1:J11"), PlotBy _
      :=xlRows
   ActiveChart.Location Where:=xlLocationAsNewSheet
   With ActiveChart
      .HasTitle = True
      .ChartTitle.Characters.Text = "Ge for Selected Thickness"
      .Axes(xlCategory, xlPrimary).HasTitle = True
      .Axes(xlCategory, xlPrimary).AxisTitle.Characters.Text = "Equations"
      .Axes(xlValue, xlPrimary).HasTitle = True
      .Axes(xlValue, xlPrimary).AxisTitle.Characters.Text = "Ge Value"
   End With
   With ActiveChart
      .HasAxis(xlCategory, xlPrimary) = True
      .HasAxis(xlValue, xlPrimary) = True
   End With
   ActiveChart.Axes(xlCategory, xlPrimary).CategoryType = xlAutomatic
   ActiveChart.HasDataTable = False

    fname = ThisWorkbook.Path & "\" & ActiveChart.Name & ".gif"
ActiveChart.Export Filename:=fname, FilterName:="GIF"
Image1.Picture = LoadPicture(fname)
Image1.PictureSizeMode = fmPictureSizeModeStretch
End Sub

Private Sub CommandButton3_Click()
  Charts.Add
   ActiveChart.ChartType = xlLineMarkers
   ActiveChart.SetSourceData Source:=Sheets("Sheet11").Range("A1000:J1020"),
PlotBy _
      :=xlRows
   ActiveChart.Location Where:=xlLocationAsNewSheet
   With ActiveChart
      .HasTitle = True
      .ChartTitle.Characters.Text = "Ge for Selectied Thickness"
      .Axes(xlCategory, xlPrimary).HasTitle = True
      .Axes(xlCategory, xlPrimary).AxisTitle.Characters.Text = "Equations"
      .Axes(xlValue, xlPrimary).HasTitle = True
      .Axes(xlValue, xlPrimary).AxisTitle.Characters.Text = "Ge Value"
   End With
   With ActiveChart
```

```
        .HasAxis(xlCategory, xlPrimary) = True
        .HasAxis(xlValue, xlPrimary) = True
    End With
    ActiveChart.Axes(xlCategory, xlPrimary).CategoryType = xlAutomatic
    ActiveChart.HasDataTable = False

     fname = ThisWorkbook.Path & "\" & ActiveChart.Name & ".gif"
  '  MsgBox fname
ActiveChart.Export Filename:=fname, FilterName:="GIF"
Image1.Picture = LoadPicture(fname)
Image1.PictureSizeMode = fmPictureSizeModeStretch
End Sub

Private Sub CommandButton4_Click()
UserForm23.Hide
UserForm14.Show
End Sub

Private Sub Image1_Click()

End Sub

Private Sub OptionButton1_Click()

End Sub

Private Sub UserForm_Click()

End Sub
```